SEARCH FOR A SCALAR PARTNER OF THE TOP QUARK IN THE JETS+$E_{\mathrm{T}}^{\mathrm{miss}}$ FINAL STATE WITH THE ATLAS DETECTOR

by

CHAOWAROJ WANOTAYAROJ

A DISSERTATION

Presented to the Department of Physics
and the Graduate School of the University of Oregon
in partial fulfillment of the requirements
for the degree of
Doctor of Philosophy

December 2016

DISSERTATION APPROVAL PAGE

Student: Chaowaroj Wanotayaroj

Title: Search for a Scalar Partner of the Top Quark in the Jets+ETMiss Final State with the ATLAS detector

This dissertation has been accepted and approved in partial fulfillment of the requirements for the Doctor of Philosophy degree in the Department of Physics by:

Stephanie Majewski	Chair
James Brau	Advisor
Steven van Enk	Member
James Isenberg	Institutional Representative

and

Scott L. Pratt	Dean of the Graduate School

Original approval signatures are on file with the University of Oregon Graduate School.

Degree awarded December 2016

DISSERTATION ABSTRACT

Chaowaroj Wanotayaroj

Doctor of Philosophy

Department of Physics

December 2016

Title: Search for a Scalar Partner of the Top Quark in the Jets+ETMiss Final State with the ATLAS detector

This dissertation presents searches for direct pair production of a scalar partner of the top quark in events with only jets and missing transverse energy in proton–proton collisions recorded during LHC Run 1 and Run 2 with the ATLAS detector. In the supersymmetry scenario, the partner is called top squark or stop. The stop ($\tilde{t}$) is assumed to decay via $\tilde{t} \to t\tilde{\chi}_1^0$, $\tilde{t} \to b\tilde{\chi}_1^\pm \to bW^{(*)}\tilde{\chi}_1^0$, or $\tilde{t} \to bW\tilde{\chi}_1^0$, where $\tilde{\chi}_1^0$ ($\tilde{\chi}_1^\pm$) denotes the lightest neutralino (chargino). Exclusion limits are reported in terms of the stop and neutralino masses.

The LHC Run 1 analysis uses an integrated luminosity of 20.1 fb^{-1} at $\sqrt{s} = 8$ TeV to exclude top squark masses in the range 270–645 GeV for $\tilde{\chi}_1^0$ masses below 30 GeV, assuming a 100% $\tilde{t} \to t\tilde{\chi}_1^0$ branching ratio (BR). For a BR of 50% to either $\tilde{t} \to t\tilde{\chi}_1^0$ or $\tilde{t} \to b\tilde{\chi}_1^\pm$, and assuming $m_{\tilde{\chi}_1^\pm} = 2m_{\tilde{\chi}_1^0}$, stop masses in the range 250–550 GeV are excluded for $\tilde{\chi}_1^0$ masses below 60 GeV.

The LHC Run 2 analysis uses an integrated luminosity of 13.3 fb^{-1} at $\sqrt{s} = 13$ TeV. Assuming a 100% $\tilde{t} \to t\tilde{\chi}_1^0$ BR, stop masses in the range 310–820 GeV are excluded for $\tilde{\chi}_1^0$ masses below 160 GeV. For $m_{\tilde{t}} \sim m_t + m_{\tilde{\chi}^0}$ scenario, the search excludes stop masses between 23–380 GeV. Additionally, scenarios where stops are produced indirectly through gluino decay but have very low p_T signature due to a very small $\Delta(m_{\tilde{t}}, m_{\tilde{\chi}^0})$, have been

considered. The result is interpreted as an upper limit for the cross section in terms of the gluino and stop masses. This excludes all models considered which include $m_{\tilde{g}}$ up to 1600 GeV with $m_{\tilde{\chi}^0} < 560$ GeV at 95% CL.

Finally, the analysis strategy from the LHC Run 1 search is applied in the broader scope of supersymmetry called Phenomenological Minimum Supersymmetric Standard Model (pMSSM). This dissertation presents a summary of the results that related to the stop search.

This dissertation includes previously published and unpublished co-authored material.

CURRICULUM VITAE

NAME OF AUTHOR: Chaowaroj Wanotayaroj

GRADUATE AND UNDERGRADUATE SCHOOLS ATTENDED:
University of Oregon
University of Oregon

DEGREES AWARDED:
Doctor of Philosophy, Physics, 2016, University of Oregon
Master of Science in Physics, 2011, University of Oregon
Bachelor of Science in Physics, 2009, University of Oregon
Bachelor of Science in Mathematics, 2009, University of Oregon

AREAS OF SPECIAL INTEREST:
Supersymmetry
Jet and Missing Transverse Momentum Measurements

PROFESSIONAL EXPERIENCE:

University Of Oregon: Graduate Research Assistant: ATLAS Collaboration, 2012-Present

University Of Oregon: Graduate Research Assistant: SiD detector for the International Linear Collider, 2010-2012

University Of Oregon: Teaching Assistant: Department of Physics, 2009-2012

GRANTS, AWARDS AND HONORS:

Magna Cum Laude in Physics with Department Honor, 2009

PUBLICATIONS:

List of publications with significant contributions:

ATLAS Collaboration. *Search for the Supersymmetric Partner of the Top Quark in the Jets+Emiss Final State at sqrt(s) = 13 TeV*. tech. rep. ATLAS-CONF-2016-077. Geneva: CERN, Aug. 2016. URL: `https://cds.cern.ch/record/2206250`

ATLAS Collaboration. "Summary of the ATLAS experiment's sensitivity to supersymmetry after LHC Run 1 — interpreted in the phenomenological MSSM". in: *JHEP* 1510 (2015), p. 134. DOI: 10.1007/JHEP10(2015)134. arXiv: 1508.06608 [hep-ex]

Chaowaroj Wanotayaroj. "The effect of ATLAS Run-1 supersymmetric searches in the pMSSM". in: *23rd International Conference on Supersymmetry and Unification of Fundamental Interactions (SUSY2015), Tahoe, CA, USA*. Aug. 2015. URL: https://cds.cern.ch/record/2047858

Chaowaroj Wanotayaroj. "Poster for LHCP2014: Search for direct pair production of the top squark in all-hadronic final states in proton-proton collisions at $\sqrt{s} = 8$ TeV with the ATLAS detector". In: *Proceedings, 2nd Conference on Large Hadron Collider Physics Conference (LHCP 2014): New York, USA, June 2-7, 2014*. June 2014. URL: https://cds.cern.ch/record/1707904

Benjamin Nachman et al. "Jets from Jets: Re-clustering as a tool for large radius jet reconstruction and grooming at the LHC". in: *JHEP* 02 (2015), p. 075. DOI: 10.1007/JHEP02(2015)075. arXiv: 1407.2922 [hep-ph]

ATLAS Collaboration. "Search for direct pair production of the top squark in all-hadronic final states in proton–proton collisions at $\sqrt{s} = 8$ TeV with the ATLAS detector". In: *JHEP* 1409 (2014), p. 015. DOI: 10.1007/JHEP09(2014)015. arXiv: 1406.1122 [hep-ex]

Spencer Chang et al. "Revisiting Theories with Enhanced Higgs Couplings to Weak Gauge Bosons". In: *Phys. Rev.* D86 (2012), p. 095015. DOI: 10.1103/PhysRevD.86.095015. arXiv: 1207.0493 [hep-ph]

Co-authored on 299 publications with minor contributions.

ACKNOWLEDGEMENTS

I would like to thank my committee: my advisor Jim Brau, the chair Stephanie Majewski, Steven van Enk, and Jim Isenberg.

I would like to thank my family, including my three extended ones:

My family of physicists: you know how I struggled, and I am glad you were there with me.

My family of runners: you push further than I ever before with your countless encouragements.

My family of “others”: we may not have a lot in common but by some miracles we met. You have added wonderful varieties to my life.

I would like to humbly dedicate this work to King Bhumibol Adulyadej Rama IX of Thailand, in honor of his 70 years of hard work to improve people's life.

and

To every teacher in my life for guiding me here.

TABLE OF CONTENTS

Chapter Page

Chapter Page

Chapter Page

LIST OF FIGURES

Figure Page

Figure Page

Figure Page

LIST OF TABLES

Table Page

Table Page

CHAPTER I

INTRODUCTION

The biggest questions in physics, and to some extent science in general, regard opposite extreme ends of scale. On the largest scale known to us, the Observable Universe, we want to know about the past, present, and the future. The subject of cosmology tries to answer these questions: How did the Universe begin? Why does it look like it does? What is its ultimate fate? At the other end on the smallest scale, we want to know: what are we made of? How many elementary particles exist? What are the interactions that govern them? Are they point-like? From molecules to atoms to sub-atomic particles, particle physicists are probing into smaller and smaller scales. This corresponds to going higher in energy, so the field is also referred to as high energy physics. A lot of progress has been made after the birth of general relativity and quantum field theory in the twentieth century and now both sets of questions are considered tightly related — the fate of the universe is most likely decided by the interactions of the fundamental particles. In hindsight, it is perhaps unsurprising but it should still be considered as very remarkable that we can connect the two scales.

The best existing theory of particle physics is the Standard Model (SM). In this model all known matter is made out of fermions, known as quarks and leptons. In each "generation", there are two quarks, the up type having $+\frac{2}{3}$ and the down type having $-\frac{1}{3}$ of the electric charge magnitude of an electron. Each generation of leptons consists of a charged particle — the electron in case of the first generation, and a neutral particle — the neutrino, referred to by its corresponding charge partner (e.g. electron neutrino). The SM has three such generations of particles, though most of the matter in everyday life can be explained using only the first. Interactions between the fermions are explained by the exchange of bosons which are the force carriers in the theory. They are the photon (γ), W

and Z bosons, and gluon. The first three are responsible for electromagnetic (EM) and weak nuclear interaction, while the gluon carries the strong nuclear interaction. Finally, the newly discovery Higgs boson [8, 9] explains the masses of these particles.

With the Higgs boson as the last piece, the SM is a self-consistent theory[1]. Up until now, most existing data from experiments on earth can be very well explained by the SM. But this is certainly not the end of high energy physics. Among many others, two big questions for the SM are hidden in the subtlety of the previous statements. First, a big puzzle for particle physics is that the SM fails to explain many observations in astronomy, which point to the existence of "dark matter"— matter that interacts gravitationally but not electromagnetically ("dark"). Second, while self-consistent, some parameters of the theory have to be at very precise numbers from a large range of possible values to explain the relatively small mass of the discovered Higgs boson. This is usually referred to as the hierarchy problem. Fortunately, there are hints that these two puzzles are tied together, and the energy scale needed to explore these questions is accessible at the Large Hadron Collider (LHC). With unprecedented collision energy and a large amount of data, the LHC is putting the SM to the test like never before.

1.1. The Standard Model

The Standard Model is a quantum field theory describing all known fundamental particles and their interactions. The fields content is the minimum number necessary to account for the observed particles in nature. It is accompanied by the most general set of interactions according to the field content, with an extra requirement that those interactions are *renormalizable*. This means that divergences only appear in a finite number of parameters and they can be extracted by measuring physical observables in experiments.

[1] Without the Higgs, some processes such as longitudinal WW scattering amplitude would blows up at high energy, for example.

The Lagrangian of the SM, written in a schematically compact form, is:

$$\begin{aligned}\mathscr{L} = &-\frac{1}{4}F_{\mu\nu}F^{\mu\nu} + i\bar{\psi}\not{D}\psi + \text{h.c.} && \rightarrow \text{Bosons and fermions kinetic terms}\\ &+ \psi_i Y_{ij}\psi_j\phi + \text{h.c.} && \rightarrow \text{Yukawa interactions}\\ &+ |D_\mu\phi|^2 + V(\phi) && \rightarrow \text{Higgs kinetic term and potential}\end{aligned} \tag{1.1}$$

$F_{\mu\nu}$ includes all gauge fields-strengths which will be defined below. ψ represents spin-1/2 fermions (see Table 1.1), and ϕ is a complex scale doublet.

1.1.1. Gauge Sector

The gauged symmetry group of the SM is $SU(3)_c \times SU(2)_L \times U(1)_Y$. The particle field content in the standard model are summarized in Table 1.1. The gauge bosons associated with each symmetry are explained below.

TABLE 1.1. Summary of SM field contents and their gauge group representations. The $SU(3)_c$ and $SU(2)_L$ representations are labeled with their dimensions, while the eigenvalues (weak hypercharge) are given for $U(1)_Y$ symmetry. Here we choose $Q_{EM} = T_3 + Y$.

Name	Field components	$SU(3)_c$, $SU(2)_L$, $U(1)_Y$	Comments
Spin-1/2 quarks			
Q	$\begin{pmatrix} u_L & d_L \end{pmatrix}$	$(3, 2, \frac{1}{6})$	×3 generations
	u_R	$(\bar{3}, 1, \frac{2}{3})$	
	d_R	$(\bar{3}, 1, -\frac{1}{3})$	
Spin-1/2 leptons			
L	$\begin{pmatrix} \nu_L & e_L \end{pmatrix}$	$(1, 2, -\frac{1}{2})$	×3 generations
	e_R	$(1, 1, -1)$	
Spin-0 Higgs			
ϕ	$\begin{pmatrix} \phi^+ & \phi^0 \end{pmatrix}$	$(1, 2, \frac{1}{2})$	
Spin-1 gauge bosons			
Gluons	$G^{1,\ldots,8}$	$(8, 1, 0)$	
W	$\begin{pmatrix} W^1 & W^2 & W^3 \end{pmatrix}$	$(1, 3, 0)$	
B	B^0	$(1, 1, 0)$	

$SU(3)_c$ Quantum chromodynamic (QCD) There are eight spin-1 gluons, G^α_μ, $\alpha = 1, \ldots, 8$ associated with $SU(3)_c$ with "c" denoting "color" quantum numbers of this gauge group. Any colored particle, in other words, a particle that will transform in respect to this symmetry, will interact with gluons. This is also called *strong* interaction. In the SM, only gluons and quarks are colored.

$SU(2)_L$ Weak Isospin The gauge boson for this symmetry is three spin-1 W^a_μ, $a = 1, 2, 3$. The subscript L refers to the fact that only the left-handed fermions transform in respect to this symmetry — they are $SU(2)$ doublets, while the right-handed components are singlets. This makes the SM a *chiral* gauge theory.

$U(1)_Y$ Weak Hypercharge There is only one spin-1 gauge boson, B, associated with this symmetry. The subscript Y distinguishes it from the electromagnetic $U(1)_{EM}$ which will manifest after $SU(2)_L \times U(1)_Y$ is spontaneously broken by the Higgs potential as discussed in Section 1.1.2.1.

The total covariant derivative is:

$$\partial_\mu \psi \to D_\mu \psi \equiv (\partial_\mu - i g_S G^\alpha_\mu \lambda^\alpha - i g W^a_\mu \frac{\sigma^a}{2} - i g' B_\mu Y)\psi \tag{1.2}$$

where g_S, g, and g' are the gauge couplings. The field strengths are:

$$G^\alpha_{\mu\nu} = \partial_\mu G^\alpha_\nu - \partial_\nu G^\alpha_\mu + g_S f^\alpha_{\beta\gamma} G^\beta_\mu G^\gamma_\nu \tag{1.3}$$

$$W^a_{\mu\nu} = \partial_\mu W^a_\nu - \partial_\nu W^a_\mu + g \epsilon_{abc} W^b_\mu W^c_\nu \tag{1.4}$$

$$B_{\mu\nu} = \partial_\mu B_\nu - \partial_\nu B_\mu \tag{1.5}$$

These are the ingredients for the first line in Eq. (1.1). Here I note that no combination of W and right-handed fermion fields can form a singlet term; therefore they do not interact. Similarly, direct mass terms such as $m^2 F^i_\mu F^i_\mu$ and $m^2_f \bar{\psi}\psi$ are forbidden by gauge invariance.

1.1.2. Higgs Sector

The gauge symmetry of the SM only allows massless spin-1 particle. On the other hand, the $W^{\pm}$ and Z are observed to be massive in nature. To fix this, the $SU(2)_L \times U(1)_Y$ symmetry must be spontaneously broken by a particle whose ground state is not invariant under the symmetry. In the SM, the scalar Higgs field is responsible for this *electroweak symmetry breaking (EWSB)*. Note that the $SU(3)_c$ symmetry is not broken thus the gluons remain massless.

1.1.2.1. Electroweak Symmetry Breaking

The most general gauge invariant Lagrangian for a complex scalar Higgs field ϕ is shown in the second and third line of Eq. (1.1). The covariant derivative for ϕ is:

$$D_\mu \phi = \partial_\mu \phi - \frac{i}{2}(g W_\mu^a \frac{\sigma^a}{2} + g' B_\mu)\phi \tag{1.6}$$

With the potential:

$$V(\phi) = \lambda(\phi^\dagger \phi - \frac{\mu^2}{2\lambda})^2 \tag{1.7}$$

$$= \lambda(\phi^\dagger \phi)^2 - \mu^2 \phi^\dagger \phi + \frac{\mu^4}{4\lambda} \tag{1.8}$$

If $\frac{\mu^2}{\lambda} > 0$, this potential has non-zero vacuum expectation value (VEV) $v^2 \equiv \frac{\mu^2}{\lambda}$. Make a gauge transformation so that:

$$\langle \phi \rangle = \frac{1}{\sqrt{2}} \begin{pmatrix} 0 \\ v \end{pmatrix} \tag{1.9}$$

Then write out the mass part of the gauge boson kinetic term $|D^\mu \phi|^2$:

$$\mathscr{L}_{mass} = -\frac{1}{8}\begin{pmatrix} 0 & v \end{pmatrix}\begin{pmatrix} gW_3 + g'B & g(W_1 - iW_2) \\ g(W_1 + iW_2) & -gW_3 + g'B \end{pmatrix}^2 \begin{pmatrix} 0 \\ v \end{pmatrix} \tag{1.10}$$

Diagonalize this mass matrix by first defining the *weak mixing angle*:

$$\tan\theta_W \equiv \frac{g'}{g} \tag{1.11}$$

and mass eigenstates:

$$W^\pm \equiv \frac{1}{\sqrt{2}}(W_1 \mp iW_2) \tag{1.12}$$

$$Z \equiv \cos\theta_W W_3 - \sin\theta_W B \tag{1.13}$$

$$A \equiv \sin\theta_W W_3 + \cos\theta_W B \tag{1.14}$$

Write out Eq. (1.10) with these fields:

$$\mathscr{L}_{mass} = -\frac{1}{4}g^2 v^2 W^+ W^- - \frac{1}{8}(g^2 + g'^2)v^2 Z^2 \tag{1.15}$$

Therefore:

$$M_W^2 = \frac{1}{4}g^2 v^2, \qquad M_Z^2 = \frac{1}{4}(g^2 + g'^2)v^2, \qquad M_A^2 = 0 \tag{1.16}$$

The massless A field indicates that there is an unbroken $U(1)$. These are identified as the massless photon and the unbroken $U(1)_{EM}$.

1.1.2.2. Higgs Boson

A complex scalar doublet has four degrees of freedom. Three become the longitudinal components of the gauge bosons as described above. The remaining degree of freedom

corresponds to a physical *Higgs boson*. To see this, use a gauge transformation to write in unitary gauge:

$$\phi = \frac{1}{\sqrt{2}} \begin{pmatrix} 0 \\ v + H(x) \end{pmatrix} \tag{1.17}$$

Now the potential reads:

$$V(\phi) = \lambda v^2 H^2 + \lambda v H^3 + \frac{\lambda}{4} H^4 \tag{1.18}$$

H is the SM Higgs boson with mass $\frac{1}{2}\lambda v^2$, presumably the one discovered in 2012 [8, 9].

1.1.2.3. Fermion Masses

SM fermions acquire their masses from the Yukawa interactions (second line in Eq. (1.1)). Writing it out more explicitly:

$$\bar{Q}_L^i Y_D^{ij} d_R^j \phi + \bar{Q}_L^i Y_U^{ij} u_R^j \tilde{\phi} + \bar{L}_L^i Y_E^{ij} e_R^j \phi + \text{h.c.}, \qquad \tilde{\phi} = \begin{pmatrix} 0 & 1 \\ -1 & 0 \end{pmatrix} \phi^* \tag{1.19}$$

After EWSB, replace ϕ by its VEV and diagonalize these mass matrices. The mass eigenstates u^I, d^I can be written as:

$$\begin{pmatrix} u_{Li}^I \\ d_{Li}^I \end{pmatrix} = (U_{uL}^\dagger)_{ij} \begin{pmatrix} u_{Lj} \\ (U_{uL} U_{dL}^\dagger)_{jk} d_{Lk} \end{pmatrix} \tag{1.20}$$

The 3×3 unitary matrix $V \equiv U_{uL} U_{dL}^\dagger$ is the Cabbibo-Kobayashi-Maskawa (CKM) matrix. It arises from the fact that the up- and down-type quarks are diagonalized differently. Note that since there is no mass term for the neutrinos, one can freely redefine neutrino fields, thus there is no such matrix in the lepton sector[2]. The absence of the CKM matrix

[2] Except that this is not true. Neutrinos oscillate so there is a neutrino mixing matrix. See Section 1.2.3.2.

for charged leptons leaves them with equal strength between flavors in the charge-current weak interactions (See Section 1.1.3.2). This feature of the SM is called *weak* or *lepton universality*.

1.1.3. Flavor Sector[3]

"Flavor" here refers to the six quarks grouped into three *families* or *generations*: (u)p and (d)own, (c)harm and (s)trange, (b)ottom and (t)op. The flavor sector has 10 physical parameters that arise from the Yukawa interactions — usually taken to be six quark masses and four from the CKM matrix.

1.1.3.1. CKM Matrix

The components of the CKM matrix can be written out as:

$$V = \begin{pmatrix} V_{ud} & V_{us} & V_{ub} \\ V_{cd} & V_{cs} & V_{cb} \\ V_{td} & V_{ts} & V_{tb} \end{pmatrix} \tag{1.21}$$

The components are not all arbitrary; there are only three real and one imaginary physical parameters for V. For the purpose of this discussion, it is convenient to choose the Wolfenstein parametrization which is an expansion in $V_{us} = \lambda \approx 0.22$. To $\mathcal{O}(\lambda^3)$. the CKM matrix is:

$$V = \begin{pmatrix} 1 - \frac{1}{2}\lambda^2 & \lambda & A\lambda^3(\rho - i\eta) \\ -\lambda & 1 - \frac{1}{2}\lambda^2 & A\lambda^2 \\ A\lambda^3(1 - \rho - i\eta) & -A\lambda^2 & 1 \end{pmatrix} \tag{1.22}$$

[3] Much of the discussion in this section is based on [10]

It is easy to see that the CKM matrix is almost diagonal with small off-diagonal terms. There is no fundamental reason in the SM for why the CKM matrix has this highly hierarchal structure. It is also referred to as the SM *flavor problem.*

1.1.3.2. Flavor Changing Interactions

Quark interactions with $W^{\pm}$ come from the kinetic term $\bar{\psi} \not{D} \psi$, written out explicitly in the interaction and mass eigenstates:

$$-\frac{g}{2}\bar{Q}_{Li}\gamma^{\mu}W_{\mu}^{a}\tau^{a}Q_{Li} + \text{h.c.} \xrightarrow[\text{eigenstates}]{\text{mass}} -\frac{g}{\sqrt{2}}\begin{pmatrix} \bar{u}_L & \bar{c}_L & \bar{t}_L \end{pmatrix}\gamma^{\mu}W_{\mu}^{+}V\begin{pmatrix} d_L \\ s_L \\ b_L \end{pmatrix} + \text{h.c.} \qquad (1.23)$$

The CKM matrix can be thought of as the rotation between these two bases. The fact that it is not diagonal makes the W interact with quarks of different flavors. This is the only flavor- and generation-changing vertice in the SM. Notice that the almost-diagonal structure of the CKM matrix makes the generation-changing processes small compared to the ones that only change flavors within the same generation.

1.1.3.3. Flavor Changing Neutral Current

"Neutral current" interactions are those between neutral gauge bosons and fermions. While flavor-conserving interactions are observed, it is an experimental fact that flavor-changing neutral current (FCNC) processes are highly suppressed. The SM ensures[4] this by having no tree-level FCNC process. There are four neutral bosons in the SM that can mediate FCNC. I will briefly discuss why they are forbidden:

[4] It is interesting to note that FCNC suppression is a built-in property of the SM, as opposed to the suppression of generation- changing charged current processes which come from the CKM parameters put in "by hand".

Gluon and photon They correspond to exact gauge symmetries. Their interactions with the fermions come from the kinetic terms. This makes their couplings flavor *universal*, meaning that they are of the same strength and diagonal in any basis. So gluons and photon can only interact with fermions from the same flavor.

Higgs boson The Higgs couplings to fermions *align* with the fermion mass matrix; they are proportional to the same Yukawa couplings. The fermion mass and Higgs interaction eigenstates are the same; therefore, Higgs interactions cannot change flavor. This can be seen when replacing ϕ in Eq. (1.19) with the right-hand side of Eq. (1.17). This feature relates to the fact that, in the SM, there is only one Higgs doublet and the only source of fermion masses is the Higgs VEV. If either or both conditions are not true, the Higgs will mediate FCNC in that theory[5].

Z boson Unlike the the charged W, the Z can only connect quarks from the same up- or down-type. When moving from the interaction to mass eigenstates, the rotation matrices involved are of the form $U_{uL}U_{uL}^{\dagger} = \mathbf{1}$, as opposed to the CKM matrix $U_{uL}U_{dL}^{\dagger}$. The couplings are therefore flavor universal. This feature comes from the fact that all fermions in the SM that belong to the same representation under the unbroken symmetries also belong to the same representation under the broken symmetries. For example, all $+\frac{2}{3}$ quarks have the the same $Y = \frac{1}{6}$ and $T_3 = \frac{1}{2}$. This does not have to be the case if all it needs is the correct $Q_{EM} = T_3 + Y$. Such theory, unlike the SM, will include FCNC via Z exchange.

Beyond the tree-level, FCNC in the SM processes are further suppressed by the diagonal and unitary structure of the CKM matrix. The latter related to the cancellations known as the *GIM mechanism*. A brief explanation is as follows: Box diagrams for meson

[5] As discussed later, Minimum Supersymmetric Standard Model satisfies neither; there are two Higgs doublets and sfermions can have bare mass terms.

mixing such as $B \leftrightarrow \bar{B}$ are shown in Fig. 1.1. If all quarks have the same mass, summing up all diagrams ($i, j = u, c, t$) gives zero amplitude due to the unitary structure of the CKM matrix. Putting in the actual quark masses break the cancellations up to $\sim m_i^2/m_W^2$. The top loop is also suppressed by the small mixing angle V_{td} and V_{ts}, making the total amplitude very small.

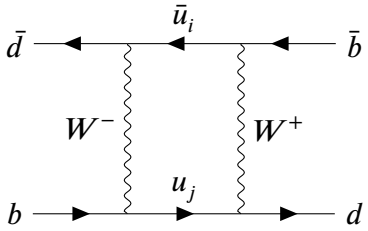

FIGURE 1.1. $B \leftrightarrow \bar{B}$ box diagrams.

1.1.3.4. Discrete Symmetries and CP Violation

There are three discrete symmetries that arise in a relativistic theory. They are parity (P), time reversal (T), and charge conjugation (C), with the first two directly related to the Lorentz group. While the combined CPT is conserved for any quantum field theory including the SM, it turns out that none of these are respected individually. C and P are maximally violated in the sense that the left- and right-handed fields belong to different gauge representations; therefore, C and P are violated regardless of the values of parameters in the SM. They only seems to be individually conserved in the low energy theory.

On the other hand, CP can be conserved with the right parameters. That is not the case in nature, so the SM must contain CP violation. The only source of CP violation in the electroweak sector[6] in the SM comes from the Yukawa interactions[7]. Under CP

[6] CP violation is suppressed in the strong sector by the value of Θ_3. The very small size of this parameter is a puzzle called the *strong CP problem* which motivates the existence of a real scalar *axion*. It is another candidate for dark matter.

[7] In a theory with extended Higgs sector such as the two Higgs doublet model, there can be other CP-violating terms

transformation, these are:

$$\bar{\psi}_L^i Y_{ij} \psi_R^j \phi + \bar{\psi}_R^i Y_{ij}^* \psi_L^j \phi \quad \underset{\text{transformation}}{\overset{\text{CP}}{\Longleftrightarrow}} \quad \bar{\psi}_R^i Y_{ij} \psi_L^j \phi + \bar{\psi}_L^i Y_{ij}^* \psi_R^j \phi \tag{1.24}$$

Therefore CP is violated if $Y_{ij} \neq Y_{ij}^*$. This requirement is manifested as the non-zero physical phase in the CKM matrix (η in Eq. (1.22)), which is indeed non-zero. It is interesting to note that the measured value, $\eta \approx 0.353$ cannot account for the baryon-antibaryon asymmetry in the universe.

1.1.4. Hadrons, Hadronization, and Jets

A unique feature of the strong interaction among others in the SM is that it gets weaker at higher energy, also called *asymptotically free*. At a sufficiently low energy, the coupling constant $\alpha_S = g_S^2/4\pi$ becomes "strong" and invalidates the perturbative treatment of α_S. The energy scale where the perturbation breakdown occurs is usually referred to as the Λ_{QCD}, which is $\sim \mathcal{O}(100\ \text{MeV})$. This leads to the color *confinement* hypothesis: the only energy eigenstates of the QCD Hamiltonian which have finite energy are $SU(3)_c$ singlets, also called *color neutral*. This hypothesis has not been rigorously proven using QCD Lagrangian, but is consistent with the fact that free quarks have never been observed[8]. These bound states singlets are called *hadrons*. They can be quark-antiquark pairs called *mesons*. Examples are the lightest states called pions: $u\bar{d}(\pi^+)$, $\bar{u}d(\pi^-)$, and $\frac{u\bar{u}-d\bar{d}}{\sqrt{2}}(\pi^0)$. Another combination is three quark states called *baryons*. Protons (uud) and neutrons (udd) are the two lightest baryonic states. Trying to break free a single quark from these bound states will require increasing amounts of energy as they are pulled further apart beyond the distance scale $1/\Lambda_{QCD}$. Eventually there will be enough energy to create quark-antiquark pairs and two hadrons are formed instead.

[8] Direct attempts to numerically compute the spectrum using lattice QCD support it.

Now one can picture what happens to gluons or quarks from high energy collision as follows: When $p_{\mathrm{T}} \gg \Lambda_{\mathrm{QCD}}$, perturbative QCD is applied. Colored quarks and gluons will radiate QCD showers. Eventually, $p_{\mathrm{T}} \sim \Lambda_{\mathrm{QCD}}$ and many colorless hadrons are formed. This process is called *hadronization*, and the ensembles of final state particles carrying the momentum of the initial quarks or gluons are called *jets*. A detailed definition of jets will be discussed later in Section 4.2. A graphic representation is shown in Fig. 1.2 and also in Fig. 3.14.

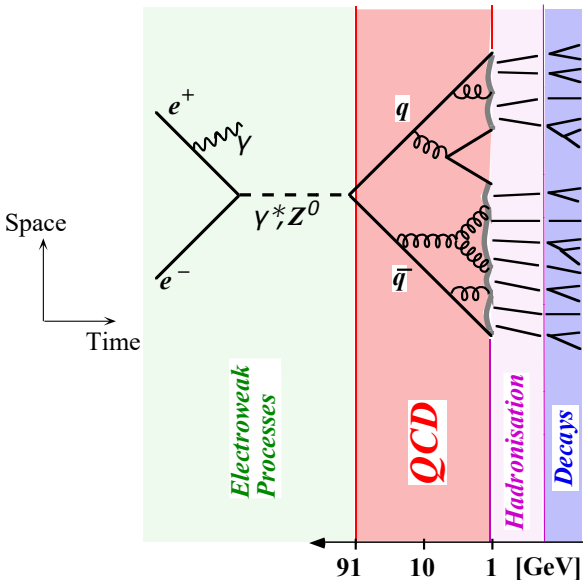

FIGURE 1.2. Taken from [11, 12]. Schematic representation of the evolution of quark produced in the final state of an interaction. Perturbative QCD are applied for QCD radiations until the energy falls below a certain threshold, then hadronization starts.

1.1.5. Top Quark Decays

The top quarks are a very important signature for this analysis, so I will discuss the decays in this section.

The top quark has a very short lifetime ($\tau \sim 5 \times 10^{-25}$ s), much shorter than the time scale for hadronization ($\Gamma_t \gg \Lambda_{\mathrm{QCD}}$) so it decays before top-flavored hadrons can form[9]. Due to the absent of FCNC in the SM[10]and the large $|V_{tb}|$, the $t \to W + b$ decay channels are vastly dominant and can be taken as 100% branching ratio (BR) in this context. The b quark final state can be identified as a b-tagged jet in the detector, so it is an important signature for top decays (See Section 4.2.5).

A W boson can decay to a pair of quarks of leptons. Due to the diagonal structure of the CKM matrix, the dominant hadronic channels are $W \to u+d$ and $c+s$. Lepton universality indicates that $W \to \ell\nu$ equally for three flavors. Quarks are triplets in $SU(3)_c$, so they have three colors. Therefore, naively, $\frac{W \to qq}{W \to \ell\nu \text{ or } qq} \sim \frac{6}{9}$. The current measurement indicates the BR $\frac{\Gamma_{had}}{\Gamma_{tot}} = 67.41 \pm 0.27\%$ [13]. This means $\sim 45\%$ of the $t\bar{t}$ decays goes to *full hadronic* channels, $\sim 10\%$ to *dileptonic* channels, and the rest $\sim 45\%$ goes to *semileptonic* channels. A graphic representation of these decays is shown in Fig. 1.3. Since tau decays very quickly compared to electrons and muons, it usually is not counted as a lepton in analyses and is considered its own channel. Therefore, the full hadronic channel has the largest branching fraction.

[9] Interestingly, the $t\bar{t}$-quarkonium-bound state has a binding time close to the top mean lifetime. This means a peak will be visible in an e^+e^- collider at the $t\bar{t}$ threshold [13].

[10] FCNC for top in the SM is bigger compared to other quarks due to the large mass hierarchy. It has not been observed, but the limits are the weakest among the quarks.

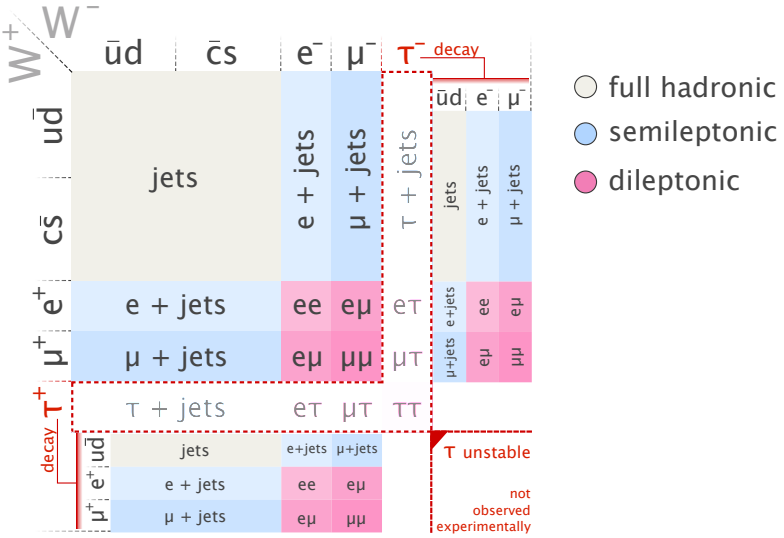

FIGURE 1.3. Taken from [14]. Graphical representation of possible final states for $t\bar{t}$ decays. The decay channels for τ lepton are also shown outside the dotted red lines. The area of each box gives an estimate of the branching ratio.

1.2. Beyond the Standard Model and Naturalness Problem

While it is very successful in explaining almost all high energy experiment results so far, the SM is widely considered to not be the complete picture. Instead, it is regarded as an effective theory valid up to some energy scale in which some new beyond Standard Model (BSM) physics becomes non-negligible. The theory contains many aspects that suggest so, and these manifest as puzzles about why measured values of some parameters are vastly different from the preferred value suggested by the structure of the theory. This is the so-called "naturalness" problem. There are several such puzzles in the SM and I will explore some of them, but first I will discuss what it means for the SM to be an effective field theory (EFT) and how it connects to the naturalness problem.

1.2.1. Standard Model as an Effective Theory

The theory of Newtonian gravity has been used to successfully explain the interaction of celestial objects in the solar system and beyond without any detail of the internal

structures except the masses. This is an example of how long-distance (low energy) interactions can be decoupled from the short- distance (high energy) ones. Effective field theory is a formal mathematical approach to this idea. By "integrating" out the high energy interaction involving heavy particles, the effective Lagrangian can be written in the form [15]:

$$\mathscr{L}_{\text{eff}} = \sum_I c_I \mathcal{O}_I(\ell_i) \tag{1.25}$$

where $\mathcal{O}_I$ are effective operators consisting of light fields ℓ_i and their derivative. If $\mathcal{O}_I$ has dimension of (mass)^d, then by a dimensional analysis argument, the effective coupling c_I has dimension (mass)$^{4-d}$. An example of this is Fermi's interaction which is an approximation of W/Z boson exchange from the full electroweak theory, shown in Fig. 1.4.

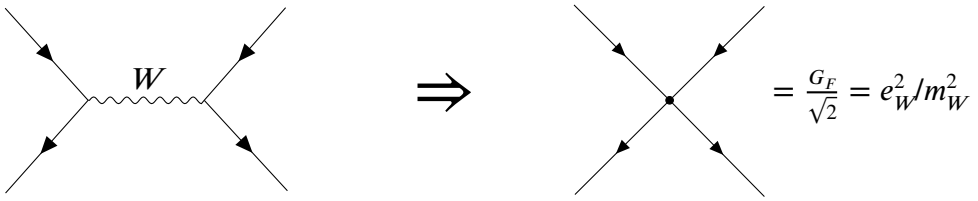

FIGURE 1.4. Low energy effective coupling (right) from W exchange (left).

In the same way that Fermi interactions can be used instead of computing the full W/Z boson exchanges when dealing with an energy well below m_W, the SM can be a low-energy approximation of a full ultraviolet (UV)-completed theory that includes higher energy interactions.

1.2.2. Naturalness Problem in the Standard Model

For a field theory in four dimensions, the fact that $c_I \propto M^{4-d}$ ensures that contributions from heavy states are suppressed for all $d > 4$ operators. However, the SM does include $d \leq 4$ interactions; therefore they are sensitive to UV scales. Most of them are $d = 4$ interactions and thus their couplings and masses can be treated as running parameters in

the Lagrangian using renormalization group equations [16]. There are two exceptions: the $d = 2$ Higgs bare mass term and the $d = 0$ cosmological constant.

1.2.2.1. The Hierarchy Problem

The hierarchy problem can be attributed to the large difference of the electroweak (EW) mass scale, $M_W \sim 100$ GeV, and the reduced Planck mass scale, $M_P \sim 2.4\times10^{18}$ GeV. One can see how the problem is manifested by looking at the Higgs mass squared parameter[11], which is the bare mass term plus quantum corrections. A contribution from a single fermion loop diagram is:

$$m_H^2 = \quad\text{+}\quad \overset{f}{\bigcirc} \quad\text{+}\ \ldots \tag{1.26}$$

$$= m_{H,bare}^2 \quad -\frac{|\lambda_f|^2}{8\pi^2}\Lambda_{\mathrm{UV}}^2 \quad +\ \ldots \tag{1.27}$$

If the SM is valid all the way through the Planck scale, Λ_{UV} should be at the M_P scale. On the other hand, $m_H^2 = -(92.9\text{ GeV})^2$ for the SM Higgs boson mass at ~ 125 GeV [16]. This means somehow the bare mass term has to be equally large but must precisely cancel the correction terms to give the relatively small physics Higgs mass. This usually is referred to as *fine-tuning*. Such precise cancellations are generally considered not *natural*. Rather, it is usually taken as a hint that SM is an EFT of a more fundamental UV-complete theory.

This quadratic divergence is unique to scalar particles. The gauge boson and other fermions' masses in SM are protected by the chiral symmetry and gauge invariance, respectively, from a direct sensitivity to quadratic divergence. They are *technically natural* because there is an enhanced symmetry in the limit of the masses going to zero. However, because they acquire masses through interactions with the Higgs, the problem can be said

[11] This is the m_H in the Higgs potential $V = m_H^2|H|^2 + \lambda|H|^4$, not the physical Higgs boson mass.

to affect all of them. Any new particle which interacts with the Higgs, directly or though a loop diagram, will give such contribution. It should be noted that these "problems" are not a difficulty within the SM itself, but rather a very disturbing sensitivity to any kind of BSM physics. One can propose that there is nothing beyond the weak scale and the SM is valid all the way to an arbitrary high energy, but that is certainly not true. For one, there is very compelling evidence from experiments which will be discussed in Section 1.2.3. Even if we were to insist on avoiding them somehow, the SM itself will eventually break down: The EM coupling grows with the energy scale according to a renormalization group equation, and will eventually diverge at an energy scale beyond M_P called the Landau pole [15]. Therefore it is expected that some new physics, for example the quantum theory of gravity, will become important and will UV-complete the theory before that happens.

1.2.2.2. The Cosmological Constant

As described in Section 1.2.1, from the EFT point of view, the correction to the $d = 0$ term should be $\Lambda_0 \sim O(m^4)$. The current measurement of the Λ_{CC} in the lambda cold dark matter (ΛCDM) model from the cosmic microwave background (CMB) is $\sim 10^{-47}$ GeV [17]. Physics at the Planck scale $M_p \sim 10^{19}$ GeV would indicate that our prediction is off by $\sim O(123)$. Even if there are some new symmetries to cancel all contributions to the Λ_0 in the UV, those from the SM do not cancel, thus the prediction would at least be $\sim m_t^4 \sim O(10^9 \text{ GeV})$ — still off by $\sim O(56)$. Worse, even at the electron mass, the prediction is already too large, and it is very difficult to propose a theory of modified physics at such low energy without running into experimental constrains. It can be argued based on the grounds of the anthropic principal that for structures to have formed in the universe [18], Λ_{CC} must be around the current measured value. However, as with all arguments based on anthropic principal, it is very hard to test.

1.2.3. Evidence for Physics Beyond the Standard Model

The existence of the gravitational interaction itself can be considered as an undeniable evidence for BSM physics. After all, the SM does not include it at all. Still, even if gravity is somehow decoupled from the SM completely and both the UV and the Landau pole can be ignored, there are several very compelling experimental results that point to physics BSM.

1.2.3.1. Dark Matter

Evidence for the existence of the large amount of non-luminous matter begins with the galactic rotational curve. For a spiral galaxy such as our milky way, most luminous matter is in the central hub. From Newtonian gravity, the velocity v of an object at a distance r from the center of the galaxy will scale like $v(r) \propto \sqrt{M(r)/r}$ where $M(r)$ is the mass inside the radius r. Inside the hub of radius r_0 where $M(r) \propto r^3$, the velocity of the object should be $v(r < r_0) \propto r$, and outside the hub it should be $v(r > r_0) \propto 1/\sqrt{r}$. However, observations show that $v(r > r_0) \propto$ constant, up to a large R_0 where there are objects to be measured. This seems to indicate that there is a halo of *dark matter* centered around the galaxy with mass density that scales like $M(r) \propto 1/r^2$.

Many similar discrepancies have been observed in other scales such as stars, gas clouds, and globular clusters. They seem to move faster than predicted from the mass of visible matter [13]. An alternative to the dark matter is the so-called Modified Newtonian Dynamics (MOND) which generally can accommodate the observations at larger scales. However, there are many problems with MOND, one of which is that it modifies the General Relativity which so far has very successfully passed all experimental tests. Nonetheless, the most convincing evidence for *particle* dark matter comes from the observation of the bullet cluster (1E0657-558) [19]. In this event, a galaxy cluster is passing by another cluster. Figure 1.5 shows the mapping of the luminous mass in red and the mass from gravitational lensing in

FIGURE 1.5. False colour image of Bullet Cluster 1E0657-558. The surface density Σ-map reconstructed from X-ray imaging observations is shown in red and the convergence κ-map as reconstructed from strong and weak gravitational lensing observations is shown in blue. Image provided courtesy of Chandra X-ray Observatory. Taken from [19].

blue. This clearly illustrates that a large amount of the masses were passing through each other with almost no interaction as opposed to the luminous, baryonic mass that interacted and decelerated.

Another proposal is that the missing masses are baryonic but not luminous. Examples of such objects are black holes and neutron stars without luminous gas surrounding them, the so-called massive compact halo objects (MACHO). The best evidence against the idea is the observed anisotropies of the CMB. The measurement can be used to extract the baryonic matter density Ω_b and the non-interacting, non-relativistic ("cold") dark matter Ω_c from the global fit to the ΛCDM model. The best fit using 6-parameters, which includes the two mentioned, from the 2015 Planck satellite results agree remarkably well as shown in Fig. 1.6. The best fit result gives $\Omega_b h = 0.02226 \pm 0.00023$, and $\Omega_c h = 0.1186 \pm 0.0020$, where h is the Hubble constant in units of 100 km/(s·Mpc). This highly disfavors MACHO to be the majority of dark matter.

Considering all these observations so far, candidates for dark matter then have to satisfy several properties. First, they cannot be charged and can only very weakly interact electromagnetically so that they are "dark". Second, they have to be stable at least on the

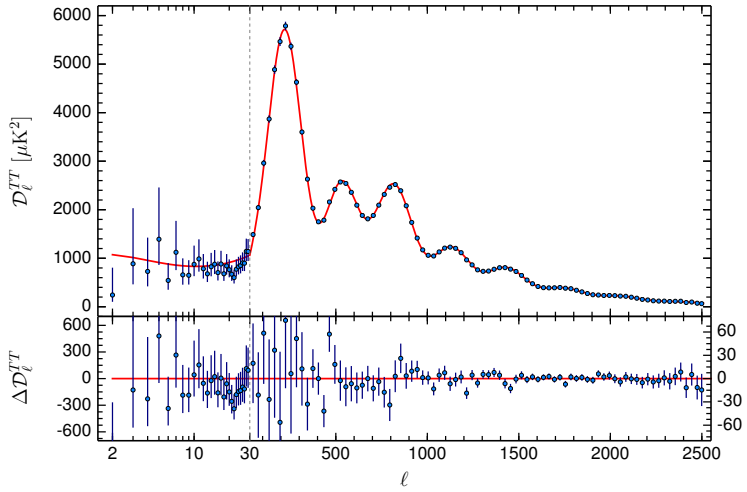

FIGURE 1.6. Planck 2015 temperature power spectrum. Taken from [17].

time scale of the age of the universe since they are still present. Next, to be responsible for forming structures in the universe, dark matter should be cold i.e. non-relativistic by the time galaxies started to form [13]. Dark matter candidates also cannot interact too strongly among themselves as they are constrained by the observation of the bullet cluster and other similar observations, as well as the fact that they need to form a halo for structures in the universe. The current results limit the dark matter self-interaction to be $\sigma/m < \mathcal{O}(1)\ \mathrm{cm}^2 g^{-1}$ [20, 21].

The candidates also should have the right relic abundance observed from CMB. If one were to assume the standard scenario as the following: dark matter was in the thermal equilibrium with SM particles, then the SM+SM $\rightarrow$ DM+DM process turned off as the universe cooled down so the dark matter density started to decrease. Finally, the DM+DM $\rightarrow$ SM+SM process also turned off when the universe expanded too much for the dark matter particles to find each other so the dark matter abundance became fixed. This process is called *freeze-out*. Using the Boltzmann equation and the observed dark matter relic abundance from the CMB gives the m_{DM} to be around 10 GeV to a few TeV, with cross-section σ_{DM+DM} to be roughly around the weak scale. This class of dark matter candidates is called a weakly

interacting massive particle (WIMP). Interestingly, any new physics that would address the hierarchy problem is expected to show up in roughly the same scale as mentioned in Section 1.2.2.1. This is usually referred to as the *WIMP miracle* and is the reason why a lot of dark matter searches are looking in the parameter space from the WIMP scenario.

1.2.3.2. Neutrino Masses

More strong evidence for a new physics scale is the neutrino masses. In the SM the neutrinos' (antineutrinos') helicity is purely left-handed (right-handed) and is massless. However, results from many experiments with solar, atmospheric, reactor, and accelerator sources all provide overwhelming evidence that neutrinos oscillate between the flavors, and therefore must have masses[12] [13]. In the see-saw theory, the SM can be extended to accommodate the neutrino masses by adding "sterile" right-handed (left-handed) neutrinos (antineutrinos) which will be much heavier than the three known ones. This not only explains the neutrino oscillation, but also provides an explanation for the mass hierarchy between neutrinos and charge leptons. Moreover, the extra CP violation[13] can potentially account for the matter-antimatter asymmetry of the universe [13]. So far there is no direct evidence for the heavy neutrinos, but the theory is still far from being ruled out [22].

1.3. Extensions to the Standard Model

The tremendous success of the SM is both a blessing and a curse. The fact that it produces many accurate predictions is a triumph for quantum field theory and tells us that we should be at least on the right track. On the other hand, it is clear that the SM is not the end of the story. The theory itself suggests that it is not valid at very high energy, and there are many observations that it cannot explain such as dark matter. The difficulty is that any proposal to

[12] Since only the $(\Delta m)^2$s have been measured, the lightest mass eigenstate can still be massless.

[13] The neutrino mixing matrix is essentially the CKM matrix for the lepton sector.

modify the SM is severely limited by experimental constraints. The cosmological constant problem, for example, is very difficult to address by a simple extension to the SM.

Fortunately, the difficulties from attempting to solve the hierarchy problem are much less severe and there are several proposals to avoid such unnatural cancellation. Moreover, they share a common feature — they require some new phenomena to emerge just above the weak scale. Therefore, unlike the cosmological constant problem, this is within reach of the current experiments and has been getting a lot of attention. Some of the leading candidates are theories with *extra dimensions* which effectively reduce the scale in which gravity becomes important. Another proposal is the *composite Higgs model* where the SM's Higgs doublet is not an elementary field and therefore the problem does not apply. However, arguably the most elegant way to solve this problem is by proposing a symmetry that will ensure systematic cancellations between the boson and fermion partners. This symmetry is known as *supersymmetry*.

CHAPTER II

SUPERSYMMETRY

Supersymmetry (SUSY) is a global symmetry relating fermions and bosons. A supersymmetry transformation will transform a boson into its fermion partner, and vice versa. While it originated from the formulation of string theory [23] as a purely theoretical framework, the study of supersymmetry (SUSY) in particle physics is largely motivated as a way to resolve the hierarchy problem.

2.1. A Solution to the Higgs Mass Hierarchy Problem

From the Higgs mass squared parameter corrections from Eq. (1.26), the term with a top quark running in the loop will be the most important due to the large top Yukawa coupling. The contribution from the diagram would be:

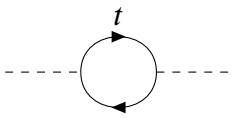

$$= -\frac{6y_t^2}{16\pi^2}\Lambda_{\text{UV}}^2 \tag{2.1}$$

Now, let us supposed that there is a scalar partner of the top, $\tilde{t}$, with the same Yukawa coupling. Then, the contribution from a one-loop diagram with this particle running in the loop for the Higgs mass would be:

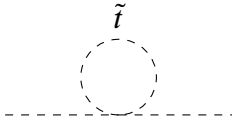

$$= +\frac{6y_t^2}{16\pi^2}\Lambda_{\text{UV}}^2 \tag{2.2}$$

And thus the two quadratic dependences on the Λ_{UV} are nicely canceled. The crucial point here is the sign flip from the difference between fermion and boson; therefore, if there is a symmetry that can ensure this type of cancellation for all particles, then the m_H will be

safe from quadratic divergence. This is essentially what SUSY does — transforms between fermion and boson in a systematic way that can guarantee these cancellations. Moreover, SUSY does this to all orders in perturbation theory and not just at the one-loop level shown here.

2.2. Supermultiplets

A supersymmetry operator Q will turn a fermion into a boson and vice versa:

$$Q|Fermion\rangle = |Boson\rangle, \quad Q|Boson\rangle = |Fermion\rangle \tag{2.3}$$

So Q and $Q^\dagger$ carry spin angular momentum 1/2. An infinitesimal SUSY transformation, therefore, will not keep the Lagrangian density, $\mathscr{L}$, invariant. Instead, it changes $\mathscr{L}$ by a total derivative and thus keeps the action $S = \int \mathrm{d}^4x\mathscr{L}$ invariant. Supersymmetry is therefore a global symmetry like translations, rotations, and Lorentz transformations rather than an internal symmetry like the gauge transformation. For a chiral theory like the SM, according to the Haag-Lopuszanski-Sohnius extension of the Coleman-Mandula theorem, Q and $Q^\dagger$ must satisfy, with spin indices suppressed [16]:

$$\{Q, Q^\dagger\} = P^\mu, \tag{2.4}$$

$$\{Q, Q\} = \{Q^\dagger, Q^\dagger\} = 0, \tag{2.5}$$

$$[P^\mu, Q] = [P^\mu, Q^\dagger] = 0 \tag{2.6}$$

The Eq. (2.5) indicates that applying a SUSY transformation successively does not keep generating new states. Therefore fermion and boson states come in pairs called *supermultiplets*, which are the irreducible representations of the SUSY algebra, and the two states are *superpartners* of each other. Following from Eq. (2.6), the square mass operator

$-P^2$ commutes with SUSY transformation; thus, particles in the same supermultiplet must have equal masses. Moreover, the SUSY generators also commute with gauge transformations, so it follows that particles in the same supermultiplet have the same quantum numbers (electric charges, weak isospins, and colors) as well.

It can be shown using Eqs. (2.4) and (2.6) that the bosonic degree of freedom n_B and fermionic degree of freedom n_F in a supermultiplet must be equal [16]. Thus, possible combinations are:

Chiral/Matter/Scalar supermultiplet consists of a 1/2-spin Weyl fermion which has two spin helicity states ($n_F = 2$) and two 0-spin real scalars ($n_B = 2\times1$). One can combine the two real scalars into a complex scalar for convenient formulation.

Gauge/Vector supermultiplet has a massless spin-1 vector boson ($n_B = 2$) and a massless spin-1/2 Weyl fermion ($n_F = 2$). A bare mass term for a spin-1 vector boson makes the theory non-renormalizable, hence the massless boson. Since they are superpartners, its fermion partner is therefore also massless.

Gravity supermultiplet has a massless spin-2 graviton which has two helicity states[1] ($n_B = 2$) and a massless spin-3/2 gravitino ($n_F = 2$).

2.3. Minimum Supersymmetric Standard Model

For a theory with only one distinct set of SUSY generators Q and $Q^\dagger$ ($N = 1$ SUSY), the other combinations of particles and spins that satisfy $n_B = n_F$ are always reducible to combinations of chiral and gauge supermultiplets. This is not true for *extended* SUSY which has more than one set of generators ($N > 1$ SUSY). However, four-dimensional field theories with extended SUSY cannot accommodate chiral fermion or

[1] Remember that gravitational waves have two polarizations just like an EM wave, but with a $\frac{\pi}{4}$ rotated angle instead ($h_+, h_\times$)

parity violation [16] which are observed in the SM. There are still possibilities using theories with extra dimensions, but we'll focus on four-dimensional field theory and thus only consider $N = 1$ SUSY extensions to the SM. Particle contents in such theories then have to come in supermultiplets, consisting of the SM particles and their undiscovered superpartners. The theory with the minimal number of new particles and interactions while still being a complete and consistent theory is called the Minimum Supersymmetric Standard Model (MSSM).

2.3.1. Particle Contents

2.3.1.1. Sleptons and Squarks

Fermions in the SM have spin 1/2, so naively they can be members of either chiral or gauge supermultiplets. However, the left-handed and right-handed components of the Weyl fermion in a gauge supermultiplet must have the same gauge transformation because their gauge boson partners must transform as the adjoint representation of the gauge group and is always its own conjugate. Since the fermions in the SM are in fact chiral, i.e. the left-handed and the right-handed components transform differently, they have to be parts of chiral supermultiplets. Their superpartners are called *sfermions* where *s* refers to the fact that they are scalars. The naming convention is also used to refer to the specific partner. For example, the scalar SUSY partner of the electron would be *selectron*, and the partner of the top quark would be *stop*, etc. The symbols for the SUSY partner are the symbols of their SM counterparts with a tilde on top such as $\tilde{e}$, $\tilde{t}$, etc. As already mentioned, the right-handed and left-handed components of a Dirac fermion in the SM get their own partners. For example, a SUSY partner of the left-handed electron would be referred to as a left-handed selectron ($\tilde{e}_{\mathrm{L}}$), with emphasis on the fact that the latter "left-handed" refers to the electron's (and not its own) helicity since it is a scalar.

2.3.1.2. Gauginos

Clearly, the vector bosons in the SM must be members of gauge supermultiplets, accompanied by their spin-1/2 partners. The naming convention for these partners is their SM counterparts with the suffix "-ino" added. So the gluons, Ws, and Bs have superpartners called gluinos, winos, and binos respectively. If SUSY is unbroken, the mass eigenstates after EWSB, Z and γ, have superpartners called Zino, with mass m_Z, and a massless photino respectively.

2.3.1.3. Higgsinos

Since it is a scalar, the Higgs boson must be in a chiral supermultiplet. With only one Higgs doublet as in the SM, however, the theory will suffer from what is known as a gauge anomaly which means it failed to be Lorentz- and gauge-invariant. Another problem with only one Higgs doublet is that the Higgs can only give masses to either up- or down-type quarks but not both, because the Yukawa terms of such forms are forbidden by the requirement that the potential has to be supersymmetric. Instead, the MSSM has two $SU(2)_L$ Higgs doublets. The one with $U(1)$ hypercharge $Y = +\frac{1}{2}$ is labeled H_u and the other is $Y = -\frac{1}{2}$, labeled H_d. The weak isospin component of H_u with $T_3 = +\frac{1}{2}$ has +1 electric charge and thus is labeled H_u^+, and the $T_3 = -\frac{1}{2}$ component H_u^0. Similarly, the H_d doublet consists of H_d^0 and H_d^- fields. Each doublet then obtains a left-handed Weyl spinor field as its superpartner, ($\tilde{H}_u^+$, $\tilde{H}_u^0$,), and ($\tilde{H}_d^0$, $\tilde{H}_d^-$).

The particle contents of the MSSM are summarized in Table 2.1. Note that the left-handed components of the electron Dirac fields and SM Higgs doublets have the same representation. One can propose that they are in the same supermultiplet. However, this does not work for the anomaly that will appear in the theory as mentioned before, as well as the fact that such theories would predict many results that do not agree with experimental

bounds. Therefore, all the superpartners to the known SM particles in MSSM are new. They are also called *sparticles*.

TABLE 2.1. Summary of MSSM particle contents, organized as pairs of known SM particles and their proposed SUSY partners.

Name	Field components		$SU(3)_c, SU(2)_L, U(1)_Y$	Comments
	SM	SUSY partners		
Spin-1/2 quarks and spin-0 squarks				
Q	$\begin{pmatrix} u_L & d_L \end{pmatrix}$	$\begin{pmatrix} \tilde{u}_L & \tilde{d}_L \end{pmatrix}$	$(3, 2, \frac{1}{6})$	×3 generations
$\bar{u}$	$u_R^\dagger$	$\tilde{u}_R^*$	$(\bar{3}, 1, -\frac{2}{3})$	
$\bar{d}$	$d_R^\dagger$	$\tilde{d}_R^*$	$(\bar{3}, 1, \frac{1}{3})$	
Spin-1/2 leptons and spin-0 sleptons				
L	$\begin{pmatrix} \nu_L & e_L \end{pmatrix}$	$\begin{pmatrix} \tilde{\nu}_L & \tilde{e}_L \end{pmatrix}$	$(1, 2, -\frac{1}{2})$	×3 generations
$\bar{e}$	$e_R^\dagger$	$\tilde{e}_R^*$	$(1, 1, 1)$	
Spin-0 Higgs and spin-1/2 Higgsinos				
H_u	$\begin{pmatrix} H_u^+ & H_u^0 \end{pmatrix}$	$\begin{pmatrix} \widetilde{H}_u^+ & \widetilde{H}_u^0 \end{pmatrix}$	$(1, 2, +\frac{1}{2})$	
H_d	$\begin{pmatrix} H_d^0 & H_d^- \end{pmatrix}$	$\begin{pmatrix} \widetilde{H}_d^0 & \widetilde{H}_d^- \end{pmatrix}$	$(1, 2, -\frac{1}{2})$	
Spin-1 gauge bosons and spin-1/2 gauginos				
Gluons	g	$\tilde{g}$	$(8, 1, 0)$	
W	$\begin{pmatrix} W^\pm & W^0 \end{pmatrix}$	$\begin{pmatrix} \widetilde{W}^\pm & \widetilde{W}^0 \end{pmatrix}$	$(1, 3, 0)$	
B	B^0	$\widetilde{B}^0$	$(1, 1, 0)$	

2.3.2. Supersymmetric Interactions in the MSSM

Similarly to the SM, the renormalizable interactions possible in the MSSM are Yukawa couplings, gauge interactions, and a scalar potential with terms up to ϕ^4. The gauge interactions are fixed by their representations as listed in Table 2.1, and the self-interactions of the gauge bosons and their gaugino partners are already supersymmetric [15]. That leaves only the non-gauge interactions of the chiral supermultiplets. After imposing that it is invariant under SUSY transformation, the most general interactions are given by a single *holomorphic* (or *complex analytic*) function of complex scalar fields ϕ_i. In other words, it can only depend on ϕ_i and not ϕ_i^*. This function, W, is called *superpotential*.

The Lagrangian[2] for a theory with complex scalars ϕ^i and left-handed Weyl fermions ψ^i in chiral supermultiplets is:

$$\mathscr{L} = -\partial^\mu \phi^{*i} \partial_\mu \phi_i + i\psi^{\dagger i} \bar{\sigma}^\mu \partial_\mu \psi_i - \frac{1}{2}\left(W^{ij}\psi_i\psi_j + W^*_{ij}\psi^{\dagger i}\psi^{\dagger j}\right) - W^i W^*_i. \tag{2.7}$$

The W terms are:

$$W = \frac{1}{2}M^{ij}\phi_i\phi_j + \frac{1}{6}y^{ijk}\phi_i\phi_j\phi_k \tag{2.8}$$

$$W^i = \frac{\delta W}{\delta \phi_i} = M^{ij}\phi_j + \frac{1}{2}y^{ijk}\phi_j\phi_k \tag{2.9}$$

$$W^{ij} = \frac{\delta^2}{\delta\phi_i\delta\phi_j}W = M^{ij} + y^{ijk}\phi_k \tag{2.10}$$

where:

- M^{ij}: Symmetric mass matrix for ϕ
- y^{ijk}: Yukawa coupling of ϕ^i, ψ^j, and ψ^k. Must be symmetric under the interchange of i, j, k.

Substituting Eqs. (2.8) to (2.10) into Eq. (2.7):

$$\begin{aligned}\mathscr{L} =& \partial^\mu \phi^{*i}\partial_\mu\phi_i - V(\phi,\phi^*) + i\psi^{\dagger i}\bar{\sigma}^\mu\partial_\mu\psi_i - \frac{1}{2}M^{ij}\psi_i\psi_j - \frac{1}{2}M^*_{ij}\psi^{\dagger i}\psi^{\dagger j} \\ & - \frac{1}{2}y^{ijk}\phi_i\psi_j\psi_k - \frac{1}{2}y^*_{ijk}\phi^{*i}\psi^{\dagger j}\psi^{\dagger k}\end{aligned} \tag{2.11}$$

[2] Not quite the most general. Here the linear term $L^i\phi_i$ in the superpotential is omitted since such a term is not allowed with MSSM field contents.

The scalar potential $V(\phi, \phi^*)$ can be explicitly written out as:

$$\begin{aligned} V(\phi, \phi^*) =& W^k W_k^* \\ =& M_{ik}^* M^{kj} \phi^{*i} \phi_j + \frac{1}{2} M^{in} y_{jkn}^* \phi_i \phi^{*j} \phi^{*k} + \frac{1}{2} M_{in}^* y^{jkn} \phi^{*i} \phi_j \phi_k + \frac{1}{4} y^{jjn} y_{kln}^* \phi_i \phi_j \phi^{*k} \phi^{*l} \end{aligned} \tag{2.12}$$

Here we can see how SUSY accomplishes the cancellation of the quadratic divergence of scalar mass mentioned in Section 2.1: The last two terms in Eq. (2.11) will produce interaction vertices needed to form the loop diagram in Eq. (2.1) and the last term in Eq. (2.12) indicates the quartic scalar interaction needed for the Eq. (2.2) diagram. They also have the same Yukawa coupling by construction.

Given the field contents discussed in Section 2.3.1, the superpotential for the MSSM is [16]:

$$W_{\text{MSSM}} = \bar{u} \mathbf{y_u} Q H_u - \bar{d} \mathbf{y_d} Q H_d - \bar{e} \mathbf{y_e} L H_d + \mu H_u H_d \tag{2.13}$$

The field components of H_u, H_d, Q, L, $\bar{u}$, $\bar{d}$, and $\bar{e}$ can be referred to from Table 2.1. It also shows why MSSM needs two Higgs doublets: Only H_u can couple to the up-type quarks and only H_d to down-type quark. For example, trying to replace $\bar{u} \mathbf{y_u} Q H_u$ with $\bar{u} \mathbf{y_u} Q H_d^*$ will not work since it is not holomorphic. For the same reason, SM Higgs mass terms, $H_u^* H_u$ and $H_d^* H_d$, are not allowed in MSSM. Instead, the Higgs mass is the last term in Eq. (2.13), also traditionally called the μ-term.

2.3.3. *R*-parity

The superpotential in Eq. (2.13) is minimal but not the most general. Unlike the SM where there is no such renormalizable term, there are baryon (B) and lepton (L) number violation terms allowed due the addition of superpartners and interactions [16]:

$$W_{\Delta \mathrm{L}=1} = \frac{1}{2}\lambda^{ijk} L_i L_j \bar{e}_k + \lambda'^{ijk} L_i Q_j \bar{d}_k + \mu'^{i} L_i H_u \tag{2.14}$$

$$W_{\Delta \mathrm{B}=1} = \frac{1}{2}\lambda''^{ijk} \bar{u}_i \bar{d}_j \bar{d}_k \tag{2.15}$$

The presence of such terms allow for a very large proton decay rate, which is very tightly constrained.

One way to forbid such interactions in the MSSM is to assume a discrete Z_2 symmetry called *matter parity* defined as:

$$P_M = (-1)^{3(B-L)} \tag{2.16}$$

Clearly, the terms in Eqs. (2.14) and (2.15) do not conserve P_M, and are thus forbidden, while those in Eq. (2.13) do. One can also define an equivalent *R-parity*:

$$P_R = (-1)^{3(B-L)+2s} \tag{2.17}$$

R-parity is more phenomenologically convenient because all particle in the SM have $P_R = +1$ and the new particle contents from MSSM have $P_R = -1$.

While the motivation for the *R*-parity in the MSSM is to avoid baryon and lepton number violation, it has other very important phenomenological consequences:

- Superpartners are always produced in even numbers. For a particle collider, this usually means they're produced in pairs.

– Similarly, all sparticles except the lightest one will eventually decay into an odd number of the lightest sparticles.

– Since it is forbidden to decay into only SM particles, the lightest supersymmetric particle (LSP) is absolutely stable. If it is also electrically neutral, it will interact only weakly with ordinary matter. Therefore, the LSP is a good candidate for dark matter in the WIMP scenario as mentioned in Section 1.2.3.1.

2.3.4. Supersymmetry Breaking

As previously mentioned in Section 2.2, particles of the same supermultiplets will have the same masses. If that is the case, then the superpartners such as the selectron would have already been detected by many experiments. Clearly, that is not the case. Therefore, to still be present in the theory, SUSY must be *spontaneously* broken by the vacuum state. However, for SUSY to still be the solution to the hierarchy problem, the relation between dimensionless couplings such as those pointed out in Eqs. (2.1) and (2.12) must be maintained. This leads to the idea called *soft supersymmetry breaking*, where the Lagrangian of the MSSM can be written as:

$$\mathscr{L} = \mathscr{L}_{\text{SUSY}} + \mathscr{L}_{\text{soft}} \tag{2.18}$$

The SUSY-conserving term $\mathscr{L}_{\text{SUSY}}$ contains all gauge and Yukawa interactions, while the SUSY-breaking term $\mathscr{L}_{\text{soft}}$ contains only mass terms and couplings with positive mass dimension.

The most general set of soft terms in the MSSM is:

$$\begin{aligned}\mathscr{L}_{\text{soft}}^{\text{MSSM}} = &-\frac{1}{2}\left(M_3\tilde{g}\tilde{g} + M_2\widetilde{W}\widetilde{W} + M_1\widetilde{B}\widetilde{B} + \text{c.c.}\right)\\ &-\left(\tilde{\bar{u}}\,\mathbf{a_u}\,\widetilde{Q}H_u - \tilde{\bar{d}}\,\mathbf{a_d}\,\widetilde{Q}H_d - \tilde{\bar{e}}\,\mathbf{a_e}\,\widetilde{L}H_d + \text{c.c.}\right)\\ &-\widetilde{Q}^{\dagger}\,\mathbf{m_Q^2}\,\widetilde{Q} - \widetilde{L}^{\dagger}\,\mathbf{m_L^2}\,\widetilde{L} - \tilde{u}\,\mathbf{m_{\bar{u}}^2}\,\tilde{\bar{u}}^{\dagger} - \tilde{\bar{d}}\,\mathbf{m_{\bar{d}}^2}\,\tilde{\bar{d}}^{\dagger} - \tilde{e}\,\mathbf{m_{\bar{e}}^2}\,\tilde{\bar{e}}^{\dagger}\\ &- m_{H_u}^2 H_u^* H_u - m_{H_d}^2 H_d^* H_d - \left(m_3^2 H_u H_d + \text{c.c.}\right)\end{aligned} \tag{2.19}$$

where:

- M_{1-3}: The bino, wino, and gluino mass terms, respectively.
- $\mathbf{a_u}, \mathbf{a_d}, \mathbf{a_e}$: 3×3 matrices in family space. Corresponding to the Yukawa couplings in the superpotential.
- $\mathbf{m_Q^2}, \mathbf{m_{\bar{u}}^2}, \mathbf{m_{\bar{d}}^2}, \mathbf{m_L^2}, \mathbf{m_{\bar{e}}^2}$: 3×3 matrices in family space. Mass terms of the squarks and sleptons.[3]
- m_{H_u}, m_{H_d}, m_3: SUSY-breaking square-mass contributions to the Higgs potential.

Unlike $\mathscr{L}_{\text{SUSY}}$ where the parameters are fixed to the SM values by supersymmetry, these parameters in $\mathscr{L}_{\text{soft}}^{\text{MSSM}}$ are free. There is a total of 105 new masses, phases, and mixing angles in MSSM in addition to the ones from SM [16].

2.3.4.1. Soft Supersymmetry Breaking Scale

The presence of SUSY-breaking terms will introduce new corrections to the Higgs mass. They are of the form:

$$\Delta m_H^2 = m_{\text{soft}}^2 \left[\frac{\lambda}{16\pi^2}\ln(\Lambda_{\text{UV}}/m_{\text{soft}}) + \ldots\right] \tag{2.20}$$

[3] Recall that, unlike their fermionic partners from SM, these scalars can have the direct mass term $m^2\phi^*\phi$.

where λ is a dimensionless coupling and m_{soft} is the largest mass scale associated from Eq. (2.19). If m_{soft} is too big, then the theory once again has to be fine-tuned to get the observed Higgs mass of 125 GeV. Coupled with the fact that most known SUSY-breaking mechanisms can only accommodate the splitting between the masses of the sparticles up to about an order of magnitude, some of the lightest superpartners are expected to be around the TeV scale. It is worth emphasizing, however, that the level of fine tuning here is much less than that from the hierarchy problem described in Section 1.2.2.1. The "soft" breaking of SUSY still retains the cancellation of the quadratic divergences to all orders in perturbation theory. Unless m_{soft} is comparable to M_P, SUSY still "solves" the hierarchy problem.

2.3.4.2. Possible Mechanism for Supersymmetry Breaking

It turns out that the actual mechanism which breaks SUSY cannot come from MSSM itself [16]. Instead, the origin of SUSY breaking is expected to be in a hidden sector that only interacts with the visible MSSM via some kind of mediator. Popular models are:

2.3.4.2.1. Gravity-mediated Supersymmetry Breaking or *Planck-scale-Mediated Supersymmetry Breaking (PMSB)*. In this scenario, the mediator mass scale M_{mess} is that of M_P and $m_{\text{soft}} \sim \frac{\langle F \rangle}{M_P}$ where $\langle F \rangle$ is the VEV of the hidden sector. A special, very simplified case in this scenario with:

$$M_3 = M_2 = M_1 = m_{1/2}, \tag{2.21}$$

$$\mathbf{m_Q^2} = \mathbf{m_{\bar{u}}^2} = \mathbf{m_{\bar{d}}^2} = \mathbf{m_L^2} = \mathbf{m_{\bar{e}}^2} = m_0^2\,\mathbf{1}, \qquad m_{H_u}^2 = m_{H_d}^2 = m_0^2, \tag{2.22}$$

$$\mathbf{a_u} = A_0\mathbf{y_u}, \quad \mathbf{a_d} = A_0\mathbf{y_d}, \quad \mathbf{a_e} = A_0\mathbf{y_e}, \tag{2.23}$$

$$m_3^2 = B_0\mu, \tag{2.24}$$

is referred to as the minimum supergravity (mSUGRA) or Constrained Minimum Supersymmetric Standard Model (CMSSM).

2.3.4.2.2. Gauge-mediated Supersymmetry Breaking (GMSB) The mediator in this model is some new chiral supermultiplets that connect the SUSY-breaking sector in the MSSM via normal $SU(3)_C \times SU(2)_L \times U(1)_Y$ gauge/gaugino interactions. An attractive common feature is that the squarks' and sleptons' masses only depend on their gauge properties and thus automatically get the mass degeneracy needed to suppress flavor-changing effects. Another distinctive feature is that the gravitino will be the LSP.

2.3.4.2.3. Extra-dimensional Supersymmetry Breaking In this case there is an actual physical distance between the hidden SUSY breaking and the visible MSSM sector. The interactions between the two sectors can be mediated by both supergravity effects and gauge supermultiplets. If the latter is also confined in the MSSM plane, then only supergravity effects act as the messenger. This scenario also know as *Anomaly-mediated Supersymmetry Breaking (AMSB)*.

2.3.5. MSSM and Gauge Coupling Unification

A nice feature of the MSSM is that it is possible to have the three-gauge coupling constants unified at an energy scale $\sim 10^{16}$ GeV, usually referred to as the grand unified theory (GUT) scale. As seen in Fig. 2.1a, after running the gauge couplings in the SM according to the renormalization equations to the higher scale, the three couplings cross over but do not unify. On the other hand, the particle contents of the MSSM can get them very close as seen in Fig. 2.1b. The perfect unification is not guaranteed in MSSM, but some adjustment can be attributed to other new physics near the GUT scale.

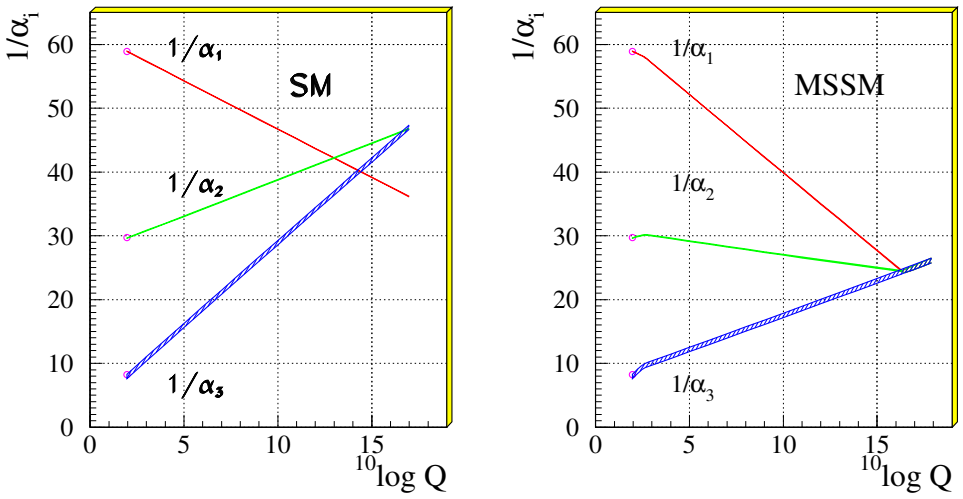

(a) SM (b) MSSM

FIGURE 2.1. Taken from [24]. Evolution of the inverse of the three coupling constants according to the renormalization group equation in the SM and MSSM. The SUSY particles are assumed to contribute only above the effective SUSY scale M_{SUSY} of about 1 TeV, which causes a change in the slope in the evolution of couplings. The thickness of the lines represents the error in the coupling constants.

2.4. Searching for Supersymmetry

Supersymmetry is a framework that can be realized in many classes of theories. The relationship between some of them are shown in Fig. 2.2. The MSSM, having the minimum number of additional field contents, is the most predictive and therefore is a good place to start. Still, the large amount of free parameters introduced by the soft SUSY-breaking sector add a lot arbitrariness to the theory compared to the SM as mentioned in Section 2.3.4. Fortunately, there are many experimental constraints and well-motivated theoretical simplifications one can use as a guide to organize the searches.

In the searches described in this dissertation, R-parity is assumed for the many nice features mentioned in Section 2.3.3, including the possibility for a dark matter candidate. A stable, weakly interacting LSP also implies an important consequence for collider search — the LSP will pass through undetected, and thus appear as missing transverse energy ($E_{\mathrm{T}}^{\mathrm{miss}}$) (See Section 3.1).

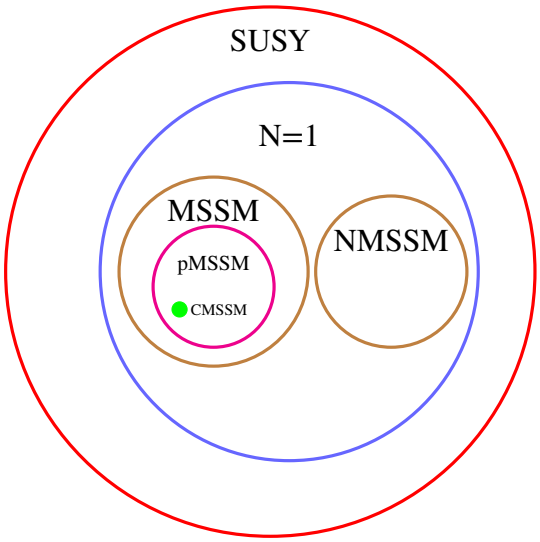

FIGURE 2.2. Relationship between various classes of supersymmetric theories. Inspired by [25].

2.4.1. Sparticles Mass Eigenstates

The next step is to look at the new field contents in the MSSM and their mass eigenstates.

2.4.1.1. Higgs Bosons in the MSSM

MSSM has two $SU(2)_L$ complex scalar Higgs doublets, and each of them gets its own VEV:

$$\langle H_u \rangle = v_u, \quad \langle H_d \rangle = v_d \tag{2.25}$$

The two complex scalar doublets have a total of eight degrees of freedom. To be compatible with the SM, three of them are Nambu-Goldstone bosons when EW is broken, and become the longitudinal modes of Z and $W^{\pm}$ massive bosons. The known m_Z and gauge coupling require:

$$v_u^2 + v_d^2 = v^2 = \frac{2m_Z^2}{(g^2 + g'^2)} \approx (246 \text{ GeV})^2 \tag{2.26}$$

The ratio between the two VEV is usually written as:

$$\tan\beta \equiv \frac{v_u}{v_d} \tag{2.27}$$

with both v_u and v_d to be real and positive, therefore $0 < \tan\beta < \frac{\pi}{2}$.

The other five degrees of freedom imply five scale Higgs mass eigenstates: two CP-even neutral h^0 and H^0 with $m_{h^0} < m_{H^0}$, one CP-odd neutral A^0, one charge $+1$ H^+, and one which is its conjugate H^- for a total of five Higgs bosons. The discovered ~ 125 GeV is usually assumed to be the lighter h^0, though the possibility that it is H^0 has not been totally ruled out.

2.4.1.2. Gauginos

In the SM, after EWSB, W^3 and B mix to become the EM neutral mass eigenstates Z and γ, and W^1, W^2 mix to become $W^\pm$. If SUSY is unbroken, there will be the corresponding Zino, photino, and charged Winos as described in Section 2.3.1.2. For MSSM, due to the SUSY being broken, the mixing among the superpartners does not have to be the same. In fact, it should be quite different, otherwise they would have already been discovered. In general, the neutral higgsinos ($\widetilde{H}_u^0$, $\widetilde{H}_d^0$) can mix with the neutral gauginos ($\widetilde{W}^0$, $\widetilde{B}$) to create four neutral mass eigenstates labeled as $\tilde{\chi}_1^0$-$\tilde{\chi}_4^0$. Similarly, the charged higgsinos and winos can mix to form four charginos $\tilde{\chi}_1^\pm$, $\tilde{\chi}_2^\pm$. The exact mixing can be completely different from model to model; therefore, from an experimental point of view it is better to focus on the charge and mass of the particle.

2.4.1.3. Gluino

Since the gluino is a color octet, it cannot mix with any other sparticles. The rough prediction for its mass parameter M_3 compared to the wino's and bino's M_1 and M_2, in models with mSUGRA or GMSB is [16] $M_3 : M_2 : M_1 \sim 6 : 2 : 1$ at near EW scale. Therefore the gluino is expected to be significantly heavier than the neutralinos and charginos.

2.4.1.4. Sfermions

Theoretically, the 3×3 matrices in the third line of Eq. (2.19) can be any hermitian matrix. However, the flavor constraints from neutral meson mixing put a very strong constraint on the mixing matrices, especially for the first two generations. One way to avoid such problems is to assume a weak version of *soft supersymmetry breaking universality* [16]:

$$\mathbf{m}_{\mathbf{Q}}^{\mathbf{2}} = m_Q^2 \mathbf{1}, \quad \mathbf{m}_{\bar{\mathbf{u}}}^{\mathbf{2}} = m_{\bar{u}}^2 \mathbf{1}, \quad \mathbf{m}_{\bar{\mathbf{d}}}^{\mathbf{2}} = m_{\bar{d}}^2 \mathbf{1}, \quad \mathbf{m}_{\mathbf{L}}^{\mathbf{2}} = m_L^2 \mathbf{1}, \quad \mathbf{m}_{\bar{\mathbf{e}}}^{\mathbf{2}} = m_{\bar{e}}^2 \mathbf{1} \tag{2.28}$$

$$\mathbf{a}_{\mathbf{u}} = A_{u0}\, \mathbf{y}_{\mathbf{u}}, \qquad \mathbf{a}_{\mathbf{d}} = A_{d0}\, \mathbf{y}_{\mathbf{d}}, \qquad \mathbf{a}_{\mathbf{e}} = A_{e0}\, \mathbf{y}_{\mathbf{e}}, \tag{2.29}$$

$$\mathrm{Im}(M_1) = \mathrm{Im}(M_2) = \mathrm{Im}(M_3) = \mathrm{Im}(A_{u0}) = \mathrm{Im}(A_{d0}) = \mathrm{Im}(A_{e0}) = 0, \tag{2.30}$$

Equation (2.28) means that the mass matrices are *flavor blind*. Equation (2.29) assumes that the scalar couplings are proportional to the Yukawa coupling matrix. Finally Eq. (2.30) requirements are to avoid a large CP-violating effect.

2.4.2. Arguments for Light Supersymmetric Top Quark Partner

The consequences of the universal soft SUSY breaking mentioned in Section 2.4.1.4 are the following:

- Flavor-blindness leaves the first two generations of squarks and sleptons largely unmixed.
- Having the same structure as the SM Yukawa coupling matrix ensures that only the third generation's couplings can be large.
- The small Yukawa couplings make the first two generations mostly mass degenerated.
- On the other hand, the third generation's mixing can be big. The mass eigenstates are usually labeled $\tilde{t}_1$, $\tilde{t}_2$, $\tilde{b}_1$, and $\tilde{b}_2$ with $m_{\tilde{t}_1} < m_{\tilde{t}_2}$ and $m_{\tilde{b}_1} < m_{\tilde{b}_2}$.
- The large Yukawa couplings also tend to drive down the third generations' masses in the renormalization group equation from the SUSY-breaking scale faster than the other two generations, making them lighter at the EW scale.

The above reasonings explain why the third generations' squarks can be much lighter than the other two, but not why it should be at the weak scale. The reason for that is once again due to naturalness. Due to the size of top Yukawa coupling, the biggest corrections to m_{h^0} come from loops involving the third generation:

$$\Delta m^2_{h^0,\text{one-loop}} = h^0 \text{ --- } \overset{t}{\bigcirc} \text{ --- } + \; h^0 \text{ --- } \overset{\tilde{t}}{\bigcirc} \text{ --- } + \; h^0 \text{ --- } \overset{\tilde{t}}{\bigcirc} \text{ --- } \tag{2.31}$$

$$\approx \frac{3}{4\pi^2}\cos^2\alpha \; y_t^2 m_t^2 \left[\ln(m_{\tilde{t}_1} m_{\tilde{t}_2}/m_t^2) + \Delta_{\text{threshold}}\right] \quad \text{if } m_{\tilde{t}} \gg m_t \tag{2.32}$$

where α is the mixing angle associated with the CP-even eigenstates, and $\Delta_{\text{threshold}}$ comes from corrections to supersymmetric Higgs quartic coupling. The crucial point here

is that if $m_{\tilde{t}}$ is too big, then fine-tuning is needed again to get the observed $m_{h^0} = 125$ GeV[4]. Therefore, $m_{\tilde{t}}$ should be rather small to avoid the theory's being unnatural, and is thus a good place to start looking for evidence for SUSY.

2.4.3. Search for Direct Pair-production of Stops

For a "natural" SUSY scenario shown in Fig. 2.3 [26], the squarks are related to the Higgs mass squared parameter at one-loop level. Among them, the third generations have much larger Yukawa coupling; therefore, they are expected to be light, typically $\lesssim$ TeV as mentioned in Section 2.4.2. The stop/sbottom mixing parameters allow some freedom to push the sbottom mass to be somewhat heavier, so the stop mass is the most strongly tired to the m_H^2. The gluino mass can be higher, but since it feeds into stop mass correction (therefore feed into m_H^2 at two-loop), it cannot be too heavy, typically around a few TeV. Such a heavy gluino is not yet excluded by the current ATLAS searches. The higgsinos are also expected to be light since their masses are related to the μ-terms and therefore relates to the m_H^2 at tree level. However, the mass spectrum is degenerated and the existing limits are very weak. Therefore, searching for the direct production of stops is important.

2.4.3.1. Stop Search with Simplified Model

If there is any departure from the SM presented in the data, it can be difficult to determine which model can explain it. For a theory with large parameter space such as the MSSM, scanning the whole phase space is unfeasible. There needs to be some kind of benchmark models to compare to data and the SM prediction with only a few parameters but that can capture most of the kinematic distributions from general MSSM models. One

[4] The full picture here is a lot more complicated. One reason is that to obtain $m_{h^0} = 125$ GeV, $m_{\tilde{t}}$ cannot be too small either. This is due to the fact that, at tree level, $m_{h^0} < m_Z |\cos(2\beta)|$. A massive $m_{\tilde{t}}$ is needed to drive the radiative correction of m_{h^0}. One-loop diagrams involving the rest of the squarks, as well as leading two-loop diagrams, can also be significant. See more discussions in Section 8.1 from [16].

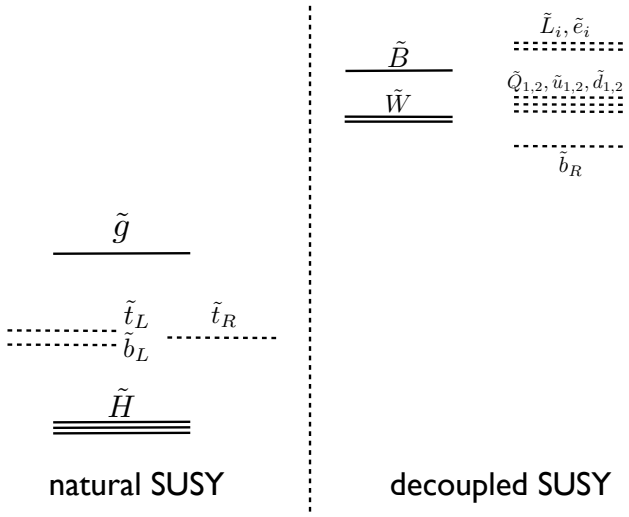

FIGURE 2.3. Taken from [26]. A "natural" SUSY mass spectrum usually require the third generation squarks to be $\lesssim$ TeV and gluino mass on the order of a few TeV. The rest of sparticle masses can be "decoupled" to a very high scale.

option is to use a small subset of the MSSM such as mSUGRA which only has four free parameters. However, it fails to cover many changes in phenomenology due to the many assumptions imposed. For example, reordering of mass spectrum is not allowed in mSUGRA.

This leads to the idea of using *simplifed models* [27] as benchmarks for the search for SUSY. Simplified models are designed to produced SUSY-like kinematics but with only a small subset of particle contents and parameters involved. Generally, simplified models have only one pair-produced species, and a few steps in a fixed decay chain. For example, in the case of the search for direct stop pair productions with 100% $t \to \tilde{t} + \tilde{\chi}_1^0$ BR, only $m_{\tilde{t}}$ and $m_{\tilde{\chi}^0}$ are free parameters. This makes it much easier to develop search strategies and present the results.

2.4.3.2. Interpreting Data with Phenomenological MSSM

While simplified models are very useful benchmarks for interpreting the data and can capture general features of SUSY phenomenology, they do not represent a lot of complexities of the full MSSM where many models can have a lot of competing species getting produced and very complex decay chains. On the other hand, the MSSM with 105 free parameters are simply too large to scan exhaustively.

A subspace of the MSSM called *Phenomenological Minimum Supersymmetric Standard Model (pMSSM)* [28] reduces the number of free parameters using a series of well-motivated assumptions from general features of possible SUSY-breaking scenarios or experimental constraints. The number of free parameters has been reduced from 105 in the MSSM to just 19 in the pMSSM. These constraints are:

- R-parity is conserved
- The LSP is the lightest neutralino
- CP-conserving. No new CP-violation in the sparticles sector
- No extra FCNC

Experimental results from precision EW and flavor measurements, as well as the search results from LEP and Tevatron are also used to reduce the size of parameter space.

The ATLAS collaboration used Run 1 data to scan the pMSSM parameter space in order to provide a very comprehensive result in [2]. The results using the direct stop pair production in all-hadronic channel analysis strategy will be presented in Section 5.4.

CHAPTER III

EXPERIMENTAL SETUP

3.1. Kinematics Measurement in a Hadron Collider

The $p - p$ collision at the LHC contains both *elastic* collisions where the final state particles are the same as the incoming ones (i.e. the protons) and *inelastic* collisions where the partons actually interact. The inelastic collisions are dominated (in term of occurrences) by *soft scatterings* which is when partons interact at low energy. The *hard interactions* which is when two partons collide head-on are where most of the interesting physics occurs.

The hard-scattered partons only carry a fraction of proton momentum, so the center-of-mass energy ($\sqrt{s}$) of the processes is less than that of the $p-p$ collision. The boost along the z-axis is unknown[1] because the two partons generally do not carry the same fraction of momentum. Therefore, the particles from a hard scattering are recognized by their large *transverse momenta* (p_{T}) defined as:

$$p_{\mathrm{T}} \equiv \sqrt{p_x^2 + p_y^2} \tag{3.1}$$

Because the total p_{T} of the incoming partons is insignificant, the total sum of the p_{T} in an event should be zero. The missing transverse momentum ($\mathbf{p}_{\mathrm{T}}^{\mathrm{miss}}$) is defined as the negative of the vectorial sum of the p_{T}:

$$\mathbf{p}_{\mathrm{T}}^{\mathrm{miss}} = -\sum_i \vec{p}_{Ti} \tag{3.2}$$

The magnitude of this vector is (confusingly) named missing transverse energy ($E_{\mathrm{T}}^{\mathrm{miss}}$). Non-zero $E_{\mathrm{T}}^{\mathrm{miss}}$ implies that some momentum is carried away by undetected particles. In

[1] This is in contrast to an e^+e^- collider where the full initial momentum is known.

the SM, these will be neutrinos. Many new physics models include such particles, so it is very important to be able to measure $E_{\mathrm{T}}^{\mathrm{miss}}$ accurately.

3.2. The Large Hadron Collider

The LHC provides the most suitable environment for testing and discovery of new physics beyond the SM, which is expected to be just above the EW scale. It is a proton-proton particle accelerator with a 27-kilometers ring of acceleration structures for boosting protons to a very high energy and superconducting dipole and quadrupole magnets for steering and focusing two particle beams to collide at four interaction points [29], ATLAS, CMS, ALICE, and LHCb. It is currently the world's most powerful particle accelerator, colliding protons at $\sqrt{s}$ of 7 and 8 TeV in Run 1 and $\sqrt{s}$ of 13 TeV in the ongoing Run 2. The very high $\sqrt{s}$ collision is achieved by accelerating protons in many stages [29]. First, hydrogen atoms are ionized to remove the electrons. Then LINAC2, the first-stage accelerator, boosts the protons' energy to 50 MeV and injects them into the Proton Synchrotron Booster (PSB) where they are accelerated further to 1.4 GeV. The process is repeated at the Proton Synchrotron (PS) to 25 GeV and the Super Proton Syncrotron (SPS) to 450 GeV before they are finally being injected into the LHC ring. The full schematic of the CERN accelerator complex is shown in Fig. 3.1.

The protons are brought to the final energy by 16 radiofrequency (RF) cavity systems operated at 400 MHz. To steer the particles around the LHC ring, 1,232 main dipoles magnets designed to produce up to 8.4 Tesla magnetic fields are used. This is achieved by using electromagnets based on niobium-titanium (NbTi) Rutherford cables operating at 11850 Amperes. To cope with the current, the magnet is cooled to 1.9K using superfluid helium. The LHC is designed to reach an energy of up to 7 TeV per beam, producing head-on collisions of up to $\sqrt{s}$=14 TeV. The LHC also collides protons at a very high rate, designed to reach the peak luminosity of $L = 10^{34}\mathrm{cm}^{-2}\mathrm{s}^{-1}$. This is very important because

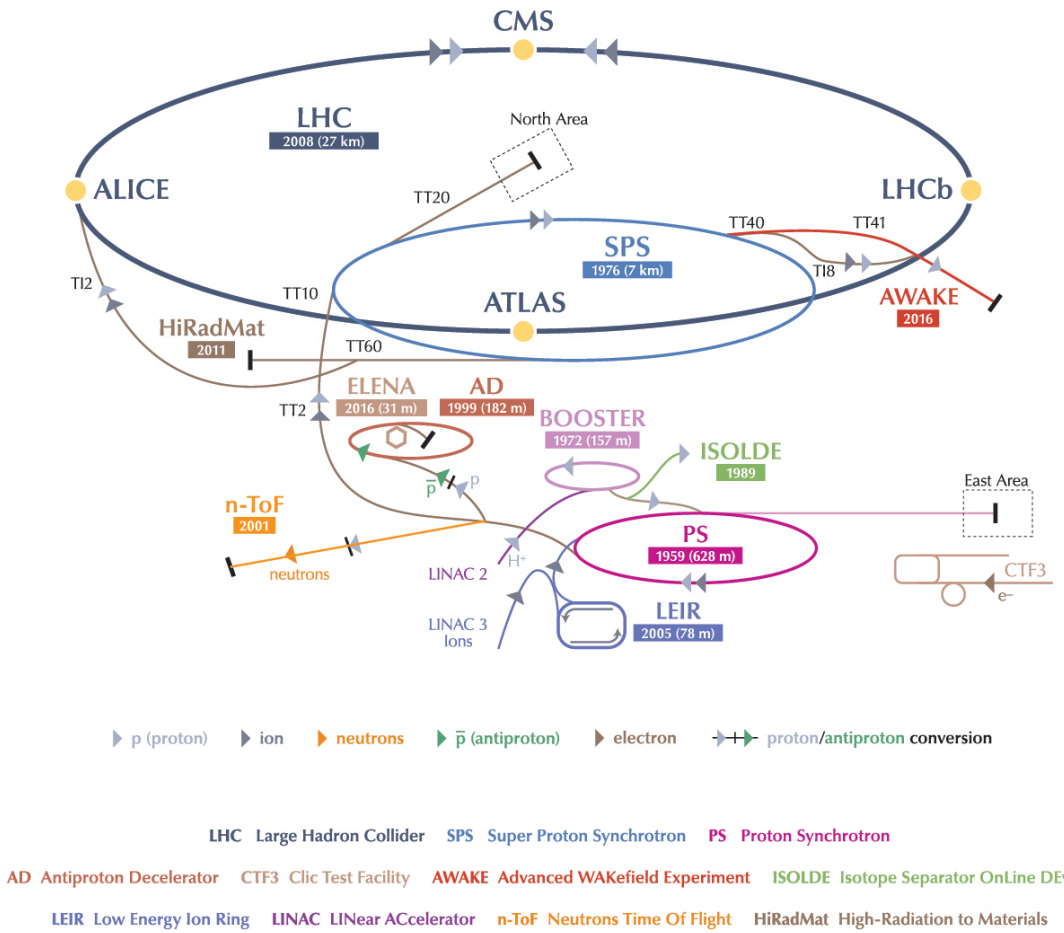

FIGURE 3.1. The CERN accelerator complex [30].

even though the high $\sqrt{s}$ gives a large increase in the cross section for many hypothetical new processes, the rates are still very low. The higher luminosity allows more data to be accumulated, and thus more chances to produce these rare events.

Apart from the main proton-proton operations, the LHC also performs experiments colliding heavy ions (Lead), the details of which are beyond the scope of this dissertation.

3.3. Overlapping Events

In the LHC environment, there can be more than one $p-p$ interaction considered to be in the same time window for an event. This is referred to as *pileup* contribution. In order to maximize the luminosity, the LHC collides protons in "bunches". In each *bunch*

crossing, there can be more than one interaction can occur and appear in the detector as overlapping events. This is called *in-time* pileup. On the other hand, *out-of-time* pileup comes from previous bunch-crossings. This happens because, as I will describe later, the time interval between bunch crossings for the LHC is shorter than the time resolution of some of the ATLAS subsystems. Pileup contribution can interfere with the interpretation of hard interaction events since they have nothing to do with the physics process of interest. Because pileup contributions are usually softer, the simplest way to reject them is to make a cut on p_{T} of the physics objects. A more complicated method is to check if the object of interest originated from the *primary vertex* which indicates the location of the hard interaction.

3.4. The ATLAS Detector

ATLAS [31] is the largest general-purpose particle detector ever build for an accelerator, measuring 25 meters in height, 44 meters in length, and with a weight of about 7,000 tonnes. ATLAS is designed to be able to enable a wide range of both SM and beyond SM searches. As described in Section 3.2, the LHC will generate collisions at a very high rate. Therefore, ATLAS components have to be not only fast but also radiation-hard. Additionally, the detector has to have high granularity in order to separate particles from overlapping events. ATLAS has tracking systems to reconstruct and measure charged particles' momenta, including a very high granularity pixel detector to reconstruct the interaction point and observe secondary vertices, which are decay vertices shifted from the primary interaction due to particles with a slightly longer lifetime such as the B-meson (see Section 4.2.5). The high-energy muons can also be measured using the dedicated muon spectrometry system. A very good EM calorimetry system is used to identify electrons and photons. ATLAS is also equipped with hadronic calorimetry for measuring jets. It is very important to be able to reconstruct and measure not only high-p_{T} objects but also all

energy deposited in both transverse (barrel) and along-the-beam (forward) directions. It is important not only because there are many interesting physics processes for both regions, but also because many new physics beyond SM including SUSY predict weakly interacting long-lived particles that will not show up in any part of the detector. Instead, these particles can be identified by the measurement of $E_{\mathrm{T}}^{\mathrm{miss}}$ in the events. It is therefore crucial for ATLAS to have very good $E_{\mathrm{T}}^{\mathrm{miss}}$ reconstruction and resolution.

The description of the ATLAS detector here is based on [31] unless noted otherwise.

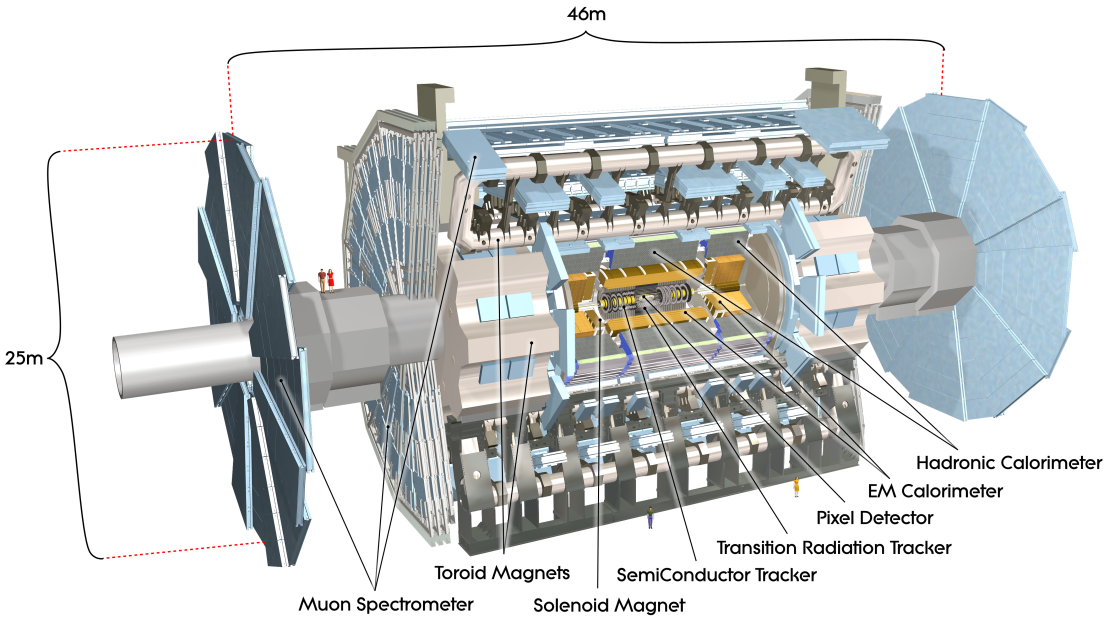

FIGURE 3.2. The ATLAS detector with a cut-away view of the subcomponents.

3.4.1. ATLAS Coordinate System

ATLAS uses right-hand Cartesian coordinates with the x-axis pointing toward the center of the LHC, the y-axis pointing upward (perpendicular to the LHC plane), and the z-axis pointing along the beam line. Since almost all physics processes do not vary in azimuthal angle, and ATLAS is designed to be as symmetric as possible in that direction, it

is usually more convenient to use a (r, ϕ, η) coordinate system where r is the radial distance from the center of the collision, ϕ is the azimuthal angle in the xy-plane, and η is the *pseudorapidity* which will be described below.

In experimental particle physics, the *rapidity* (y) is defined as:

$$y \equiv \frac{1}{2} \ln \frac{E + p_z}{E - p_z} \tag{3.3}$$

where E is the energy and p_z is the momenta along the z-axis. Under a Lorentz boost along the z-axis, the rapidity transforms as $y \to y - \tanh^{-1} \beta$. Therefore, any distribution dN/dy and a difference in rapidity Δy is invariant unlike the polar angle θ along the $y - z$ plane. For a high energy experiment such as ATLAS, the momentum of a particle is usually much higher than its mass. If $p \gg m$, one can write:

$$\begin{aligned} y &= \frac{1}{2} \ln \frac{\cos^2 \frac{\theta}{2} + \frac{m^2}{4p^2} + \dots}{\sin^2 \frac{\theta}{2} + \frac{m^2}{4p^2} + \dots} \\ &\approx -\ln \tan \frac{\theta}{2} \equiv \eta \end{aligned} \tag{3.4}$$

Where $\cos\theta \equiv \frac{p_z}{p}$. Pseudorapidity η is approximately equal to rapidity y in the $p \gg m$ and $\theta \gg \gamma^{-1}$ limit. The advantage is that it can be measured without one's knowing the mass or momentum of the particle.

The $\eta = 0$ direction is the same as the y-axis. The low value $|\eta|$ region is referred to as the central part of the detector, as opposed to the forward part which is where the $|\eta|$ is large. It turns out that in the range where most physics processes are concerned, $|\Delta\eta|$ represents roughly the same physical distance as $|\Delta\phi|$. Therefore, it is useful to define

$$(\Delta R)^2 \equiv (\Delta\phi)^2 + (\Delta\eta)^2 \tag{3.5}$$

as a measure of distance between two points in the detector.

3.4.2. Magnet System

The ATLAS magnet system consists of four large superconducting magnets — central solenoid, barrel toroid, and two endcap toroids. Their layout is shown in Fig. 3.3.

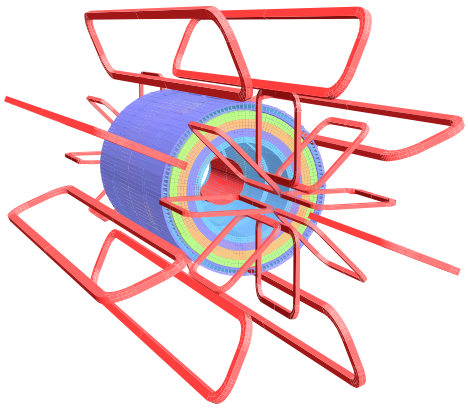

FIGURE 3.3. Geometry of the ATLAS magnet system.

3.4.2.1. Central Solenoid

The central solenoid magnet provides a 2 T axial field to the inner detector (ID) at the nominal operational current of 7.730 kA. Since it is sitting inside the calorimeter and thus can directly impact the performance of the calorimetry system, the solenoid magnet is designed to be as thin as possible. To meet this requirement, the solenoid magnet is made with a specially developed Al-stabilized NbTi single-layer coil wrapping inside a 12 mm thick Al 5083 support cylinder. To minimize the amount of materials and achieve the operating temperature of 4.5 K, the solenoid magnet also needs to share the same vacuum vessel as the liquid argon (LAr) calorimeter. It is approximately 0.66 radiation lengths at a normal incident angle. A heat shield of 2 mm-thick aluminum is also put in between the solenoid and the inner wall of the cryostat.

3.4.2.2. Barrel and Endcap Toroids

The toroid magnets produce a magnetic field of ∼0.5 T and ∼1 T for the barrel and endcap muon detectors, respectively. Both are made with an Al-stabilized Nb/Ti/Cu conductor operating at 4.5 K. The barrel toroid consists of eight coils supported by eight inner and eight outer rings with installed dimensions of 25.3 m in length and 20.1 m in height.

3.4.3. Inner Detector

The ATLAS inner detector refers to the components that are immersed in a 2 T solenoid field up to roughly 1 m away from the beam line. Physics requirements set the performance goal for the resolution of charged particles' momenta as $\sigma_{p_T}/p_T = 0.05\% p_T \bigoplus 1\%$, even at a detection rate of roughly 1000 particles for every 25 ns. It consists of three independent but complementary subcomponents to increase the robustness of the detector. Closest to the interaction point (IP) is the silicon pixel detector providing high- resolution trajectories of the outgoing charged particles to accurately reconstruct collision vertices. Next, the semiconductor tracker (SCT) is used to identify the curved trajectories of charged particles due to the magnetic field at the larger radii to measure the momentum of the particles using the curvature. The pixel detector and SCT together form the precision tracking system. Farthest from the IP is the transition radiation tracker (TRT) which provides a large number of hits (∼36) per track to improve the momentum measurement of the tracks and also give complementary information for electron identification to the calorimetry system. In the barrel region, all three subcomponents are arranged in concentric cylinders around the beam axis. The precision tracking system extends out to $|\eta| < 2.5$ and the TRT extends out to $|\eta| < 2.0$. In the endcap region, they are arranged as disks perpendicular to the beam axis.

The cut-away view of the ID is shown in Fig. 3.4 and the arrangements of both barrel and endcap components are shown in Fig. 3.5

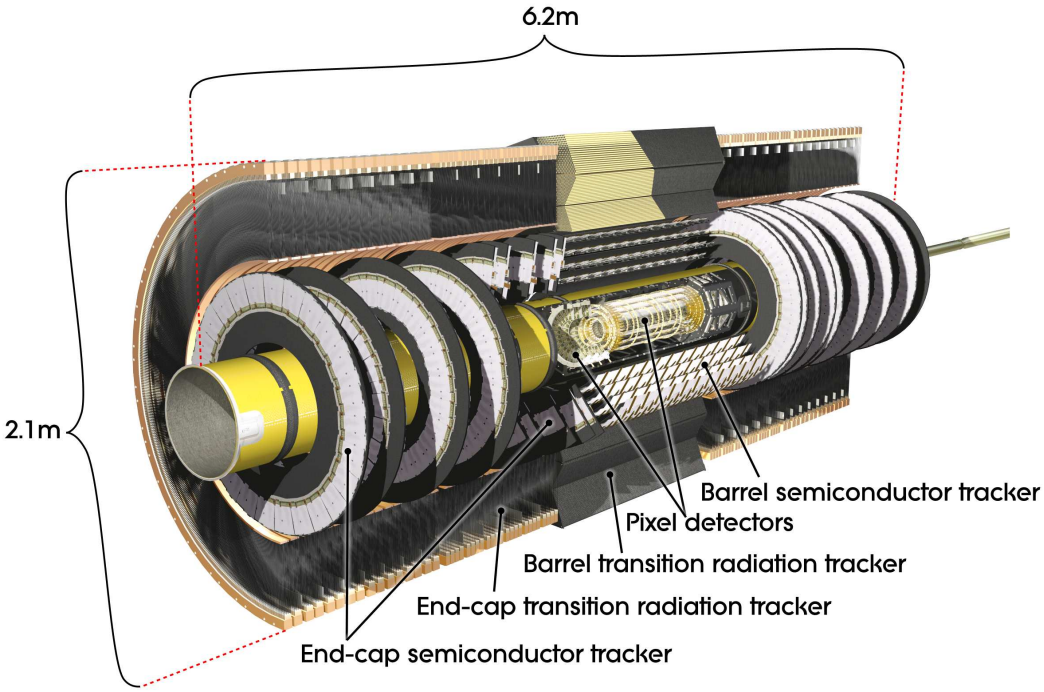

FIGURE 3.4. The cut-away view of the ATLAS inner detector

3.4.3.1. Pixel Detector

The silicon pixel detector has the highest granularity of all the detectors. Its design also has very stringent requirements on radiation hardness and thickness due to its close proximity to the interactions. The sensors use oxygenated n-type wafers with readout pixels on the n^+ implants and are expected to last for ten years. An exception is the innermost layer, which is needed to be replaced in three years. The pixels are arranged in three concentric cylinders in the barrel and three disks in the endcap region to achieve signal in three layers for each particle. There are a total of 1744 sensors with 80.4 million readout channels with a minimum size of $(R-\phi)\times z = 50\times 400$ μm^2 giving a resolution of 10 μm $(R-\phi)$ and 115 μm(z in the barrel and R in the disk). The high resolution is needed for not only

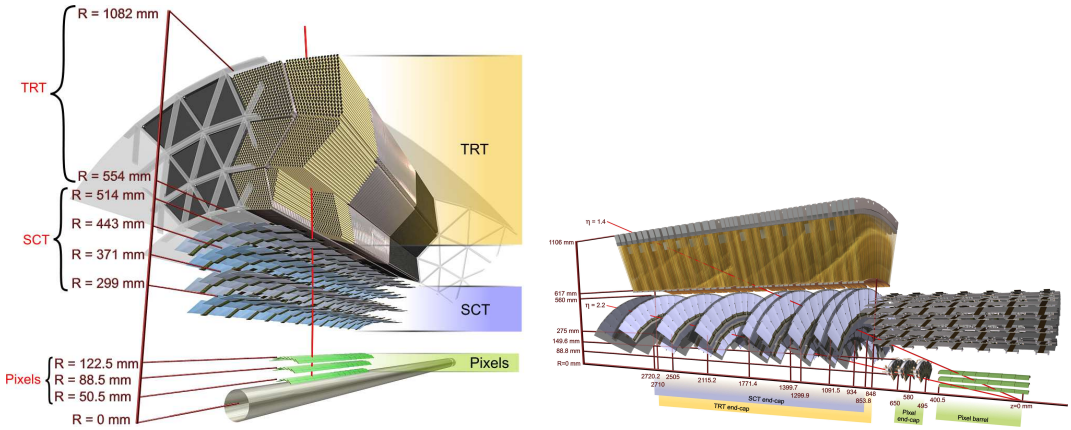

(a) Barrel region (b) Endcap region

FIGURE 3.5. The arrangement of sensors and structure elements of the ATLAS ID

reconstructing the interaction point but also for a secondary vertex for particles such as *B*-meson decays, which is crucial for jet b-tagging algorithms (See Section 4.2.5).

The pixel detector was upgraded during the long shutdown 1 (2013-2014) with an additional layer called the insertable *B*-layer (IBL), which sits between the new beam pipe and the previously innermost layer. This improves the quality of impact parameter reconstruction for tracks, and thereby improves vertexing and b-tagging performance [32].

3.4.3.2. Semiconductor Tracker

Similar to the pixel detector, the SCT is made of silicon sensors but uses a classic single-sided p-in-n junction technology for cost and reliability reasons. Two 6.4 cm-long silicon strips are chained together to form a micro strip. Then 768 of these micro strips are lined up with a 80 µm pitch to form a rectangular active sensor for the barrel region. Each SCT module consists of two silicon sensors bonded to an electronic hybrid [33]. The two sensors are not parallel with one another– one is parallel to the beam axis and another is rotated by 40 mrad around the axis perpendicular to the sensor's plane (stereo angle). This angle is chosen to help minimize ghost hits after information from both sensors is processed. For the barrel region, these modules form four concentric cylindrical layers with 12 modules

in each row. In the endcap region, the micro strips are similar but are lined up with a slight angle to form a trapezoidal-shaped sensor. These sensors are then formed into nine disks for each side of the endcap.

3.4.3.3. Transition Radiation Tracker

Very high energy particles bend less in a magnetic field, thus the momentum resolution typically gets worse as p_{T} increases. To improve the resolution, the TRT is designed to follow up on charge particle tracks up to $|\eta| < 2.0$. It take advantage of the fact that a high energy particle will emit photons as it passes thru the boundary between materials with different index of refraction (transition radiation). The photon flux depends on the Lorentz factor γ and the number of boundary crossings.

The TRT is made from over 300,000 polyimide drift tubes of 4 mm diameter. In the barrel region, each straw is 144 cm long arranged in the direction parallel to the beam. For the endcap region, each on is 37 cm long and arranged radially to form disks. Initially, the straws are filled with gas mixture of 70% Xe for efficient x-ray conversion, 27% CO_2 for high drift velocity, and 3% O_2 for photon quenching and stability [33]. During 2012 run, several leaks developed in the TRT exit gas pipes. During Run 2, in straws belong to modules with large leak, the Xe in the gas mixture has been replaced with Argon [34]. When low energy charged particles pass through and ionize the gas mixture, the electrons are collected by the anodes at the end of the straws. On the other hand, when photons from transition radiation are produced by high energy particles, they get absorbed by the Xe and produce much larger signal amplitude which can be detected. The ratio between these high to low threshold hit is then use to help differentiate between high and low Lorentz factor γ particles.

3.4.4. Calorimetry

The primary function of the calorimetry system is to measure the energy of electrons, photons and hadronic showers. The basic principle for a calorimeter detector is having the incoming particle interacts with material and produces a subsequent set of particles, usually in many steps (showering). The detector then measures the energy of these children to determine the energy of the parent particle. Using this simple concept, the measured energy and its uncertainty are:

$$E_m = \epsilon N E_c \tag{3.6}$$

$$\sigma_m = \sigma_\epsilon N E_c \oplus \epsilon \sigma_N E_c \oplus \sigma_n \tag{3.7}$$

where

- E_m is the energy of the incoming (mother) particle
- ϵ is the efficiency of the detector
- N is the number of child particles
- E_c is the energy of the child particles
- σ_ϵ is the uncertainty of the efficiency
- σ_N is the uncertainty from counting number of particles
- σ_n is the uncertainty from noise

Assuming normal distribution for N particles produced, then $\sigma_N = \sqrt{N}$. We have:

$$\frac{\sigma_m}{E_m} = \frac{\sigma_\epsilon N E_c}{\epsilon N E_c} \oplus \frac{\epsilon\sqrt{N}E_c}{\epsilon N E_c} \oplus \frac{\sigma_n}{\epsilon N E_c} \tag{3.8}$$

$$= \frac{\sigma_\epsilon}{\epsilon} \oplus \frac{1}{\sqrt{N}} \oplus \frac{\sigma_n}{E_m} \tag{3.9}$$

$$= \underbrace{\frac{\sigma_\epsilon}{\epsilon}}_{\text{Efficiency}} \oplus \underbrace{\frac{\sqrt{\epsilon E_c}}{\sqrt{E_m}}}_{\text{Stochastic}} \oplus \underbrace{\frac{\sigma_n}{E_m}}_{\text{Noise}} \tag{3.10}$$

At high energy, the stochastic term will dominate. We can see here that the resolution of a calorimeter detector improves as the energy of the incoming particle grows as opposed to a tracking system's resolution which gets worse as momentum of the particle increases. Therefore, a calorimetry system is useful for measuring the energy of neutral particles (which cannot be done in a tracker) and for providing complementary information for very high momentum particles.

For electrons and photons, early in the shower development, the radiative processes, Bremsstrahlung and e^+e^- pair production (Fig. 3.6), dominate. Thus the number of particles increase. Afterwards, Compton scattering, photoelectric, and ionization processes take over. Finally, the particles' energy is low enough to get absorbed by the atoms of the material so the numbers start to fall. The radiation length (X_0) for electrons depends on the material, for example $X_0 = 0.56$ cm in lead [11]. It can be shown that the photon's mean free path is about $\frac{9}{7}X_0$. Since generally an EM shower stops after roughly 20 radiation lengths [11], they are quite compact compared to hadronic showers described below.

The equivalent of X_0 for a hadron is λ_{int}, which is generally much bigger for a hadronic shower because radiation processes are suppressed for heavier particles or, in case of neutral particles, do not occur at all. Hadronic showers are governed by strong interactions which are more complex in general. A smallest pion interaction length found in a very dense

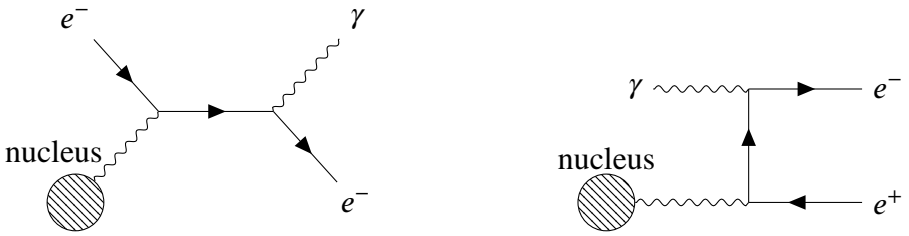

(a) Bremsstrahlung (b) Pair production

FIGURE 3.6. Radiative processes

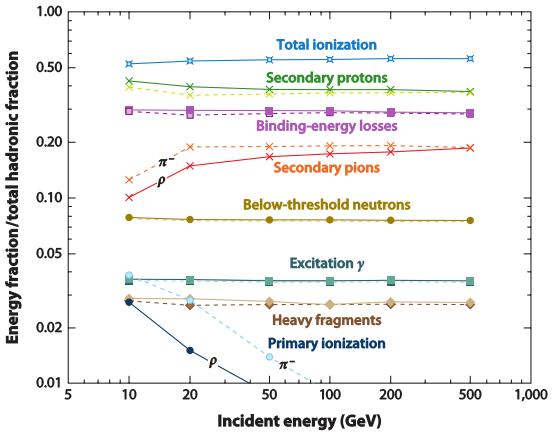

FIGURE 3.7. Taken from [36]. Energy loss of the non-π^0 components of the hadron shower initiated by protons (solid lines) and negative pions (dashed lines) in iron, in a fraction of the total non-π^0 energy, estimated by CALOR simulation

material is about 20 cm [13, 35][2], making hadronic showers generally much larger than an EM shower. This can also be used to distinguish between the two. Moreover, some of these processes, such as releasing a nucleon from its nuclei which accounts for 30%-40% of the energy on average for a hadronic shower [36], are invisible from the calorimeter. The energy loss of a hadron shower is summarized in Fig. 3.7. All of these result in the fact that hadronic shower is harder to measure in general. However, being able to do so is crucial not only for any physics process involving jets but also the measurement of $E_{\mathrm{T}}^{\mathrm{miss}}$. The calorimeter also has a secondary purpose of containing the full hadronic shower and preventing it from reaching the muon system.

[2] See http://pdg.lbl.gov/2016/AtomicNuclearProperties/HTML/lead_Pb.html

Building a calorimetry system with purely active material is prohibitively expensive; therefore, for a large detector such as ATLAS, it is common to use a sampling calorimeter. Usually, it consists of very dense metal to act as absorber alternating with a lighter active material for the actual energy measurement. ATLAS uses liquid argon (LAr) as the active medium for most of the calorimeter systems, taking advantage of the fact that LAr is intrinsically radiation-hard because argon is a monoatomic noble gas. The barrel hadronic calorimeter suffers less from radiation; therefore, a scintillator is used instead. Various metals have been chosen as absorbers, depending on the subcomponents. ATLAS calorimeter systems are shown in Fig. 3.8 and described below.

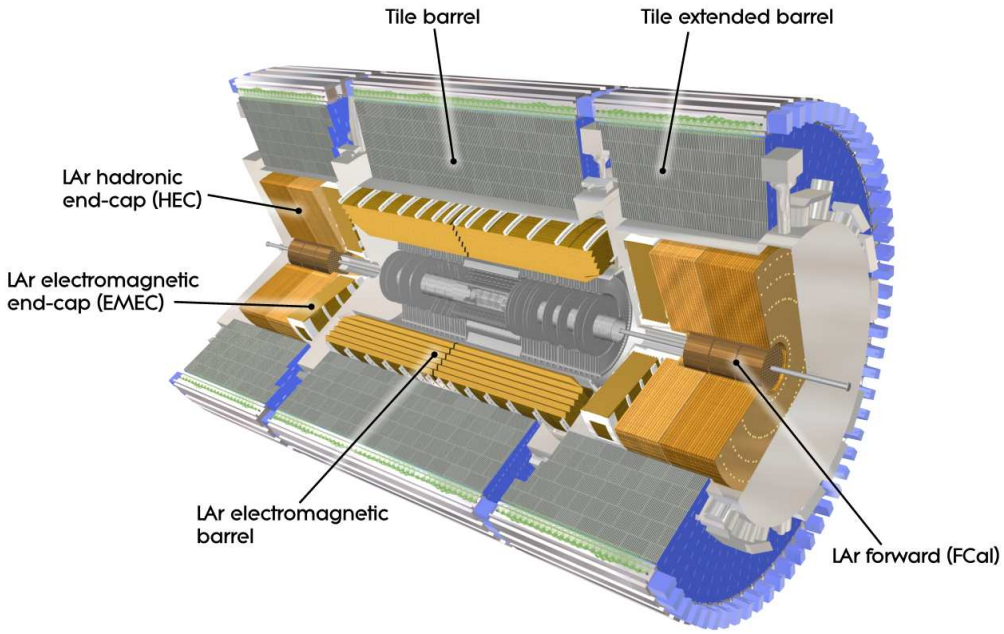

FIGURE 3.8. The cut-away view of the ATLAS calorimetry system

3.4.4.1. LAr Electromagnetic Calorimeter

The electromagnetic LAr calorimeter consists of the barrel and endcap cryostats. The barrel is subdivided into two identical half-barrel pieces separated by a 4 mm gap at $z = 0$. Both of them have lead acting as an absorber submerged in LAr operating at 89 K. The

absorbers are arranged in an accordion geometry to provide full ϕ coverage without any gap needed for support structures. The EM barrel LAr calorimeter is divided into three layers in depth for the $|\eta| < 2.5$ region and segmented in $\eta - \phi$ as shown in Fig. 3.9. The electrodes, consisting of three conductive copper layers, are also arranged in such a way that particles coming from the interaction point are hitting the modules at a uniform incident angle along the η as seen in Fig. 3.10. For $|\eta| < 1.8$, an instrumented presampler layer is placed in between the solenoid magnet and first LAr calorimeter layer to measure the energy lost from early showering.

The electromagnetic hadronic endcap calorimeter (EMEC) consists of two wheels, one on each side, which cover the regions $1.375 < \eta < 3.2$. Each wheel itself contains two — an inner and an outer — coaxial wheels with a boundary at $|\eta| = 2.5$. Each wheel is divided further into eight wedge-shaped pieces, also with the lead absorber arranged in accordion geometry to avoid gaps in azimuthal angle. In the high precision region of EMEC ($1.5 < \eta < 2.5$), it is divided into three layers. The first layer, $4.4X_0$ thick, is segmented along η direction as shown on the bottom in Fig. 3.10. The middle layer of EMEC has roughly the same granularity as the barrel ($\Delta\eta \times \Delta\phi = 0.025 \times 0.025$), while the outer layer is twice as coarse as that in η. The innermost layer η-granularity varies to keep the copper strip in the electrodes from being too thin. Since there are inactive materials amounting to several X_0, a presampler is also put in front of the EMEC in the $1.5 < \eta < 1.8$ region to improve energy measurement.

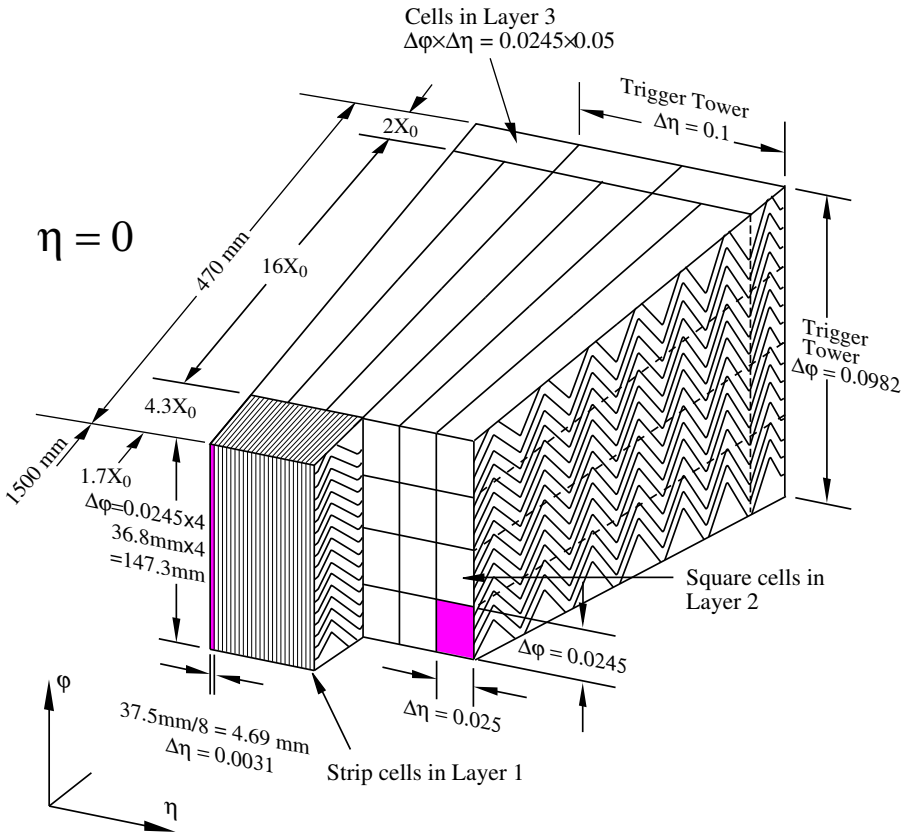

FIGURE 3.9. Sketch of a EM LAr calorimeter module showing the layout and granularity as well as the radiation length (X_0) for each layer.

3.4.4.2. LAr Hadronic Endcap Calorimeter

The LAr hadronic endcap calorimeter (HEC) covers the $1.5 < |\eta| < 3.2$ region. It uses copper as the absorber and LAr and the active material in a flat-plate design. The cell size is $\Delta\eta \times \Delta\phi = 0.1 \times 0.1$ for $|\eta| < 2.5$ and 0.2×0.2 for the rest. As seen in Fig. 3.8 in two different shades, the HEC consists of an inner and outer wheel on each side and two longitudinal layers each.

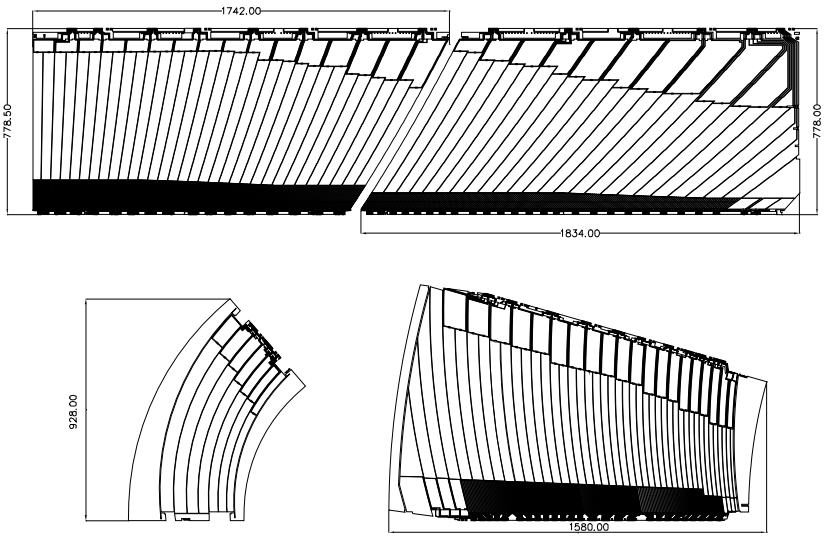

FIGURE 3.10. Layout of the electrodes for a single layer EM-LAr calorimeter in the barrel (top), endcap inner wheel (bottom left), and endcap outer wheel (bottom right).

3.4.4.3. LAr Forward Calorimeter

The very high $|\eta|$ region (up to 4.9) is covered by a forward calorimeter (FCal) consisting of one EM module (FCal1) and two hadronic modules (FCal2 and 3). They use LAr as the active medium and copper (FCal1) or tungsten (FCal2 and 3) as the absorber.

3.4.4.4. Tile Calorimeter

The tile calorimeter (TileCal) acts as the hadronic barrel calorimeter. It uses steel as the absorber and scintillating tiles as the active material. The system is separated into a 5.8 m-long barrel and two 2.6 m-long extended barrel modules covering up to $|\eta| < 1.7$. The light produced by ionizing particles going through the scintillator is collected by wavelength-shifting fibers. The grouping of the fibers defines the cell structure of the TileCal. They form three layers in depth with $\Delta\eta \times \Delta\phi = 0.1 \times 0.1$ for the first two layers and 0.2×0.1 in the outermost layer. Each tile module is approximately $7.4\lambda_{\text{int}}$ deep. Figure 3.11 shows how the steel, the scintillator, and the readout fibers are assembled.

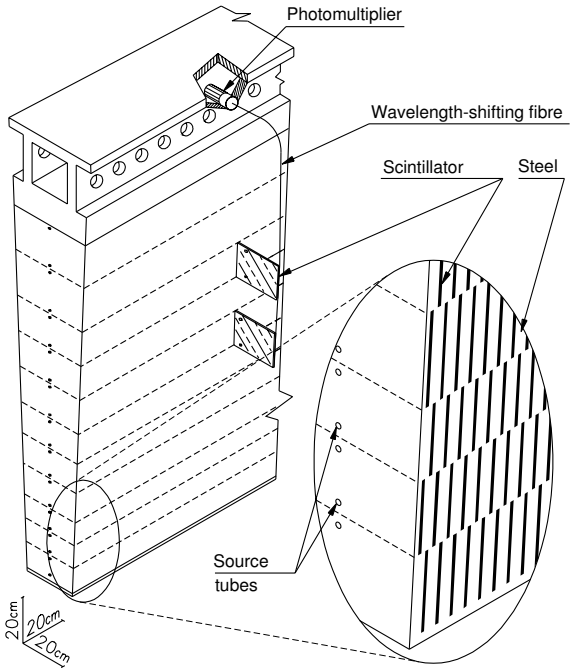

FIGURE 3.11. Layout of a TileCal module containing the steel absorber, scintillator active material, and the optical readout

3.4.5. Muon Spectrometer

The radiative processes of high energy muons are suppressed by their mass and, unlike hadrons, they do not strongly interact. These muons can pass through the calorimeters as minimum ionizing particles without losing much of their energy. Therefore, in addition to the tracker in the ID, ATLAS has a dedicated muon system designed for measuring the momentum of these muons. The muon trajectory is bent by the barrel (endcap) toroid magnet and in the $1.6 < |\eta| < 2.7$ ($|\eta| < 1.4$) region. The magnetic field in the region between the two toroids is provided by a combination of the two toroids and is referred to as the transition region.

The ATLAS muon system can be divided into the precision tracker and trigger chambers. The monitored drift tube (MDT) chambers are arranged in three concentric cylindrical layers centered on the beam axis in the barrel and three planes perpendicular to the beam axis. The MDTs have good resolution ($\sim$ 80 μm) but have a maximum drift

time of up to 700 ns which becomes the dead time for the system. This is too high for the LHC which operates at 25 ns (50 ns in Run 1) bunch crossing. Therefore, it is complemented by the resistive plate chambers (RPC) in the barrel and the thin gap chambers (TGC) in the endcap region. These two systems form the trigger chambers. They provide fast information on muon tracks within a few tens of nanoseconds after the passage of the particle, suitable for the trigger system covering the range $|\eta| < 2.4$. Due to the higher rate in the $2.0 < |\eta| < 2.7$ region, the first layers of the MDT system are replaced by the cathode strip chambers (CSC). These have fewer measurements per track but better spatial and time resolution compared to the MDT.

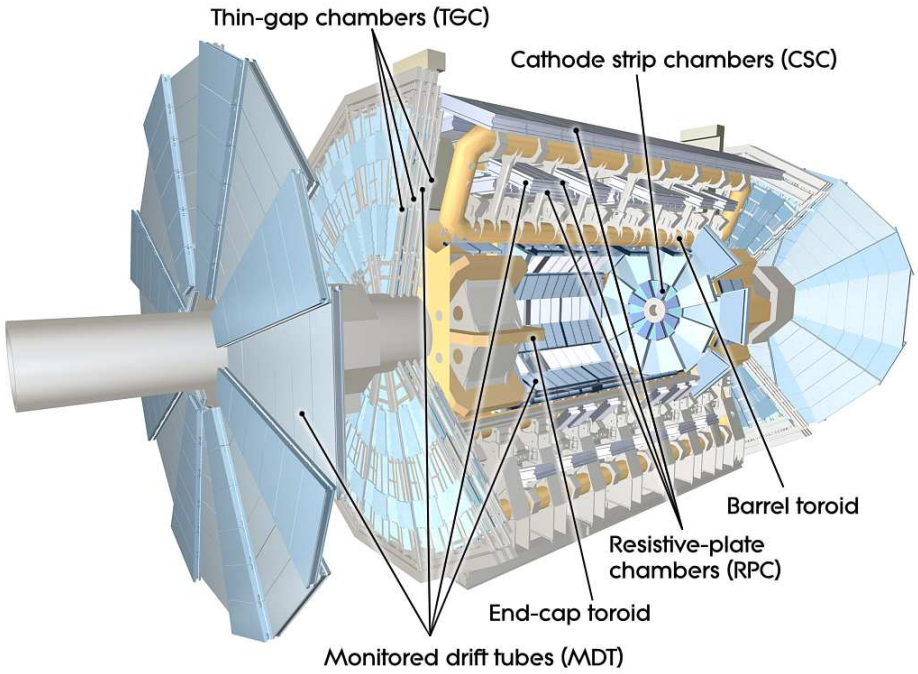

FIGURE 3.12. Layout of the muon spectrometer chambers.

3.4.6. Trigger and Data Acquisition

The proton bunch crossings every 25 ns from the LHC (50 ns in Run 1) present several challenges for the ATLAS trigger and data acquisition (TDAQ) system. The sheer size

itself is already a problem. Even at the speed of light, a particle can only travel $\sim$ 7.5 m in 25 ns. This means when the next bunch crossing arrives, particles from the last collision still have not fully transversed the detector. Adding the necessity to gather, process, and make decisions on the data only adds more latency. This high event rate also manifests as a problem of how to choose what to keep. The typical proton-proton event size for ATLAS is 1.3 megabytes. With bunch crossings every 25 ns, keeping every event would mean recording $\sim$50 terabytes per second, which is unfeasible. The TDAQ system must select the events of interest to physics out of the uninteresting background events and lower the recording rate down to $\sim$1kHz. The selections are based on various physics processes of interest such as very energetic events or those with large $E_{\mathrm{T}}^{\mathrm{miss}}$. The ATLAS trigger system in Run 1 consisted of one hardware and two software trigger levels. In Run 2, taking advantage of faster hardware, the two software levels are merged.

3.4.6.1. Level 1 Trigger

The Level 1 trigger is implemented as analog electronics. For the calorimeter, the level 1 calorimeter trigger (L1Calo) uses reduced granularity information from all subdetectors to identify EM cluster objects (electrons and photons) as well as jets and hadronic τ decays. For the muon spectrometer, the Level 1 muon trigger uses information from the muon trigger chambers, RPC and TGC, to identify high-p_{T} muon tracks consistent with the interaction region. The Level 1 trigger also indicates the region of interest (RoI) where those objects are detected and feeds them to the downstream trigger systems. The Level 1 trigger is designed to reduce the rate to $\sim$75 kHz in Run 1 and $\sim$100 kHz in Run 2 [37]. The Level 1 buffer is used to keep the information for events that are waiting for Level 1 decision. The maximum latency for the Level 1 trigger decision is 2.5 µs or about 100 bunch crossings.

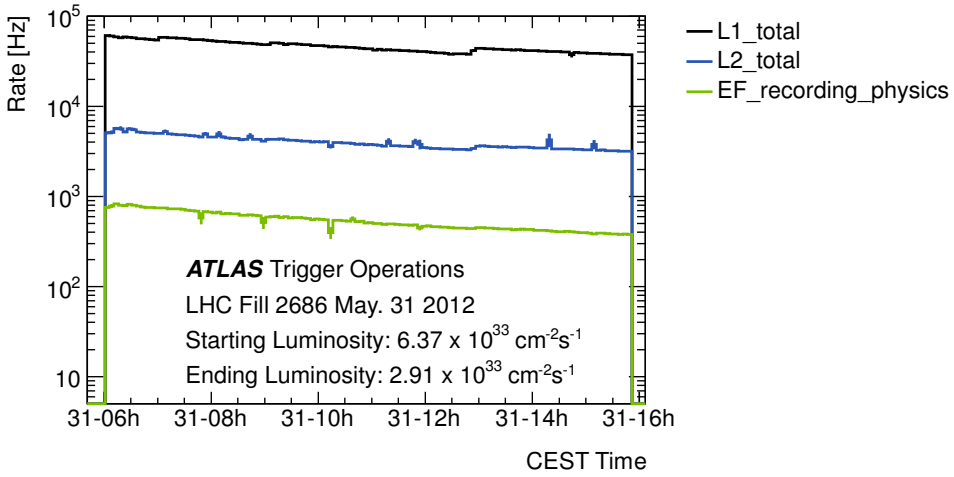

FIGURE 3.13. Data trigger output and recording rate at ATLAS [38]

3.4.6.2. High Level Trigger

The Level 2 and event filter (EF) trigger systems together form the high-level trigger (HLT) system. They use software algorithms running on a general-purpose computing cluster. In Run 1, the Level 2 trigger retrieved the full granularity information for the RoI indicated by the Level 1 system, and Level 2 used the extra information to further reduce the rate to below 3.5 kHz within 40 ms for each event. Finally, the EF system fully assembled the information from the detectors and fully reconstructed the objects to make the final decision before writing the event to permanent storage. The typical rates of accepted events for each trigger level in Run 1 can be seen in Fig.3.13.

As mentioned above, in Run 2 the HLT system has been merged into a single computing cluster system. It still retains the ability to do the on-demand readout of the Level 2 system and also use offline algorithms similar to the EF in Run 1. The merged HLT system reduces code duplication and increases the flexibility of software algorithms [37].

3.4.7. Luminosity Measurement

Apart from the main detector system, there are also three smaller detectors: LUminosity measurement using Cherenkov Integrating Detector (LUCID), Absolute Luminosity For ATLAS (ALFA), and Zero-Degree Calorimeter (ZDC). The first two are used to measure luminosity[3]. LUCID is a pair of Cherenkov detectors consisting of 20 1.5-m-long tubes surrounding the beam pipe located $\pm$17 m from the interaction point. It is the main relative luminosity detector designed to detect inelastic $p-p$ scatterings in the forward direction. LUCID relies on the assumption that the number of interactions per bunch crossing (μ) is proportional to the number of particles detected. LUCID can be used to measure both the integrated and instantaneous luminosities. ALFA is made of scintillating-fiber trackers inside Roman pots at $\pm$240 m from the interaction point. This detector extracts luminosity by measuring elastic scattering at small angles (3 μrad) and uses its relation to the total cross section from the optical theorem. The scattering angle required is smaller than the nominal beam divergence so measurements can only be made during specially prepared beam conditions.

3.5. Simulation

Interpreting ATLAS data requires comparing many observables with the theory predictions. Most of these are very difficult, if not outright impossible, to calculate in $p-p$ collisions. In order to obtain the correct distributions many experimental effects such as detector acceptance or trigger efficiency also have to be taken into account. Computer simulation using the Monte Carlo (MC) method is used to accomplish this.

[3] ZDC is used to determine the center of the collision during heavy-ion operation.

3.5.1. Event Generator

Many MC generators are used to produce the full picture of how an event will be seen by the detector. Figure 3.14 shows a simplified picture of how an event is generated. The fraction of incoming protons' momentum carried by the partons is controlled by the parton distribution function (PDF) which has to be measured from an experiment due to the non-perturbative nature of the strong interaction. The hard interaction and the immediately following decays are usually what are shown as Feynman diagrams. This is also referred to as the matrix element (ME) part of an event generator and is calculated to a fixed order in perturbation theory. Generators' precision of this modeling is used to classify them into leading order (LO), next-to-leading order (NLO), etc. Colored partons (gluons, quarks) can emit QCD radiation, usually classified as initial state radiation (ISR) (dark blue line) and final state radiation (FSR) (light green line). This process is simulated by a parton shower (PS) generator. The precision of a PS is characterized by the number of loops which show up as "towers" of $[\alpha_s \log k_\perp^2 \log k_\parallel]$ in the calculation [39], so a PS is classified as leading logarithm (LL), next-to-leading logarithm (NLL), etc. The final state partons are then hadronized and decay to final state *particles*. In order to understand the full picture, such as a $t\bar{t}H$ event shown in Fig. 3.15, the secondary (big yellow blob) interactions from the same collision, also called *underlying events (UEs)*, have to be included as well. Photon radiation can also occur at any stage [40].

The generators mentioned in this dissertation are summarized below:

SHERPA [40]: Multi-parton LO generator with emphasis on ME+PS merging.

PYTHIA [43, 44]: Multi-purpose LO generator. Mostly used for QCD final state and showering in ATLAS.

POWHEG [45]: Positive Weight Hardest Emission Generator[4]. A NLO event generator.

[4] Despite its name, POWHEG does produce events with negative weight.

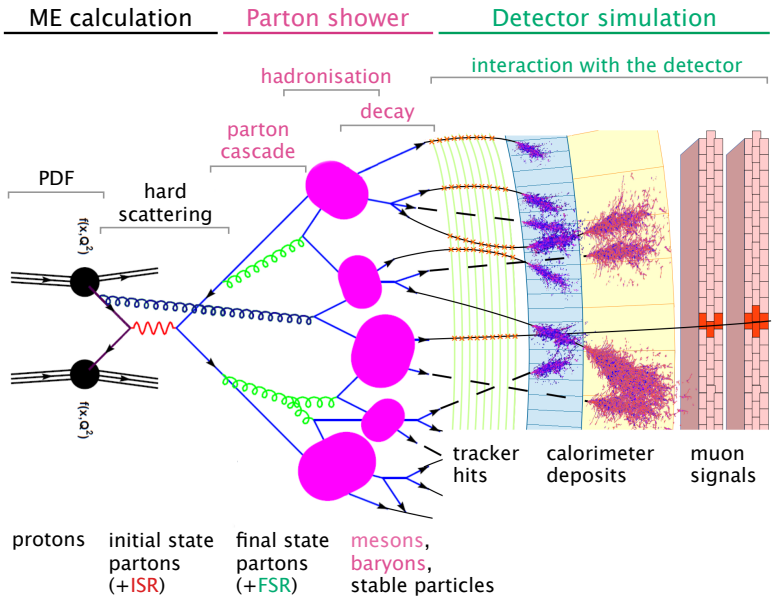

FIGURE 3.14. Taken from [41]. Pictorial representation of how an event is generated.

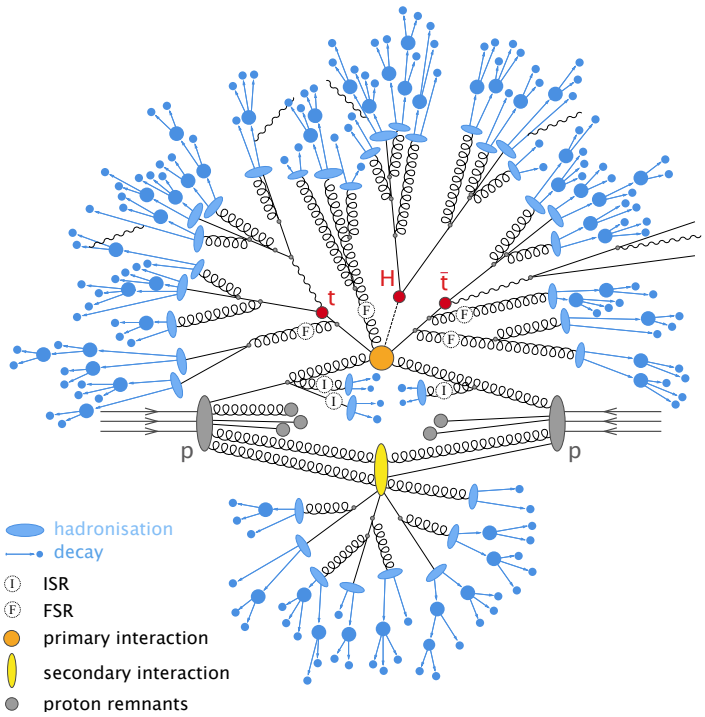

FIGURE 3.15. Taken from [42] and inspired by [40]. Pictorial representation of a $t\bar{t}h$ event as produced by an event generator.

MadGraph_aMC@NLO [46]: An amplitude and event generator at LO and NLO for various models.

EvtGen [47] A packaged specialized in *B*-hadron decays.

3.5.2. Detector Simulation

The final state particles are fed into the detector simulation (the right half of Fig. 3.14). ATLAS uses a GEANT4-based [48] suite to simulate how particles interact with the ATLAS detector and magnetic fields. In the full simulation, particles' interactions with every part of ATLAS is simulated with a full-detail model. In the alternative Atlfast-II simulation, the showers in the electromagnetic and hadronic calorimeter are produced using per-particle average shower shapes. The energy deposits are then processed in the digitizer to simulate the ATLAS readout system and are finally turned into a raw data format identical to that from real collisions.

CHAPTER IV

EVENT RECONSTRUCTION

In a way, event reconstruction is an attempt to "rewind" what was described in Section 3.5 but also for real data. First the collections of "hits" are grouped into either "tracks" (tracker) or "clusters" (calorimeter) to represent the final state particles (the output of the event generator after hadronization for MC). Then another set of algorithms will try to combine these tracks and clusters to identify the original physics objects "partons", typically associated with the outgoing particles in a Feynman diagram (the output of the ME calculation for MC). This process is, of course, not perfect. Signatures from two types of objects can look similar, and some particles do not interact with the detector. Not to mention the various detector effects (inactive material, noise, etc.) that are responsible for loss of information. The goal is to have the best possible efficiency and fake rejection rate.

Typical interactions for various types of particles with ATLAS subcomponents are shown in Fig. 4.1, and will be described in more detail later.

4.1. Particle Identification

The two most relevant particle identification methods in ATLAS for the analyses present in the dissertation are *tracks* from the tracking system, and *topoclusters* from the calorimeter system.

4.1.1. Tracks

Charged particles traveling through ATLAS's magnetic field can be identified as tracks in the inner detector, and the ratio of the charge and momentum (q/p) of these particles can be determined from the curvature of the tracks. ATLAS track reconstruction [49, 50] begins by turning raw data from Pixel and SCT detectors into three-dimensional measurements

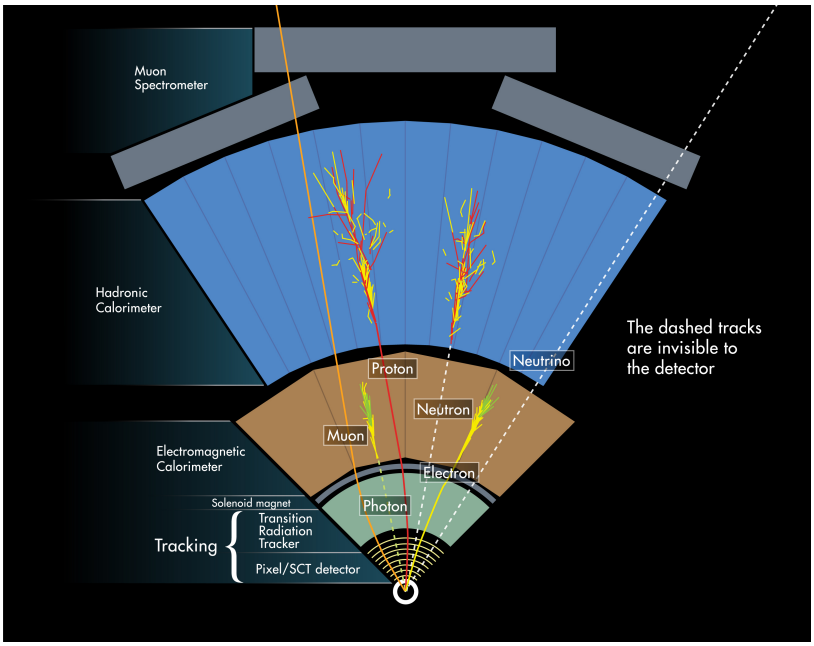

FIGURE 4.1. Cross section of the ATLAS detector showing how each type of particles interact with each subdetector.

referred to as space-points. Seeds are made from sets of three space-points to form crude tracks. After a number of criteria are applied to maximize purity, the chosen seeds are then used to build track candidates with a combinatorial Kalman filter [51]. There can be more than one track candidate per seed. The track candidates are then processed by the ambiguity resolver to choose the final reconstructed tracks collection.

4.1.2. Topocluster

Topologically connected calorimeter cell signals (topoclusters) are the basic building blocks for reconstructing hadronic final states (jet, isolated hadron, and hadronicially decayed τ lepton) in ATLAS [52]. They also represent the energy and direction of soft particles which are needed for reconstructing the missing transverse energy. Topoclusters used in ATLAS are three dimensional objects aimed to provide the measurement of energy

and direction of the final state particles[1]. They also provide suppression of noise and pileup contribution by taking advantage of the high granularity of the ATLAS calorimeters.

The cells are classified using the ratio of cell energy over the average noise level $\varsigma_{\text{cell}} \equiv \frac{|E_{\text{cell}}|}{\sigma_{\text{noise}}}$. There are three thresholds for this variable: seed (S), neighbor (N), and boundary (P). The default value that ATLAS uses is $(S, N, P) = (4, 2, 0)$, also referred to as the 4-2-0 topocluster scheme. Topoclusters are formed by first making a collection of cells above the S threshold called proto-clusters and ordering them by ς_{cell}. The cells above the N threshold that are neighbors of the boundary are added to the proto-cluster. This step is repeated until the neighbors of the boundary are below the N but above the P threshold. If two seeds are neighbors or only separated by cells above the N threshold, the proto-cluster are merged. After this step, topoclusters with two or more local maxima will be processed by a cluster-splitting algorithm to avoid biasing jet finding or jet substructure analysis and to improve $E_{\text{T}}^{\text{miss}}$ resolution.

Note that ς_{cell} is defined in term of the absolute value for cell energy. Negative cell energies from the ATLAS calorimeter system usually originate from out-of-time pileup or noise. Cells with negative energy provide a suppression of pileup contributions due to the fact that the time averaged between the in-time and out-of-time pileup is approximately canceled. Topoclusters take advantage of this feature by allowing negative energy cells to participate in the clustering process. The usage of these cells can also suppress random noise by letting the positive and negative fluctuations cancel each other out.

[1] However, one-to-one mapping between topoclusters and particles may not be expected, depending on the particle type.

4.1.2.1. Local Hadronic Cell Weighting (LCW)

The "local" here refers to the fact that this is a calibration for topoclusters which is relatively localized and small compared to regular physics objects. The scheme aims to mainly address three calorimeter signal inefficiencies:

Non-compensating calorimeter response ATLAS calorimeter measurement at the cell level does not correct for the difference between hadrons' and electron/photons' detector response ($e/\pi > 1$).

Signal losses due to clustering Topoclusters include the intrinsic noise suppression from negative energy cells as mentioned above. Overcompensation from this can occur depending on the pileup condition and noise threshold.

Signal losses due to energy lost in inactive material Energy lost due to nearby inactive material is different for each calorimeter module.

Corrections for these effects can be applied cluster-by-cluster without any assumption about the target physics object, so it can benefit any downstream reconstruction algorithms that use topoclusters as input.

4.2. Jet

In the most general sense, a jet is a collection of particles from a common source. From the theoretical point of view, a jet represents the energy flow of a quark's or gluon's final state before parton showering and hadronization. In an actual experiment, a jet is defined by a *jet finder*—an algorithm used to group particles. A jet in this case can represent more than one parton depending on the chosen algorithm. A jet finder may also include a kinematic threshold for its input, making some partons fail to be reconstructed as a jet.

4.2.1. Requirements for a Jet Finder

Jet finding is intrinsically a very complex problem. The algorithms not only have to satisfy practical requirements such as being able to run quickly, but they also have to pass the following requirements:

Infrared safety Adding or removing a soft particle should not change the final jet collections (Fig. 4.2a).

Collinear safety Splitting or merging of high p_{T} particles should not change the result of the algorithm (Fig. 4.2b)

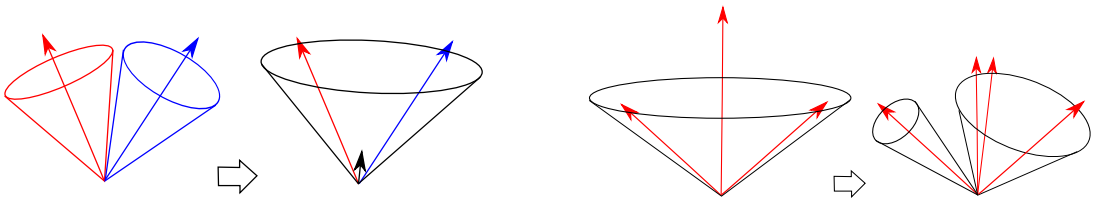

(a) Infrared sensitivity (b) Collinear sensitivity

FIGURE 4.2. The effects which a good jet finder should be insensitive to. The arrows represent particles and the cone represent jets. On the left, soft radiation (black arrow) causes the two jets to merge. On the right, a collinear splitting of a particle can split the jet.

A simple way to understand why these requirements are important is the following: consider a dijet QCD process at a LO calculation in Fig. 4.3a. A NLO calculation will include the diagram with a FSR gluon shown in Fig. 4.3b. If the FSR gluon is soft or collinear with regards to the quark from which it radiated, the final jet collections should not change. If this is not true, in other words, if the result of the jet finder depends on the precision of the calculation, then its result from simulation cannot be trusted; after all, there is no order in perturbation for a real experiment.

(a) A LO diagram (b) A NLO diagram

FIGURE 4.3. A QCD Process

4.2.2. Anti-k_t Algorithm

There are many jet finders available. One of the earliest ideas was to simply find a high p_{T} seed and draw a cone around it. Unfortunately this algorithm is not infrared safe. It also suffers from what is called the "dark tower" problem, which happens when the seed falls out of the cone after softer particles are added. Another algorithm, the SISCone [53] algorithm, does not have seeds but instead looks for a stable cone of a given size. It also has to be accompanied by a split-and-merge algorithm because the final jets can overlap. While it is infrared safe, SISCone still suffers from irregularity at the boundary in the presence of pileup or underlying events [54] as seen in Fig. 4.4a. It is computationally very slow as well.

Another class of jet finder is the recursive recombination algorithms called the k_t *family*. It begins by making a list of the distance parameters between all pair combinations of input proto-jets, d_{ij} and between input proto-jets and the beam, d_{iB}:

$$d_{ij} = \min(k_{ti}^{2p}, k_{tj}^{2p}) \frac{(\Delta R)_{ij}^2}{R}, \tag{4.1}$$

$$d_{iB} = k_{ti}^{2p} \tag{4.2}$$

$k_t = p_{\mathrm{T}}$ in this case. ΔR is defined in Eq. (3.5). R is a parameter of the algorithm sometimes referred to as the "cone size", the reason for which will be clear shortly. For the moment, I

will set $p = 1$. If the smallest value in a $\{d_{ij}, d_{iB}\}$ list is a d_{iB}, that proto-jet is considered a jet and is taken out of the list. If the smallest value is a d_{ij}, then the pair is added together and the list is recomputed. For this reason, the parameter R controls how "far" a pair of proto-jets will be combined. The bigger R is, the larger final jets will become. The process is repeated until there is no more proto-jet.

The exponent p controls the p_{T} order of the recombination. In theory it can take on any value, but in practice the most common values are (1, 0, -1) which are the three algorithms in the k_t family. The oldest one is the k_t algorithm [55] with $p = 1$, so the softest proto-jet is considered first. This idea originated as an attempt to "rewind" the parton fragmentation by starting from the end of the decay chain and working backward. The next proposal is the Cambridge/Aachen (CA) algorithm [56] with $p = 0$, meaning only ΔR is used in the ordering.

The recursive recombination algorithm has a nice feature of being intrinsically infrared and collinear safe, as well as guaranteeing no overlapping between jets. Both k_t and CA algorithms also have a meaningful recombination order as mentioned above. Unfortunately, they both suffer from having irregular jet boundaries in the presence of soft radiation as seen in Figs. 4.4b and 4.4c.

It was not until the early days of the LHC that the anti-k_{t} algorithm [54] with $p = -1$ emerged as the standard jet finder. One of the reasons is that traditional implementations of k_t family algorithms are too slow, but this was solved with the invention of FastJet [57, 58]. The anti-k_t algorithm has the infrared and collinear safe features of the k_t family and, as seen in Fig. 4.4d, the jets are generally circular in shape. The softer jets have a "moon shape" because anti-k_{t} combines the hardest proto-jets first. The shapes of the jets are stable against pileup and underlying events. This feature is also very important for energy calibration of the jets. The downside of the anti-k_{t} algorithm is that its recombination order has no meaningful interpretation from a theoretical point of view. This is acceptable for energy and

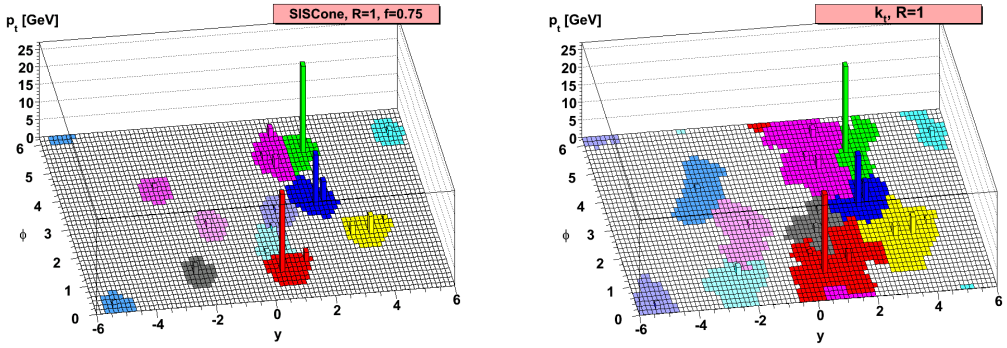

(a) SISCone (b) k_t

(c) Cambridge/Aachen (d) Anti-k_t

FIGURE 4.4. Taken from [54]. A sample parton-level event (generated with HERWIG) with the ghost area shown for each jet (See Section 4.2.3).

mass measurement of the jets. However, it can be problematic when one tries to analyze *jet substructure* where the jet can represent more than one parton.

4.2.3. Ghost Active Jet Area and Jet Ghost Association

For an infrared safe jet finder, the area of a jet can be defined by clustering a very soft "ghost" with real particles. This represents the active catchment of the jets called *ghost area*. Infrared safety ensures that this does not interfere with the actual jet. Illustrations of the ghost areas for various algorithms are shown in Fig. 4.4. Following this idea, one can assign other objects (e.g. tracks) to a jet by making a ghost with the same (η, ϕ) and

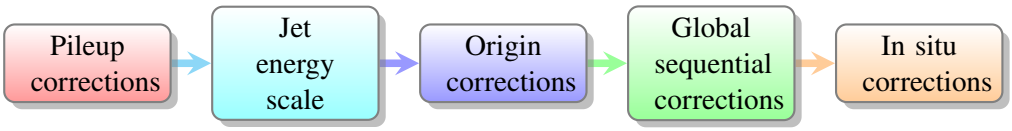

FIGURE 4.5. Jet calibration steps in ATLAS.

letting it cluster along with actual particles. An object that has its ghost clustered into a jet is referred to as being *ghost associated* to the jet.

4.2.4. Jet Measurement in ATLAS

The standard jet collections in ATLAS are built from topoclusters using an anti-k_t algorithm with $R = 0.4$. The topoclusters can be either with LCW applied (LCTopo jet) or without (EMTopo jet). However, before these jets can be used in analyses they have to be corrected for experimental and detector effects and it must be ascertained that they came from hard interactions.

4.2.4.1. Jet Energy Calibration and Resolution

The jet calibration [59] procedure in ATLAS is shown in Fig. 4.5. The steps are the following:

Pileup correction A ghost area-based subtraction is used to reduce the effect of pileup. The observables used in the technique are the ghost area (A) and the average energy density in the $\eta \times \phi$ plane (ρ). Additionally corrections as a function of the number of primary vertex (N_{PV}) and the average number of interactions per bunch crossing ($\langle\mu\rangle$) are also applied in Run 2.

Jet energy scale (JES) Jet energy is corrected for detector effects using the scales derived from jet energies of isolated truth particles in simulation. The JES is binned in η and p_T of the measured jet.

Origin correction In some areas of the detector it is found that the reconstructed jets have a bias in η direction. This effect also shows up in the gap and transition area. The jets are therefore corrected to point to the primary vertex which improve the p_{T} measurement.

Global sequential corrections (GSC) After the above steps, the jets are found to still have a dependence on some observables from the detector. The following corrections are applied in order to correct for the biases:

1. The fraction of energy deposited in the first layer of the Tile calorimeter.
2. The fraction of energy deposited in the third layer of the electromagnetic calorimeter.
3. The number of tracks ghost-associated with the jet.
4. The p_{T}-weighted width of the tracks associated to the jet.
5. The number of muon segments associated with the jet.

In situ corrections These aim to correct the difference between data and MC due to the imperfect simulation. They are derived from events where well-measured reference objects are back-to-back with jets. The reference objects used are photons, Z bosons, and well-measured soft jets (used to calibrate very high p_{T} jets).

There are a total of 74 systematic uncertainty terms associated with the JES from various observables. Propagating this full set to obtain all correlations is often unnecessary. One reduction scheme reduced them to 18 nuisance parameters with minimal loss of correlation. Another scheme used in ATLAS has only three parameters with an acceptable loss in correlation for the analysis present in this dissertation.

4.2.4.2. Jet Mass Measurement and Uncertainty

The standard $R = 0.4$ anti-k_t jets in ATLAS traditionally have mass but are not calibrated beyond the jet energy calibrations described in the previous section. Since the longitudinal boost of the system is not known in a hadron collider the object balance technique cannot be used, unlike the p_T measurement. One way to approximate the jet mass uncertainty is to use the *R-track double ratios* method [60]. First, define

$$r^m_{trackjet} \equiv \frac{m^{calo}}{m^{track}} \tag{4.3}$$

where m^{calo} is the regular calorimeter jet mass while m^{track} is the mass of the vector sums of track ghosts associated to the jet. The average values $\langle r^m_{trackjet} \rangle$ are plotted in bins of an observable (e.g. jet mass, p_T, etc.). The distributions are obtained for both data ($\langle r^m_{trackjet} \rangle_{data}$) and MC ($\langle r^m_{trackjet} \rangle_{MC}$). The departure of $R_{trackjet} \equiv \frac{\langle r^m_{trackjet} \rangle_{data}}{\langle r^m_{trackjet} \rangle_{MC}}$ from 1 can be used as a proxy to estimate mass uncertainty from mis-modeling in the calorimeters. An example of such distribution is shown in Fig. 4.6a. The study for Run 1 shows that the jet mass scale uncertainty is below the level of 5% for $p_T > 50$ GeV. This technique can also be used to study the effect of close-by jets by binning this ratio in close-by observables such as the ΔR distance to the leading jet. An example is shown in Fig. 4.6b. Close-by effects are determined to be well-modeled by MC.

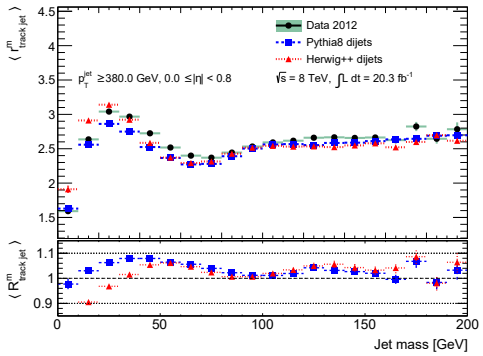

(a) Jet mass scale uncertainty study in bins of mass.

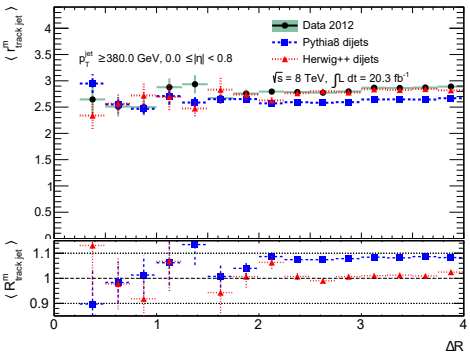

(b) In bins of ΔR to the leading jet for close-by effect study

FIGURE 4.6. Example of distributions of $\langle r^m_{trackjet} \rangle$ and $R_{trackjet}$. The mass uncertainty can be derived from the differences between the data and MC.

4.2.4.3. Jet Cleaning

There can be contributions from pileup, underlying events, or noise that survive suppressions at the calorimeter cell or topocluster level and made it into a jet. Jet cleaning [61] is an attempt to reject these "fake" jets that do not originate from the hard interaction with observables at the jet level. There are three main sources:

Beam-induced background These fake jets come from proton interactions outside of the collision region in ATLAS.

Cosmic ray High energy particles from space hitting the atmosphere can produce showers of particles that reach the detector.

Calorimeter noise Large scale coherent noise can produce a jet.

The first set of variables for jet cleaning derived from LAr cell-level quality ($Q^{\mathrm{LAr}}_{\mathrm{cell}}$) represents how well the measured pulse samples match to the expected shapes. $Q^{\mathrm{LAr}}_{\mathrm{cell}}$ ranges from 0 to $2^{16} - 1$. The observables are:

$\langle Q \rangle$ The average jet quality is defined as the energy–squared weighted average of the pulse quality of the calorimeter cells ($Q_{\text{cell}}^{\text{LAr}}$) in the jet. This quantity is normalized such that $0 < \langle Q \rangle < 1$

$f_{\text{Q}}^{\text{LAr}}$ Fraction of the energy in the LAr calorimeter cells of a jet with poor signal shape quality defined as $Q_{\text{cell}}^{\text{LAr}} > 4000$

$f_{\text{Q}}^{\text{HEC}}$ Fraction of the energy in the HEC calorimeter cells of a jet with poor signal shape quality defined as $Q_{\text{cell}}^{\text{LAr}} > 4000$

Another cell-based variable is:

E_{neg} The sum of all cells with negative energy. Jets that are dominated by negative energy cells tend to be fake.

Jets that come from noise or beam-induced backgrounds tend to be more localized longitudinally in the calorimeters. There are three energy ratio variables that exploit this feature:

f_{EM} The ratio of the energy deposited in the electromagnetic calorimeter to the total energy of the jet

f_{HEC} The ratio of the energy deposited in the HEC calorimeter to the total energy

f_{max} The maximum energy fraction in any single calorimeter layer

Real jets contain charged hadrons that leave tracks in the tracker. This fact is used by another jet-cleaning variable:

f_{ch} The ratio of the scalar sum of the p_{T} of the tracks coming from the primary vertex associated to the jet divided by the jet p_{T}

The nominal jet cleaning criteria is called “BadLooser” in Run 1 and “BadLoose” in Run 2. It is designed to be very efficient ($\gtrsim 98\%$) while rejecting as many fake jets as possible. The criteria for a fake jet contains the following cuts:

1. $f_{\text{HEC}} > 0.5$ and $| f_{\text{Q}}^{\text{HEC}} | > 0.5$ and $\langle Q \rangle > 0.8$
2. $| E_{\text{neg}} | > 60$ GeV
3. $f_{\text{EM}} > 0.95$ and $f_{\text{Q}}^{\text{LAr}} > 0.8$ and $\langle Q \rangle > 0.8$ and $| \eta | < 2.8$
4. $f_{\text{max}} > 0.99$ and $| \eta | < 2$
5. $f_{\text{EM}} < 0.05$ and $f_{\text{ch}} < 0.05$ and $| \eta | < 2$
6. $f_{\text{EM}} < 0.05$ and $| \eta | \geq 2$

The first two criteria target sporadic noise bursts in the HEC. The third selection helps identify jets from large coherent noise. The last three requirements are more general and are used to identify hardware issues, beam-induced background, and cosmic muon showers [61].

4.2.4.4. Jet Vertex Tagger

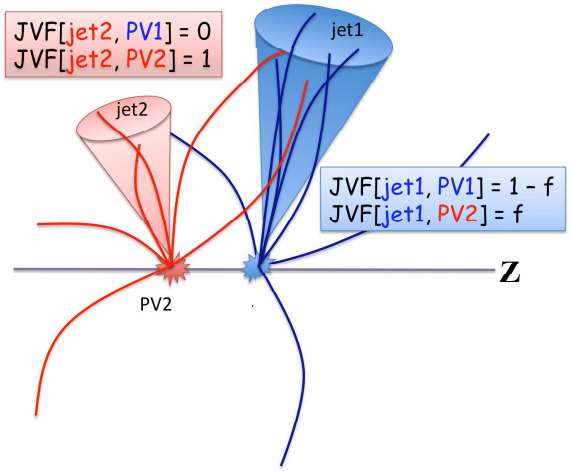

FIGURE 4.7. Taken from [62]. Schematic representation of how to compute jet vertex fraction (JVF).

Track and vertex information can be used to identify which interaction point the jet came from. Taken from the idea originally developed by the D0 collaboration [63], the JVF is used by ATLAS in Run 1. It assigns a probability of the jet coming from a given vertex. Figure 4.7 shows how is it computed schematically. In Run 2, the JVF has been further

developed to correct for contribution from pileup tracks (corrJVF). Another variable, R_{pT}, is defined as the scalar p_{T} sum of the tracks that are ghost associated with the jet and originate from the hard-scatter vertex divided by the fully calibrated jet p_{T}, which includes pileup subtraction:

$$R_{pT} \equiv \frac{\sum_k p_{\mathrm{T}}^{\mathrm{track,k}}(\mathrm{PV0})}{p_{\mathrm{T}}^{\mathrm{jet}}} \tag{4.4}$$

The two variables are then combined using a multivariate technique into the jet vertex tagger (JVT) [64], which is used in Run 2 to identify pileup jet at low p_{T} (< 60 GeV).

4.2.5. *b*-tagging

Light quarks[2] and gluon final states hadronize and produce many secondary colorless particles, mostly pions, leaving many tracks in the tracker system and living long enough to reach the calorimeters. On the other hand, the top quark's lifetime is too short and so it decays before having a chance to hadronize. The hadronic decay of the bottom quark is dominated by the $b \to cW^{*-}$ process with the virtual W decaying to $\ell + \nu$ as shown in Fig. 4.8 ("semileptonic decay"). The rate of this process is $\propto \alpha_W^2 \frac{m^5}{M_W^4}$, so it is suppressed by M_W^4 and the off-diagonal value of the CKM matrix V_{cb}. This makes the lifetime of the bottom quark long enough for the B meson to travel a few hundred μm. When the bottom quark decays, it produces many tracks that do not originate from the primary vertex, which together can be used to reconstruct a *secondary vertex* within a jet. ATLAS's pixel detector (Section 3.4.3.1) can resolve a separation down to 50 μm in R, therefore it is capable of reconstructing this secondary vertex and use that to "tag" the jet that originated from a b quark.

Unfortunately, similar features can also happen in a jet originating from a charm quark. Dominant decay modes for the charm, such as $c \to s + e^+ + \nu_e$, are similarly suppressed

[2] Generally, "light flavors" refer to all quarks from the 1st and 2nd generations, but in the context of *b*-tagging, the charm quark is sometimes excluded.

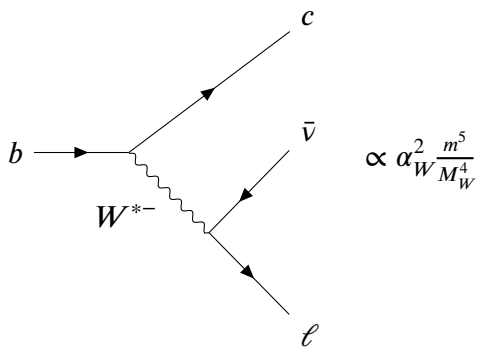

FIGURE 4.8. Dominate hadronic b "semileptonic" decay process.

by the M_W^4 but the element from the CKM is ~ 1. On other hand, the bottom is about four times heavier than the charm quark. The two competing factors make the charm and bottom quark have a lifetime in the same order of magnitude. In the particle rest frame, they are, in distance unit [11]:

$$c\tau \sim (124 - 320)\,\mu\text{m} \qquad c \text{ quarks}$$
$$\sim (468 - 495)\,\mu\text{m} \qquad b \text{ quarks}$$

So the charm jets are the largest source of background for b-tagging.

ATLAS b-tagging [65, 66] uses three classes of algorithm to tag a b-jet:

Impact parameter-based algorithms The impact parameter of a track is defined as the distance of closest approach to the primary vertex. The transverse ($R\times\phi$) component is labeled d_0 (Fig. 4.9) and the longitudinal component is z_0.

Secondary vertex-based algorithms The secondary vertex is reconstructed and its properties are used to discriminate between b-jet and light jets.

JetFitter algorithm Exploit the topology of weak b and c hadrons decay.

In Run 1, ATLAS used a neural network (NN) or boosted decision tree (BDT) trained for each algorithm, then combined them with another NN to obtain the b-tag weight called

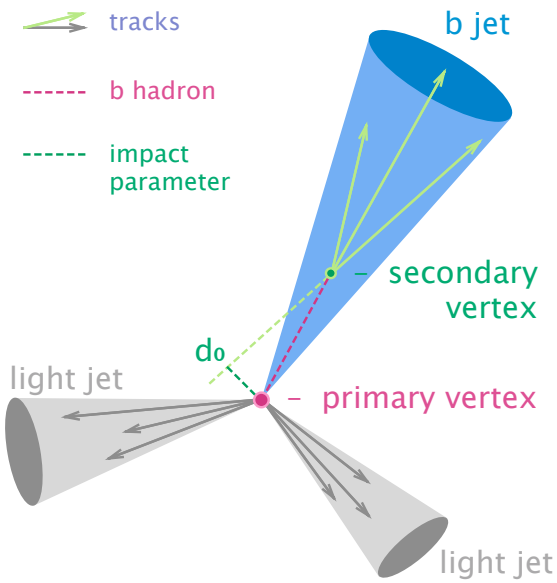

FIGURE 4.9. Taken from [67]. Graphical representation of the transverse impact parameter d_0 in $R \times \phi$ plane of the detector.

MV1. The main working point has 70% b-jet efficiency, c-jet rejection rate[3] of $\sim$ 5, and light jet rejection of $\sim$ 100 [65]. In Run 2, the inputs from all algorithms are combined using a BDT to obtain the weight called MV2c10. The main working point has 77% b-jet efficiency, and c-jet, light jet, and τ-jet rejection rate of 6, 134, and 22 respectively [66, 68][4].

4.3. Electron

Signatures of a "prompt" electron from a hard interaction are an EM shower as described in Section 3.4.4 and a matching track. In ATLAS, electrons are reconstructed using the following steps [69]:

1. Seed clusters are built using a sliding-window algorithm [70] in the electromagnetic calorimeter (ECAL).

[3] Defined as total background/backgrounds that passed the selection.

[4] The performance numbers are derived from simulated $t\bar{t}$ samples. The truth label is obtained by finding either a truth b hadron, a c hadron, and a τ lepton within $\Delta R < 0.3$ of the jet.

2. Tracks are reconstructed using a similar method as that described in Section 4.1.1, but using an electron hypothesis[5] which allows more energy loss due to the bremsstrahlung process (See Fig. 3.6a).

3. Tracks and seed clusters are then matched to obtain electron candidates.

The next step is to determine if an electron candidate is signal- or background-like. The discrimination variables can be grouped into hadronic leakage, ECAL information, track conditions, TRT, and track-cluster matching variables. The details can be found in [69]. For Run 2, ATLAS uses a likelihood-based method to derive three operation points, Loose, Medium, and Tight, in order of increasing background rejection. The looser selections are subset of the tighter ones, so all Tight electrons are also Medium and Loose. There are also the "VeryLoose" criteria with even better efficiency. This is used for vetoing electrons in this analysis.

4.4. Photon

Conceptually, a "prompt" photon appears as an EM shower in the ECAL (similar to an electron), but without any track associated with it. In reality, reconstruction of a photon is complicated by the fact that it can "convert" into an e^+e^- pair (See Fig. 3.6b) as it passes through the trackers, so the algorithm also has to take this topology into account. In ATLAS, the EM clusters and tracks are built the same way as described in Section 4.3, but tracks that are consistent with a photon conversion are also built and loosely matched to seed clusters. ATLAS uses a cut-based method to derive two operation points, Loose and Tight, using discriminating variables from hadronic calorimeter (HCAL) leakage and ECAL information. The details of these variables can be found in [71].

[5] The standard assumption is for pion tracks.

4.5. Muon

As mentioned in Fig. 3.12, high energy muons behave as minimum ionization particles as they pass through the detector, so ATLAS has dedicated muon chambers to capture their trajectory at a larger radius. Main types of muons used in this analysis are obtained by matching tracks constructed independently in the ID and the muon system. They are called "combined" muons in ATLAS [72, 73]. The tracks in the ID are reconstructed as described in Section 4.1.1. In the muon spectrometer, a Hough transform [74] is used to search for hits aligned on a trajectory in the bending plane of the detector. The combined tracks are then formed using a global fit with an outside-in pattern recognition; the muon tracks in the muon systems are extrapolated inward to match a track in the ID. The other two types of muons are segment-tagged, where a track in ID is matched to at least one track segment in the muon chambers, and is calorimeter-tagged, where a track in ID is matched to a minimum ionizing particle trajectory in the calorimeters.

Muon identification aims to suppress non-prompt muons, mainly from pion and kaon decays. The variables used are:

Number of hits Number of hits in each detector system and holes (active layers that a track passes through but have no hits).

$\boldsymbol{q/p}$ **significance** $= \left| \frac{(q/p)_{\mathrm{ID}} - (q/p)_{\mathrm{MS}}}{\sqrt{(q/p)^2_{\mathrm{ID}} + (q/p)^2_{\mathrm{MS}}}} \right|$, where MS refers to muon spectrometer.

$\boldsymbol{\rho'} = \left| \frac{p_{\mathrm{T}}^{\mathrm{ID}} - p_{\mathrm{T}}^{\mathrm{MS}}}{p_{\mathrm{T}}^{\text{combined track}}} \right|$.

Combined fit qaulity Normalized χ^2 of the combined track fit.

There are four types of identification selections, Loose, Medium, Tight, and High-p_{T}. The last three are in an order of increasing background rejection and the tighter ones are a subset of the looser selections. High-p_{T} selection is optimized for maximum momentum resolution for $>$ 100 GeV muons.

4.6. Electron, Muon, and Photon Isolation

Contributions from pileup, underlying events, and nearby jet activities can interfere with the measurement of electrons and photons, or even fake it. In the case of a muon, energy deposits outside the track suggest that it may not come from the hard interaction. For example, it can be a muon from a semileptonic decay such as the one in Fig. 4.8. To avoid these problems, isolation requirements are applied. ATLAS typically does this by looking at the energy deposited in a cone around the object in the trackers ($p_{\mathrm{T}}^{\mathrm{cone}}$) or calorimeters ($E_{\mathrm{T}}^{\mathrm{cone}}$). Cuts are applied on the ratio between the energy in the cone and of the object. The sizes of the cones are usually between $\Delta R = 0.2$ to 0.4 depending on the analysis.

4.7. Missing Transverse Momentum

Once all other objects are reconstructed, building the $\mathbf{p}_{\mathrm{T}}^{\mathrm{miss}}$ should be simple; simply vector summing over all objects. In practice, a lot of complications arise from energy deposits from objects that fall below thresholds, pileup, and underlying events. In ATLAS, the final $\mathbf{p}_{\mathrm{T}}^{\mathrm{miss}}$ [75] is built by summing over $\mathbf{p}_{\mathrm{T}}^{\mathrm{miss}}$ from each calibrated object type plus unused "soft terms":

$$\mathbf{p}_{\mathrm{T}}^{\mathrm{miss}} = \mathbf{p}_{\mathrm{T}}^{\mathrm{miss}}(e) + \mathbf{p}_{\mathrm{T}}^{\mathrm{miss}}(\gamma) + \mathbf{p}_{\mathrm{T}}^{\mathrm{miss}}(\mathrm{jets}) + \mathbf{p}_{\mathrm{T}}^{\mathrm{miss}}(\mu) + \mathbf{p}_{\mathrm{T}}^{\mathrm{miss}}(\mathrm{soft}) \tag{4.5}$$

To avoid double-counting, the tracks and topoclusters (collectively called constituents in this section) are associated to the reconstructed objects in the order written in Eq. (4.5). The object will only be used if its constituents have not been associated with another object earlier in the order. For jets, the non-overlapping parts can be used. The leftover tracks and topoclusters are called track soft terms (TSTs) and calorimeter soft terms (CSTs) respectively.

For the analysis presented here, CST $E_{\mathrm{T}}^{\mathrm{miss}}$ is used in Run 1 result. For Run 2, TST $E_{\mathrm{T}}^{\mathrm{miss}}$ is used instead, taking advantage of its better robustness against pileup. Missing transverse momentum built purely from tracks ($\mathbf{p}_{\mathrm{T}}^{\mathrm{miss,track}}$) is also used to reject $E_{\mathrm{T}}^{\mathrm{miss}}$ from jet mis-modeling.

4.8. Tau

Due to the signal efficiency requirement, tau leptons are not fully reconstructed in this analysis and are not included as objects in the $E_{\mathrm{T}}^{\mathrm{miss}}$ reconstruction. Instead, very loose tau candidates are identified and used to suppress events with hadronic tau decay[6]. Since hadronic tau decay can only have either 1 or 3 charged hadrons plus neutrinos, tau "jets" have fewer tracks and are closed to the $E_{\mathrm{T}}^{\mathrm{miss}}$. In this analysis, a jet is considered a tau candidate if:

- It is the closest jet to the $\mathbf{p}_{\mathrm{T}}^{\mathrm{miss}}$.
- $\Delta\phi(\mathbf{p}_{\mathrm{T}}^{\mathrm{miss}}, \mathrm{jet}) < \pi/5$.
- It is not b-tagged.
- There are less than four tracks associated to it.

[6] Events with leptonic tau decay are rejected by identifying the lepton daughter.

CHAPTER V

SEARCH FOR A SCALAR PARTNER OF THE TOP QUARK IN THE JETS+$E_{\mathrm{T}}^{\mathrm{miss}}$ FINAL STATE

This chapter will describe the search for a scalar partner of the top quark with jets+$E_{\mathrm{T}}^{\mathrm{miss}}$ final state. The lightest supersymmetric top ($\tilde{t}_1$) will be the main candidate for the partner and *direct* pair production will be the main focus, though other scenarios of which this search is sensitive to will also be discussed. First, the overview of the analysis will be presented in Section 5.1. Subsequently, Run 1 search [6] strategies and results will be summarized in Section 5.2, followed by the description of Run 2 search [1] in Section 5.3. Finally, a brief summary of pMSSM interpretations [2] will be presented in Section 5.4.

5.1. Analysis Overview

5.1.1. Stop Production at the LHC

Leading order stop pair-production diagrams for a hadron collider are shown in Fig. 5.1. For a high energy $p-p$ collisions, such as the ones done with the LHC, gluon fusion (Fig. 5.1a) is the dominant process, followed by $q\bar{q}$ scattering. Notice that these vertices are part of $\mathscr{L}_{\mathrm{soft}}$ as described in Section 2.3.4, so cross-sections for stop pair productions are largely determined by the QCD strength in the SM. This is not the case for NLO predictions, though the dependences are still mild [76–78]. The NLO cross-sections for stop (and other colored particles) are shown in Fig. 5.2 [79]. The results are also corrected for soft gluon emission for NLO diagrams at the NLL accuracy.

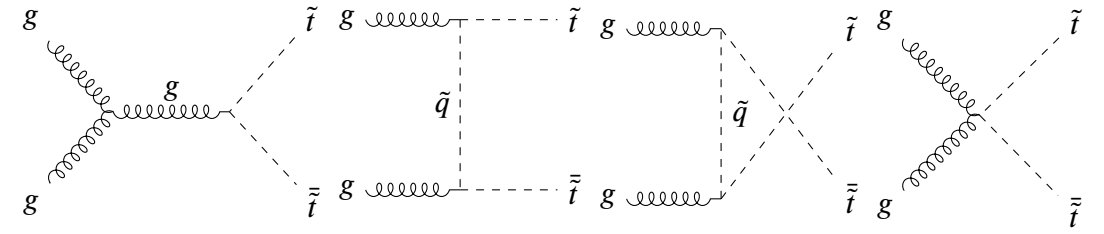

(a) Gluon fusion

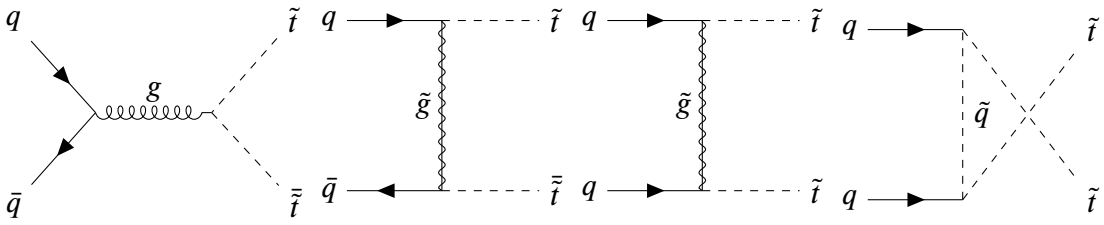

(b) Squark-(anti)squark scattering

FIGURE 5.1. Stop pair-production diagrams

5.1.2. Stop Decay

There are three decay channels of the stop considered in this analysis:

$$\tilde{t} \to t\tilde{\chi}_1^0 \qquad \text{where} \qquad \Delta m(\tilde{t}, \tilde{\chi}_1^0) > m_t \tag{5.1}$$

$$\tilde{t} \to b\tilde{\chi}_1^\pm \to bW^{(*)}\tilde{\chi}_1^0 \qquad \text{where} \qquad m(\tilde{\chi}_1^\pm) = 2m(\tilde{\chi}_1^0) \tag{5.2}$$

$$\tilde{t} \to bW\tilde{\chi}_1^0 \qquad \text{where} \qquad m(b) + m(W) < \Delta m(\tilde{t}, \tilde{\chi}_1^0) < m_t \tag{5.3}$$

They are illustrated in Fig. 5.3. The branching ratios (BRs) are free parameters of the models. In the $\tilde{t} \to b\tilde{\chi}_1^\pm \to bW^{(*)}\tilde{\chi}_1^0$ decays scenario, the two gauginos masses are fixed to be $m(\tilde{\chi}_1^\pm) = 2m(\tilde{\chi}_1^0)$, motivated by gaugino universality. In all cases, only the all hadronic channels of the W are considered. Therefore, the signatures for this analysis are multi-jets and $E_{\mathrm{T}}^{\mathrm{miss}}$[1]. The benefits are higher BR (See Section 1.1.5) and no neutrino contribution

[1] The main difference between this and inclusive 0L search in ATLAS are the stops, which generally imply that there are top or bottom quarks that can be reconstructed.

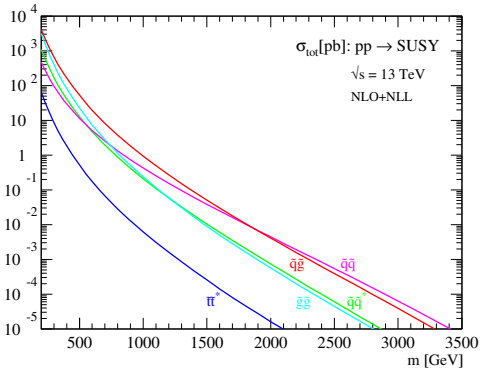

(a) Cross sections for colored sparticles as a function of their masses.

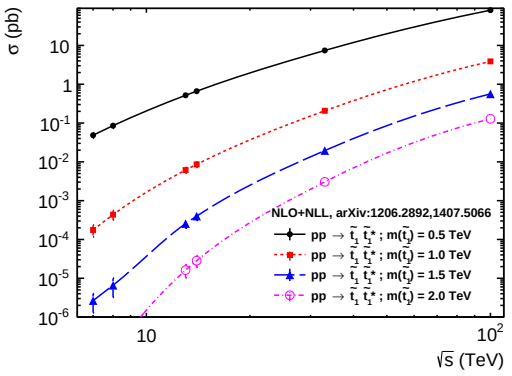

(b) Cross sections for stop as a function of $\sqrt{s}$.

FIGURE 5.2. Taken from [79]. Stop pair-production cross section in the simplified model at the LHC.

to the $E_{\mathrm{T}}^{\mathrm{miss}}$ from the hard scattering[2]. One of the main challenge are higher rates of SM backgrounds.

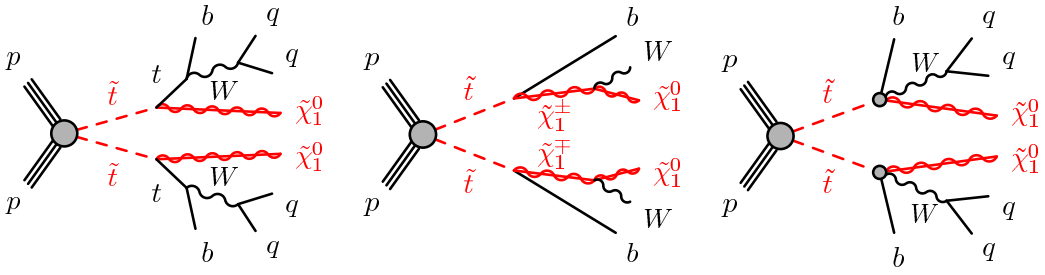

(a) $\tilde{t} \to t\tilde{\chi}_1^0$ (b) $\tilde{t} \to b\tilde{\chi}_1^{\pm} \to bW^{(*)}\tilde{\chi}_1^0$ (c) $\tilde{t} \to bW\tilde{\chi}_1^0$

FIGURE 5.3. Stop decay channels considered in this analysis.

5.1.3. Standard Model Backgrounds

The major backgrounds for this analysis are:

Z+jets When $Z \to \nu\bar{\nu}$ is produced, usually in a Drell-Yan process, in association with b-jets, it can looks like a signal event. The cross-section is falling very quickly with additional jets and b-jets, but it is still large compared to stop.

[2] Semileptonic b decays can contribution to the $E_{\mathrm{T}}^{\mathrm{miss}}$.

Semileptonic $t\bar{t}$ A top with the W daughter decay leptonically can have large $E_{\mathrm{T}}^{\mathrm{miss}}$ from the neutrino. If the lepton is either lost or misidentified as a jet, it can fake a signal event.

$t\bar{t} + Z$ If the tops decay hadronically and $Z \to \nu\bar{\nu}$, it can look very much like the signal

***Wt*-channel single top decay** When the top decay hadronically and the W decays leptonically, it can fake the signal event similar to the semileptonic $t\bar{t}$ events.

Figure 5.4 summarized theory predictions and ATLAS measurements for various SM production cross-section, for comparison with the stop cross-sections in Fig. 5.2.

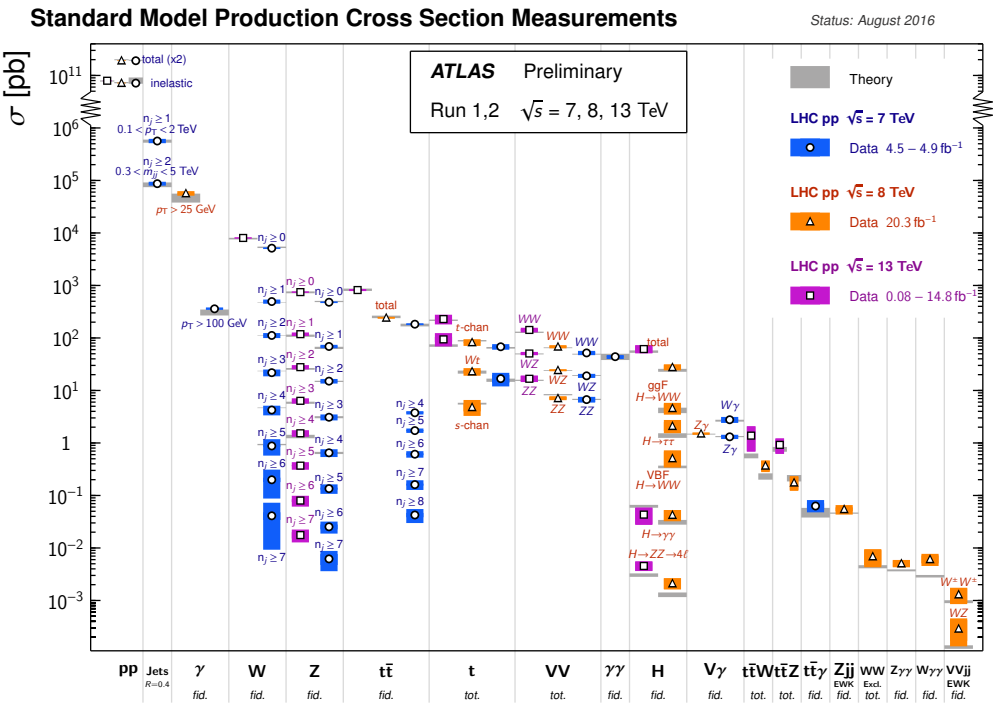

FIGURE 5.4. Summary of several Standard Model total and fiducial production cross section measurements, corrected for leptonic branching fractions, compared to the corresponding theoretical expectations [80].

5.1.3.1. Control Regions

The background estimation is derived mainly from simulation. Control regions (CRs) are defined for the major backgrounds of each signal region (SR) to correct for normalizations while the shape and extrapolation from CR to SR is taken from simulation. The exceptions are QCD multijet and all hadronic $t\bar{t}$ contributions which are derived from data using multijet CR. CRs are designed to be orthogonal to all SRs while still be as close kinematically as possible to the target SR to minimize systematic uncertainties due to the extrapolation. In order to reduce the statistic uncertainty of the normalization for background estimate, CRs need to have a large amount of data, especially compared to the SRs. Signal contamination in CRs also needs to be avoid. The general strategy used for defining CRs is explained below:

1-lepton This type of control region requires only one well-identified electron or muon in the event to be orthogonal to the SRs, and treat it as a non-b-tagged jet. It is very useful to obtain enhanced samples of SM background events with one W decay leptonically. The CRs of this type include semileptonic $t\bar{t}$, W + jets, and sigle top productions. For semileptonic $t\bar{t}$ CR, variable $m_{\mathrm{T}}\left(\ell, E_{\mathrm{T}}^{\mathrm{miss}}\right)$, defined as the m_{T} between the lepton and the $E_{\mathrm{T}}^{\mathrm{miss}}$, can also be used to enhance the purity.

2-lepton Used for Z + jets, this CR take advantage of the lepton universality to mimic $Z(\nu\nu)$ + jets with $Z(ee)$ + jets and $Z(\mu\mu)$ + jets events. By requiring exactly two well-identified opposite sign electrons or muons with the vector sum's invariant mass in the Z mass window, a very pure sample of Z productions can be obtained from the data. The leptons are then treated as invisible and their p_{T} are added to the $E_{\mathrm{T}}^{\mathrm{miss}}$ to mimic the $Z(\nu\nu)$ + jets events. The modified $E_{\mathrm{T}}^{\mathrm{miss}}$ is called $E_{\mathrm{T}}^{\mathrm{miss}'}$.

Multijet For the processes where no neutrino from the hard interaction is present such as QCD multijet production of all hadronic $t\bar{t}$ events, large $E_{\mathrm{T}}^{\mathrm{miss}}$ mainly comes from the

mismodeling of the jets. To estimate this background, a technique called jet smearing is used [81]. The idea is to take well-measured (low $E_{\mathrm{T}}^{\mathrm{miss}}/\sqrt{\Sigma E_T}$) multijet events in data and smear them. The smearing is applied to the jet momentum with a jet response function, derived from simulated dijet events and cross-checked with data, to simulate events with jet mismodeling.

5.1.3.2. Simultaneous fit to determine SM background

The SM background estimates in each signal region are determined from a profile likelihood fit using the observed numbers of events in the control regions. The common systematic uncertainties between CRs and SRs and their correlations are treated as nuisance parameters in the fit and are modeled by Gaussian probability density functions. A normalization factor for each background source is derived from the fit. For a background process where a CR is not defined, the estimate contribution is fixed at the expected value from the simulation using the most accurate theoretical cross sections available.

5.1.3.3. Validation Regions

The general idea of a validation region (VR) is to define a region that is orthogonal to the targed SR(s), but being as closed as possible in the kinematic and event composition. Most of the VR in this analysis are also orthogonal to the corresponding CR. The normalization factors from the CR are applied to the VR and the distributions are checked against data. It is especially useful when the CR is "further" away from the SR in kinematic behavior. Such an example from this analysis is the Z + jets CR; since the $Z \to \ell\ell$ branching ratio is smaller than that of $Z \to \nu\nu$, the selections are looser in the CR than the ones in the SR. Defining a VR for this can help validate the simulation.

5.1.4. Discriminating Variables

Apart from the main signature of number of jets and large $E_{\mathrm{T}}^{\mathrm{miss}}$, other variables considered in signal regions optimization are listed below:

$\boldsymbol{N_{b-\mathrm{tag}}}$ Number of b-tagged jets.

$\boldsymbol{|\Delta\phi\left(\mathrm{jet}^{i}, E_{\mathrm{T}}^{\mathrm{miss}}\right)|}$ The difference in ϕ between the jet and $E_{\mathrm{T}}^{\mathrm{miss}}$, for the ith leading jet in the event, where $i = 0 - 5$. These variables reject events with fake $E_{\mathrm{T}}^{\mathrm{miss}}$ from QCD, hadronic $t\bar{t}$, and detector effects.

$\boldsymbol{|\Delta\phi\left(E_{\mathrm{T}}^{\mathrm{miss}}, E_{\mathrm{T}}^{\mathrm{miss,track}}\right)|}$ The difference in ϕ between the calorimeter $E_{\mathrm{T}}^{\mathrm{miss}}$ and the $E_{\mathrm{T}}^{\mathrm{miss}}$ derived from the sum of the transverse momenta of the tracks in the event ($\mathbf{p}_{\mathrm{T}}^{\mathrm{miss,track}}$). This variable discriminates between events with fake $E_{\mathrm{T}}^{\mathrm{miss}}$ and events with real $E_{\mathrm{T}}^{\mathrm{miss}}$.

$\boldsymbol{H_{\mathrm{T}}}$ The scalar sum of the p_{T} of all signal anti-k_{t} $R = 0.4$ jets.

$\boldsymbol{E_{\mathrm{T}}^{\mathrm{miss}}/\sqrt{H_{\mathrm{T}}}}$ An alternate definition of $E_{\mathrm{T}}^{\mathrm{miss}}$ significance, where the ΣE_T is replaced by H_{T}.

$\boldsymbol{m_{\mathrm{T}}^{i}}$ The transverse mass (m_{T}) between the ith jet and the $E_{\mathrm{T}}^{\mathrm{miss}}$ in the event. The massless approximation is used for this and all following m_{T} variables:

$$m_{\mathrm{T}}^{i} = \sqrt{2 p_{\mathrm{T}}^{\mathrm{jet},i} E_{\mathrm{T}}^{\mathrm{miss}} \left(1 - \cos\Delta\phi\left(\mathrm{jet}^{i}, E_{\mathrm{T}}^{\mathrm{miss}}\right)\right)} \tag{5.4}$$

where $p_{\mathrm{T}}^{\mathrm{jet},i}$ is the transverse momentum of the ith jet.

$\boldsymbol{m_{\mathrm{T}}^{b,\mathrm{min}}}$ Transverse mass between closest b-jet to $E_{\mathrm{T}}^{\mathrm{miss}}$ and $E_{\mathrm{T}}^{\mathrm{miss}}$. This variable has an endpoint at the top mass for semileptonic $t\bar{t}$ background events, providing a very good separation from the signal events which tends to be at the higher value. Figure 5.5 shows a comparison of the various signals and backgrounds process for this variable.

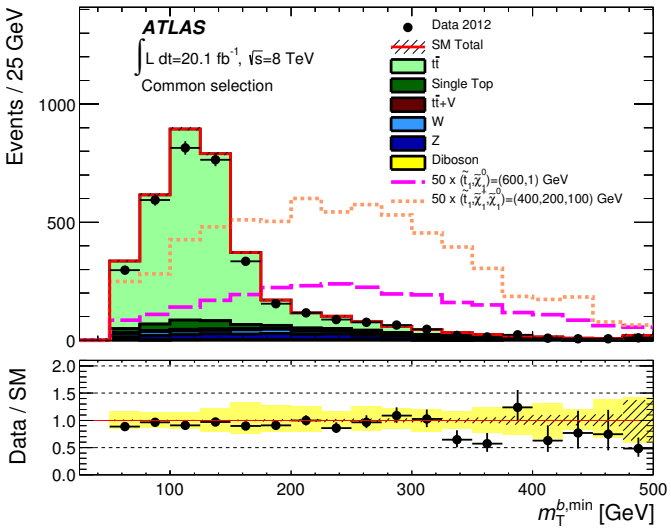

FIGURE 5.5. The distribution of $m_{\mathrm{T}}^{b,\mathrm{min}}$ in events with at least four jets that pass the common selection requirements used in Run 1, excluding the requirement on $m_{\mathrm{T}}^{b,\mathrm{min}}$. The stacked histograms show the SM expectation from simulation compared to the data (points). Simulated signal samples where $m_{\tilde{t}} = 600$ GeV, $m_{\tilde{\chi}_1^0} = 1$ GeV (pink dashed line) and $m_{\tilde{t}} = 400\mathrm{GeV}, m_{\tilde{\chi}_1^\pm} = 200\mathrm{GeV}, m_{\tilde{\chi}_1^0} = 100\mathrm{GeV}$ (orange dotted line) are overlaid; the expected number of signal events is multiplied by a factor of 50 for improved visibility. The "Data/SM" plot shows the ratio of data events to the total Standard Model expectation. The rightmost bin includes all overflows. The hatched uncertainty band around the Standard Model expectation shows the statistical uncertainty and the yellow band (shown only for the "Data/SM" plot) shows the combination of statistical and experimental systematic uncertainties.

$\boldsymbol{m_{\mathrm{T}}^{b,\mathrm{max}}}$ Transverse mass between farest b-jet to $E_{\mathrm{T}}^{\mathrm{miss}}$ and $E_{\mathrm{T}}^{\mathrm{miss}}$.

$\boldsymbol{m_{\mathrm{T}}^{\mathrm{min}}}$ Transverse mass between closest non-b-jet to $E_{\mathrm{T}}^{\mathrm{miss}}$ and $E_{\mathrm{T}}^{\mathrm{miss}}$.

$\boldsymbol{m_T\left(\mathrm{jet}^3, \mathrm{p}_{\mathrm{T}}^{\mathrm{miss}}\right)}$ Transverse mass between the lowest p_{T} anti-k_{t} $R = 0.4$ jets and $E_{\mathrm{T}}^{\mathrm{miss}}$.

$\boldsymbol{|\Delta\phi\,(b,b)|}$ The azimuthal angle between the two leading b-tagged jets in the event.

$\boldsymbol{\Delta R\,(b,b)}$ The angular separation between the two jets with the highest b-tag weight.

$\boldsymbol{\Delta R\left(b\bar{b}, \mathrm{jet}\right)}$ The angular separation between the vector sum of the two leading b-tagged jets in the event (presumably from gluon splitting to $b\bar{b}$ in $Z(\nu\bar{\nu}) + b\bar{b} + \mathrm{jets}$) and the closest non b-tagged jet.

$\Delta R\left(b\bar{b},\text{jet}\right)/H_{\mathrm{T}}$ The same variable as above, normalized by the H_{T}.

The reclustering technique (will be described in Section 5.2.1.2) yields additional quantities for background rejection:

m^0_{AkT12} Mass of the leading p_{T} anti-k_{t} $R = 1.2$ RC jet

m^1_{AkT12} Mass of the sub-leading p_{T} anti-k_{t} $R = 1.2$ RC jet

m^0_{AkT8} Mass of the leading p_{T} anti-k_{t} $R = 0.8$ RC jet

m^1_{AkT8} Mass of the sub-leading p_{T} anti-k_{t} $R = 0.8$ RC jet

$p^0_{T,AkT12}$ Leading anti-k_{t} $R = 1.2$ RC jet p_{T}

$p^1_{T,AkT12}$ Sub-leading anti-k_{t} $R = 1.2$ RC jet p_{T}

$p^0_{T,AkT8}$ Leading anti-k_{t} $R = 0.8$ RC jet p_{T}

$p^1_{T,AkT8}$ Sub-leading anti-k_{t} $R = 0.8$ RC jet p_{T}

5.1.5. Interpretation

When no significant excess is observed. The 95% confidence level (CL) upper limit of BSM events can be obtained using CL_s method. This can also be interpreted as the model-independent limits on the visible BSM cross sections, $\sigma_{\mathrm{vis}} \equiv \sigma \cdot A \cdot \epsilon$, where σ is the production cross section, A is the acceptance, and ϵ is the selection efficiency for a BSM signal.

The simultaneous fit to the SRs and CRs are used to set limits on direct top squark pair production using the CL_s prescription [82, 83] and asymptotic formulae [84] (See Appendices A.3.1.2 and A.3.2). A fixed signal component is used and signal contaminations in the CRs are taken into account. The lowest 95% CL_s value is chosen for each ($m_{\tilde{t}}$, $m_{\tilde{\chi}^0}$).

Two type of limits are evaluated; "Expected" limits are obtained by setting the nominal event yield in each SR to the mean background expectation. The $\pm 1\sigma$ contours are also evaluated using the $\pm 1\sigma$ uncertainties of the background estimates. "Observed" limits, on the other hand, using the actual event yields, and the $\pm 1\sigma$ contours are obtained by varying the signal cross section by $\pm 1\sigma$ of the theory uncertainties.

5.2. Run 1 Search

This section will summarized the search using data from $p-p$ collisions at $\sqrt{s} = 8$ TeV during LHC Run 1. An integrated luminosity of 20.1 ± 0.6 fb^{-1} have been recorded by the ATLAS detector [6]. The data have been collected using a trigger requiring $E_{\mathrm{T}}^{\mathrm{miss}} > 80$ GeV, corresponding to a full efficiency for offline $E_{\mathrm{T}}^{\mathrm{miss}}$ reconstruction at > 150 GeV. The basic preselections are described below:

1. For data samples only, events must be in the Good Runs List (GRL), where the detector are in a condition suitable for physics measurement.
2. The event must pass the $E_{\mathrm{T}}^{\mathrm{miss}}$ trigger.
3. The primary vertex in the event is required to have at least 5 tracks with $p_{\mathrm{T}} > 400$ MeV.
4. Events must not contain any BadLooser Jets with $p_{\mathrm{T}} > 20$ GeV (at any η) (See Section 4.2.4.3).
5. The events must have at least four calibrated jets with $p_{\mathrm{T}} > 35$ GeV and $|\eta| < 2.8$.
6. The event must contain exactly 0 baseline electrons and 0 baseline muons with $p_{\mathrm{T}} > 10$ GeV with $|\eta|$ requirement of < 2.47 and < 2.4 respectively.
7. The event must have $E_{\mathrm{T}}^{\mathrm{miss}} > 150$ GeV.
8. Events with large $E_{\mathrm{T}}^{\mathrm{miss}}$ due to mismodeling of the jets are suppressed by requiring $\Delta\phi$ between the first three leading p_{T} jets and $E_{\mathrm{T}}^{\mathrm{miss}}$ to be greater than $\pi/5$,

$\Delta\phi(\mathbf{p}_{\mathrm{T}}^{\mathrm{miss,track}}, \mathbf{p}_{\mathrm{T}}^{\mathrm{miss}}) < \pi/3$, and $\mathbf{p}_{\mathrm{T}}^{\mathrm{miss,track}}$ of at least 30 GeV. This set of requirements are also referred to as the "FakeMet" cuts.

9. The event must contain at least 2 b-tagged jet at 70% efficiency working point for MV1 tagger.
10. $m_{\mathrm{T}}^{b,\mathrm{min}} > 175$ GeV

5.2.1. The Boosted Signal Region (SRB)

Prior to this analysis with Run 1 data [6], the signature for ATLAS all hadronic channel is the six "fully resolved" $R = 0.4$ jets from tops' daughters. However, this is not the case for roughly half of the signal events, where less than six jets are reconstructed, as shown in Fig. 5.6. In this analysis, boosted signal regions (SRB) are developed to enhance the sensitivity of the search, especially in the cases where the stop are heavy compared to the LSP. SRB targets the events where only four or five jets are present, which can occur when one or more jets are too soft or one of the tops is given enough Lorentz boost to become collimate, also referred to as the "partially resolved" cases.

5.2.1.1. Top Reconstruction and Jet Reclustering

For signal region where top quarks are present, reconstructing at least one top can help reducing QCD multi-jets, W + jets, and Z + jets backgrounds. Being able to reconstruct both tops can help reducing the semileptonic $t\bar{t}$ background as well. For the resolved analysis, the ΔR_{min} method are used. The steps for ΔR_{min} algorithm in this analysis are:

1. Put the two highest b-tag (MV1) weight jets aside.
2. For the rest of the "light" jets, the two closest ones are combined and the nearest b-jet is added to form the first top candidate.
3. Repeat the last step with the reminding light and b-tagged jets.

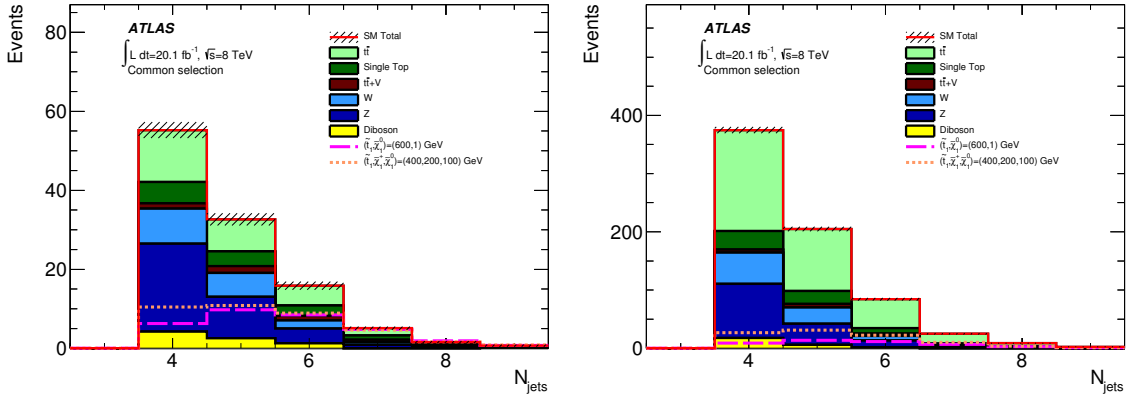

(a) $E_{\mathrm{T}}^{\mathrm{miss}} > 300$ GeV (b) $E_{\mathrm{T}}^{\mathrm{miss}} > 150$ GeV

FIGURE 5.6. Distributions of the number of $R = 0.4$ jets ($p_{\mathrm{T}} > 35$GeV, $|\eta| < 2.8$) for the dominant background contributions (stacked, filled histograms). The common selection criteria is applied to both distributions; Simulated signal samples where $m_{\tilde{t}} = 600$ GeV and $m_{\tilde{\chi}_1^0} = 1$ GeV (pink dashed line) and where $m_{\tilde{t}} = 400$ GeV, $m_{\tilde{\chi}_1^\pm} = 200$ GeV, and $m_{\tilde{\chi}_1^0} = 100$ GeV (orange dotted line) are overlaid.

As shown in Fig. 5.7, the ΔR_{min} method has very good efficiencies for reconstructing top quarks while a moderate background rejection can be obtained by cutting out the high mass tails.

5.2.1.2. Jet Reclustering

In the partially resolved case, there are either four or five jets in the events, which means the ΔR_{min} method will always fail to reconstruct the second top. While there are various ways one can modify the ΔR_{min} method to accommodate events with less than six jets, a simple and effective strategy is to run the anti-k_{t} algorithm with a larger distance parameter, R, over the calibrated anti-k_{t} $R = 0.4$ jets collection. This will be referred to as the jet *reclustering (RC)* technique.

For this analysis the value of R for the RC jets with the best hadronic top quark reconstruction efficiency that retains a reasonable background rejection is 1.2. To yield additional background rejection power, RC jets with $R = 0.8$, which can be thought of as the

"W candidates" are also considered. While this approach forgoes most of the substructure information compared to jets clustered from topoclusters with a large R, the advantage of jet reclustering is that the calibrations are well tested since they are simply those of the anti-k_t $R = 0.4$ jets. In addition to having a trivial calibration the RC jets are also independent of pileup (Fig.5.8) because the constituent jets are pileup corrected. Finally, systematic uncertainties of reclustered can be propagated from the input small-R jets.

For the remainder of this document, the convention is followed that the highest p_T object is designated by a "0" superscript, the second-highest p_T object by a "1", and so on. The reclustering technique is particularly good at reconstructing the leading p_T top quark but shows poorer efficiency for the sub-leading p_T top. The distribution of the mass of the leading p_T RC jet (m^0_{AkT12}) has a clear peak at the top mass and a smaller peak at the W/Z mass. On the other hand, the same distribution for the sub-leading p_T RC jet (m^1_{AkT12}) peaks at low mass, and at the W/Z mass, with a much smaller peak at the top mass. In order to utilize the discriminating power from the sub-leading p_T RC jet mass while keeping the signal efficiency as high as possible, events are separated into two categories by the top mass asymmetry $\mathcal{A}_{m_t}$ defined as the difference in the mass of the two leading p_T top candidates in the event divided by the sum of their masses.

$$\mathcal{A}_{m_t} = \frac{|m^0_{AkT12} - m^1_{AkT12}|}{m^0_{AkT12} + m^1_{AkT12}}. \tag{5.5}$$

The distributions of the $\mathcal{A}_{m_t}$ for both the four and five jet multiplicities are shown in Fig. 5.9. For signal events which have two equally massive RC jets, the $\mathcal{A}_{m_t}$ is expected to be small. However, when the two top quarks are close to each other, the anti-k_t algorithm may cluster the decay products from the two tops together; in this case the $\mathcal{A}_{m_t}$ will be close to unity. Typical topologies for when the $\mathcal{A}_{m_t}$ is large and for when it is small are shown in Fig. 5.10. Events with $\mathcal{A}_{m_t} < 0.5$ are henceforth labeled as SRB1 while those with $\mathcal{A}_{m_t} > 0.5$ are labeled as SRB2. The mass distributions of the leading and sub-leading RC jet p_T in

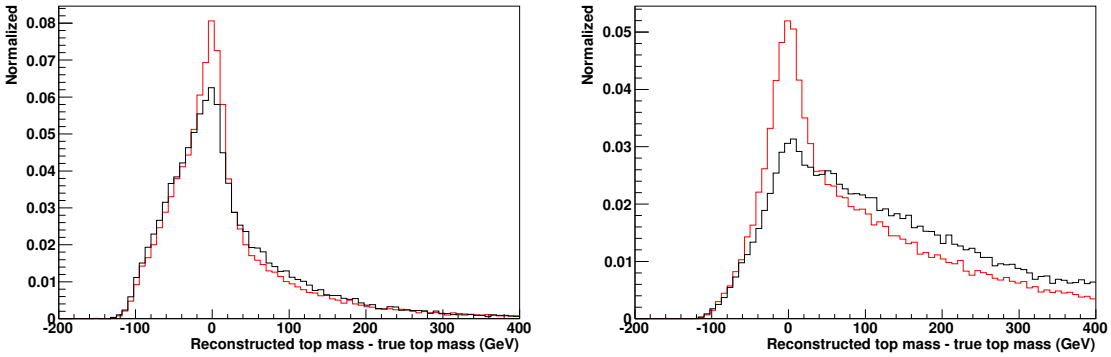

FIGURE 5.7. The difference between the reconstructed top mass and the true top mass in $t\bar{t}$ MC using the ΔR_{min} method. The black curve shows the lepton+jets $t\bar{t}$ MC and the red curve shows a signal sample with stop mass of 600 GeV. The first top candidate is shown on the left and the second on the right. The events shown are all of those which pass the pre-selection criteria.

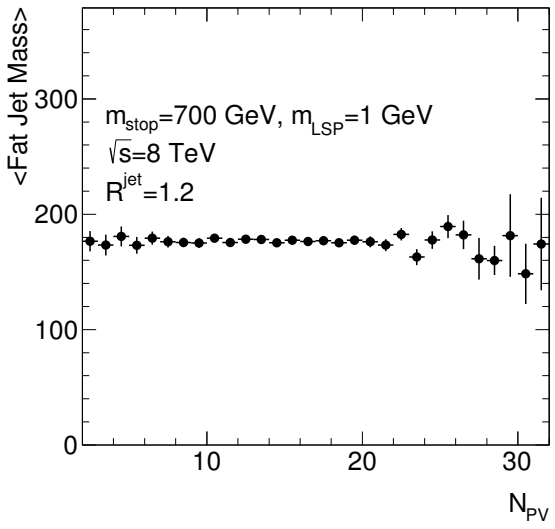

FIGURE 5.8. The average mass of the anti-k_t $R = 1.2$ RC jets plotted as a function of number of primary vertices in the event. Since the constituents of the RC jets are area-subtracted anti-k_t R=0.4 jets no dependence on pileup is expected or observed.

each case is shown in Fig. 5.11 and 5.12. For SRB1, both jet masses are considered in the optimization of the selection criteria, while only the mass of the leading p_{T} jet is considered in SRB2. As a cross check, the mass distributions for both MC and data are compared in a 1-lepton control region and found to show good agreement.

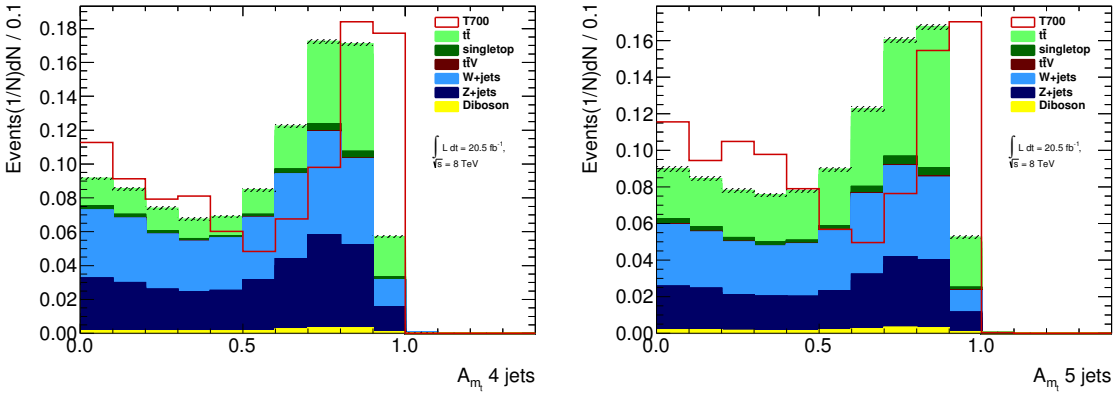

FIGURE 5.9. Distribution of $\mathscr{A}_{m_t}$ for the 4 and 5 jet cases. The distribution is shown for the various backgrounds (stacked) and for the signal point $\tilde{t}$ mass at 700 GeV and $\tilde{\chi}_1^0$ mass of 1 GeV. Both the total backgrounds and signal histogram are normalized to unit area.

5.2.2. Signal Region Definitions

The Run 1 analysis has three signal regions (SRs):

SRA Targeting fully resolved topology, where there are ≥ 6 jets in the events. The majority of the backgrounds in this SR are semileptonic $t\bar{t}$, which are mostly rejected by $m_{\mathrm{T}}^{b,\mathrm{min}}$ cut. The electroweak backgrounds are suppressed by the jet multiplicity requirement. SRA is divided into four overlapping signal region, SRA1-4, in the increasing $E_{\mathrm{T}}^{\mathrm{miss}}$ cut order. The cuts are summarized in Table 5.1.

SRB Targeting partially resolved topology. It is designed to be orthogonal to SRA by requiring 4 or 5 jets in the events only. SRB is subdivided into two orthogonal SRs, SRB1-2,

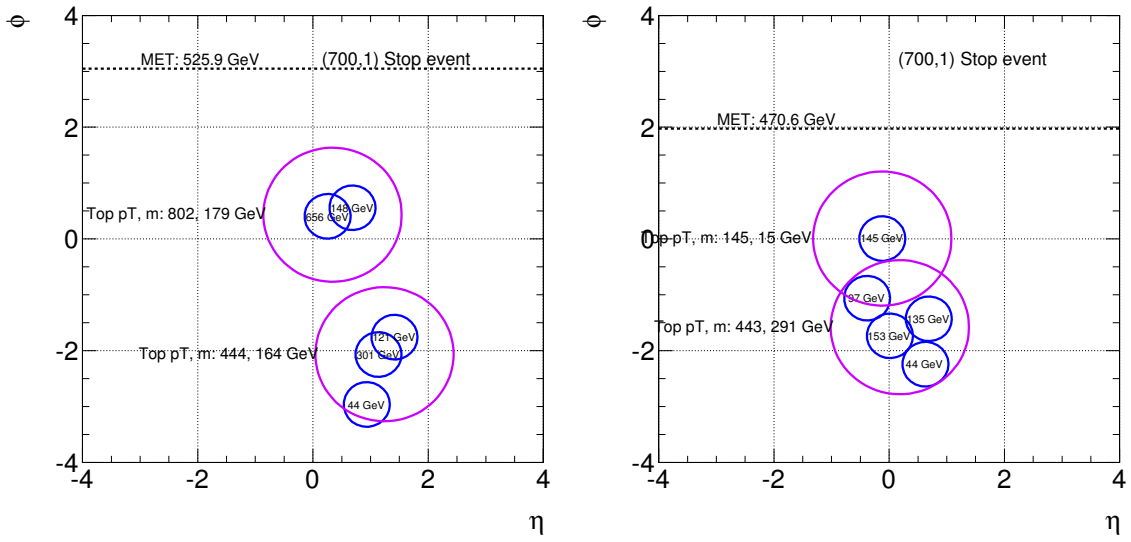

FIGURE 5.10. Simplified event displays of selected SRB1 (left) and SRB2 (right) topologies. In SRB1 the decay daughters of the two top quarks are well separated while in SRB2 they are bundled together.

to maximized signal efficiencies for different topologies. The selections are shown in Table 5.2.

SRC Targeting the scenario where one of the stop decays via $\tilde{t} \rightarrow b\tilde{\chi}_1^{\pm}$ channel. This SR targets event with five jets in order to increase the search sensitivity for the case where $m_{\tilde{\chi}_1^{\pm}} - m_{\tilde{\chi}_1^0}$ is smaller. SRC only includes five-jets events, so it is orthogonal to SRA. It is subdivided into three overlapping SRs, SRC1-3, in the increasing $E_{\mathrm{T}}^{\mathrm{miss}}$ cut order. The cuts are summarized in Table 5.3.

5.2.3. Background Estimation

The major backgrounds for all SRs are semileptonic $t\bar{t}$, $Z(\nu\nu)$ + jets, and $t\bar{t}$+Z where $Z \rightarrow \nu\bar{\nu}$, which is the irreducible background. For SRB, contribution of W + jets events are also significant. Control regions have been defined for these backgrounds for each signal

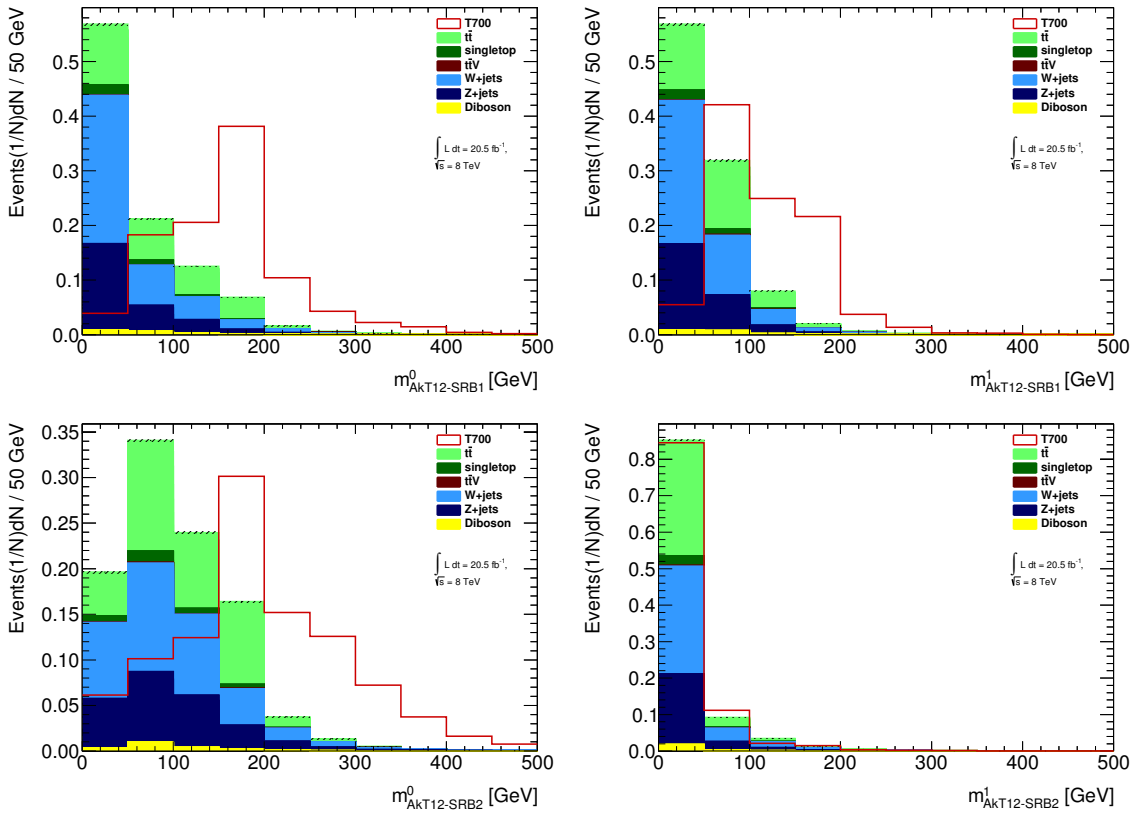

FIGURE 5.11. The two reconstructed top masses for the partially resolved analysis. SRB1 is shown on the top row and SRB2 is shown on the bottom. The leading p_{T} RC jet is on the left while the sub-leading p_{T} RC jet is on the right. The result of the reconstruction is shown for the various backgrounds (stacked) and for the signal point $m_{\tilde{t}}$=700 GeVand a neutralino mass of 1 GeV. Both backgrounds stack and signal histogram are normalized to unit area.

region shown in Tables 5.1 to 5.3. The scale factors derived from these CRs are summarized in Section 5.2.3.

5.2.4. Systematic Uncertainties

The impact of each systematic uncertainty are quantified as a percentage of background estimation. The main sources of detector-related uncertainties come from jet energy resolution (JER) (6–15% in SRA, 16% in SRB, and 3–6% in SRC) follow by JES (5–9% in SRA, 6% in SRB, and 8–11% in SRC). Other uncertainties from modeling of b-tagging, pileup, the τ veto, and $E_{\mathrm{T}}^{\mathrm{miss,track}}$ are small by comparison. The uncertainty of the luminosity

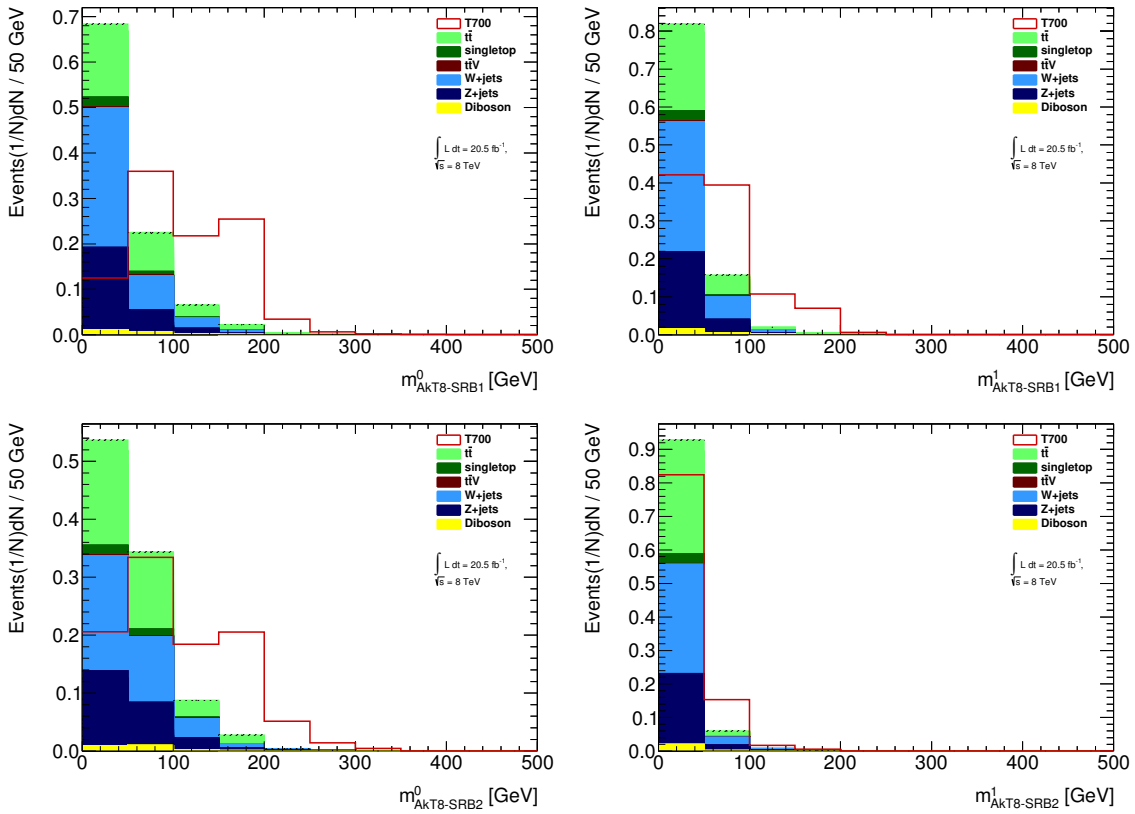

FIGURE 5.12. The two reconstructed anti-k_t $R = 0.8$ RC jet masses for the partially resolved analysis. SRB1 is shown on the top row and SRB2 is shown on the bottom. The leading p_T RC jet is on the left while the sub-leading p_T RC jet is on the right. The result of the reconstruction is shown for the various backgrounds (stacked) and for the signal point $m_{\tilde{t}}$=700 GeVand a neutralino mass of 1 GeV. Both backgrounds stack and signal histogram are normalized to unit area.

measurement is 2.8%. Theoretical uncertainties from SM background modelings are evaluated and most of them have $\lesssim 10\%$ impact on the total backgrounds. Their effects are reduced by normalization factor from the CRs as well. Uncertainties on signal acceptance are including as nuisance parameters in the fit. They are dominated by JES, b-tagging, and JER and are in the order of $< 10\%$.

TABLE 5.1. Selection criteria for SRA, the fully resolved topology, with ≥ 6 anti-k_t $R = 0.4$ jets.

	SRA1	SRA2	SRA3	SRA4
anti-k_t $R = 0.4$ jets	≥ 6, $p_T > 80, 80, 35, 35, 35, 35$ GeV			
m^0_{jjj}	< 225GeV		[50,250] GeV	
m^1_{jjj}	< 250GeV		[50,400] GeV	
$\min[m^i_T]$	–		> 50 GeV	
τ veto	yes			
E_T^{miss}	> 150 GeV	> 250 GeV	> 300 GeV	> 350 GeV

TABLE 5.2. Selection criteria for SRB, the partially resolved topology, with four or five anti-k_t $R = 0.4$ jets, reclustered into anti-k_t $R = 1.2$ and $R = 0.8$ jets.

	SRB1	SRB2
anti-k_t $R = 0.4$ jets	4 or 5, $p_T > 80, 80, 35, 35, (35)$ GeV	5, $p_T > 100, 100, 35, 35, 35$ GeV
$\mathscr{A}_{m_t}$	< 0.5	> 0.5
$p^0_{T,AkT12}$	–	> 350 GeV
m^0_{AkT12}	> 80 GeV	$[140, 500]$ GeV
m^1_{AkT12}	$[60, 200]$ GeV	–
m^0_{AkT8}	> 50 GeV	$[70, 300]$ GeV
m_T^{min}	> 175 GeV	> 125 GeV
$m_T\left(\text{jet}^3, \mathbf{p}_T^{miss}\right)$	> 280 GeV for 4-jet case	–
$E_T^{miss}/\sqrt{H_T}$	–	$> 17\sqrt{\text{GeV}}$
E_T^{miss}	> 325 GeV	> 400 GeV

5.2.5. Results and Interpretation

The observed numbers of events in each signal regions are shown in Table 5.8. The total background estimates are derived using profile likelihood method including both CRs and SRs. The E_T^{miss} distributions from SRA1+2, SRA3+4, SRB, and SRC1-3 are shown in Fig. 5.13. No significant excess is observed. The 95% CL upper limit of BSM events and the model-independent limits on the visible BSM cross sections as described in Section 5.1.5 are obtained and the results have been included in Table 5.8.

TABLE 5.3. Selection criteria for SRC, targeting the scenario in which one top squark decays via $\tilde{t} \to b\tilde{\chi}_1^{\pm}$, with five anti-$k_t$ $R = 0.4$ jets.

	SRC1	SRC2	SRC3
anti-k_t $R = 0.4$ jets	5, $p_T > 80, 80, 35, 35, 35$ GeV		
$\lvert\Delta\phi(b,b)\rvert$	$> 0.2\pi$		
$m_T^{b,\min}$	> 185 GeV	> 200 GeV	> 200 GeV
$m_T^{b,\max}$	> 205 GeV	> 290 GeV	> 325 GeV
τ veto	yes		
E_T^{miss}	> 160 GeV	> 160 GeV	> 215 GeV

TABLE 5.4. Normalization of the $t\bar{t}$, W + jets, and Z + jets SM background as obtained from the background fits for SRA, SRB and SRC.

Background Source	SRA	SRB	SRC
$t\bar{t}$	1.24 ± 0.13	$1.00^{+0.10}_{-0.05}$	1.07 ± 0.11
W + jets	–	1.0 ± 0.4	–
Z + jets	$0.94^{+0.16}_{-0.15}$	1.07 ± 0.07	1.07 ± 0.07

TABLE 5.5. Selection criteria for control regions associated with SRA. Only the requirements that differ from the common selection in table 5.11 and those in table 5.1 are listed; "same" indicates the same selection as the signal region.

	$t\bar{t}$ CR	**Z + jets CR**	**Multijet CR**
Trigger	electron (muon)	electron (muon)	same
N_{lep}	1	2	same
p_T^{ℓ}	$> 35(35)$GeV	$> 25(25)$GeV	–
$p_T^{\ell_2}$	same	$> 10(10)$GeV	same
$m_{\ell\ell}$	–	[86, 96]GeV	–
$E_T^{\text{miss,track}}$	–	–	same
$\left\lvert\Delta\phi\left(E_T^{\text{miss}}, E_T^{\text{miss,track}}\right)\right\rvert$	–	–	–
$\left\lvert\Delta\phi\left(\text{jet}, E_T^{\text{miss}}\right)\right\rvert$	$> \pi/10$	–	< 0.1
$m_T^{b,\min}$	> 125GeV	–	–
$m_T\left(\ell, E_T^{\text{miss}}\right)$	[40, 120]GeV	–	–
$\min[m_T^i]$	–	–	–
m_{jjj}^0 or m_{jjj}^1	< 600GeV	–	–
E_T^{miss}	> 150GeV	< 50GeV	> 150GeV
$E_T^{\text{miss}'}$	–	> 70GeV	–

TABLE 5.6. Selection criteria for control regions associated with SRB. Only the requirements that differ from the common selection in table 5.11 and those in table **??** are listed; "same" indicates the same selection as the signal region.

	$t\bar{t}$ **CR**	W**+jets CR**	Z**+jets CR**	**Multijet CR**
Trigger	electron (muon)	electron (muon)	electron (muon)	same
N_{lep}	1	1	2	same
p_{T}^{ℓ}	$> 35(35)$GeV	$> 35(35)$GeV	$> 25(25)$GeV	–
$p_{\text{T}}^{\ell_2}$	same	same	$> 10(10)$GeV	same
$m_{\ell\ell}$	–	–	$[86, 96]$GeV	–
anti-k_{t} $R = 0.4$ jets	[4,5]	[4,5]	5	same
$p_{\text{T}}^{\text{jet}}$	$> 80, 80, 35, 35, (35)$GeV			same
$N_{b\text{-jet}}$	same	1	same	same
$E_{\text{T}}^{\text{miss,track}}$	–	–	–	same
$\left\lvert\Delta\phi\left(E_{\text{T}}^{\text{miss}}, E_{\text{T}}^{\text{miss,track}}\right)\right\rvert$	–	–	–	–
$\left\lvert\Delta\phi\left(\text{jet}, E_{\text{T}}^{\text{miss}}\right)\right\rvert$	$> \pi/10$	$> \pi/10$	–	< 0.1
$m_{\text{T}}^{b,\text{min}}$	–	–	–	–
$m_{\text{T}}\left(\ell, E_{\text{T}}^{\text{miss}}\right)$	$[40, 120]$GeV	$[40, 120]$GeV	–	–
$E_{\text{T}}^{\text{miss}}$	> 150GeV	> 150GeV	< 50GeV	> 150GeV
$E_{\text{T}}^{\text{miss}'}$	–	–	> 70GeV	–
$p_{\text{T},AkT12}^{0}$	–	–	–	–
$m_{\text{T}}^{\text{min}}$	–	–	–	–
$m_T\left(\text{jet}^3, \mathbf{p}_{\text{T}}^{\text{miss}}\right)$	–	–	–	–
$\mathscr{A}_{m_t}$	< 0.5 for 4-jet case	< 0.5	–	–
m_{AkT12}^{0}	–	< 40GeV	–	–
m_{AkT12}^{1}	–	–	–	–
m_{AkT8}^{0}	–	–	–	–
$E_{\text{T}}^{\text{miss}}/\sqrt{H_{\text{T}}}$	–	–	–	–

TABLE 5.7. Selection criteria for control regions associated with SRC. Only the requirements that differ from the common selection in table 5.11 and those in table **??** are listed; "same" indicates the same selection as the signal region.

	$t\bar{t}$ **CR**	Z **+ jets CR**	**Multijet CR**
Trigger	electron (muon)	electron (muon)	same
N_{lep}	1	2	same
p_{T}^{ℓ}	$>$ 35(35)GeV	$>$ 25(25)GeV	–
$p_{\text{T}}^{\ell_2}$	same	$>$ 10(10)GeV	same
$m_{\ell\ell}$	–	[86, 96]GeV	–
$E_{\text{T}}^{\text{miss,track}}$	–	–	same
$\left\lvert\Delta\phi\left(E_{\text{T}}^{\text{miss}}, E_{\text{T}}^{\text{miss,track}}\right)\right\rvert$	–	–	–
$\left\lvert\Delta\phi\left(\text{jet}, E_{\text{T}}^{\text{miss}}\right)\right\rvert$	$> \pi/10$	–	< 0.1
$\lvert\Delta\phi\left(b, b\right)\rvert$	same	–	–
$m_{\text{T}}^{b,\text{min}}$	$>$ 150GeV	–	–
$m_{\text{T}}^{b,\text{max}}$	$>$ 125GeV	–	–
$m_{\text{T}}\left(\ell, E_{\text{T}}^{\text{miss}}\right)$	[40, 120]GeV	–	–
$E_{\text{T}}^{\text{miss}}$	$>$ 100GeV	$<$ 50GeV	$>$ 150GeV
$E_{\text{T}}^{\text{miss}'}$	–	$>$ 70GeV	–

TABLE 5.8. Event yields in each signal region (SRA, SRB, and SRC) are compared to the background estimate from the profile likelihood fit. Statistical, detector, and theoretical systematic uncertainties are included; the total systematic uncertainty in the background estimate includes all correlations. For each signal region, the 95% CL upper limits on the expected (observed) visible cross sections σ_{vis} (exp) (σ_{vis} (obs)) and the expected (observed) event yields N^{95}_{exp} (N^{95}_{obs}) are summarized.

	SRA1	SRA2	SRA3	SRA4	SRB	SRC1	SRC2	SRC3
Observed events	11	4	5	4	2	59	30	15
Total SM	15.8 ± 1.9	4.1 ± 0.8	4.1 ± 0.9	2.4 ± 0.7	2.4 ± 0.7	68 ± 7	34 ± 5	20.3 ± 3.0
$t\bar{t}$	10.6 ± 1.9	1.8 ± 0.5	1.1 ± 0.6	0.49 ± 0.34	$0.10\ ^{+0.14}_{-0.10}$	32 ± 4	12.9 ± 2.0	6.7 ± 1.2
$t\bar{t} + W/Z$	1.8 ± 0.6	0.85 ± 0.29	0.82 ± 0.29	0.50 ± 0.17	0.47 ± 0.17	3.2 ± 0.8	1.9 ± 0.5	1.3 ± 0.4
Z + jets	1.4 ± 0.5	0.63 ± 0.22	1.2 ± 0.4	0.68 ± 0.27	1.23 ± 0.31	15.7 ± 3.5	9.0 ± 1.9	6.1 ± 1.3
W + jets	1.0 ± 0.5	0.46 ± 0.21	0.21 ± 0.19	$0.06\ ^{+0.10}_{-0.06}$	0.49 ± 0.33	8 ± 4	4.8 ± 2.2	2.8 ± 1.2
Single top	1.0 ± 0.4	0.30 ± 0.17	0.44 ± 0.14	0.31 ± 0.16	0.08 ± 0.06	7.2 ± 2.9	4.5 ± 1.8	2.9 ± 1.4
Diboson	< 0.4	< 0.13	0.32 ± 0.17	0.32 ± 0.18	0.02 ± 0.01	1.1 ± 0.8	$0.6\ ^{+0.7}_{-0.6}$	$0.6\ ^{+0.7}_{-0.6}$
Multijets	< 0.001	< 0.001	< 0.001	< 0.001	< 0.001	0.24 ± 0.24	0.06 ± 0.06	0.01 ± 0.01
σ_{vis} (obs) [fb]	0.33	0.29	0.33	0.32	0.21	0.78	0.62	0.40
σ_{vis} (exp) [fb]	$0.48\ ^{+0.21}_{-0.14}$	$0.29\ ^{+0.13}_{-0.09}$	$0.29\ ^{+0.14}_{-0.09}$	$0.25\ ^{+0.13}_{-0.07}$	$0.24\ ^{+0.13}_{-0.06}$	$1.03\ ^{+0.42}_{-0.29}$	$0.73\ ^{+0.31}_{-0.21}$	$0.55\ ^{+0.24}_{-0.15}$
N^{95}_{obs}	6.6	5.7	6.7	6.5	4.2	15.7	12.4	8.0
N^{95}_{exp}	$9.7\ ^{+4.3}_{-3.0}$	$5.8\ ^{+2.6}_{-1.8}$	$5.9\ ^{+2.8}_{-1.9}$	$5.0\ ^{+2.6}_{-1.4}$	$4.7\ ^{+2.6}_{-1.2}$	$20.7\ ^{+8.4}_{-5.8}$	$14.7\ ^{+6.2}_{-4.2}$	$11.0\ ^{+4.9}_{-3.1}$

Each of the SRA1-4 is statistically combined with either SRB or one of the SRC1-3, and the lowest 95% CL_s value is chosen for each ($m_{\tilde{t}}$, $m_{\tilde{\chi}^0}$) grid point. The SRA+B combinations are usually more sensitive to the larger $m_{\tilde{t}} - m_{\tilde{\chi}^0}$ while the SRA+C combinations are better for smaller mass differences. The exclusion contours are shown in Fig. 5.14. Figure 5.14a are for the scenarios where $\tilde{t} \to t\tilde{\chi}_1^0$ exclusively, where $m_{\tilde{t}}$ in the range 270–645 GeV are excluded for a $m_{\tilde{\chi}_1^0} < 30$ GeV. Figure 5.14b shows similar contours but allows BR($\tilde{t} \to b\tilde{\chi}_1^\pm \to bW^{(*)}\tilde{\chi}_1^0$) = 50% with $m(\tilde{\chi}_1^\pm) = 2m(\tilde{\chi}_1^0)$, where $m_{\tilde{t}}$ in the range 250–550 GeV are excluded for a $m_{\tilde{\chi}_1^0} < 60$ GeV. Finally, Fig. 5.14c shows the expected and observed limit for different BRs.

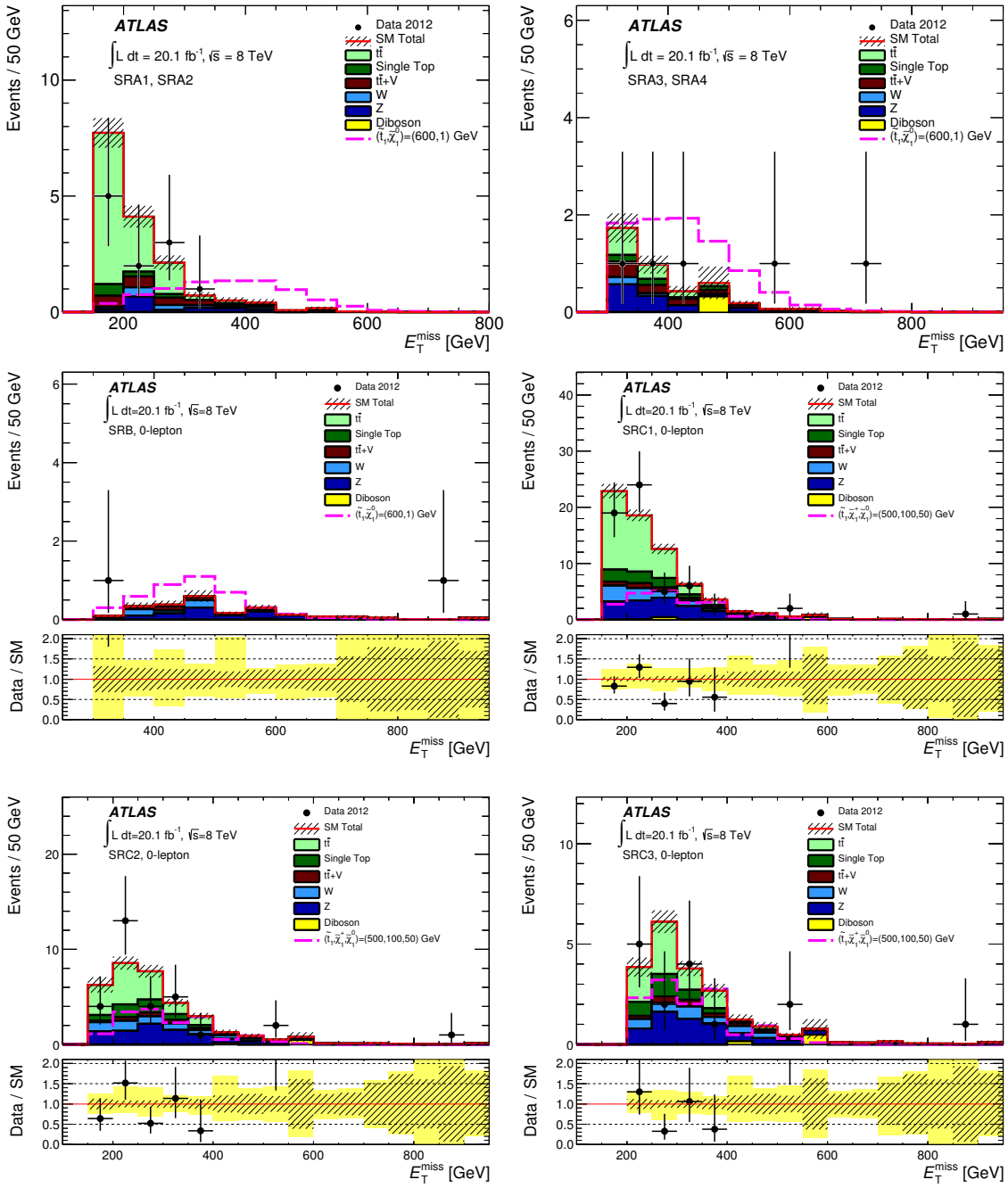

FIGURE 5.13. The $E_{\mathrm{T}}^{\mathrm{miss}}$ distributions for SRA, SRB, and SRC. SRA1 and SRA2 (SRA3 and SRA4) differ only by the $E_{\mathrm{T}}^{\mathrm{miss}}$ requirement. The background expectation (data) are represented by the stacked histogram (black points). For SRA and SRB, the simulated signal distribution for $m_{\tilde{t}} = 600$ GeV, $m_{\tilde{\chi}_1^0} = 1$ GeV is overlaid (pink dashed line), while for SRC the simulated signal distribution for $m_{\tilde{t}} = 400$ GeV, $m_{\tilde{\chi}_1^\pm} = 200$ GeV, and $m_{\tilde{\chi}_1^0} = 100$ GeV is overlaid (orange dotted line). The hatched band on the SM total histogram represents the MC statistical uncertainty only.

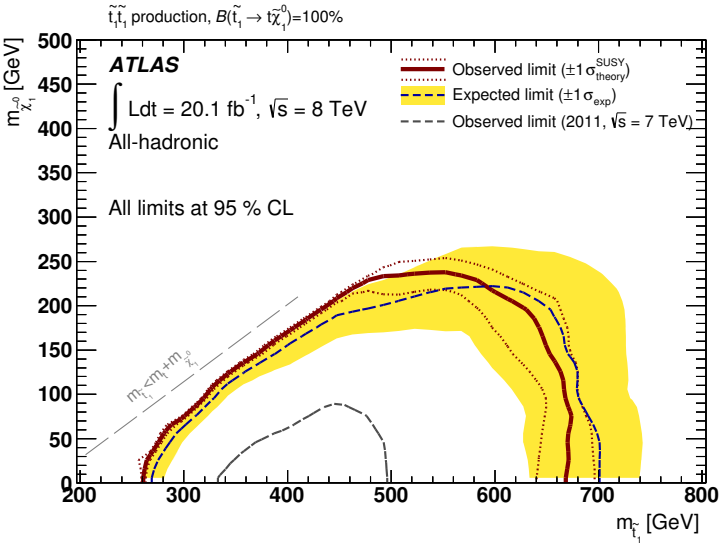

(a) BR($\tilde{t} \to t\tilde{\chi}_1^0$) = 100%

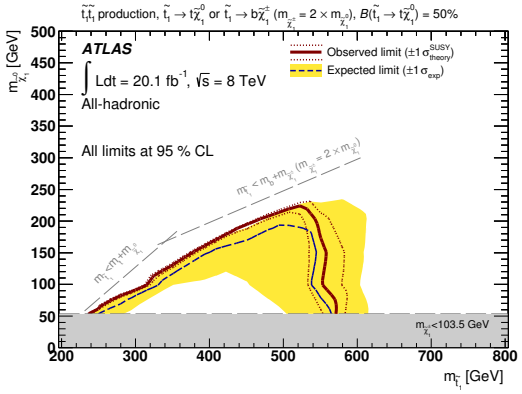

(b) BR($\tilde{t} \to b\tilde{\chi}_1^{\pm} \to bW^{(*)}\tilde{\chi}_1^0$) = 50%

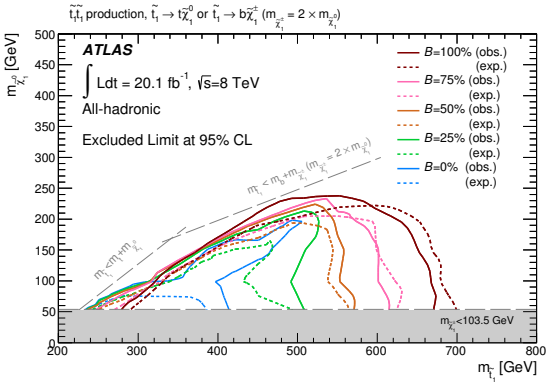

(c) BR($\tilde{t} \to t\tilde{\chi}_1^0$) = $(0, 25, 50, 75, 100)$% from inner to outer contour.

FIGURE 5.14. Exclusion contours at 95% CL in various scenarios. The blue dashed line indicates the expected limit, and the yellow band indicates the $\pm 1\sigma$ uncertainties, which include all uncertainties except the theoretical uncertainties in the signal. The red solid line indicates the observed limit, and the red dotted lines indicate the sensitivity to $\pm 1\sigma$ variations of the signal theoretical uncertainties. The observed limit from the all-hadronic $\sqrt{s} = 7$TeV search [85] is overlaid for comparison.

5.3. Run 2 Search

The Run 2 search [1] uses $\int \mathscr{L} dt = (13.3 \pm 0.4)$ fb^{-1} of data from $p-p$ collision at $\sqrt{s} = 13$ TeV with 25 ns bunch spacing recorded by the ATLAS detector from August to November 2015 and April to July 2016. The sensitivity to the $\tilde{t} \to t\tilde{\chi}_1^0$ scenario with high $m_{\tilde{t}}$ has been enhanced by optimizing each SR for different event topologies based on the reconstructed top mass. A signal region, SRF, has been designed specifically for models which have very high Lorentz boost tops in the final state. SRs targeting $\tilde{t} \to b\tilde{\chi}_1^{\pm} \to bW^{(*)}\tilde{\chi}_1^0$ have been improved by vetoing reconstructed top candidates. In the case where $m_{\tilde{t}} - m_{\tilde{\chi}_1^0} \sim m_t$, which typically has very small p_{T} jets and $E_{\mathrm{T}}^{\mathrm{miss}}$, better search sensitivity has been archived by exploiting the event with ISR jets.

Two alternative scenarios beside stop production are considered in this analysis. Figure 5.15a shows gluino decays to a top and an invisible stop. This will be discussed in more details in Section 5.3.1. Figure 5.15b is where top quark pairs produced in association with a pair of dark matter particles (χ) which couple to the SM via a scalar (φ) or pseudoscalar (a) mediator [86, 87].

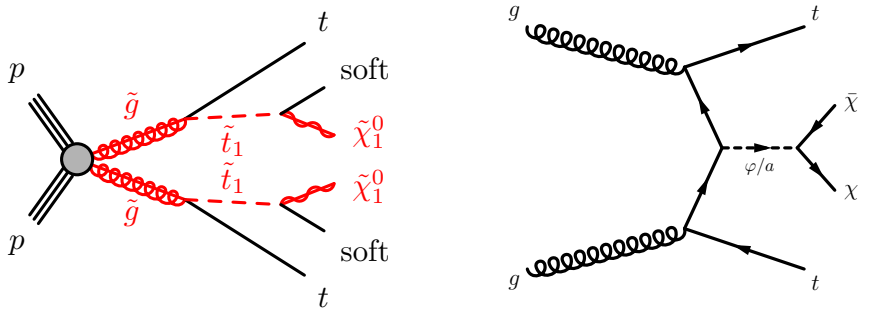

(a) $\tilde{g} \to t\tilde{t} \to t\tilde{\chi}_1^0$+soft (b) DM+$t\bar{t}$

FIGURE 5.15. Alternative scenarios considered in the Run 2 analysis with the similar final state to direct stop pair production.

5.3.1. Gluino Mediated Compressed Stop

In this scenario, the pair produced gluinos decay to stops and tops then a stop will decay to a charm (labeled "soft") and a $\tilde{\chi}_1^0$ as shown in Fig. 5.15a. However, the masses of $\tilde{t}$ and $\tilde{\chi}_1^0$ are very closed (set to 5 GeV in this analysis), therefore the $\tilde{t}$ decay are completely invisible. The signatures are thus almost identical to the decay for directly pair produced $\tilde{t}$. Since the cross section for this process depends on the properties of the gluino rather that the stop, its gains more from the increase in center-of-mass energy. Moreover, the fact that the energy available to the tops ($m_{\tilde{g}}$ - $m_{\tilde{t}}$ splitting) is decoupled from the production cross section ($m_{\tilde{g}}$) leads to a new scenario in which there are very boosted objects in the events from models with a relatively high production cross section compared to direct pair production of stops.

5.3.2. Trigger and Data Collection

The 2015 data have been collected using the trigger based on $E_{\mathrm{T}}^{\mathrm{miss}}$ measured by projective trigger towers with a threshold of 70 GeV. In 2016, due to the increase in the instantaneous luminosity, a trigger requiring $E_{\mathrm{T}}^{\mathrm{miss}}$ reconstructed from jets greater than 100 GeV is used instead. All data used in this analysis are require to have the offline reconstructed $E_{\mathrm{T}}^{\mathrm{miss}}$ as explained in Section 4.7 to be greater than 250 GeV to ensure that they are in the region where both triggers used are fully efficient.

Data for the control regions with leptons are collected using electron and muon trigger. For 2015 data, the thresholds for electrons and muons are 24 and 20 GeV respectively. For 2016, they are both raise to 26 GeV with tight isolation requirement due to the higher instantaneous luminosity. To recover some efficiency with high p_{T} leptons, data passing signal electron (muon) trigger with looser isolation requirements but has p_{T} threshold at 60 GeV (50 GeV), and a signal electron trigger with looser identification but with a higher

p_{T} threshold (120 GeV in 2015, 140 GeV in 2016) have also been included. A p_{T} requirement of 2 GeV above the trigger threshold are applied offline to ensure > 99% efficiency.

Finally, for the mulitijet control region (See Section 5.1.3.1), data are collected using triggers based on the jets p_{T}. Only a known fraction of events passing the requirement are recorded in order to stay within the bandwidth of the trigger system.

5.3.3. Simulations

Simulated signal samples with pair production of stops are generated in a grid across the plane of $m_{\tilde{t}}$ and $m_{\tilde{\chi}^0}$, with most of the spacing at 50 GeV. Three configurations are included; each one corresponds to when both stops decay according to one of the diagrams shown in Fig. 5.3[3]. For gluino mediated stop scenarios, the samples are produced in grid of $m_{\tilde{g}}$ and $m_{\tilde{t}}$ with $m_{\tilde{t}} - m_{\tilde{\chi}^0}$ fixed at 5 GeV to ensure the "compressed" scenario.

The dark matter scenario (Fig. 5.15b) assumes Yukawa-like couplings between the SM and dark matter sector to satisfy flavor constrains, which also favor the decays to heavy flavors in the final state. There are five parameters for these model:

1. Mass of the mediator. Produced in grid.
2. Mass of the dark matter particle. Produced in grid.
3. Mediator's coupling to quark. Produced in $0.1 - 3.5$ range.
4. Mediator's coupling to dark matter. Equal to the coupling to quark.
5. Mediator's width. Smallest possible according to other parameters in the model.

The generators and prescriptions to generate these signal as well as SM background process samples are listed in Tables 5.9 and 5.10. More details can be found in Refs. [88–92].

[3] Unlike Run 1, mixed decays are not covered in this analysis.

TABLE 5.9. Generators used for matrix element (ME), parton shower (PS), and their matching prescriptions for each sample.

Process	ME	PS	ME+PS Matching
Stop	MadGraph[ab]	PYTHIA8	CKKW-L [93]
DM	MadGraph	PYTHIA8	CKKW-L
Z/W+jets	SHERPA v2.2.0	SHERPA v2.2.0	CKKW-L
Semileptonic $t\bar{t}$	Powheg-Boxv.2	PYTHIA6	PYTHIA6
$t\bar{t}$+Z/W	MadGraph	PYTHIA8	CKKW-L
Dibosons	SHERPA v2.1.1	SHERPA v2.1.1	CKKW-L

[a] MadGraph5_aMC@NLO

[b] With up to two additional partons emissions

TABLE 5.10. Generators used for hadronization, source of parton distribution function (PDF), and the underlying event (UE) tune. The EvtGen is used as afterburner to improve B-hadron decays.

Process	Hadronization	PDF	UE	Afterburner
Stop	PYTHIA8	NNPDF2.3LO [94]	A14 [95]	EvtGen v1.2.0
DM	PYTHIA8	NNPDF3.0NLO	A14	EvtGen v1.2.0
Z/W+jets	SHERPA v2.2.0	NNPDF3.0NNLO	Default	
Semileptonic $t\bar{t}$	PYTHIA6	CT10 [96]	P2012 [97]	
$t\bar{t}$+Z/W	PYTHIA8	NNPDF3.0NLO	A14 with NNPDF2.3LO	EvtGen v1.2.0
Dibosons	SHERPA v2.1.1	CT10	SHERPA v2.1.1	

The detector simulation is done as described in Section 3.5.2. Several signal samples have also been generated using the full simulation to validate the Atlfast-II simulation. All samples are simulated with varying pileup contributions, which have been reweighted to match the distribution from the data. The differences between data and simulation due to the lepton trigger and reconstruction efficiencies, momentum scale, energy resolution, isolation, and the efficiency of b-tagging together with the probability for mis-tagging light-flavor and charm quarks, are also corrected as per-event weights.

5.3.4. Event and Physics Object Reconstruction

A summary of various object reconstructions are listed below. More details can be found in Chapter IV.

Primary Vertex The event is required to have a primary vertex with at least two $p_{\mathrm{T}} > 400$ MeV tracks in the luminous region. If there are more than one vertex satisfy the requirements, the one with largest Σp_{T}^2 is picked.

Jet Calibrated anti-k_{t} $R = 0.4$ EMTopo jets with $p_{\mathrm{T}} > 20$ GeV, $|\eta| < 2.8$ are used. Events with BadLoose jets are rejected. JVT selections are applied for $p_{\mathrm{T}} < 60$ GeV, $|\eta| < 2.4$ jets.

***b*-jet** b-jets within the inner detector acceptance ($|\eta| < 2.5$) are identified with MV2c10 algorithm using the 77% working point.

Electron VeryLoose criteria are used for electron candidates. They are required to have $p_{\mathrm{T}} > 7$ GeV, $|\eta| < 2.47$.

Muon Muon candidates are Loose combine muon with $p_{\mathrm{T}} > 6$ GeV, $|\eta| < 2.7$

$\boldsymbol{E_{\mathrm{T}}^{\mathrm{miss}}}$ Track soft term $E_{\mathrm{T}}^{\mathrm{miss}}$ is used. The soft terms are built with the $p_{\mathrm{T}} > 400$ MeV and matched to the primary vertex requirements on the tracks.

$\mathbf{p_{\mathrm{T}}^{miss,track}}$ The $\mathbf{p}_{\mathrm{T}}^{\mathrm{miss,track}}$ is built from the vector sum of $p_{\mathrm{T}} > 500$ GeV, $|\eta| < 2.5$ tracks associated with the primary vertex.

For CRs and VRs where "signal" leptons are required, the criteria are tighten. Both electron and muon are required to have $p_{\mathrm{T}} > 20$ GeV as well as satisfied the "Tight" isolation criteria. The operation point for electron and muon identification are "Tight" and "Medium" respectively.

The ambiguity between overlapping jets, b-jets, electrons, and muons are resolved using the following steps:

1. If an electron and a jet is within $\Delta R < 0.2$, keep the electron and remove the jet. Unless the jet is considered a b-jet, then keep the jet and remove the electron.
2. If an electron and a jet is within $0.2 \leq \Delta R < 0.4$, the electron is removed.
3. If a muon and a jet is within $\Delta R < 0.4$, the muon is removed.

5.3.5. Signal Regions

The common preselections for all SRs are summarized in Table 5.11. There are six SRs designed for different topologies and kinematic regime. SRA and SRB both are designed for heavy stop mass, with SRA targeting larger $m_{\tilde{t}} - m_{\tilde{\chi}^0}$ while SRB target the smaller ones. SRC targets the $\tilde{t} \rightarrow b\tilde{\chi}_1^{\pm}$ decays where there should be no top in the event. SRD aims for $\Delta m(\tilde{t}, \tilde{\chi}^0) \sim m_t$ scenario. SRE looks for dark matter + $t\bar{t}$final state. Finally, SRF is specialized in the very high Lorentz boost scenario from the gluino mediated stop.

TABLE 5.11. Selection criteria common to all signal regions.

$E_{\mathrm{T}}^{\mathrm{miss}}$	> 250 GeV
N_{lep}	0
anti-k_{t} $R = 0.4$ jets	≥ 4, $p_{\mathrm{T}} > 80, 80, 40, 40$ GeV
b-tagged jets	≥ 1
$\left\lvert \Delta\phi\left(\mathrm{jet}^{0,1}, E_{\mathrm{T}}^{\mathrm{miss}}\right)\right\rvert$	> 0.4
$E_{\mathrm{T}}^{\mathrm{miss,track}}$	> 30 GeV
$\left\lvert \Delta\phi\left(E_{\mathrm{T}}^{\mathrm{miss}}, E_{\mathrm{T}}^{\mathrm{miss,track}}\right)\right\rvert$	$< \pi/3$

5.3.5.1. Signal Region A and B

SRA and SRB targets the $\tilde{t} \rightarrow t\tilde{\chi}_1^0$ decays with high stop mass. SRA is optimized for $m_{\tilde{t}} = 800$ GeV, $m_{\tilde{\chi}^0} = 1$ GeV, representing the model with large $\Delta m(\tilde{t}, \tilde{\chi}^0) \sim m_t$. The

benchmark for SRB is $m_{\tilde{t}} = 600$ GeV, $m_{\tilde{\chi}^0} = 300$ GeV to optimize for the smaller mass difference.

Nominally, the six daughters from two tops hadronic decays can be reconstructed. However, the case where the tops or W daughters have enough Lorentz boost to fall within a single anti-k_t $R = 0.4$ jet amount to a significant portion of the signal events. In order to be inclusive, the jet reclustering introduced in Section 5.2.1.2 has been used to reconstruct top (W) candidates with anti-k_t $R = 1.2(0.8)$. Two top candidates are required in each event. Figure 5.16 shows the mass distribution of the leading-p_T $R = 1.2$ jets and $m_T^{b,\min}$ after preselections and $m_T^{b,\min} > 50$ GeV are applied. The mass asymmetry separation has been evolved to the full mass categorization shown in Fig. 5.17. The "TT" category has two well-reconstructed top candidates. The "TW" category has one top and one W candidate from anti-k_t $R = 1.2$ algorithm. Finally, the "T0" category has only a single top candidate. The "other" category, where the leading-p_T top candidate has a smaller invariant mass compared to the subleading one, is not included in this analysis due to the small signal-to-background ratio. The signal and background compositions are different for each categories (See Figs. 5.18 and 5.19), therefore they are optimized separately.

The most discriminating variables for semileptonic $t\bar{t}$ background are E_T^{miss}, and $m_T^{b,\min}$. The τ-veto are also applied to reject the contribution from hadronic τ decays. For SRB, $m_T^{b,\max}$ and $\Delta R(b,b)$ provides extra rejection on the background events. The latter are specially targeting the case where the two b-jets come from a gluon splitting. The distribution for these variables are shown in Fig. 5.19. The selections for SRA and SRB are summarized in Table 5.12.

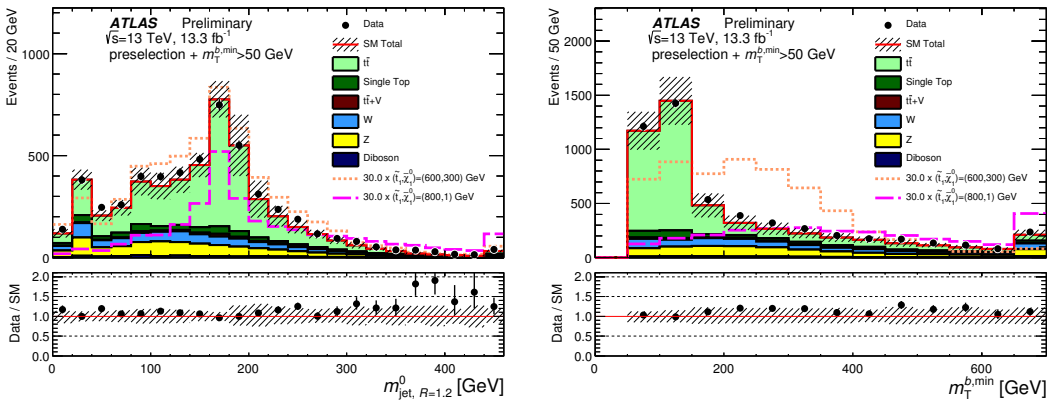

(a) (b)

FIGURE 5.16. Distributions of discriminating variables after the common preselection and an additional $m_{\mathrm{T}}^{b,\mathrm{min}} > 50$ GeV requirement. The stacked histograms show the SM expectation, normalized using scale factors derived from the simultaneous fit to all backgrounds. The "Data/SM" plots show the ratio of data events to the total SM expectation. The hatched uncertainty band around the SM expectation and in the ratio plots illustrates the combination of statistical and detector-related systematic uncertainties. The rightmost bin includes all overflows.

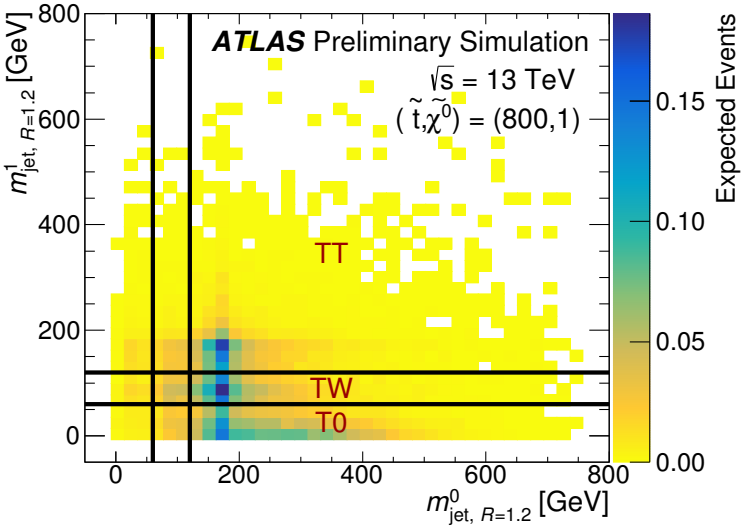

FIGURE 5.17. Illustration of signal region categories (TT, TW, and T0) based on the $R = 1.2$ reclustered top candidate masses for simulated direct top squark pair production with $(\tilde{t}, \tilde{\chi}_1^0) = (800, 1)$GeV after the loose preselection requirement described in the text.

TABLE 5.12. Selection criteria for SRA and SRB, in addition to the common preselection requirements described in the text. The signal regions are separated into topological categories based on reconstructed top candidate masses.

Signal Region		**TT**	**TW**	**T0**
	m^0_{AkT12}	> 120GeV	> 120GeV	> 120GeV
	m^1_{AkT12}	> 120GeV	$60 - 120$GeV	< 60GeV
SRA	m^0_{AkT8}	> 60GeV		
	b-tagged jets	≥ 2		
	$m_{\mathrm{T}}^{b,\mathrm{min}}$	> 200GeV		
	τ-veto	yes		
	$E_{\mathrm{T}}^{\mathrm{miss}}$	> 400GeV	> 450GeV	> 500GeV
SRB	b-tagged jets	≥ 2		
	$m_{\mathrm{T}}^{b,\mathrm{min}}$	> 200GeV		
	$m_{\mathrm{T}}^{b,\mathrm{max}}$	> 200GeV		
	τ-veto	yes		
	$\Delta R\,(b,b)$	> 1.2		
	$E_{\mathrm{T}}^{\mathrm{miss}}$	> 250GeV		

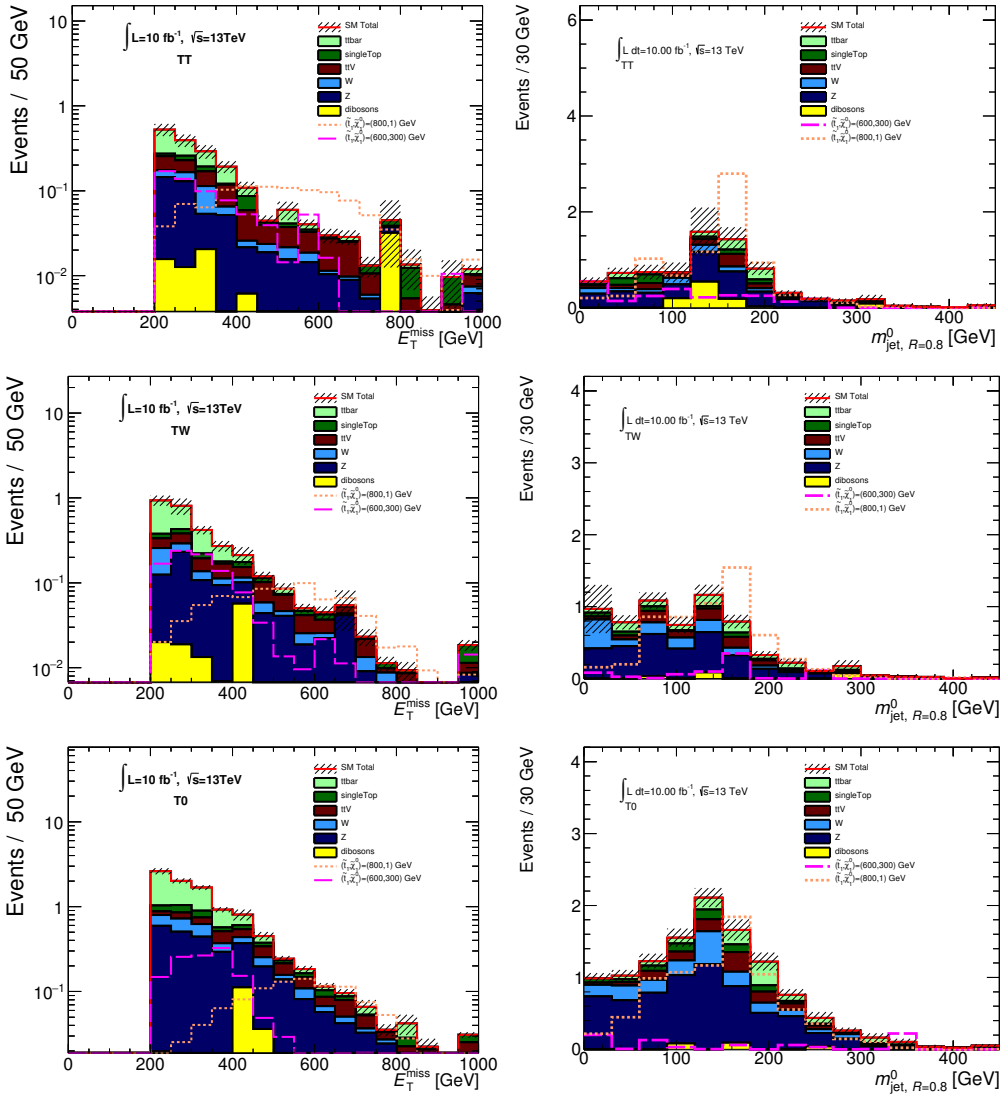

FIGURE 5.18. Distributions of the $E_{\mathrm{T}}^{\mathrm{miss}}$ and the m^0_{AkT8} for SRA-TT, SRA-TW, and SRA-T0 after all requirements (except for the $E_{\mathrm{T}}^{\mathrm{miss}}$ and m^0_{AkT8}, respectively) of Table 5.12 are made. The stacked histogram represent the total expected background estimated from MC while the hashed area represents the uncertainty due to MC statistics. Signal is shown in dashed and dotted lines for the $m_{\tilde{t}} = 600\mathrm{GeV}, m_{\tilde{\chi}^0} = 300\mathrm{GeV}$ and $m_{\tilde{t}} = 800\mathrm{GeV}, m_{\tilde{\chi}^0} = 1\mathrm{GeV}$ benchmarks, respectively.

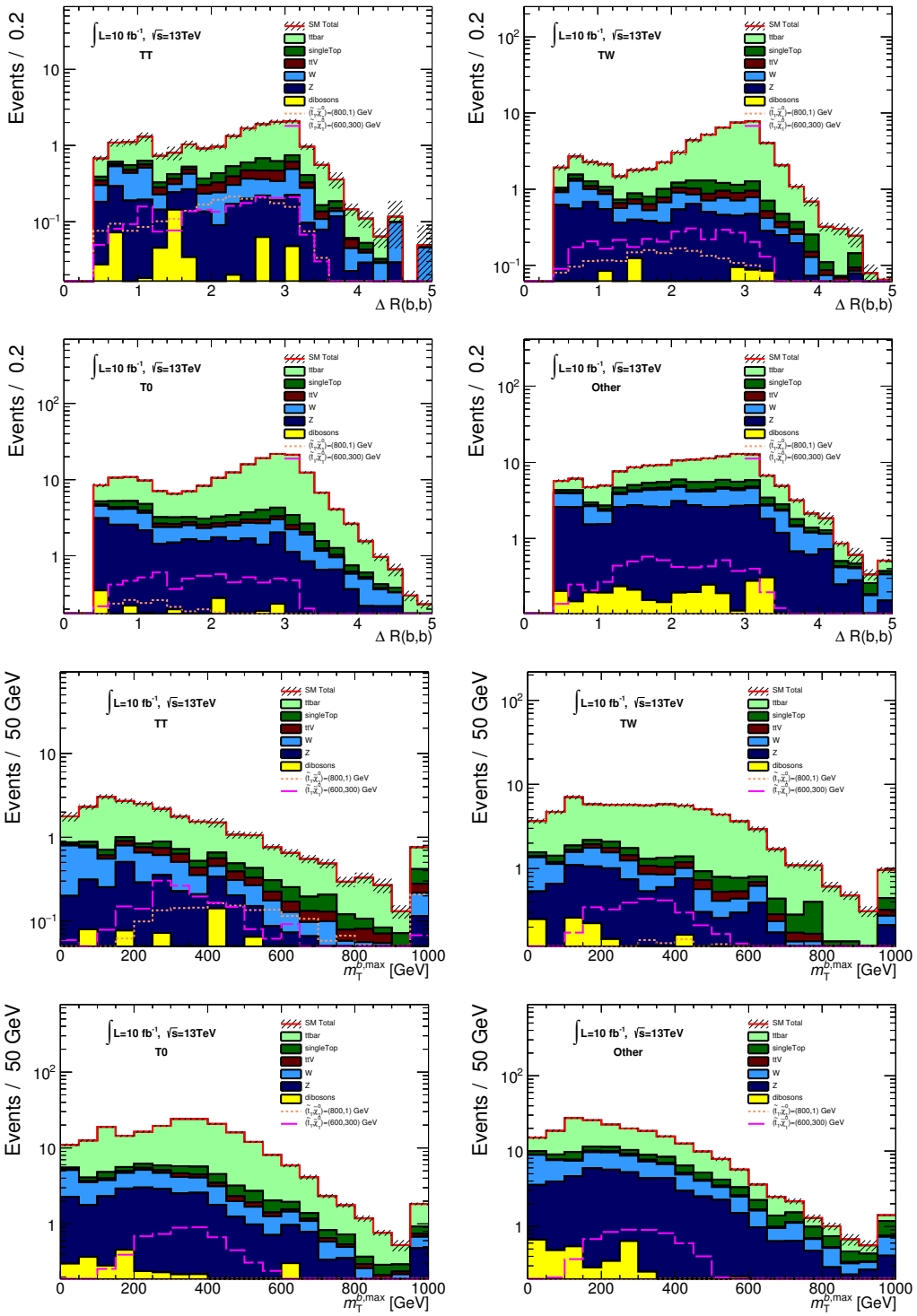

FIGURE 5.19. Distributions of the $\Delta R\,(b,b)$ for SRB-TT, SRB-TW, SRB-T0 and SRB-Other after all requirements (except for the $\Delta R\,(b,b)$) of Table 5.12 are made. The $m_{\mathrm{T}}^{b,\mathrm{max}}$ distributions are also shown with all but the $m_{\mathrm{T}}^{b,\mathrm{max}}$ requirements made. The stacked histogram represent the total expected background estimated from MC while the hashed area represents the uncertainty due to MC statistics. Signal is shown in dashed and dotted lines for the $m_{\tilde{t}} = 600$ GeV, $m_{\tilde{\chi}^0} = 300$ GeV and $m_{\tilde{t}} = 800$ GeV, $m_{\tilde{\chi}^0} = 1$ GeV benchmarks, respectively.

5.3.5.2. Signal Region C

SRC aims for the scenario where both pair-produced stops decay via $\tilde{t} \to b\tilde{\chi}_1^{\pm}$ channel. Unlike SRA and SRB, no reconstructed top is expected in this case. The ΔR_{min} algorithm described in Section 5.2.1.1 is used to loosely identify a top candidate for vetoing. In order to offset for the lack of background rejection from reconstructed tops, SRCs have more stringent requirements on the $R = 0.4$ jet p_{T} and adding a cut on $E_{\text{T}}^{\text{miss}}/\sqrt{H_{\text{T}}}$. SRC is divided into three overlapping SRs, SRC-low, -med, and -high, targeting three different ranges of $m_{\tilde{t}}$. The benchmark points are $(m_{\tilde{t}}, m_{\tilde{\chi}^0}) = (400, 50), (600, 100), (700, 50)$ GeV respectively. The selections are shown in Table 5.13

TABLE 5.13. Selection criteria for SRC, in addition to the common preselection requirements described in the text.

Variable	SRC-low	SRC-med	SRC-high
m_{bjj}	> 250 GeV		
b-tagged jets	≥ 2		
p_{T}^0	> 150 GeV	> 200 GeV	> 250 GeV
p_{T}^1	> 100 GeV	> 150 GeV	> 150 GeV
$m_{\text{T}}^{b,\text{min}}$	> 250 GeV	> 300 GeV	> 350 GeV
$m_{\text{T}}^{b,\text{max}}$	> 350 GeV	> 450 GeV	> 500 GeV
$\Delta R(b, b)$	> 0.8		
$E_{\text{T}}^{\text{miss}}/\sqrt{H_{\text{T}}}$	$[5, 12]\sqrt{\text{GeV}}$	$[5, 12]\sqrt{\text{GeV}}$	$[5, 17]\sqrt{\text{GeV}}$
$E_{\text{T}}^{\text{miss}}$	> 250 GeV		

5.3.5.3. Signal Region D

In the scenarios where $\Delta m(\tilde{t}, \tilde{\chi}_1^0) \sim m_t$, the signal topology is very similar to the semileptonic $t\bar{t}$ background. However, if there are high p_{T} ISRs in the event, the ratio of the $E_{\text{T}}^{\text{miss}}$ to the p_{T} of the ISR system in the CM frame ($p_{\text{T}}^{\text{ISR}}$), defined as R_{ISR}, is proportional to

the ratio of the $\tilde{\chi}_1^0$ and $\tilde{t}$ masses [98, 99]:

$$R_{\mathrm{ISR}} \equiv \frac{E_{\mathrm{T}}^{\mathrm{miss}}}{p_{\mathrm{T}}^{\mathrm{ISR}}} \sim \frac{m_{\tilde{\chi}_1^0}}{m_{\tilde{t}}}. \tag{5.6}$$

A recursive jigsaw reconstruction technique can be used to divide jets and $E_{\mathrm{T}}^{\mathrm{miss}}$ in the event into two groups. In short, the algorithm looks for the "thrust axis" where the p_{T}-projection of all jets and $E_{\mathrm{T}}^{\mathrm{miss}}$ in the event is maximized. The thrust axis is used to define the perpendicular plane which divide the space into two hemispheres. The one with $E_{\mathrm{T}}^{\mathrm{miss}}$ is labeled "sparticle" and the other is "ISR" hemisphere. A graphic representation of this is shown in Fig. 5.20. More details can be found in Ref. [100].

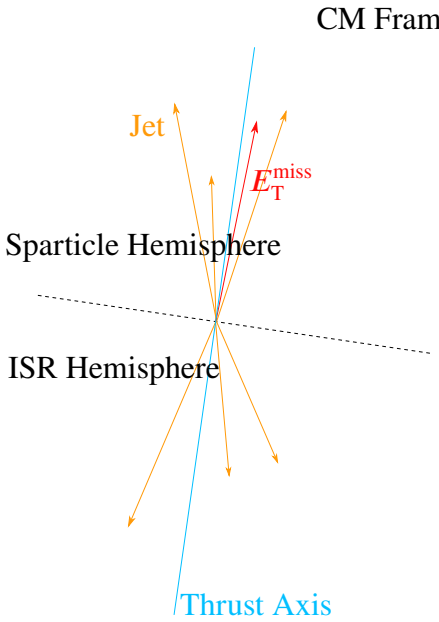

FIGURE 5.20. A graphic representation of how the algorithm used in SRC group the object in the events. The thrust axis defined a perpendicular plane which separated the objects into the one which include the $E_{\mathrm{T}}^{\mathrm{miss}}$ labeled "sparticle" and the other one "ISR".

Various discriminating variables are then constructed from this assignment:

$\boldsymbol{N_{\mathrm{jet}}^{\mathrm{S}}}$ number of jets associated with the sparticle hemisphere.

$\boldsymbol{p_{\mathrm{T}}^{b\text{-tag},S}}$ p_{T} of the leading b-jet in the sparticle hemisphere.

$\boldsymbol{p_{\mathrm{T}}^{\mathrm{jet\,4},S}}$ p_{T} of the fourth jet ordered in p_{T} in the sparticle hemisphere.

$\boldsymbol{\Delta\phi_{\mathrm{ISR}}}$ angular separation in ϕ of the ISR and the $E_{\mathrm{T}}^{\mathrm{miss}}$in the CM frame.

$\boldsymbol{p_{\mathrm{T}}^{\mathrm{ISR}}}$ p_{T} of the ISR system, evaluated in the CM frame.

$\boldsymbol{M_{\mathrm{T}}^{S}}$ transverse mass between the whole sparticle system and $E_{\mathrm{T}}^{\mathrm{miss}}$.

$\boldsymbol{R_{\mathrm{ISR}}}$ Ratio between invisible system ($E_{\mathrm{T}}^{\mathrm{miss}}$in CM frame) and $p_{\mathrm{T}}^{\mathrm{ISR}}$

SRD is subdivided into eight overlapping SRs with increasing range of R_{ISR}. The benchmark point for SRD1-4 and SRD5-8 are $(m_{\tilde{t}}, m_{\tilde{\chi}^0}) = (250, 77), (450, 277)$ GeV respectively. SRA1-4 require at least 1 b-jet, while SRD5-8 require at least 2, and share the rest of the cuts. The selections are summarized in Table 5.14.

TABLE 5.14. Selection criteria for SRD, in addition to the common preselection requirements described in the text. The signal regions are separated into windows based on ranges of R_{ISR}.

Variable	**SRD1**	**SRD2**	**SRD3**	**SRD4**	**SRD5**	**SRD6**	**SRD7**	**SRD8**
min R_{ISR}	0.25	0.30	0.35	0.40	0.45	0.50	0.55	0.60
max R_{ISR}	0.40	0.45	0.50	0.55	0.60	0.65	0.70	0.75
b-tagged jets	≥ 2				≥ 1			
$N_{\mathrm{jet}}^{\mathrm{S}}$	≥ 5							
$p_{\mathrm{T}}^{\mathrm{ISR}}$	> 400 GeV							
$p_{\mathrm{T}}^{b\text{-tag},S}$	> 40 GeV							
$p_{\mathrm{T}}^{\mathrm{jet\,4},S}$	> 50 GeV							
M_{T}^{S}	> 300 GeV							
$\Delta\phi_{\mathrm{ISR}}$	> 3.0 radians							

5.3.5.4. Signal Region E

SRE target the dark matter + $t\bar{t}$ final state. This SR considers a similar set of discrimination variables as those from SRA-C, but optimized for $m_{\varphi} = 350\text{GeV}, m_{\chi} = 1$ GeV simplified model. The selections are summarized in Table 5.15.

5.3.5.5. Signal Region F

SRF is designed for scenarios where the tops received very large Lorentz boosted. Such signatures can either come from direct stop pair production with a very high stop mass, or in the gluino-mediated compressed-stop scenario with large $m_{\tilde{g}} - m_{\tilde{t}}$ described in Section 5.3.1. The benchmark for this signal region is when $(m_{\tilde{g}}, m_{\tilde{t}}, m_{\tilde{\chi}^0}) = (1400, 400, 395)$ GeV. Due to the large boost, the top daughters are more collimated compared to typical topology expected in SRA. This is illustrated in Fig. 5.21. Compared to direct stop pair production with $m_{\tilde{t}} = 800$ GeV and $m_{\tilde{\chi}^0} = 1$ GeV, the ΔR separation between the W and the bottom quark tends to be smaller. Therefore, anti-k_{t} $R = 0.8$ reclustered jets collection will be considered as the top candidates instead of $R = 1.2$ jets in other signal regions. Table 5.15 shows the selection criteria for SRF. Figure 5.22 shows the distributions of variables used in optimization with cuts in Table 5.15 applied except for the one in the plot shown.

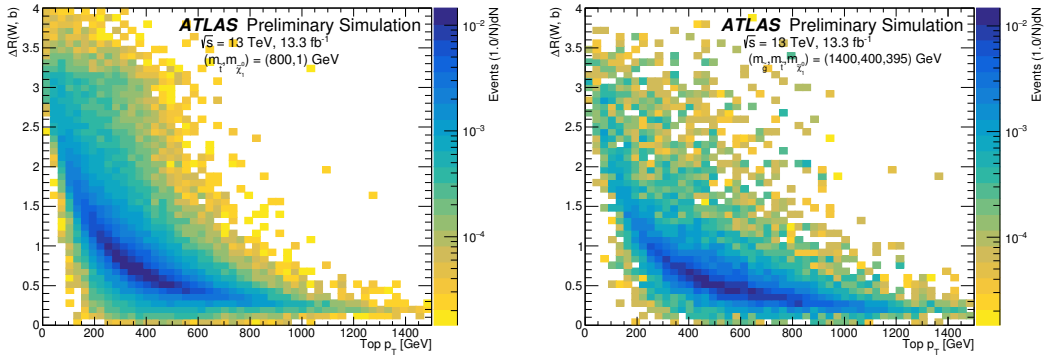

(a) $m(\tilde{t}, \tilde{\chi}_1^0) = (800, 1)$ GeV (b) $m(\tilde{g}, \tilde{t}, \tilde{\chi}_1^0) = (1400, 400, 395)$ GeV

FIGURE 5.21. The true ΔR between the W and the b-quark vs. the true top p_{T}. The common preselection criteria are applied with the exception of the b-jet requirement. The histograms are normalized to unity to illustrate the increased boost of the top quarks in the gluino-mediated top squark decays compared to direct top squark production.

TABLE 5.15. Selection criteria for SRE and SRF, in addition to the common preselection requirements described in the text.

Variable	**SRE**	**SRF**
b-tagged jets	$\geq$2	
m^0_{AkT12}	$>$ 140 GeV	-
m^1_{AkT12}	$>$ 60 GeV	-
m^0_{AkT8}	-	$>$ 120 GeV
m^1_{AkT8}	-	$>$ 60 GeV
$m_{\mathrm{T}}^{b,\mathrm{min}}$	$>$ 200 GeV	$>$ 175 GeV
$\tau-$veto	yes	no
$\Delta R(b, b)$	$>$ 1.5	-
$E_{\mathrm{T}}^{\mathrm{miss}}$	$>$ 300GeV	$>$ 250GeV
H_{T}	-	$>$ 1100GeV
$E_{\mathrm{T}}^{\mathrm{miss}}/\sqrt{H_{\mathrm{T}}}$	$>$ 14$\sqrt{\mathrm{GeV}}$	$>$ 15$\sqrt{\mathrm{GeV}}$

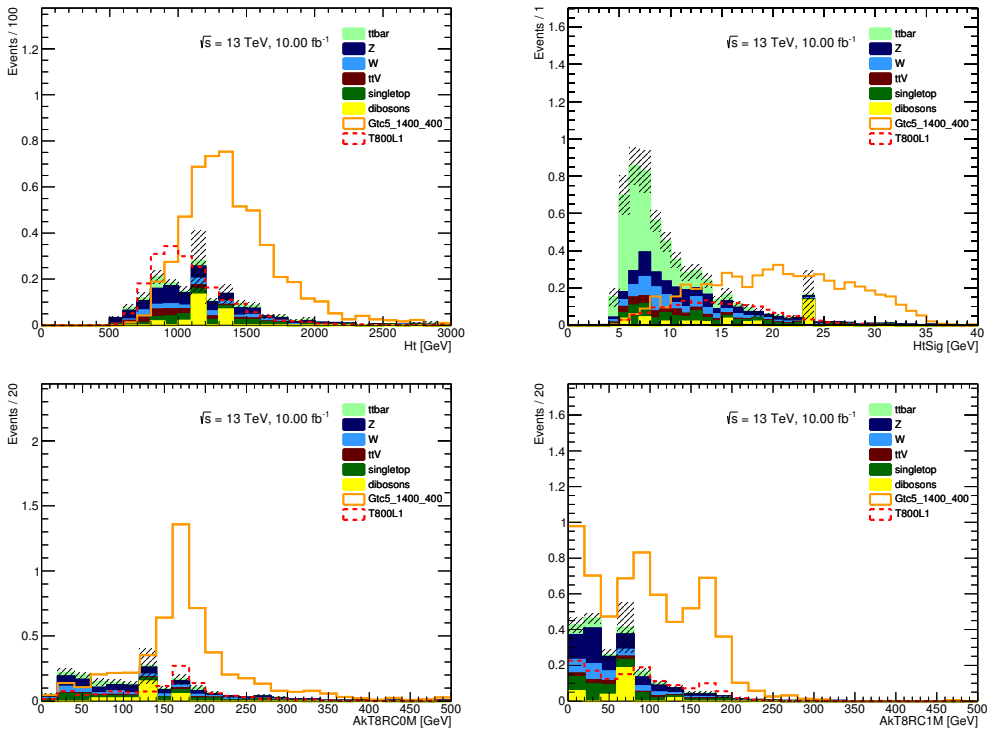

FIGURE 5.22. Distribution of H_{T}, $E_{\mathrm{T}}^{\mathrm{miss}}/\sqrt{H_{\mathrm{T}}}$, m^{0}_{AkT8}, and m^{1}_{AkT8}. The selections listed in Table 5.15 are applied except for the variable shown in each plot.

5.3.6. Background Estimation

The main background for all signal regions except SRD is $Z(\nu\nu)$ + jets where at least one of the jets originate from a b quark. The second most dominant background is the semileptonic $t\bar{t}$ event, which is also the main background for SRD. Other SM backgrounds are explained in Section 5.1.3. The backgrounds composition and the list of CR used to estimated them for each SR are summarized in Table 5.16. The normalization scale factor from a simultaneous fit (See Section 5.1.3.2) are given as well. The signal contamination is below 16% for all signal models not excluded by the Run 1 search.

Strategies for defining CRs follow the descriptions in Section 5.1.3.1. The CR for $Z(\nu\nu)$ + jets, semileptonic $t\bar{t}$, W + jets, and single top processes are shared among all SRs, except for SRD where the vast majority of the background are $t\bar{t}$ events and a dedicated CR is defined using similar variables used in SRD. The definitions for all CRs are summarized in

TABLE 5.16. Summary of control regions used to estimate the background contributions for each signal region. The percentages indicate the relative contribution of each background process; for example, SRA contains predominantly Z + jets and the normalization of the simulation is determined by data-MC comparison in CRZ. The ranges in percentages correspond to the variation across the signal subregions. The contributions may not total 100% since sub-dominant background contributions from $t\bar{t} + W/Z$, diboson, all-hadronic $t\bar{t}$, and multijet processes are not listed. Normalization scale factors (SF) for each CR calculated from a simultaneous fit (described in Section 5.1.3.2) to all backgrounds in all the CRs are also presented; the given uncertainty is the combination of the corresponding MC statistical and detector-related systematic uncertainties.

	Z + jets	$t\bar{t}$		W + jets	single top
	CRZ	CRT	CRT-ISR	CRW	CRST
SF	1.20±0.26	0.91±0.18	0.78±0.19	1.21±0.21	0.86±0.33
SRA	34%-58%	9%-14%	-	10%-11%	6%-9%
SRB	22%-42%	22%-25%	-	9%-13%	10%
SRC	37%-39%	6%-17%	-	18%-25%	20%-26%
SRD1-4	0%	-	91%-92%	2%	1%-4%
SRD5-8	2%-10%	-	70%-84%	5%-9%	4%-8%
SRE	38%	12%	-	8%	10%
SRF	32%	10%	-	12%	17%

Table 5.17. The requirements on $\left|\Delta\phi\left(\text{jet}^{0,1}, E_{\text{T}}^{\text{miss}}\right)\right|$, minimum $m_{\text{T}}(\ell, E_{\text{T}}^{\text{miss}})$, and m^{0}_{AkT12}[4] aims to reduce the contributions from SM multijet processes. For CRZ, orthogonality is ensured by the requirement on the maximum $m_{\text{T}}(\ell, E_{\text{T}}^{\text{miss}})$ and the minimum ΔR between the two highest-weight b-tagged jets and the lepton, $\Delta R\,(b,\ell)_{\text{min}}$. Contaminations from $t\bar{t}$ events in the single top control region (CRST) is suppressed by the requirement on the invariant mass of the two highest-weight b-tagged jets, m_{bb}. Various distributions from the CRs are shown in Figs. 5.23 and 5.23.

TABLE 5.17. Selection criteria for the control regions used to estimate the background contributions in the signal regions.

Selection	CRZ	CRT	CRT-ISR	CRST	CRW
Trigger	electron (muon)	$E_{\text{T}}^{\text{miss}}$			
N_{ℓ}	2	1			
p_{T}^{ℓ}	$>$ 20 GeV				
$m_{\ell\ell}$	[86,96] GeV	-			
N_{jet}	≥ 4	≥ 4 (including leptons)			
jet p_{T}	(40, 40, 20, 20)GeV	(80, 80, 40, 40) GeV			(80, 80, 20, 20) GeV
$E_{\text{T}}^{\text{miss}}$	$<$ 50 GeV	$>$ 250GeV			
$E_{\text{T}}^{\text{miss}'}$	$>$ 70 GeV	-			
b-tagged jets	≥ 2	≥ 2	≥ 1	≥ 2	$= 1$
$\left\|\Delta\phi\left(\text{jet}^{0,1}, E_{\text{T}}^{\text{miss}}\right)\right\|$	-	$>$ 0.4			
min $m_{\text{T}}(\ell, E_{\text{T}}^{\text{miss}})$	-	30 GeV	-	30 GeV	30 GeV
max $m_{\text{T}}(\ell, E_{\text{T}}^{\text{miss}})$	-	120 GeV	80 GeV	120 GeV	100 GeV
m^{0}_{AkT12}	-	$>$ 70 GeV	-	$>$ 70 GeV	$<$ 60 GeV
$m_{\text{T}}^{b,\text{min}}$	-	$>$ 100 GeV	-	$>$ 175 GeV	-
$\Delta R\,(b,\ell)_{\text{min}}$	-	$<$ 1.5	$<$ 2.0	$>$ 1.5	$>$ 2.0
m_{bb}	-	-	-	$>$ 200 GeV	-
$N_{\text{jet}}^{\text{S}}$	-	-	≥ 5	-	-
$N_{b\text{-tag}}^{\text{S}}$	-	-	≥ 1	-	-
$p_{\text{T}}^{\text{ISR}}$	-	-	$\geq$ 400 GeV	-	-

[4] Only real jets are used for these variables, not the lepton-as-jet.

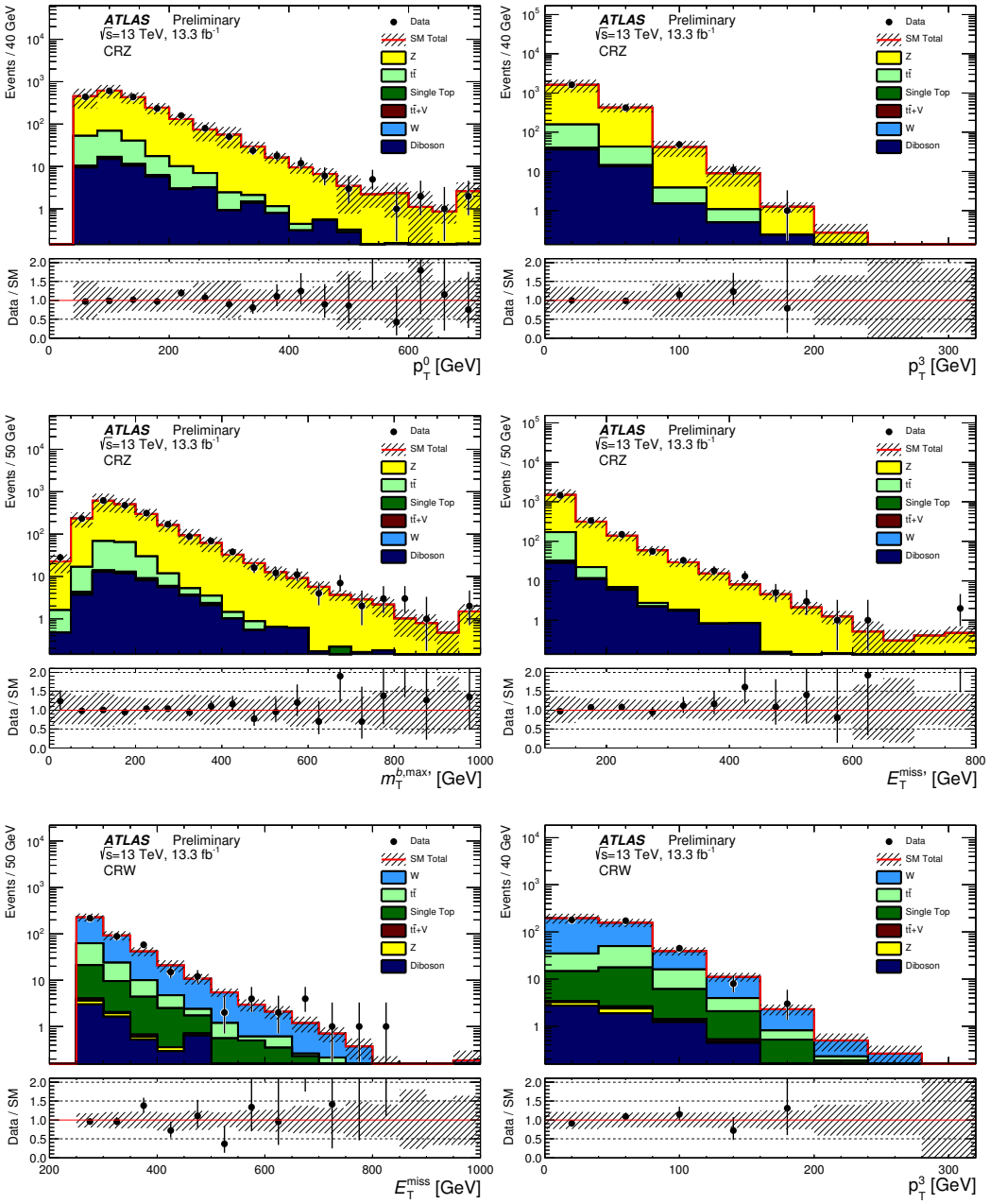

FIGURE 5.23. Transverse momenta of (a) the leading-p_{T} jet, (b) the fourth-leading-p_{T} jet, (c) the $m_{\mathrm{T}}^{b,\mathrm{max}\prime}$ distribution, and (d) the $E_{\mathrm{T}}^{\mathrm{miss}\prime}$ distribution in CRZ, and (e) the $E_{\mathrm{T}}^{\mathrm{miss}}$ and (f) the transverse momentum of the fourth-leading-p_{T} jet in CRW. The stacked histograms show the SM expectation, normalized using scale factors derived from the simultaneous fit to all backgrounds. The "Data/SM" plots show the ratio of data events to the total SM expectation. The hatched uncertainty band around the SM expectation and in the ratio plot illustrates the combination of MC statistical and detector-related systematic uncertainties. The rightmost bin includes all overflows.

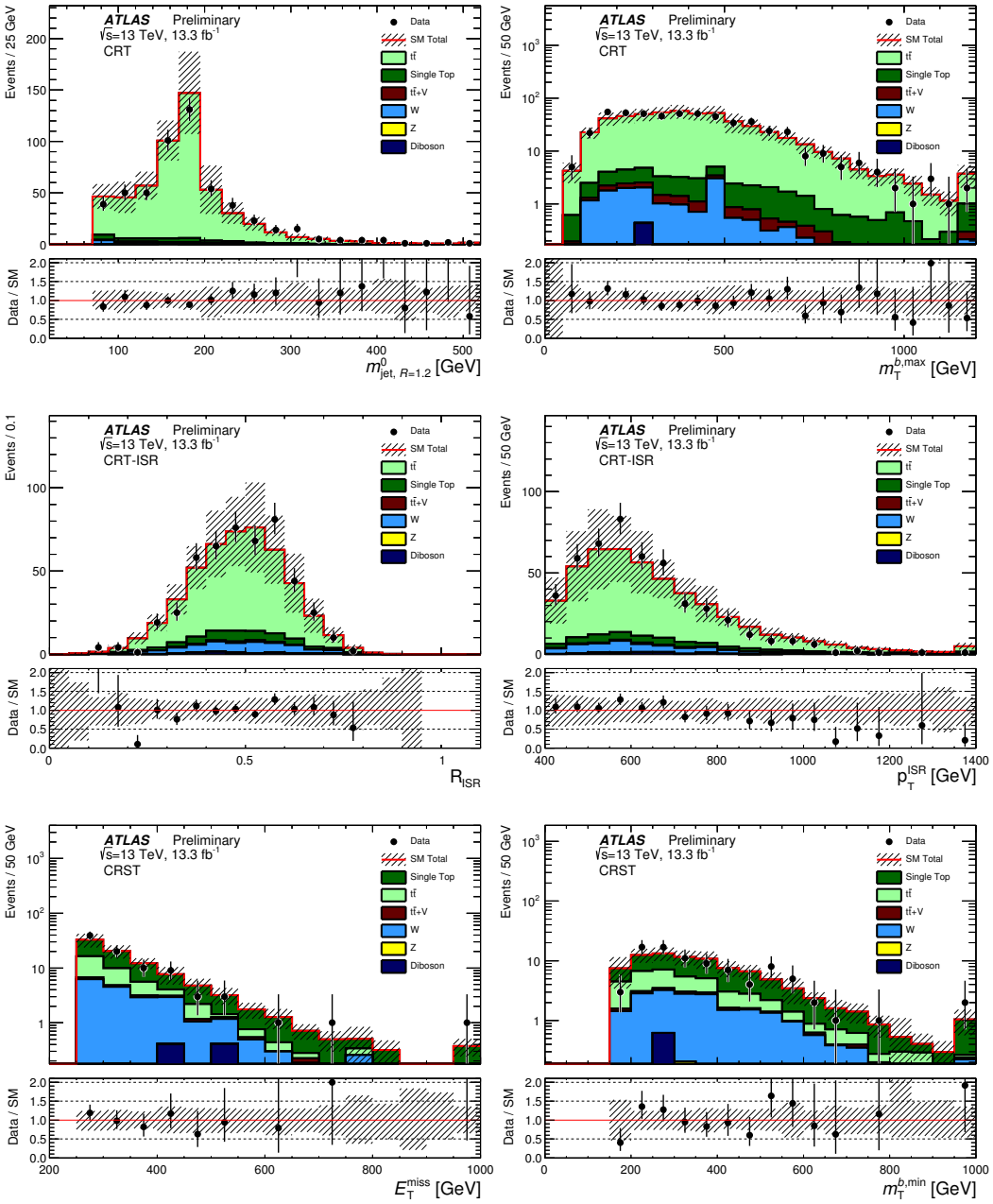

FIGURE 5.24. Distributions of (a) m^{0}_{AkT12} and (b) $m_{\mathrm{T}}^{b,\mathrm{max}}$ in CRT, (c) R_{ISR} and (d) $p_{\mathrm{T}}^{\mathrm{ISR}}$ in CRT-ISR, and (e) $E_{\mathrm{T}}^{\mathrm{miss}}$ and (f) $m_{\mathrm{T}}^{b,\mathrm{min}}$ in CRST. The stacked histograms show the SM expectation, normalized using scale factors derived from the simultaneous fit to all backgrounds. The "Data/SM" plots show the ratio of data events to the total SM expectation. The hatched uncertainty band around the SM expectation and in the ratio plots illustrates the combination of MC statistical and detector-related systematic uncertainties. The rightmost bin includes all overflows.

Background contributions from Diboson and $t\bar{t}+W/Z$ production are estimated purely from simulation and found to be sub-dominant. The multijet and all-hadronic $t\bar{t}$ backgrounds are estimated using the procedure outlined in Section 5.1.3.1 and found to be negligible.

5.3.6.1. Validation Region

Several validation regions (VRs) are defined with the strategy for each process explained below:

Z + jets VRZs are defined for all SRs except the SRD. The selections are tighter than those in CRZs to be kinematically closer to the SRs. The requirements in addition to those listed in Table 5.17.

W + jets VRW is defined to be similar to CRW, but tighten to 2 b-jets and requires $m_{\mathrm{T}}^{b,\mathrm{min}} > 150$ GeV to be closer to the SRs. In order to increase the statistic, two cuts are relax: $m^{0}_{AkT12} <$ 70GeV, and $\Delta R\,(b,\ell)_{\mathrm{min}} > 1.8$.

$t\bar{t}$ Four VRs are defined. VRT-high and VRT-low aim to validate the $t\bar{t}$ estimates for SRA/F and SRB/C/E respectively. Unlike the CRT, VRT-high and -low use the same preselections as the SRs, but require 2 b-jets and tighten $E_{\mathrm{T}}^{\mathrm{miss}}$ cuts ($>$ 250 and $>$ 350 GeV respectively). The $m_{\mathrm{T}}^{b,\mathrm{min}} <$ 150 GeV is used as the orthogonal requirements for these two VRs. The other two VRs, VRT-ISR-1b and VRT-ISR-2b, are designed specifically for SRD1-4 and SRD5-8 respectively. They are orthogonal to the SRs by inverting the R_{ISR} requirement to < 3.0. To increase the statistic, M_{T}^{S} requirement is relaxed to $M_{\mathrm{T}}^{S} > 100$ GeV, the $N_{\mathrm{jet}}^{\mathrm{S}}$ requirement is relaxed to $N_{\mathrm{jet}}^{\mathrm{S}} \geq 4$, and the $p_{\mathrm{T}}^{\mathrm{jet}\,4,S}$ requirement is removed. An additional requirement on the ratio of the transverse mass of the visible part of the sparticle system ($M_{\mathrm{T}}^{S,\mathrm{Vis}}$) to M_{T}^{S} is imposed: $M_{\mathrm{T}}^{S,\mathrm{Vis}}/M_{\mathrm{T}}^{S} < 0.6$ to suppress the contamination from signal and multijet events.

The background estimates for VRs are obtained from the combine fit to the CRs. The predictions agrees with the data and they are present in Tables 5.19 and 5.20. Distribution from VRZ/W and VRTs are shown in Figs. 5.25 and 5.26 respectively.

TABLE 5.18. Selection criteria for the Z + jets validation regions corresponding to SRA−C, SRE and SRF. The criteria listed are in addition to those applied to CRZ.

Selection	VRZA	VRZB	VRZC	VRZE	VRZF
$E_{\mathrm{T}}^{\mathrm{miss}'}$	$>$ 200 GeV				
$m_{\mathrm{T}}^{b,\mathrm{min}}$	$>$ 100 GeV				
m_{AkT12}^{0}	$>$ 60 GeV	$>$ 60 GeV	-	$>$ 60 GeV	-
$\Delta R\,(b,b)$	-	$>$ 0.8	$>$ 0.8	$>$ 0.8	-
$m_{\mathrm{T}}^{b,\mathrm{max}}$	-	$>$ 100 GeV	$>$ 200 GeV	$>$ 100 GeV	-
H_{T}	-	-	-	-	$>$ 300 GeV
$E_{\mathrm{T}}^{\mathrm{miss}}/\sqrt{H_{\mathrm{T}}}$	-	-	-	$>10\sqrt{\mathrm{GeV}}$	$>8\sqrt{\mathrm{GeV}}$
m_{AkT8}^{0}	-	-	-	-	$>$ 30 GeV

TABLE 5.19. Event yields in the Z + jets validation regions compared to the background estimates obtained from the profile likelihood fit. Statistical and systematic uncertainties in the number of fitted background events are shown.

	VRZA	VRZB	VRZC	VRZE	VRZF
Observed	135	104	164	92	117
Total SM	127 ± 31	94 ± 23	156 ± 36	80 ± 20	110 ± 26
$t\bar{t}$	0.80 ± 0.22	0.80 ± 0.22	0.75 ± 0.28	0.54 ± 0.19	0.61 ± 0.18
W + jets	−−	−−	−−	−−	−−
Z + jets	119 ± 32	89 ± 24	148 ± 37	76 ± 21	103 ± 26
$t\bar{t}$+W/Z	< 0.01	< 0.01	< 0.01	< 0.01	−−
Single top	0.06 ± 0.04	0.06 ± 0.04	0.06 ± 0.05	0.06 ± 0.04	0.06 ± 0.04
Dibosons	6.8 ± 1.5	4.6 ± 1.0	8.0 ± 1.5	3.66 ± 0.78	6.4 ± 1.2
Multijets	−−	−−	−−	−−	−−

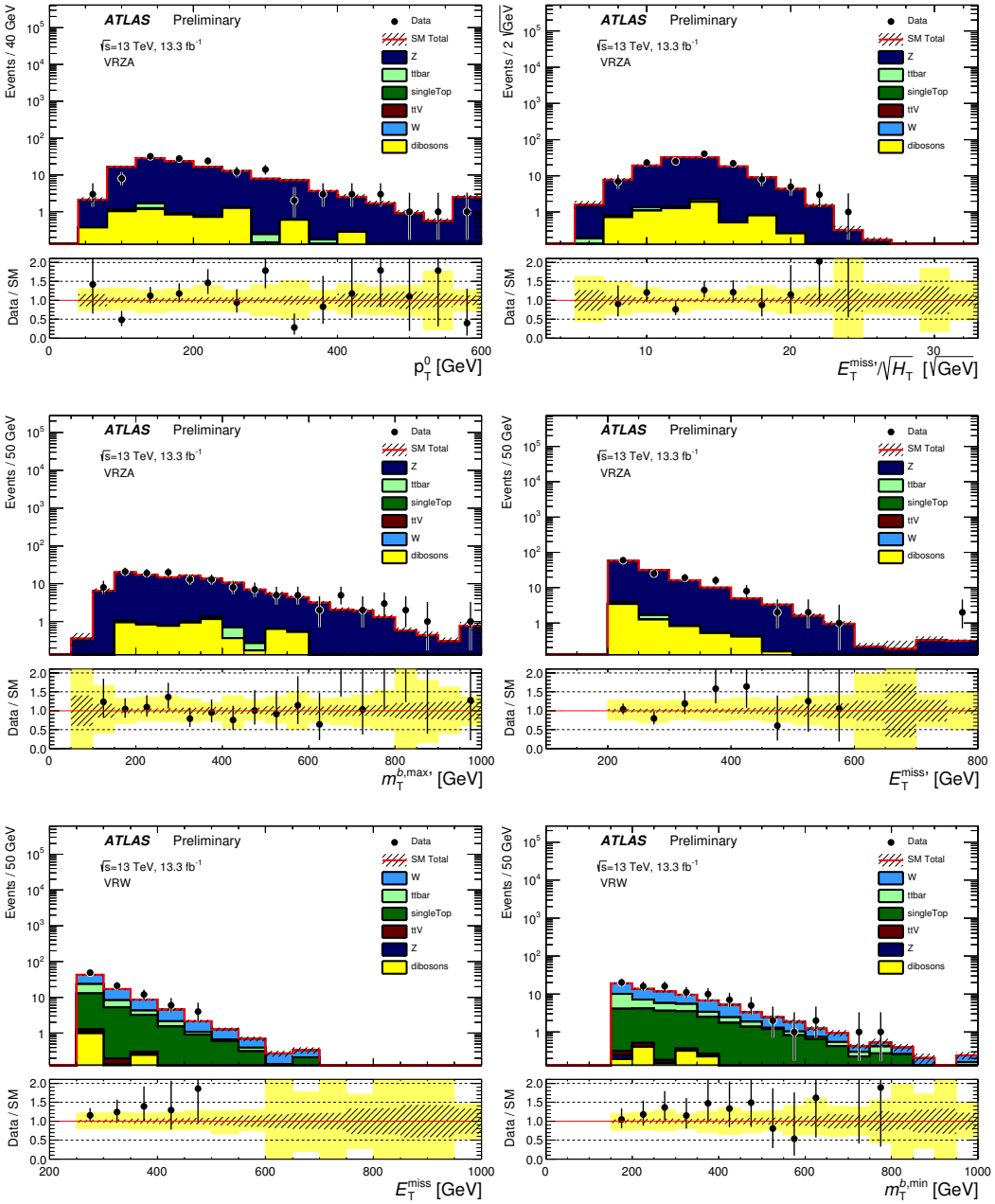

FIGURE 5.25. Distributions of (a) p_{T} of the leading jet, (b) $E_{\mathrm{T}}^{\mathrm{miss}'}/\sqrt{H_{\mathrm{T}}}$, (c) $m_{\mathrm{T}}^{b,\mathrm{max}}$ and (d) $E_{\mathrm{T}}^{\mathrm{miss}'}$ in the VRZA, and (e) $E_{\mathrm{T}}^{\mathrm{miss}}$ and (f) the fourth-leading jet p_{T} in VRW. The stacked histograms show the SM expectation, normalized using scale factors derived from the simultaneous fit to all backgrounds. The hatched uncertainty band around the SM expectation shows the statistical uncertainty. The "Data/SM" plots show the ratio of data events to the total SM expectation. The yellow band illustrates the combination of statistical and detector-related systematic uncertainties. The rightmost bin includes all overflows.

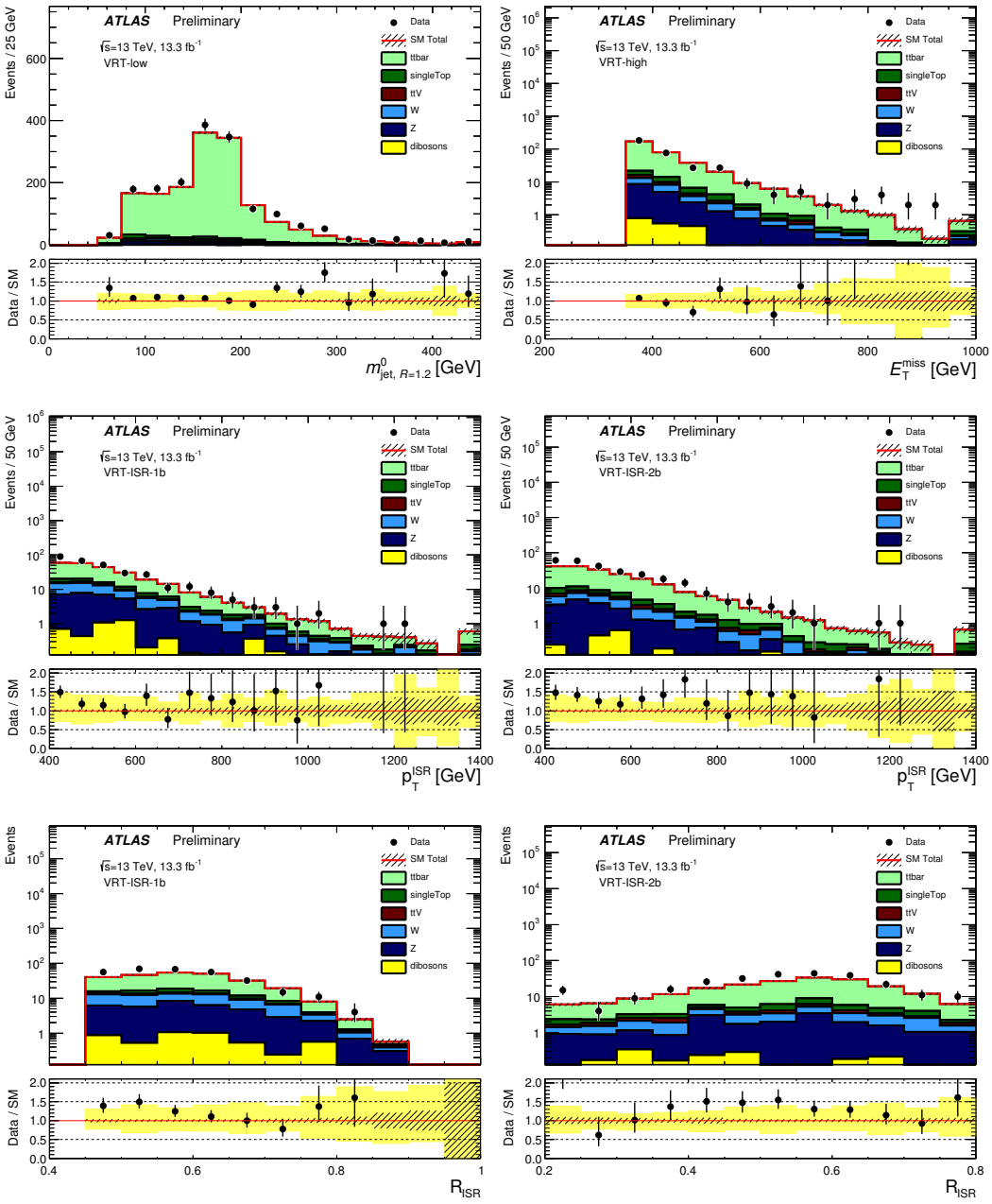

FIGURE 5.26. Distributions of (a) m^0_{AkT12} in VRT-low, (b) $E_{\mathrm{T}}^{\mathrm{miss}}$ in VRT-high, (c) $p_{\mathrm{T}}^{\mathrm{ISR}}$ in VRT-ISR-1b , (d) $p_{\mathrm{T}}^{\mathrm{ISR}}$ VRT-ISR-2b, (e) R_{ISR} in VRT-ISR-1b, and (f) R_{ISR} in VRT-ISR-2b. The stacked histograms show the SM expectation, normalized using scale factors derived from the simultaneous fit to all backgrounds. The hatched uncertainty band around the SM expectation shows the statistical uncertainty. The "Data/SM" plots show the ratio of data events to the total SM expectation. The yellow band illustrates the combination of statistical and detector-related systematic uncertainties. The rightmost bin includes all overflows.

TABLE 5.20. Event yields in the $t\bar{t}$ and W validation regions compared to the background estimates obtained from the profile likelihood fit. Statistical and systematic uncertainties in the number of fitted background events are shown.

	VRT-low	VRT-high	VRW	VRT-ISR-2b	VRT-ISR-1b
Observed	1735	345	92	270	312
Total SM	1564 $\pm$ 350	330 $\pm$ 71	77 $\pm$ 14	199 $\pm$ 42	252 $\pm$ 58
$t\bar{t}$	1379 $\pm$ 330	278 $\pm$ 65	15.8 $\pm$ 4.0	144 $\pm$ 40	158 $\pm$ 45
W + jets	40 $\pm$ 10	11.3 $\pm$ 2.8	36.8 $\pm$ 8.6	14.0 $\pm$ 4.1	34 $\pm$ 11
Z + jets	58 $\pm$ 17	17.2 $\pm$ 4.5	0.16 $\pm$ 0.08	17.4 $\pm$ 4.2	32 $\pm$ 12
$t\bar{t}$+W/Z	22.9 $\pm$ 3.0	6.32 $\pm$ 0.81	0.27 $\pm$ 0.05	6.1 $\pm$ 1.5	5.4 $\pm$ 1.4
Single top	57 $\pm$ 24	14.7 $\pm$ 6.3	23 $\pm$ 10	13.8 $\pm$ 5.3	16.5 $\pm$ 6.8
Dibosons	5.1 $\pm$ 1.1	2.06 $\pm$ 0.54	1.50 $\pm$ 0.26	1.98 $\pm$ 0.56	4.9 $\pm$ 2.6
Multijets	$1.0^{+2.1}_{-1.0}$	$0.17^{+0.35}_{-0.17}$	$--$	$1.3^{+2.7}_{-1.3}$	$0.7^{+1.4}_{-0.7}$

5.3.7. Systematic Uncertainties

Background estimate for all signal regions except for SRB-T0 are dominated by the statistic uncertainty. The main sources of detector-related systematic uncertainty are:

JES and JER The effect of JES on the background estimates is 1-4% in SRA and SRB, 1-5% in SRC, 2-9% in SRD, 5% in SRE and 2% in SRF.

***b*-tagging efficiency** Also gives a relatively large contributions. It is 1-5% in SRA, 1-3% in SRB, 1-8% in SRC, 1-4% in SRD and is about 12% for SRE and 23% for SRF.

Lepton reconstruction and identification They are considered but have small effects.

$\boldsymbol{E}_{\mathrm{T}}^{\mathrm{miss}}$ All jet- and lepton-related uncertainties, as well as those from the energy and and resolution of the soft terms are propagated to the reconstruction of the $E_{\mathrm{T}}^{\mathrm{miss}}$. SRD and SRE/F are the most sensitive to the uncertainties of the soft terms, which are $\sim 1-10\%$ and $\sim 7\%$ respectively.

Pileup This uncertainty comes from reweighting the simulation to match the pileup profile in data. It is 1-6% in SRA, 1-3% in SRB, 1-2% in SRC, 2-15% in SRD, 3% in SRE and 10% in SRF.

Luminosity 2.9% across all signal and background estimates derived from simulation.

Theoretical uncertainties from the modeling of SM background processes are evaluated:

***W/Z* + jets** Obtained by varying the renormalization and factorization scales, and the merging (CKKW) and resummation scales in SHERPA. The impact relative to the total background yields for Z + jets (W + jets) are 7-12% (2%) for SRA, 4-9% (1-3%) for SRB, 8% (2-3%) for SRC, less than 1% for SRD, 8% (1%) for SRE and 7% (2%) for SRF.

tt̄ Evaluated by comparing with alternative generator: MadGraph5aMC@NLO vs POWHEG-BOX for hard scattering generator, PYTHIA vs. Herwig++ for parton shower and emission of ISR and FSR. The largest impact occurs in SRD at $\sim$ 22%, follow by SRC at 10%.

tt̄*+*W/Z Theoretical uncertainty for $t\bar{t}$+W and $t\bar{t}$+Z are dominated by the 13% uncertainty on the production cross section. The choice of renormalization and factorization scales are considered by each varied up and down by a factor of two. Comparison between SHERPA at NLO with MadGraph5aMC@NLO is used to evaluate the uncertainty from the choice of the generator.

Signal top Uncertainties from the choice of parton shower and emission of ISR/FSR are evaluated by comparing PYTHIA with Herwig++. The effects are about 10% in SRA and SRB, 17-25% in SRC, 10% in SRE and 16% in SRF. The effect of the interference between single-top quark and $t\bar{t}$ production are assigned with 100% uncertainty.

When setting limits, signal systematic uncertainties due to detector and acceptance effects are taken into account. The major contributions come from JER (3-23%), JES (6-16%), and pileup (6-20%). Uncertainty due to the production cross section are evaluated by computing the limits with $\pm 1\sigma$ change in cross sections. The effect is ∼15% for direct top squark production, ∼30% for $t\bar{t}$ production in association with two DM particles, and ∼20% for gluino production.

5.3.8. Results and Interpretation

The observed event yield for each signal region compared to background estimates from the simultaneous fit procedure are shown in Tables 5.21 to 5.25. Figure 5.27 shows the distribution of the $E_{\mathrm{T}}^{\mathrm{miss}}$ and $m_{\mathrm{T}}^{b,\mathrm{max}}$ for the combined SRAs and SRBs respectively. In Fig. 5.28, the distribution of $m_{\mathrm{T}}^{b,\mathrm{max}}$ in the most inclusive region of SRC, SRC-low, is shown. R_{ISR} is shown for the combined region of SRD1−4 and SRD5−8 in Fig. 5.29. Finally, Fig. 5.30 shows the $E_{\mathrm{T}}^{\mathrm{miss}}/\sqrt{H_{\mathrm{T}}}$ and H_{T} distributions for SRE and SRF, respectively. The background expectations in these figures are normalized to the values determined from the simultaneous fit.

TABLE 5.21. Expected and observed yields for SRA for $\int \mathscr{L} dt = 13.3\,\mathrm{fb}^{-1}$.

	SRA-TT	SRA-TW	SRA-T0
Observed	8	5	16
Total SM	5.2 ± 1.4	5.7 ± 1.6	11.3 ± 2.6
$t\bar{t}$	$0.78\ ^{+0.84}_{-0.78}$	0.60 ± 0.34	1.13 ± 0.79
W + jets	0.48 ± 0.19	0.54 ± 0.18	1.13 ± 0.31
Z + jets	1.83 ± 0.55	3.0 ± 1.2	6.7 ± 2.1
$t\bar{t}$+W/Z	1.03 ± 0.33	0.84 ± 0.26	1.29 ± 0.57
Single top	$0.45\ ^{+0.53}_{-0.45}$	$0.34\ ^{+0.40}_{-0.34}$	$0.88\ ^{+0.97}_{-0.88}$
Dibosons	0.62 ± 0.44	0.31 ± 0.20	0.18 ± 0.14
Multijets	$0.02\ ^{+0.05}_{-0.02}$	$0.01\ ^{+0.02}_{-0.01}$	$0.02\ ^{+0.05}_{-0.02}$

TABLE 5.22. Expected and observed yields for SRB for $\int \mathscr{L}\, dt = 13.3\,\text{fb}^{-1}$.

	SRB-TT	SRB-TW	SRB-T0
Observed	17	18	84
Total SM	10.6 ± 2.3	16.7 ± 3.6	60 ± 14
$t\bar{t}$	2.5 ± 1.5	4.4 ± 2.6	14.7 ± 4.4
W + jets	1.33 ± 0.35	1.44 ± 0.46	6.2 ± 1.5
Z + jets	2.40 ± 0.70	5.1 ± 1.6	26.0 ± 8.8
$t\bar{t}$+W/Z	2.51 ± 0.64	3.15 ± 0.79	6.0 ± 1.4
Single top	$1.1\ ^{+1.2}_{-1.1}$	$1.7\ ^{+1.9}_{-1.7}$	$6.1\ ^{+6.7}_{-6.1}$
Dibosons	0.70 ± 0.44	$0.87\ ^{+0.96}_{-0.87}$	1.33 ± 0.75
Multijets	$0.06\ ^{+0.13}_{-0.06}$	$0.04\ ^{+0.08}_{-0.04}$	$0.14\ ^{+0.29}_{-0.14}$

TABLE 5.23. Expected and observed yields for SRC, SRE, and SRF for $\int \mathscr{L}\, dt = 13.3\,\text{fb}^{-1}$.

	SRC-low	SRC-med	SRC-high	SRE	SRF
Observed	36	14	9	9	3
Total SM	23.9 ± 7.5	9.4 ± 3.5	10.5 ± 3.7	7.1 ± 1.8	2.8 ± 1.0
$t\bar{t}$	4.4 ± 3.3	1.4 ± 1.3	0.72 ± 0.54	0.92 ± 0.48	0.32 ± 0.29
W + jets	4.4 ± 1.3	1.85 ± 0.69	2.51 ± 0.57	0.56 ± 0.17	0.33 ± 0.12
Z + jets	9.5 ± 3.7	3.5 ± 1.6	4.0 ± 1.4	2.78 ± 0.98	0.92 ± 0.52
$t\bar{t}$+W/Z	0.60 ± 0.21	0.19 ± 0.10	0.32 ± 0.14	1.46 ± 0.55	0.28 ± 0.11
Single top	$4.5\ ^{+4.9}_{-4.5}$	$2.3\ ^{+2.5}_{-2.3}$	$2.7\ ^{+3.1}_{-2.7}$	$0.70\ ^{+0.80}_{-0.70}$	$0.46\ ^{+0.55}_{-0.46}$
Dibosons	$0.44\ ^{+0.66}_{-0.44}$	0.07 ± 0.07	$0.13\ ^{+0.30}_{-0.13}$	0.63 ± 0.48	0.50 ± 0.31
Multijets	$0.09\ ^{+0.19}_{-0.09}$	$0.05\ ^{+0.11}_{-0.05}$	$0.04\ ^{+0.08}_{-0.04}$	$0.01\ ^{+0.02}_{-0.01}$	$0.01\ ^{+0.02}_{-0.01}$

TABLE 5.24. Expected and observed yields for SRD for $\int \mathscr{L}\, dt = 13.3\,\text{fb}^{-1}$.

	SRD1	SRD2	SRD3	SRD4
Observed	4	5	9	9
Total SM	4.3 ± 1.9	7.1 ± 3.2	8.8 ± 3.4	9.4 ± 3.7
$t\bar{t}$	3.9 ± 1.9	6.5 ± 3.3	8.0 ± 3.4	8.5 ± 3.8
W + jets	$0.14\ ^{+0.25}_{-0.14}$	$0.18\ ^{+0.27}_{-0.18}$	$0.24\ ^{+0.31}_{-0.24}$	0.26 ± 0.20
Z + jets	0.04 ± 0.02	0.06 ± 0.03	0.08 ± 0.06	$0.08\ ^{+0.28}_{-0.08}$
$t\bar{t}$+W/Z	0.11 ± 0.08	0.16 ± 0.12	0.20 ± 0.10	0.15 ± 0.13
Single top	$0.09\ ^{+0.14}_{-0.09}$	$0.19\ ^{+0.29}_{-0.19}$	$0.29\ ^{+0.57}_{-0.29}$	$0.42\ ^{+0.54}_{-0.42}$
Dibosons	$--$	$--$	$--$	$--$
Multijets	$0.04\ ^{+0.08}_{-0.04}$	$0.04\ ^{+0.08}_{-0.04}$	$0.03\ ^{+0.06}_{-0.03}$	$0.02\ ^{+0.04}_{-0.02}$

TABLE 5.25. Expected and observed yields for SRD for $\int \mathscr{L} dt = 13.3\,\text{fb}^{-1}$.

	SRD5	SRD6	SRD7	SRD8
Observed	11	6	5	1
Total SM	11.6 ± 3.6	8.6 ± 3.5	5.2 ± 2.1	2.56 ± 0.86
$t\bar{t}$	9.7 ± 3.7	6.8 ± 3.5	4.0 ± 2.0	1.77 ± 0.67
W + jets	0.68 ± 0.40	0.68 ± 0.23	0.37 ± 0.22	0.25 ± 0.18
Z + jets	$0.27\ ^{+0.52}_{-0.27}$	$0.23\ ^{+0.43}_{-0.23}$	0.36 ± 0.13	0.30 ± 0.13
$t\bar{t}$+W/Z	0.26 ± 0.06	0.16 ± 0.11	$0.08\ ^{+0.09}_{-0.08}$	$0.02\ ^{+0.02}_{-0.02}$
Single top	$0.54\ ^{+0.64}_{-0.54}$	$0.48\ ^{+0.56}_{-0.48}$	$0.31\ ^{+0.35}_{-0.31}$	$0.22\ ^{+0.25}_{-0.22}$
Dibosons	0.16 ± 0.13	0.16 ± 0.11	0.16 ± 0.14	$--$
Multijets	$0.03\ ^{+0.06}_{-0.03}$	$0.02\ ^{+0.03}_{-0.02}$	$0.01\ ^{+0.01}_{-0.01}$	$--$

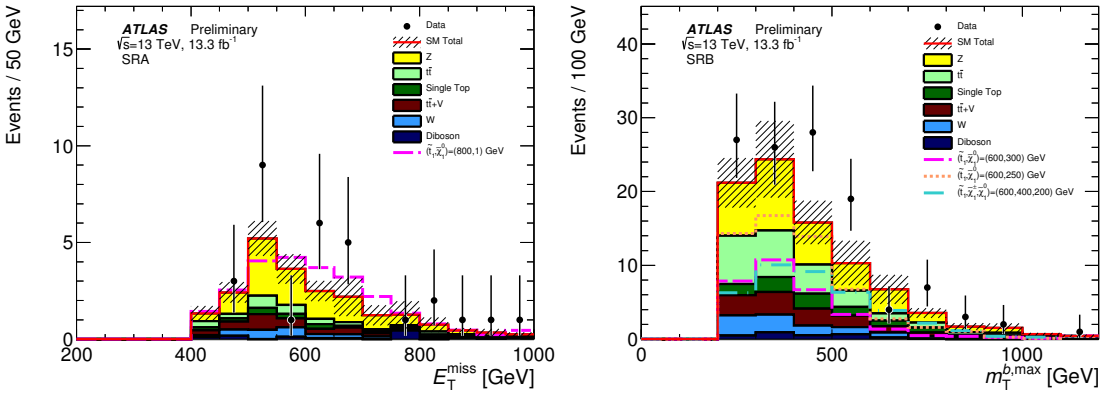

FIGURE 5.27. Distributions of $E_{\text{T}}^{\text{miss}}$ for SRA and $m_{\text{T}}^{b,\text{max}}$ for SRB. The categories have been combined in these distributions. The stacked histograms show the SM expectation and the hatched uncertainty band around the SM expectation shows the MC statistical and detector-related systematic uncertainties.

No significant excess above the SM expectation is observed in any of the signal regions. The model independent limits on the cross section and number of BSM events are evaluated as described in Section 5.1.5 and present in Table 5.26. The discovery p-value are also shown. In the case where the number of observed event is below the background expectation, the p-value is set to 0.50. The smallest p-values are 8%, 10%, and 13% for SRB-TT, SRC-low, and SRB-T0, respectively. The combined p-value of

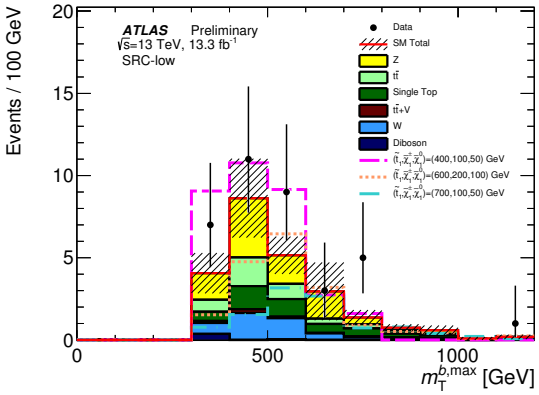

FIGURE 5.28. Distribution of $m_{\mathrm{T}}^{b,\mathrm{max}}$ in SRC-low. The stacked histograms show the SM expectation and the hatched uncertainty band around the SM expectation shows the MC statistical and detector-related systematic uncertainties.

SRAs and SRBs are 0.10, assuming signal shape of $m_{\tilde{t}} = 800$ GeV, $m_{\tilde{\chi}^0} = 1$ GeV and $m_{\tilde{t}} = 600$ GeV, $m_{\tilde{\chi}^0} = 300$ GeV, respectively.

The detector acceptance multiplied by the efficiency ($A \cdot \epsilon$) for signal regions aimed at high energy final states, SRA, SRE, SRF, ranges between 4.1% and 6.5% for their respective signal benchmark points of $m_{\tilde{t}} = 800$ GeV, $m_{\tilde{\chi}^0} = 1$ GeV, $m_{\varphi} = 350$ GeV, $m_{\chi} = 1$ GeV, and $m_{\tilde{g}} = 1400$ GeV, $m_{\tilde{t}} = 400$ GeV, $m_{\tilde{\chi}^0} = 395$ GeV. For SRB and SRC-low, the $A \cdot \epsilon$ is 1.2% and 1.3% for $m_{\tilde{t}} = 600$ GeV, $m_{\tilde{\chi}^0} = 300$ GeV and $m_{\tilde{t}} = 700$ GeV, $m_{\tilde{\chi}_1^\pm} = 100$, $m_{\tilde{\chi}^0} = 50$ GeV, respectively. Finally, combined SRD1-4 and SRD5-8 has an $A \cdot \epsilon$ of 0.12% and 0.22% for $m_{\tilde{t}} = 350$ GeV, $m_{\tilde{\chi}^0} = 177$ GeV and $m_{\tilde{t}} = 450$ GeV, $m_{\tilde{\chi}^0} = 277$ GeV.

Exclusions contours are obtained using the method described in Section 5.1.5. Orthogonal signal subregions are statistically combined (e.g. SRA-TT/TW/T0). In the cases of overlapping signal subregions of SRC and SRD, the smallest 95% CL_s value is picked for each model.

For $\tilde{t}$-$\tilde{\chi}_1^0$ signal grid, the smallest 95% CL_s value from SRA, SRB, and SRD is chosen. The result is shown in Fig. 5.31a. Top squark masses in the range 310–820 GeV for $\tilde{\chi}_1^0$ masses below 160 GeV are excluded at 95% CL, extending Run 1 limits by 100 GeV.

TABLE 5.26. Left to right: 95% CL upper limits on the visible cross section ($\langle\epsilon\sigma\rangle^{95}_{\text{obs}}$) and on the number of signal events (S^{95}_{obs}). The third column (S^{95}_{exp}) shows the 95% CL upper limit on the number of signal events, given the expected number (and $\pm 1\sigma$ excursions on the expectation) of background events. The two columns before last indicate the discovery p-value ($p(s = 0)$) and the the significance for the p-value (σ). The p-value is set to 0.50 when the observed event yield is less than the expected event yield.

Signal channel	$\langle\epsilon\rangle^{95}_{\text{obs}}$[fb]	S^{95}_{obs}	S^{95}_{exp}	$p(s = 0)$	σ
SRA-TT	0.72	9.5	$6.9^{+3.3}_{-2.1}$	0.18	0.92
SRA-TW	0.46	6.1	$6.6^{+3.3}_{-2.0}$	0.50	0.00
SRA-T0	1.05	14.0	$10.1^{+4.4}_{-2.9}$	0.16	0.99
SRB-TT	1.17	15.5	$10.0^{+4.3}_{-2.9}$	0.08	1.41
SRB-TW	0.97	12.9	$12.1^{+4.8}_{-3.5}$	0.41	0.23
SRB-T0	3.91	52.1	$38.2^{+12.9}_{-10.0}$	0.10	1.28
SRC-low	2.19	29.1	$21.9^{+7.4}_{-5.7}$	0.13	1.13
SRC-med	1.10	14.6	$11.3^{+4.5}_{-3.2}$	0.19	0.88
SRC-high	0.66	8.8	$9.6^{+3.8}_{-2.6}$	0.50	0.00
SRD1	0.45	6.0	$6.1^{+3.1}_{-2.0}$	0.50	0.00
SRD2	0.47	6.2	$7.6^{+3.1}_{-2.1}$	0.50	0.00
SRD3	0.69	9.2	$9.0^{+3.7}_{-2.7}$	0.49	0.03
SRD4	0.67	8.9	$9.2^{+3.8}_{-2.7}$	0.50	0.00
SRD5	0.69	9.2	$9.6^{+4.1}_{-2.8}$	0.50	0.00
SRD6	0.50	6.6	$8.1^{+3.6}_{-2.2}$	0.50	0.00
SRD7	0.50	6.6	$6.8^{+3.2}_{-1.9}$	0.49	0.03
SRD8	0.28	3.7	$4.7^{+2.6}_{-1.2}$	0.50	0.00
SRE	0.72	9.5	$7.9^{+3.6}_{-2.3}$	0.29	0.55
SRF	0.42	5.6	$5.4^{+2.6}_{-1.6}$	0.47	0.08

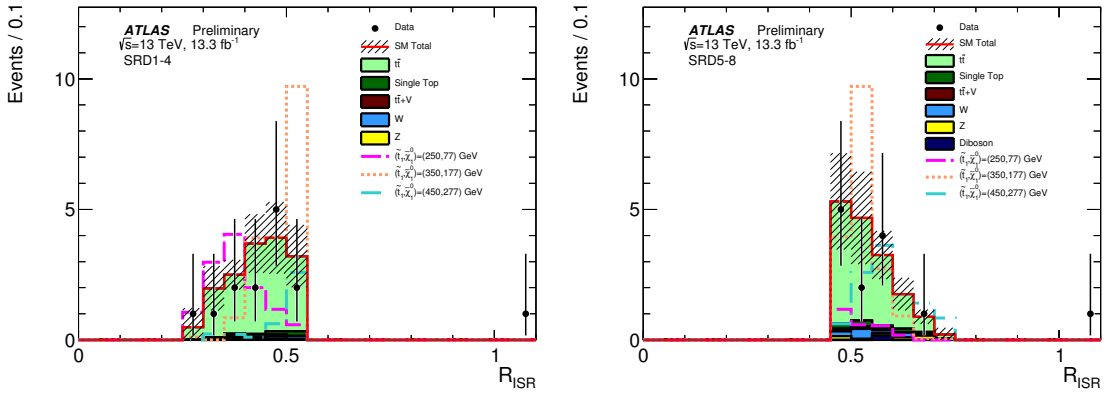

FIGURE 5.29. Distributions of R_{ISR} for SRD1-SRD4 and SRD5-SRD8. The stacked histograms show the SM expectation and the hatched uncertainty band around the SM expectation shows the MC statistical and detector-related systematic uncertainties.

Additional constraints are set in the case when $m_{\tilde{t}} \sim m_t + m_{\tilde{\chi}^0}$, where the $m_{\tilde{t}}$ between 23–380 GeV are excluded.

The smallest 95% CL_s value from SRB and SRC is chosen when setting limits for signal models in the b-$\tilde{\chi}_1^{\pm}$ grid, and the result is shown in Fig. 5.31b. SRC is more sensitive for very light $\tilde{\chi}_1^0$ while SRB is more sensitive along the "diagonal" where $m_{\tilde{t}} = m_b + m_{\tilde{\chi}_1^{\pm}}$. The observed limits are restricted to the $\tilde{\chi}_1^{\pm} < 150$ GeV while the expected limits extend to higher values due to the mild excess in SRB.

The results for SRE are interpreted in terms of simplified models of top quarks produced in association with DM particles as a function of the DM and mediator masses. The exclusion limits contour for the nominal coupling $g = 3.5$ on the m_χ vs. m_φ and on the m_χ vs. m_a plane are shown in Fig. 5.32. Additionally, upper limits on the coupling are indicated by the numbers on the figure. For both the scalar (φ) and pseudoscalar (a) interpretation the strongest limits on g are in region where both the mass of DM particle and mediator are small.

The SRF results are interpreted for indirect top squark production through gluino decays in terms of the $\tilde{\chi}_1^0$ vs. $\tilde{g}$ mass plane with $\Delta m(\tilde{t}, \tilde{\chi}_1^0) = 5$GeV. All grid points shown

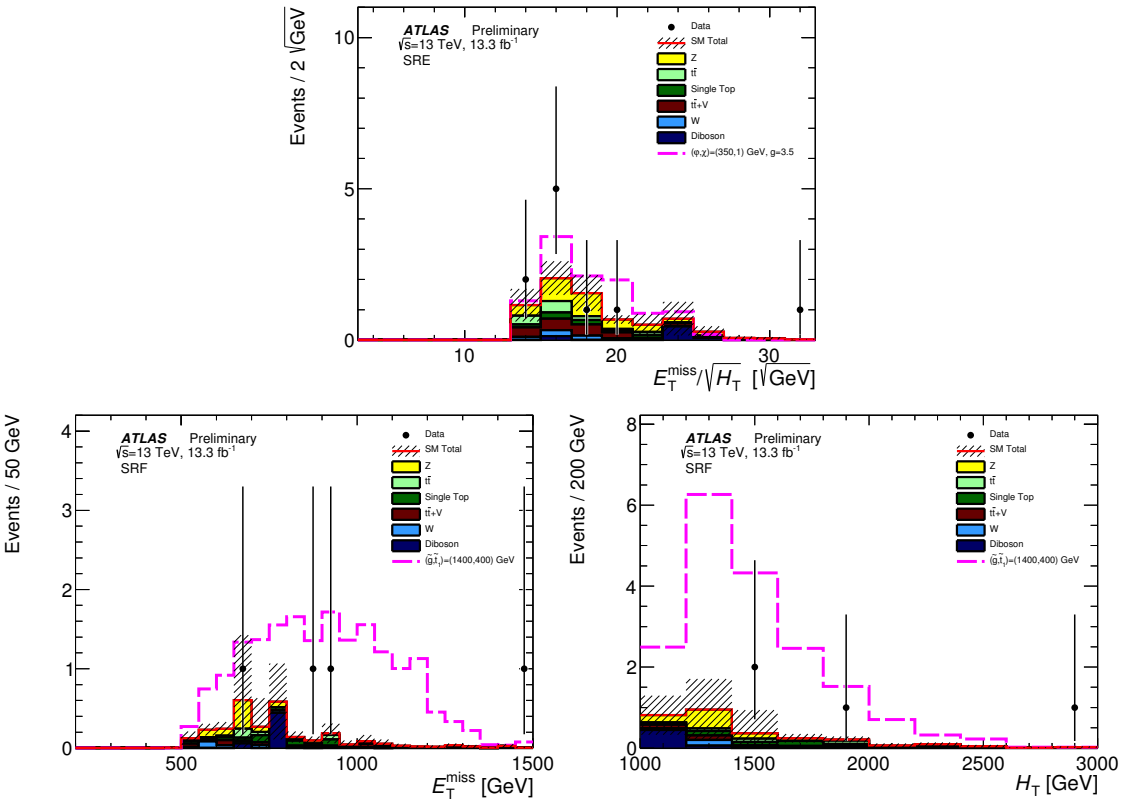

FIGURE 5.30. Distributions of $E_{\mathrm{T}}^{\mathrm{miss}}/\sqrt{H_{\mathrm{T}}}$ for SRE, and $E_{\mathrm{T}}^{\mathrm{miss}}$ and H_{T} for SRF. The stacked histograms show the SM expectation and the hatched uncertainty band around the SM expectation shows the MC statistical and detector-related systematic uncertainties.

in Fig. 5.33 with $m_{\tilde{g}}$ up to 1600 GeV with $m_{\tilde{\chi}^0} < 560$GeV are excluded. The upper limits on the gluino pair production cross section are set and shown in Fig. 5.33.

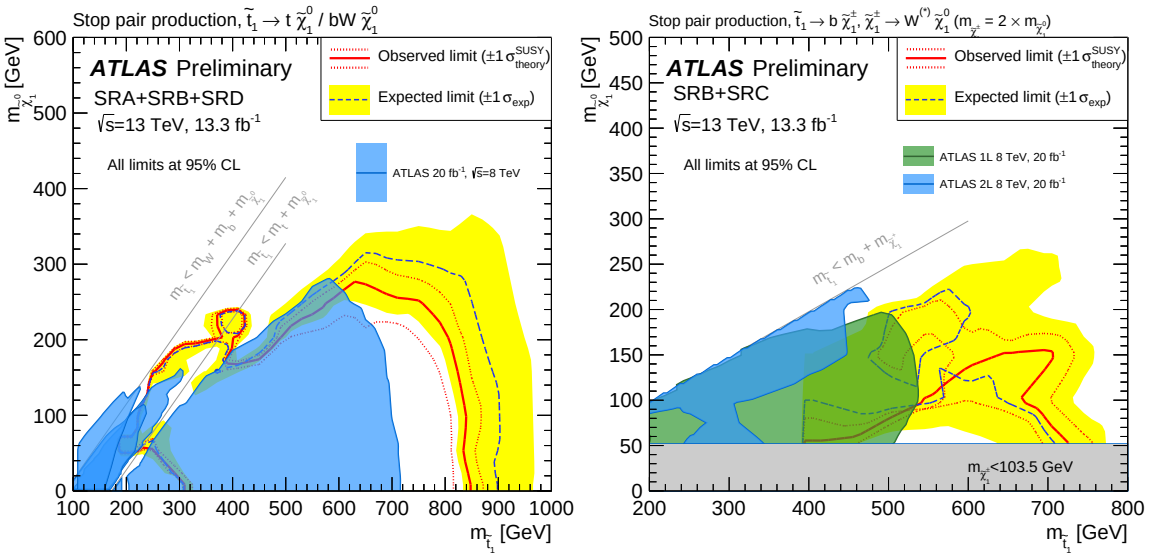

(a) $\tilde{t} \to t\tilde{\chi}_1^0$

(b) $\tilde{t} \to b\tilde{\chi}_1^\pm$, $\tilde{\chi}_1^\pm \to W^{(*)}\tilde{\chi}_1^0$ and the $W^{(*)}$ decays hadronically

FIGURE 5.31. Expected (blue dashed line) and observed (red solid line) exclusion limits at 95% CL as a function of $\tilde{t}$ and $\tilde{\chi}_1^0$ masses in the scenario where both top squarks decay via the channel labeled. Uncertainty bands corresponding to the $\pm1\sigma$ variation on the expected limit (yellow band) and the sensitivity of the observed limit to $\pm1\sigma$ variations of the signal theoretical uncertainties (red dotted lines) are also indicated. Observed limits from the Run 1 search [101–104] are overlaid for comparison.

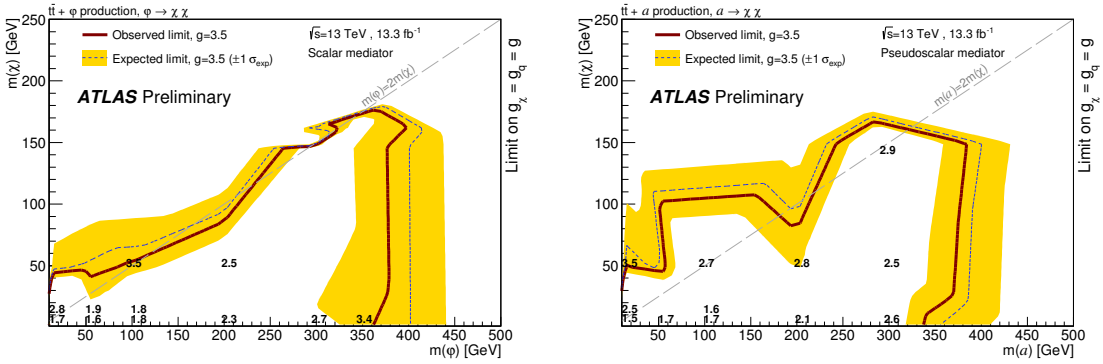

FIGURE 5.32. Expected (blue dashed line) and observed (red solid line) $g = 3.5$ exclusion limits at 95% CL as a function of φ and χ masses (left) and a and χ masses (right) in the DM+$t\bar{t}$ scenario. Uncertainty bands corresponding to the $\pm1\sigma$ variation on the expected limit (yellow band) and the sensitivity of the observed limit to $\pm1\sigma$ variations of the signal theoretical uncertainties (red dotted lines) are also indicated. The numbers on the plots indicate the limits on the coupling. Couplings above the perturbativity limit ($g = 3.5$) are not considered.

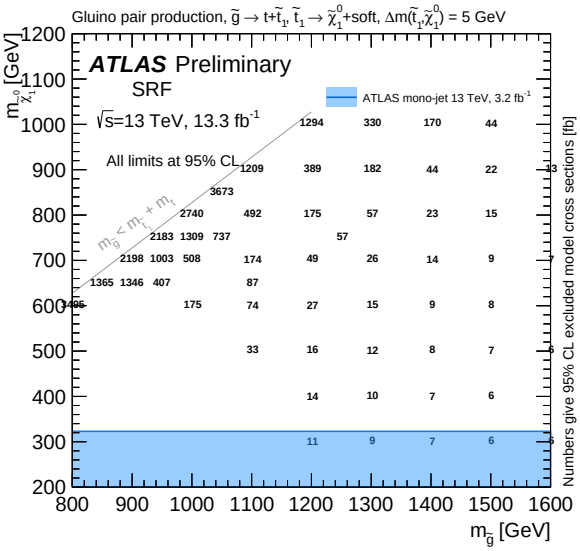

FIGURE 5.33. Cross section limits at 95% CL exclusion as a function of $\tilde{g}$ and $\tilde{\chi}_1^0$ masses in the scenario where both gluinos decay via $\tilde{g} \to t\tilde{t}\tilde{\chi}_1^0 \to t\tilde{\chi}_1^0$+soft and $\Delta m(\tilde{t}, \tilde{\chi}_1^0) = 5$GeV.

5.4. pMSSM Search

The analysis strategy from the Run 1 search (Section 5.2) has been used to reinterpret the result in the context of pMSSM [2]. The full machinery of the dedicated analysis has been employed in order to cover the widest range of the pMSSM parameter space.

The selection of model points follow the original procedure present in Ref. [28], but with several important changes including new experimental constrains and better simulation tools. The exact assumptions about the MSSM used in this search are [2]:

1. R-parity is exactly conserved.
2. The soft parameters are real, so that no new sources of CP violation exist beyond that present in the CKM matrix.
3. Minimal Flavour Violation is imposed at the electroweak scale.
4. The first two generations of squarks and sleptons with the same quantum numbers are mass degenerate, and their Yukawa couplings are too small to affect sparticle production or precision observables.
5. The LSP is the lightest neutralino.

5.4.1. Model Point Generation

The assumptions listed above reduced the MSSM down to 19 parameters. It is still too big to exhaustively scan using a grid sampling. Instead, each parameter is sampled using a flat probability distribution. The upper and lower values for each parameters are listed in Table 5.27. The upper limit on most of the sparticle masses are chosen at 4 TeV to make them accessible at the LHC.

TABLE 5.27. Scan ranges used for each of the 19 pMSSM parameters. Where the parameter is written with a modulus sign both the positive and negative values are permitted. In the above, "gen(s)" refers to generation(s).

Parameter	Min value	Max value	Note
$m_{\tilde{L}_1}(= m_{\tilde{L}_2})$	90 GeV	4 TeV	Left-handed slepton (first two gens.) mass
$m_{\tilde{e}_1}(= m_{\tilde{e}_2})$	90 GeV	4 TeV	Right-handed slepton (first two gens.) mass
$m_{\tilde{L}_3}$	90 GeV	4 TeV	Left-handed stau doublet mass
$m_{\tilde{e}_3}$	90 GeV	4 TeV	Right-handed stau mass
$m_{\tilde{Q}_1}(= m_{\tilde{Q}_2})$	200 GeV	4 TeV	Left-handed squark (first two gens.) mass
$m_{\tilde{u}_1}(= m_{\tilde{u}_2})$	200 GeV	4 TeV	Right-handed up-type squark (first two gens.) mass
$m_{\tilde{d}_1}(= m_{\tilde{d}_2})$	200 GeV	4 TeV	Right-handed down-type squark (first two gens.) mass
$m_{\tilde{Q}_3}$	100 GeV	4 TeV	Left-handed squark (third gen.) mass
$m_{\tilde{u}_3}$	100 GeV	4 TeV	Right-handed top squark mass
$m_{\tilde{d}_3}$	100 GeV	4 TeV	Right-handed bottom squark mass
$\lvert M_1\rvert$	0 GeV	4 TeV	Bino mass parameter
$\lvert M_2\rvert$	70 GeV	4 TeV	Wino mass parameter
$\lvert\mu\rvert$	80 GeV	4 TeV	Bilinear Higgs mass parameter
M_3	200 GeV	4 TeV	Gluino mass parameter
$\lvert A_t\rvert$	0 GeV	8 TeV	Trilinear top coupling
$\lvert A_b\rvert$	0 GeV	4 TeV	Trilinear bottom coupling
$\lvert A_\tau\rvert$	0 GeV	4 TeV	Trilinear τ lepton coupling
M_A	100 GeV	4 TeV	Pseudoscalar Higgs boson mass
$\tan\beta$	1	60	Ratio of the Higgs vacuum expectation values

5.4.2. Model Point Selection

Selected model points are required to be consistent with EWSB, have a scalar potential that do not break color or electric charge, have positive mass-squared values for all particles, and must not contain theoretical pathologies. Then, experimental constrains shown in Table 5.28 are applied.

Generally, models with bino-like LSP tend to overproduce dark matter, so after applying the constrains in Table 5.28, such models are under-sampled. However, bino-like models are the ones that can produce the correct dark matter relic density with the LSP light enough to be produce at $\sqrt{s} = 8$ TeV, and they contain unique phenomenology. To compensate for this, the bino-like models are oversampled compared to the wino- and

TABLE 5.28. Constraints on acceptable pMSSM points from considerations of precision electroweak and flavor results, dark matter relic density, and other collider measurements. A long dash (—) indicates that no requirement is made. Further details may be found in Ref. [2].

Parameter	**Minimum value**	**Maximum value**
$\Delta\rho$	-0.0005	0.0017
$\Delta(g-2)_\mu$	-17.7×10^{-10}	43.8×10^{-10}
BR($b\to s\gamma$)	2.69×10^{-4}	3.87×10^{-4}
BR($B_s\to\mu^+\mu^-$)	1.6×10^{-9}	4.2×10^{-9}
BR($B^+\to\tau^+\nu_\tau$)	66×10^{-6}	161×10^{-6}
$\Omega_{\tilde{\chi}_1^0}h^2$	—	0.1208
$\Gamma_{\text{invisible(SUSY)}}(Z)$	—	2 MeV
Masses of charged sparticles	100 GeV	—
$m(\tilde{\chi}_1^\pm)$	103 GeV	—
$m(\tilde{u}_{1,2},\ \tilde{d}_{1,2},\ \tilde{c}_{1,2},\ \tilde{s}_{1,2})$	200 GeV	—
$m(h)$	124 GeV	128 GeV

Higgsino-like models, then an "importance" weight is applied to correct for this fact. These are summarized in Table 5.29.

5.4.3. Signal Simulation and Search Evaluation

The 310,327 model points sampled and passed all constrains are evaluated in three steps:

Cross section The production cross sections for sparticles are calculated. The processes are categorized into strong, electroweak (subdivided into gauginos and sleptons), and mixed productions. The models are then required to have at least one production process with large enough cross section to be observed at the LHC.

Particle level selection Model points passing the cross section requirement are then generated and selections from analyses are applied at the truth particle level. Inefficiency due to the detector-level reconstruction are estimated from signal

TABLE 5.29. Categorization of the 310,327 model points by the type of the LSP (assumed to be the $\tilde{\chi}_1^0$) according to the neutralino mixing matrix parameters N_{ij}, where the first index indicates the neutralino mass eigenstate and the second indicates its nature in the lexicographical order ($\tilde{B}, \tilde{W}, \tilde{H}_1, \tilde{H}_2$). For example, $N_{1,2}$ is the amplitude for the LSP to be $\tilde{W}$. The final two columns indicate the fraction of model points in that category that are sampled, and their weighted fraction after importance sampling.

LSP type	**Definition**	**Sampled**	**Simulated**		**Weight**
			Number	**Fraction**	
'Bino-like'	$N_{11}^2 > \max(N_{12}^2,\ N_{13}^2 + N_{14}^2)$	480×10^6	103,410	35%	1/24
'Wino-like'	$N_{12}^2 > \max(N_{11}^2,\ N_{13}^2 + N_{14}^2)$	20×10^6	80,233	26%	1
'Higgsino-like'	$(N_{13}^2 + N_{14}^2) > \max(N_{11}^2,\ N_{12}^2)$		126,684	39%	1
Total		500×10^6	310,327		

efficiency for each signal region from the original analysis. The event yield, N_{sig}, is compared to the model independent limit, N_{max}^{95}, reported for the SR in the search. Model points are categorized into three group:

1. $N_{sig} \gg N_{\text{max}}^{95}$: These model are excluded.
2. $N_{sig} \ll N_{\text{max}}^{95}$: These model are not excluded.
3. $N_{sig} \cong N_{\text{max}}^{95}$: These model will need detector simulation.

The exact criteria for the first two categories is determined separately for each SR based on how accurate the particle level simulation reproduces the result that includes the detector simulation and full reconstruction. 5% of the models in the first category receive the full treatment described in the next step to validate the result.

Full reconstruction selection 44,559 models in the last category from the previous step are simulated at the detector level using Atlfast-II and full event reconstruction is performed. These model points are evaluated with 95% CL_s value using the same calculation[5] as the original analysis. Note that no combination of analyses is attempted.

[5] Using HistFitter framework.

5.4.4. Constraint on the Third Generation Squarks

The fractions of pMSSM models excluded in $m_{\tilde{t}}$–$m_{\tilde{\chi}_1^0}$ plane using all ATLAS SUSY searches considered in Ref. [2] are shown in Fig. 5.34a. There are relatively few model points with low $m_{\tilde{t}}$ due to the requirement to get the Higgs mass at 125 GeV (See Section 2.4.2), but they are well covered; most points with $m_{\tilde{t}} < 600$ GeV are excluded. It is useful to compare the pMSSM result with the interpretation using simplified model, superimposed as a white solid line. While a general agreement can be seen, they are expected to be different; the pMSSM models can have much more complicated production channels and decay chains. The exclusions are weaker at the heavier stop mass. This is due to the assumption $\mathrm{BR}(\tilde{t} \to t\tilde{\chi}_1^0) = 100\%$ from the simplified models. On the other hand, the pMSSM model points along the "diagonal" outside the simplified model exclusion region are well-cover by monojet searches. Figure 5.34b shows a similar plot to Fig. 5.34a, but use the result from third generation searches only. A noticeable different from all-searches result is the absent of the extended sensitivity for $m_{\tilde{\chi}_1^0} < 250$ GeV, which largely comes from the disappearing track analysis[6].

5.4.5. Robustness of Discrimination Variables

The fully simulated pMSSM model points can be used to study the robustness of discrimination variables used to define signal regions. Figure 5.35 show the distribution of the signal efficiency for each discrimination variable:

2bjet Require two or more b-tagged jet with MV1 tagger at 70% working point.

Met300 $E_{\mathrm{T}}^{\mathrm{miss}} > 300$ GeV.

MtBMin175 $m_{\mathrm{T}}^{b,\mathrm{min}} > 175$ GeV.

[6] This search is motivated by the scenario where the charged wino is slightly (~ 160 MeV) heavier than the LSP. In this case, the $\tilde{\chi}_1^{\pm}$ can travel a few tens of centimeters before decay into a LSP and an invisible low p_{T} charged pion. This create a distinct signature where a high p_{T} track from $\tilde{\chi}_1^{\pm}$ disappeared inside the detector.

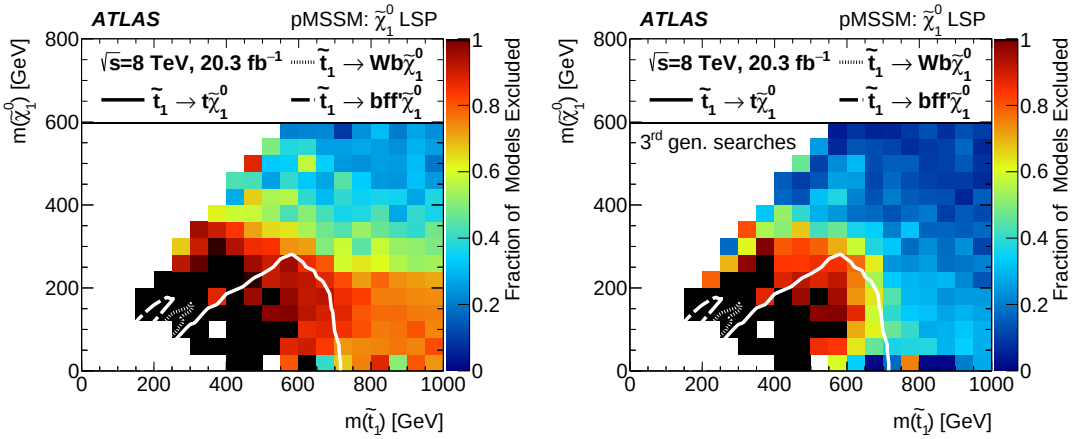

(a) All pMSSM points, all searches (b) All pMSSM points, 3rd gen. searches

FIGURE 5.34. Taken from [2]. Fraction of pMSSM points excluded in the $\tilde{t}_1$–$\tilde{\chi}_1^0$ plane. The color scale indicates the fraction of pMSSM points excluded in each mass bin, with black squares indicating 100% of model points being excluded. The white regions indicate places where no model points were sampled which satisfied the constraints of Table 5.28. The impact of all searches on the left and only the third-generation searches on the right. There are relatively few pMSSM points at low $\tilde{t}_1$ mass for the reasons described in the text. The simplified-model limit overlaid is set assuming directly produced top squark pairs, with each decaying to a top quark and neutralino, $\tilde{t}_1 \to t\tilde{\chi}_1^0$.

MtBMax290 $m_{\mathrm{T}}^{b,\mathrm{max}} < 290$ GeV.

Top0M120 $m_{AkT12}^{1} > 120$ GeV.

dRMin0M250 First ΔR_{min} top candidate mass < 250 GeV without b-tagging information.

dRMinB0M250 First ΔR_{min} top candidate mass < 250 GeV with b-tagging information.

W0M50 $m_{AkT8}^{0} > 50$ GeV.

LowAsym $\mathcal{A}_{m_t} < 0.5$.

TauCand No τ-lepton candidate.

FakeMet Selections to suppress fake $E_{\mathrm{T}}^{\mathrm{miss}}$ due to jet mismodeling described in Section 5.2.

dRBBJet ΔR between the vector sum of the two highest MV1 weight and its closest jet.

A model point represent an entry in each column in Fig. 5.35. The frequencies are represent using the color scale. The y-value (CutEfficiency_Norm) is obtained by first compute the signal efficiency for the selection from the model point, then normalized it

by the same efficiency from the benchmark point, $(m_{\tilde{t}}, m_{\tilde{\chi}^0}) = (700, 1)$ GeV. The signal efficiency is defined as the number of events passing the selection divided by the number of events after the common selections described in Section 5.2.

In general, the selections that make used of b-tagging information tends to be less robust for pMSSM model points. Also, comparing to Fig. 5.35a, Fig. 5.35b shows that the variables are relatively more stable among the wino- and Higgsino-like LSP model when compared to bino-like LSP models. The result can be useful for defining a dedicated signal region for pMSSM model interpretation in the future.

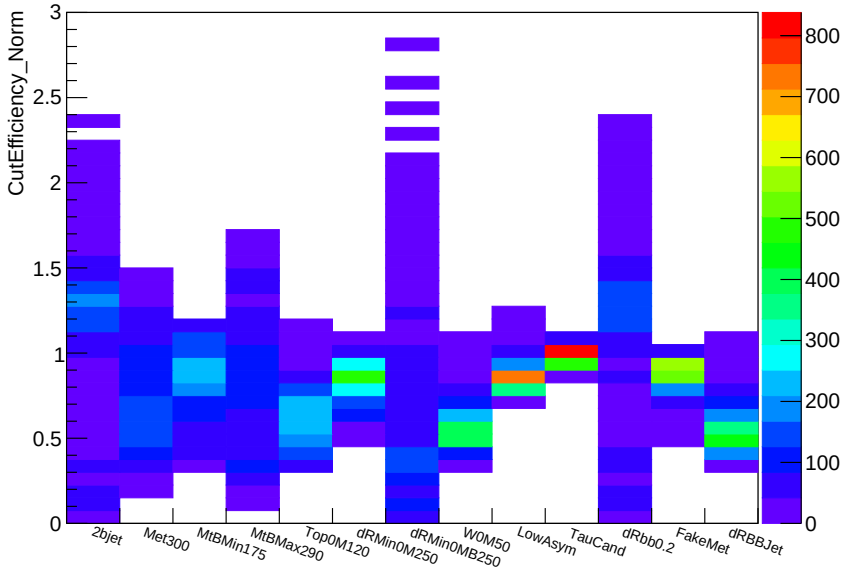

(a) Bino-like LSP models

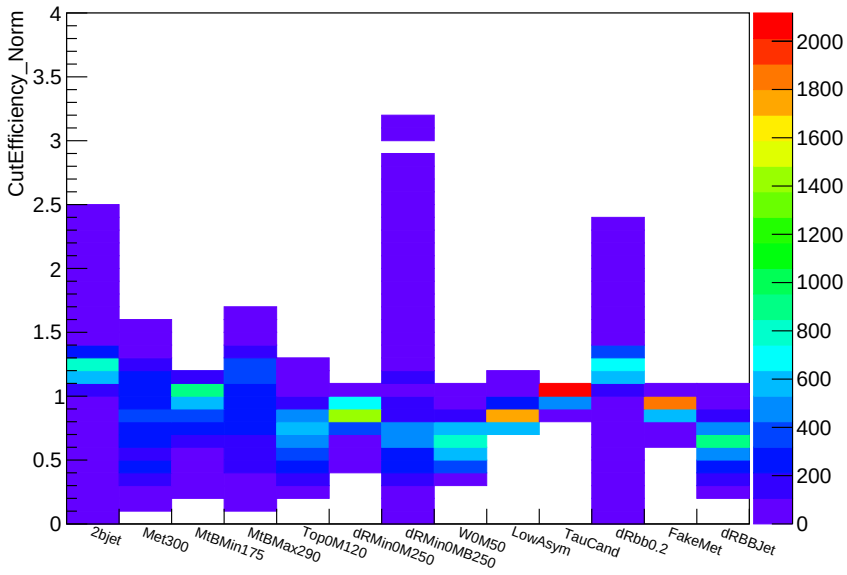

(b) Wino- or Higgsino-like LSP models

FIGURE 5.35. Selection efficiency for various discrimination variables used in the all hadronic final state search for stop. Each column represent a selection and described in the text. The Y-axis are the signal efficiency for a pMSSM model point divided by signal efficiency of the benchmark point, $(m_{\tilde{t}}, m_{\tilde{\chi}^0}) = (700, 1)$ GeV. The signal efficiency is defined as the number of events passing the selection divided by the number of events after the common selections described in Section 5.2. The color scale indicates the number of model points.

CHAPTER VI

CONCLUSIONS AND OUTLOOK

Searches for scalar top partners in jets+$E_{\mathrm{T}}^{\mathrm{miss}}$ final state using Run 1 and Run 2 are presented. The result has been interpreted using simplified SUSY model with stop pair production and various decay channels, where stop with mass up to 820 GeV assuming BR($\tilde{t} \to t\tilde{\chi}_1^0$) = 100% has been excluded at 95% CL. Interpretations using simplified model with top quark produced in association with dark matter particle and indirect production of stop from gluinos decay, which have similar signatures, are also included. Additionally, Run 1 analysis strategy has been used to interpret the result in context of 19-pMSSM-parameters space, which represent a broader range of SUSY scenarios.

The LHC has been operating very well and even exceeding the initial expectation during 2016 operation. The increasing amount of data will surely keep pushing limits for the stop mass. Figure 6.1 shows the expected sensitivity, represented as significance Z (See Appendix A.3.1.1), for $(m_{\tilde{t}}, m_{\tilde{\chi}^0}) = (1000, 1)$ GeV and 100% $\tilde{t} \to t\tilde{\chi}_1^0$ BR in each categories of SRA. Exclusion may even be possible at $\sim$ 25 fb^{-1} of data, which has already been collected as of this writing [105].

However, the increasing amount of data will be offset by the more background, as well as quickly the smaller cross section for the heavier stop. Therefore, it is very important to keep improving the analysis. Categorizations using top mass have been utilized both in Run 1 and Run 2 search, and proved to be useful for maximizing the sensitivity. Any improvement for this idea can be very crucial for the analysis. One possibility is categorization with another quantity such as number of b-jets, which are already implemented in Run 2's SRDs. Additionally, a more sophisticated reconstruction technique such as reclustering using variable-R jet [107], identifying top jets with jet

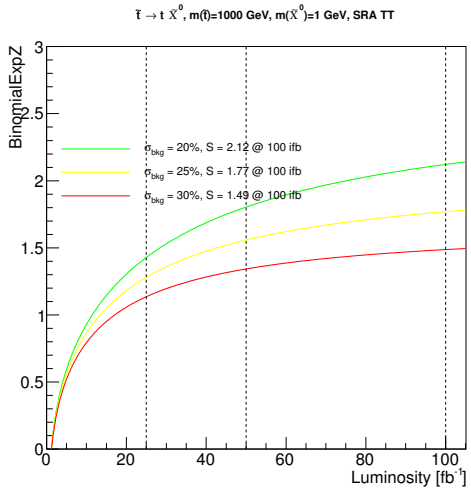

(a) SRA-TT

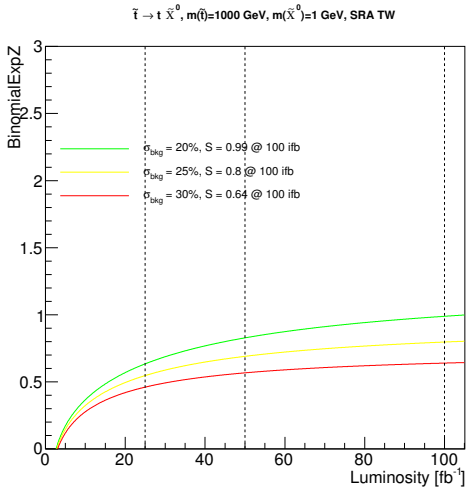

(b) SRA-TW

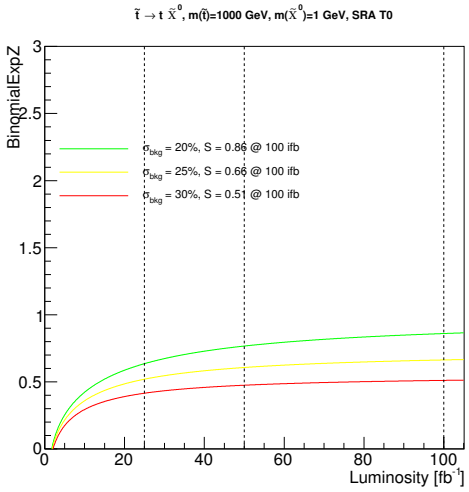

(c) SRA-T0

FIGURE 6.1. Signal significant as a function of integrated luminosity for simplified model with $(m_{\tilde{t}}, m_{\tilde{\chi}^0}) = (1000, 1)$ GeV and 100% $\tilde{t} \to t\tilde{\chi}_1^0$ BR for SRA subregions [106]. The color lines represent different levels of background estimate uncertainty.

substructure, or using multivariate techniques such as BDT or neural network to combine discrimination variables will most likely play an important role in the future analysis.

The exclusion limits using simplified model in $(m_{\tilde{t}}, m_{\tilde{\chi}^0})$ plane using ATLAS third generation searches, including the one described in this dissertation, are shown in Fig. 6.2. It is interesting to note that the observed limits from the similar search but with one lepton in the final state [108] (semileptonic decay of the tops) are smaller than the expected

limit, similar to the result present in Section 5.3.8. The reason is that mild excesses are also observed in that channel. These excess from both searches are still too small to be significant, but it will be important to keep a closed watch on them as more data are collected.

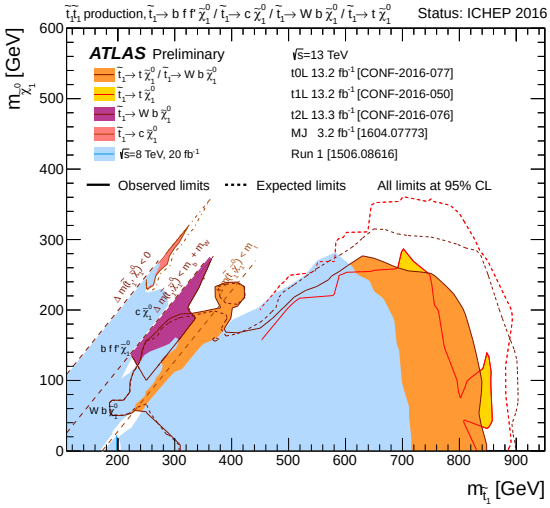

FIGURE 6.2. Summary of the dedicated ATLAS searches for top squark (stop) pair production based on 13 fb^{-1} of pp collision data taken at $\sqrt{s} = 13$ TeV [109]. Exclusion limits at 95% CL are shown in the $\tilde{t}$–$\tilde{\chi}_1^0$ mass plane. The dashed and solid lines show the expected and observed limits, respectively, including all uncertainties except the theoretical signal cross section uncertainty (PDF and scale). Four decay modes are considered separately with 100% BR: $\tilde{t}_1 \to \tilde{\chi}_1^0$ (where the $\tilde{t}_1$ is mostly $\tilde{t}_R$), $\tilde{t} \to W + b + \tilde{\chi}_1^0$ (3-body decay for $m_{\tilde{t}} < m_t + m_{\tilde{\chi}^0}$), $\tilde{t} \to c + \tilde{\chi}_1^0$ and $\tilde{t} \to f + f' + b + \tilde{\chi}_1^0$ (4-body decay). The latter two decay modes are superimposed.

The ongoing lack of any significant deviation from the SM from the LHC experiments and the corresponding higher limit on the stop mass does make one question about the "naturalness" of SUSY itself. However, we need to remind ourselves that the limits are generally derived from a very simplified picture of SUSY. While the scan of pMSSM parameters indicate that generally the results derived from these simplified models are good indicators, they are by no mean equivalent. It is also re-highlight the fact that the LHC limits for superpartners that do not strongly interact can be much weaker, as shown in Fig. 6.3.

This is expected from the nature of being a hadron collider, so hopefully there will be a future e^+e^- collider to fill this gap.

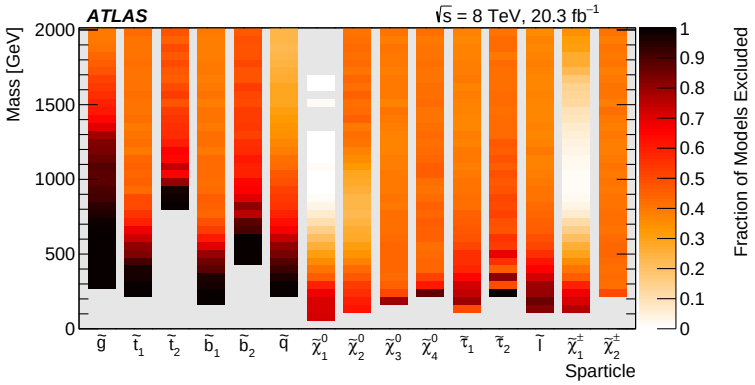

FIGURE 6.3. Taken from [2]. Each vertical bar is a 1D projection of the fraction of model points excluded, with color coding representing the fraction of model points excluded for each sparticle.

Finally, one need to remember that most of SUSY signatures are generic to any new physics. Put it in another way, from an experimental point of view, SUSY can simply be thought of as a benchmark to optimized the search for new physics. For this reason, most of the other solutions to the Higgs mass hierarchy problem are similarly constrained, and in fact some of them are even ruled out [16]. Therefore, if the hierarchy problem does have a solution at the TeV scale, SUSY is still very much a front runner.

Let us be optimistic and keep looking. If a superpartner is found, it will surely open a new era of fundamental physics. If not, it can be an indication that we made a big mistake somewhere. One way or another, it will surely bring us a step closer to unveil another mystery of the universe.

APPENDIX A

STATISTICAL METHODS

Statistic methods connect theories with experiments; it gives prescriptions on how to interpret the data. Are the data compatible with this particular model? How confident we are on that statement? Etc. In this chapter, I will give a quick review on some of the statistical methods used in this analysis [1].

A.1. Preamble

Outcomes of an experiment can be written as a vector of observed values from many trials, $\vec{x} = (x_1, x_2, \ldots, x_n)$. The probability to an outcome of a measurement to be x given the hypothesis H is called probability density (mass) function (PDF)[2] for continuous (discrete) variable x, written as $P(x|H)$. If we regard $P(x|H)$ as a function of H for a given data, then it is called likelihood, usually written as $L(H)$. In the cases where H can be characterized by one or more parameters θ ("class of models"), one can write $L(\theta) = P(x|\theta)$ for a given outcome x. Note that PDF is normalized:

$$\int_{-\infty}^{+\infty} P(x)dx = 1 \tag{A.1}$$

but the likelihood does not:

$$\int_{-\infty}^{+\infty} L(\theta)d\theta \neq 1 \tag{A.2}$$

[1] Based on [13, 110, 111].

[2] Not to be confused with parton distribution function. PDF will only refers to probability density function in this chapter.

A.2. Maximum Likelihood Fit

A function of data that which outputs the values of the parameters is called an *estimator*, written as $\hat{\theta}(\vec{x})$. One of the most used estimators is that which maximizes the likelihood:

$$\hat{\theta}(\vec{x};\theta) = \max_{\theta} L(\theta) \tag{A.3}$$

This choice of estimator is called the *maximum likelihood method*. The maximum likelihood fit will give the parameters of the model best fitted to the data, but it does not provide information as to how well the fit is. Instead, the goodness-of-fit can be quantify using other methods such as the χ^2.

In the case of model with many parameters, the *parameters of interest* are usually only a subset of them; The rest are called *nuisance parameters*. Another way to think of the nuisance parameters is as systematic uncertainties. It "enlarges" the model class by adding more parameters to make sure the "true value" is covered. For example, if there is an excess in this analysis, it is important to know which stop mass is the most compatible with the data so it is a parameter of interest, while the exact value for the JES are not important so they are nuisance parameters.

When the nuisance parameters are used in the fit, we can keep the same form for Eq. (A.3) but replacing $L(\theta)$ with using *profile likelihood*:

$$L_p(\theta) = L(\theta, \hat{\hat{\nu}}) \tag{A.4}$$

where υ is the nuisance parameters. The double-hat notation indicates the *profiled* value of ν which maximized the likelihood for a given θ.

A.3. Statistic Tests

Consider a background-only hypothesis H_0, a statistic test for H_0 can be defined by first picking a subspace of data called *critical region (w)* such that, given H_0, the probability for the observed value to be in w is less than a chosen (small) α. In other words,

$$P(x \in w | H_0) \leq \alpha \tag{A.5}$$

In general there can be an infinite number of w's that satisfy Eq. (A.5). To pick a critical region, an alternative (signal, usually BSM) hypothesis H_1 has to be taken into account. Usually, the critical region is chosen by specifying the maximum probability of rejecting H_0 when it is true. This is the *false positive*, α, or the "size" of the test. At the same time, the probability of rejecting H_1 when it is true is minimized. This is the *false negative*, or β. The *power* of the test is defined as $1-\beta$, i.e. the bigger it is, the less probability for rejecting a signal model when it is actually true. I would like to remind the reader here that the nature of statistic tests are to *reject* a hypothesis. To accept a BSM model (H_1), one need to show that the data is incompatible with the SM model (H_0). On the other hand, if one wants to exclude a BSM model, it has to be shown that the data is in a better agreement with the SM model.

A.3.1. Test Statistic

In a simple event counting experiment, the data space are the number of events, n. Ignoring the cases where there can be quantum interference which have to be treated differently, possible values of n are $[0, +\infty)$, with the null (background) hypothesis H_0 predicts expectation value, $\mathrm{E}[n] = b$ events and signal hypothesis H_1 predicts $\mu s + b$ events, where μ is the signal strength (for H_0, $\mu = 0$). In this case, the *test statistic* can simply be the counted number of events for each measurement. The critical region can be defined by

choosing to place a cut x_{cut} on the number of events corresponding to the chosen α. In this case, the power of the test $(1-\beta)$ is automatically maximized. Figure A.1 illustrate this.

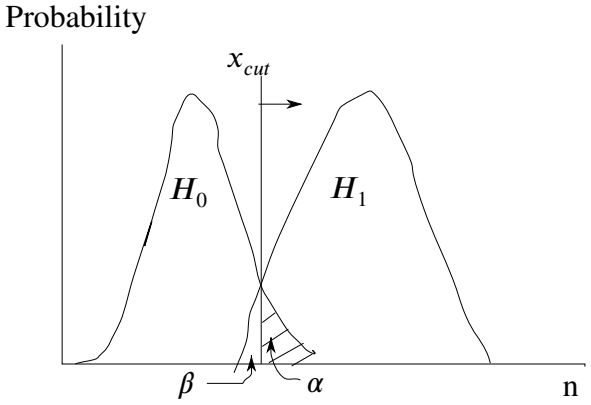

FIGURE A.1. Graphic representation of a statistic test in a simple event counting experiment.

However, if there is more than one parameters, choosing the test statistic and critical region can be complicated. The Neyman-Pearson lemma indicates that the best test statistic to maximize $1-\beta$ given α is the likelihood ratio:

$$q(\vec{x}) = \frac{f(\vec{x}|H_1)}{f(\vec{x}|H_0)} \tag{A.6}$$

where f is the PDF. Note that the closed form of f is not typically known, hence we usually derive its approximate behavior from Monte Carlo simulations. In which case the number of events needed to be generated grow exponentially with the number of the parameters. This is where multivariate techniques such as neural network or boosted decision tree can help map them to a single variable.

A.3.1.1. *p*-value and the Confidence Level

One can quantify the compatibility of the observed data x_{obs} with the null hypothesis H_0 without referring to the alternative H_1 using the *p-value* for H_0, defined as the probability to observe data with equal or lesser compatibility with H_0 than the observed

x_{obs}. For a test statistic such as the one in Eq. (A.6), where the bigger number associated with less compatible with the test hypothesis H_0, the p-value is:

$$p = \int_{q_{\text{obs}}}^{\infty} f(q|H_0)dq \tag{A.7}$$

The p-value can be converted into the *significance* Z, defined as the number of upward standard deviation of a Gaussian random variable such that the upper tail area equal to p:

$$Z = \Phi^{-1}(1-p) \tag{A.8}$$

where Φ is the cumulative distribution of the standard Gaussian, and the Φ^{-1} is the inverse (quantile) function. In the high energy physics, a discovery claim traditionally requires a 5σ effect, which correspond to p-value of 2.87×10^{-7}. A graphic representation of p-value and Z is shown in Fig. A.2.

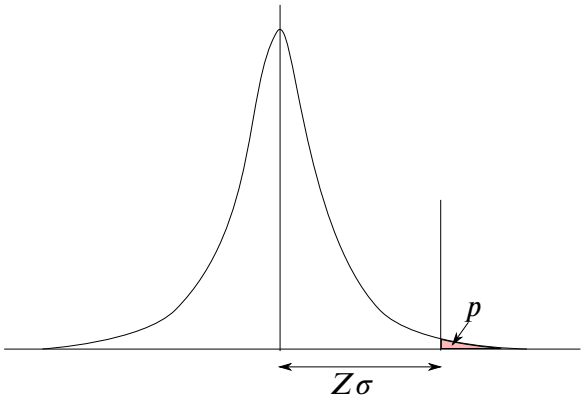

FIGURE A.2. Graphic representation of the p-value and the significance Z

Suppose we perform a test of size α for all possible value of μ. A value of μ is rejected if,

$$p_\mu = \int_{q_{obs}}^{\infty} f(q_{\mu,\text{obs}}|\mu)dq_\mu \leq \alpha \tag{A.9}$$

The values of μ that are not rejected make up the *confidence interval* for μ at the *confidence level (CL)* $= 1 - \alpha$. The edges of the confidence interval are the lower and upper "limits" for μ.

A.3.1.2. Profile Likelihood Ratio

If present, the p-value also depends on the nuisance parameters. Strictly speaking, to reject a value of μ, $p_\mu(\nu) \leq \alpha$ must be satisfied for all nuisance parameters, ν. To avoid this difficulty of scanning over all ν's, we need to define the test statistic such that it is independent of ν. This can be archived approximately using the *profile likelihood ratio*:

$$\lambda(\mu) = \frac{\overbrace{L(\mu, \hat{\hat{b}}, \hat{\hat{\nu}})}^{\text{Max } L \text{ for a given } \mu}}{\underbrace{L(\hat{\mu}, \hat{b}, \hat{\nu})}_{\text{Max } L \text{ for any } \mu,b,\nu}} \tag{A.10}$$

The distribution of $\lambda(\mu)$ becomes independent of ν in the limit of large data sample.

A.3.1.3. Test Statistic q_μ for Upper Limits

To derive an upper limit for signal strength μ, we can use the test statistic q_μ defined as:

$$q_\mu = \begin{cases} -2 \ln \lambda(\mu) & \hat{\mu} \leq \mu \\ 0 & \hat{\mu} > \mu \end{cases} \tag{A.11}$$

Once again I will note that bigger q_μ means less compatibility with the signal hypothesis. The likelihood ratio $\lambda(\mu)$ is smaller the further away the estimated $\hat{\mu}$ is from the testing μ, so q_μ increases as $\hat{\mu}$ becomes smaller than μ. On the other hand, if $\hat{\mu} > \mu$, we does not regard that as incompatible with the data, so we set $q_\mu = 0$ in that case[3]. Now we can

[3] If this is still not clear, think back to simple event counting experiment. If the counted number of events is greater than $s + b$, it is compatible with the signal hypothesis, not the other way around.

quantify the compatibility between the data and hypothesis with a value of μ using p-value from Eq. (A.9).

Using large sample approximation, the closed form of $f(q_\mu|\mu)$ can be derived [84]. Using these results, one can obtain:

$$p_\mu = 1 - \Phi(\sqrt{q_\mu}) \tag{A.12}$$

$$Z_\mu = \sqrt{q_\mu} \tag{A.13}$$

These are some of the *asymptotic formulae* present in Ref. [84]. Others includes those for other test statistics such as the discovery test statistic (q_0), etc. Using Eq. (A.12), we can set $p_\mu = \alpha$, (typically $\alpha = 0.05$ i.e. 95% CL) and solve for the upper limit of μ.

A.3.2. The CL$_s$ Prescription [82, 83]

Let us recall the setup of the test to set an upper limit of a new process; we have a signal hypothesis which predicts $\mu s + b$ events, where μ proportional to the signal cross section. We will preform a test of size $\alpha = 0.05$ for all values of μ. After we obtain x_{obs} from the experiment, we use Eq. (A.9) to reject values of μ. What is left is the confidence interval where we claim that μ fall into with 95% confidence level.

For a very small value of μ, the prediction of the outcome is almost identical to the background-only hypothesis. We do not expect the experiment to have any sensitivity to such low μ. Indeed, when defining the critical region with $\alpha = 0.05$, the result of the test will have very low power; expectedly slightly larger than α. Therefore, we do not want to claim that these small μ's are excluded. However, by construction of the test, the probability of rejecting the signal model is 5%. In a search where a wide range of μ are tested, it is unavoidable that some μ's are excluded even if there is no sensitivity.

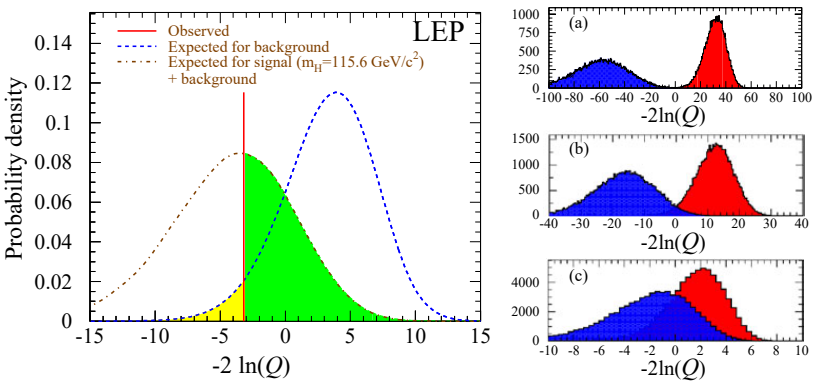

FIGURE A.3. Taken from [83]. Left: PDFs of the combined Higgs search at LEP. The yellow area on the left of the observation line is p_b $(1 - \mathrm{CL}_b)$ and the green area on the right is p_μ (CL_{s+b}). Right: As the hypothesized Higgs mass increases, the production cross section decrease. This reflects in the evolution of the PDFs as shown from (a) to (c).

To avoid this problem, we use the measure CL_s, which increases as the sensitivity decreases. The CL_s is defined as:

$$\mathrm{CL}_s = \frac{p_\mu}{1 - p_b} \tag{A.14}$$

Where p_b is the p-value of the background-only hypothesis. Then we reject μ if $\mathrm{CL}_s(\mu) \leq \alpha$. As the sensitivity decreases, p_b also increases, so the condition is not satisfied. Since $p_b \geq 0$, CL_s is always bigger than p_μ. Therefore, CL_s will be more conservative on rejecting μ's. These concepts are illustrated in Fig. A.3.

APPENDIX B

PHOTON+JETS CONTROL REGION

B.1. Photon Definition

The photon reconstruction is only considered in the photon control region. Photon candidates are obtained and calibrated using `GetPhoton` function in `SUSYTools`. A signal photon must pass the selection requirements that are described in Table B.1.

TABLE B.1. Photon selection criteria.

Cut	Value
Acceptance	$p_{\mathrm{T}} > 130$GeV, $\lvert\eta\rvert < 2.37$
Quality	`Tight`
Isolation	`FixCutLoose`

The p_{T} requirement is to ensure that the event is on the plateau of the photon trigger `HLT_g120_loose`.

B.2. Description of the Method

An alternative method to estimate the $Z(\nu\nu)$ + jets background is to use γ+jets events and then treat the photon as invisible. The advantage of this compared to $Z \to \ell\ell$+jets method described in Section 5.1.3 is the larger statistics, which can be crucial for tight signal regions. The γ + jets process has higher cross section and does not suffer from the branching ratio like $Z \to \ell\ell$ while still being relatively easy to select a reasonably pure sample. The main disadvantage is the differences in kinematics of the photon and Z.

The sample for γ+jets control region (CRγ) is obtained by looking for at least one high quality photon in the event as defined in B.1. The events are collected using photon trigger `HLT_g120_Loose`. The leading p_{T} photon in the event is considered the signal photon.

The exact definition of the CR is as follows:

1. At least one photon as defined in B.1
2. The signal photon must match the one that fired the trigger
3. The signal photon must pass `FixedCutTight` isolation requirement
4. To reduce the contamination from processes with real $E_{\mathrm{T}}^{\mathrm{miss}}$ such as $t\bar{t}\gamma$, an upper cut at $E_{\mathrm{T}}^{\mathrm{miss}} < 50$ GeV is applied
5. To be in the region where kinematics of $Z(\nu\nu)$ + jets and γ +jets events to be similar, the signal photon's $p_{\mathrm{T}} > 200$GeV cut is applied
6. The transverse momentum of the signal photon is vectorially removed from the $E_{\mathrm{T}}^{\mathrm{miss}}$ calculation in order to treat the photon as Z decays to neutrinos; Labeled as $E_{\mathrm{T}}^{\mathrm{miss}'}$.

A summary of the CR pre-selection can be found in Appendix B.2.

TABLE B.2. Selection for the γ + jets CR.

Selection	Requirement
Trigger	`HLT_g120_loose`
Photon quality	Tight
Number of photon	≥ 1
Signal photon	Leading-p_{T} photon and trigger matched
Signal photon Isolation	FixedCutTight
E_T^{miss}	$E_{\mathrm{T}}^{\mathrm{miss}} < 50$GeV
Signal Photon p_{T}	$p_{\mathrm{T}} > 200$GeV
jet multiplicity	$p_{\mathrm{T}} \geq (80, 80, 20, 20)$GeV

After the preselections there are two discrepancies between the data and MC. First, the MC underestimated the data by about 30% as seen in Fig. B.1-B.7. The other issue is the distribution of real $E_{\mathrm{T}}^{\mathrm{miss}}$ as seen in Fig. B.1a which shows a trend in the normalization. On the other hand, the $E_{\mathrm{T}}^{\mathrm{miss}'}$ shows a good agreement with the data (apart from the normalization as mentioned) as seen in Fig. B.1b.

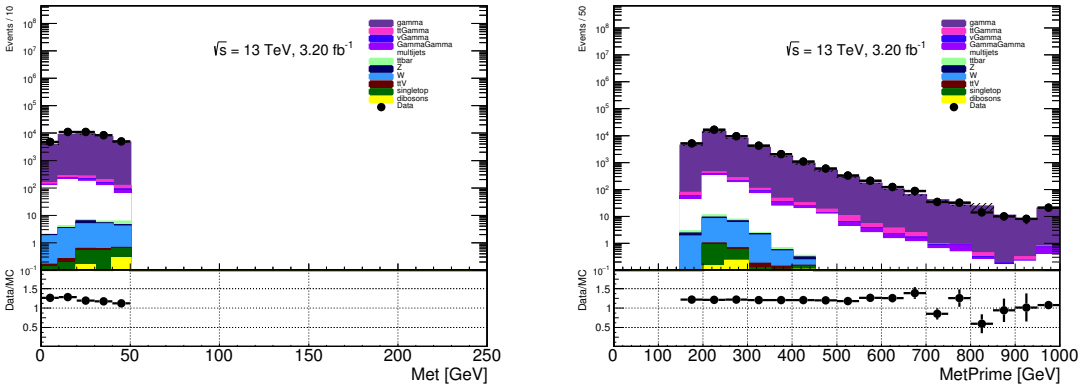

(a) Real $E_{\mathrm{T}}^{\mathrm{miss}}$ (b) $E_{\mathrm{T}}^{\mathrm{miss}}$ after adding the signal photon p_{T}

FIGURE B.1. $E_{\mathrm{T}}^{\mathrm{miss}}$ distributions.

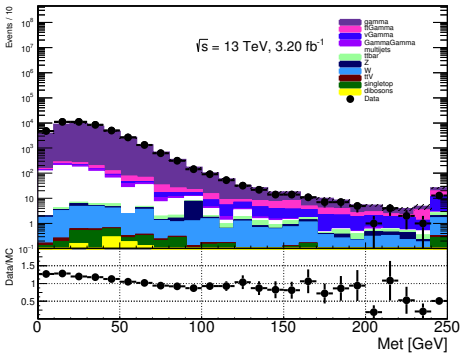

FIGURE B.2. Real $E_{\mathrm{T}}^{\mathrm{miss}}$ similar to Fig. B.1a but without the $E_{\mathrm{T}}^{\mathrm{miss}}$ cut applied.

B.3. Results

A normalization factor is defined as the fellowing. The effect of non-unity normalization factor from non-γ + jets samples is neglected due to a very high γ + jets purity of this CR. Therefore:

$$SF = \frac{N_{CR\gamma}^{Data} - N_{non-\gamma}^{MC}}{N_{\gamma}^{MC}} = \frac{N_{\gamma}^{Data}}{N_{\gamma}^{MC}} \tag{B.1}$$

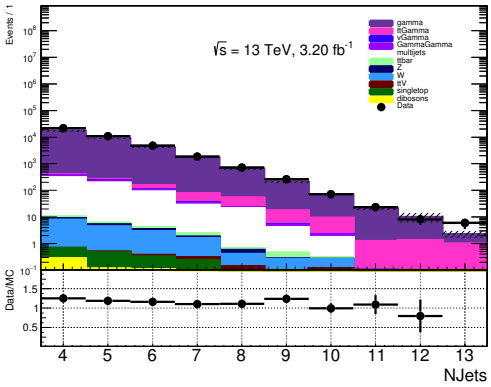

(a) Jet Multiplicities

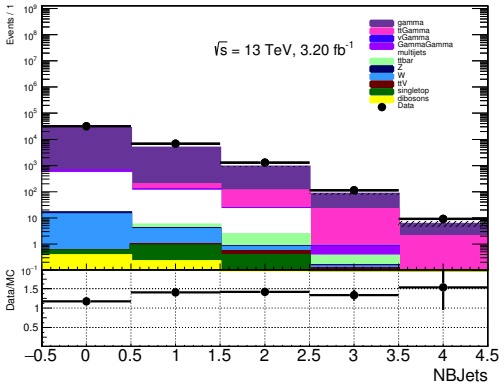

(b) Number of b-tagged jets

FIGURE B.3. Jet and b-tagged jets multiplicities

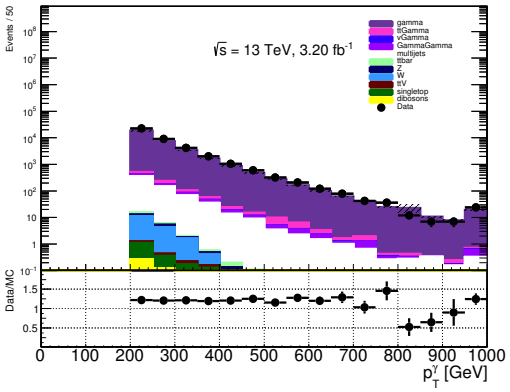

(a) Photon p_{T}

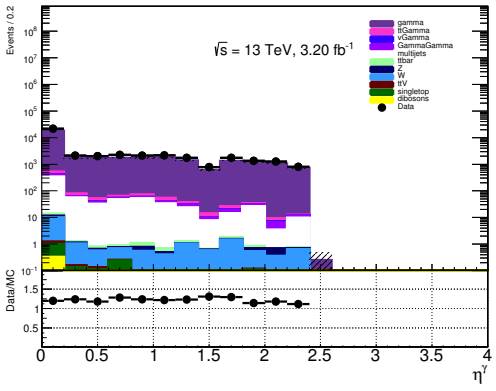

(b) Photon

FIGURE B.4. Properties of the signal photons.

In other words, the normalization factor in this case is simply the Data/MC ratio. The backgrounds composition and scale factors is shown in Table B.3

Since the statistics are very high in this region, the selection can be tightened to be closer to the Signal Regions compared to the nominal $Z \to \ell\ell$+jets method.

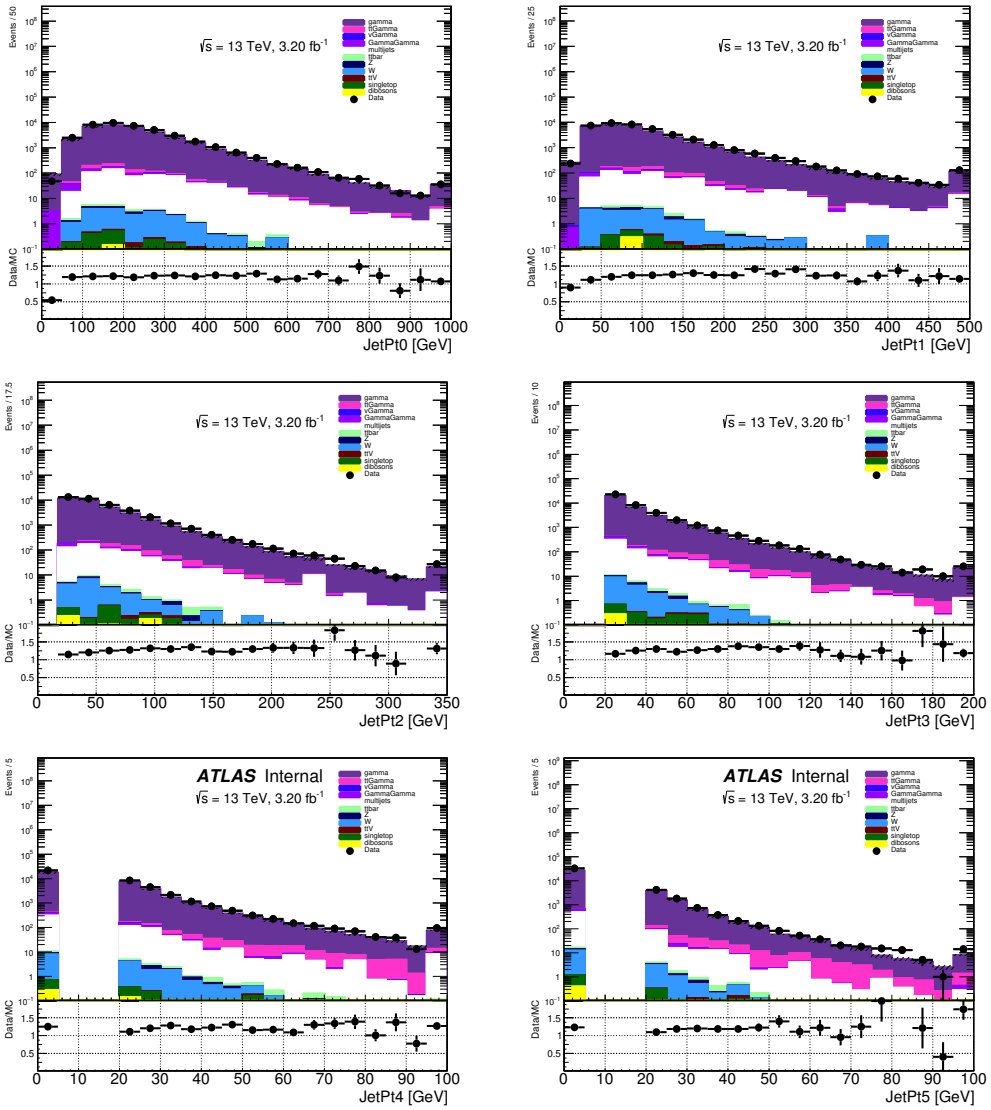

FIGURE B.5. Distributions of the p_{T} of the six leading jets are shown. The ratio between data and MC are given in the bottom panel. The hashed area in both the top and lower panel represent the uncertainty due to MC statistics.

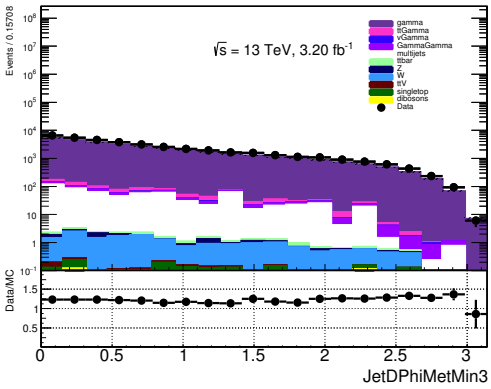

(a) $\left|\Delta\phi\left(\text{jet}^{i}, E_{\text{T}}^{\text{miss}}\right)\right|$ for $i = 3$

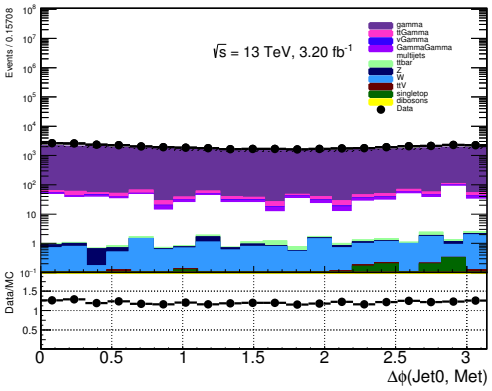

(b) $\left|\Delta\phi\left(\text{jet}^{1}, E_{\text{T}}^{\text{miss}}\right)\right|$

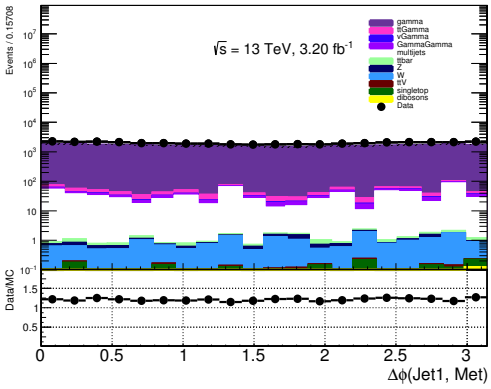

(c) $\left|\Delta\phi\left(\text{jet}^{2}, E_{\text{T}}^{\text{miss}}\right)\right|$

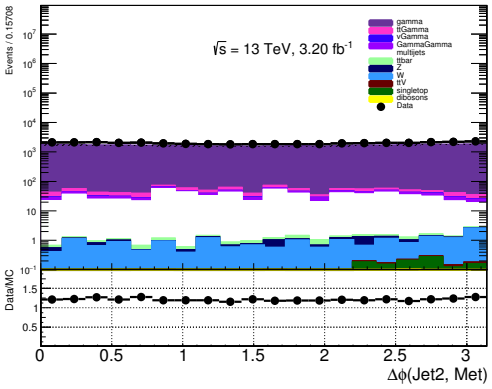

(d) $\left|\Delta\phi\left(\text{jet}^{2}, E_{\text{T}}^{\text{miss}}\right)\right|$

FIGURE B.6. $\Delta\phi$ between jets and $E_{\text{T}}^{\text{miss}}$

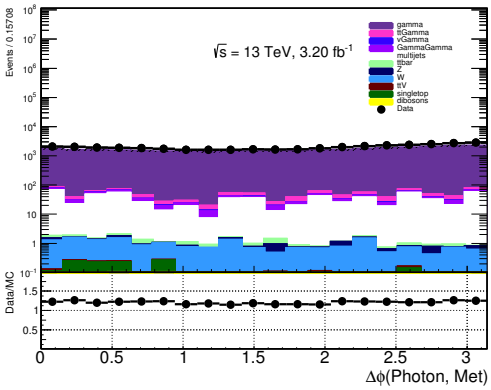

(a) $\left|\Delta\phi\left(, E_{\text{T}}^{\text{miss}}\right)\right|$

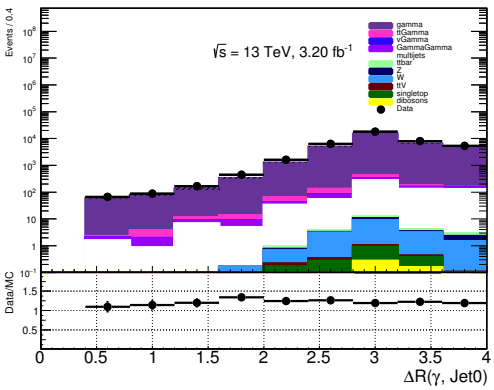

(b) $|\Delta R\,(, jet)|$

FIGURE B.7. $\Delta\phi$, ΔR between photon and jet and $E_{\text{T}}^{\text{miss}}$

TABLE B.3. Background composition of CRγ

Sample	CRγ_0b	CRγ_2b
Data	39984 ± 199.96	1420 ± 37.68
gamma	31976.87 ± 70.88	873.17 ± 13.54
ttGamma	193.42 ± 8.47	108.77 ± 6.36
vGamma	24.96 ± 0.34	0.81 ± 0.05
GammaGamma	117.49 ± 3.27	1.82 ± 0.43
multijets	613.82 ± 67.66	18.59 ± 8.6
ttbar	3.69 ± 0.38	1.75 ± 0.26
Z	2.90 ± 0.57	0.06 ± 0.02
W	15.43 ± 1.48	0.27 ± 0.07
ttV	0.35 ± 0.01	0.2 ± 0.01
singletop	1.27 ± 0.19	0.45 ± 0.11
dibosons	0.58 ± 0.15	0 ± 0
Total MC	32950.79 ± 153.40	1005.89 ± 29.45
SF	1.21 ± 0.01	1.41 ± 0.06

ΛCDM lambda cold dark matter.

$\langle Q \rangle$ The average jet quality is defined as the energy–squared weighted average of the pulse quality of the calorimeter cells ($Q_{\text{cell}}^{\text{LAr}}$) in the jet. This quantity is normalized such that $0 < \langle Q \rangle < 1$.

$E_{\mathbf{T}}^{\mathbf{miss}'}$ $E_{\text{T}}^{\text{miss}}$ after objects treated as invisible are added to the $E_{\text{T}}^{\text{miss}}$. Usually used in 2-lepton CR.

$E_{\mathbf{T}}^{\mathbf{miss}}$ missing transverse energy.

$E_{\mathbf{neg}}$ The sum of all cells with negative energy.

M_P Plank mass scale $\sqrt{8\pi G_{\text{Newton}}}$.

N_{PV} number of primary vertex.

***R*-parity** A discrete Z_2 symmetry imposed in addition to SUSY to prevent baryon and lepton number violation terms in the MSSM.

X_0 Radiation length. Defined as a distance in which an electron or position lose $1 - e^{-1}$ of its energy [13]. See http://pdg.lbl.gov/2016/reviews/rpp2016-rev-passage-particles-matter.pdf.

$\Delta R_{\mathbf{min}}$ Top reconstruction by combining the closest three jets.

$\Lambda_{\mathbf{CC}}$ Cosmological constant.

$\Lambda_{\mathbf{UV}}$ The UV cutoff for Standard Model as effective theory.

$\Lambda_{\mathbf{QCD}}$ The energy scale which α_{S} become strong.

$\lambda_{\mathbf{int}}$ Nuclear interaction length. Defined as the average distance a high-energy hadron has to travel inside the medium before a nuclear interaction occurs [13]. See http://pdg.lbl.gov/2016/reviews/rpp2016-rev-passage-particles-matter.pdf.

$\mathbf{p_T^{miss}}$ missing transverse momentum.

$\mathbf{p_T^{miss,track}}$ $\mathbf{p}_{\mathrm{T}}^{\mathrm{miss}}$ from tracks only.

$\mathbf{m}$ micrometer (10^{-6}).

$\sqrt{s}$ center-of-mass energy.

$\mathbf{CL}_s$ See Appendix A.3.2.

$f_{\mathbf{EM}}$ The ratio of the energy deposited in the electromagnetic calorimeter to the total energy of the jet.

$f_{\mathbf{HEC}}$ The ratio of the energy deposited in the HEC calorimeter to the total energy.

$f_{\mathbf{ch}}$ The ratio of the scalar sum of the p_{T} of the tracks coming from the primary vertex associated to the jet divided by the jet p_{T}.

$f_{\mathbf{max}}$ The maximum energy fraction in any single calorimeter layer.

$f_{\mathbf{Q}}^{\mathbf{HEC}}$ Fraction of the energy in the HEC calorimeter cells of a jet with poor signal shape quality defined as $Q_{\mathrm{cell}}^{\mathrm{LAr}} > 4000$.

$f_{\mathbf{Q}}^{\mathbf{LAr}}$ Fraction of the energy in the LAr calorimeter cells of a jet with poor signal shape quality defined as $Q_{\mathrm{cell}}^{\mathrm{LAr}} > 4000$.

$t_{\mathbf{jet}}$ Time of the calorimeter cell energy deposits by constructing the weighted average of the time of the energy deposits in the jet, weighted by the square of the cell energies.

LAr calorimeter liquid argon calorimeter.

ALFA Absolute Luminosity For ATLAS.

AMSB Anomaly-mediated Supersymmetry Breaking.

BDT boosted decision tree.

BR branching ratio.

BSM beyond Standard Model.

CA Cambridge/Aachen.

CKM Cabbibo-Kobayashi-Maskawa.

CL confidence level.

CMB cosmic microwave background.

CMSSM Constrained Minimum Supersymmetric Standard Model.

CR control region.

CSC cathode strip chambers.

CST calorimeter soft term.

dark matter See Section 1.2.3.1.

ECAL electromagnetic calorimeter.

EF event filter.

EFT effective field theory.

EM electromagnetic.

EMEC electromagnetic hadronic endcap calorimeter.

EW electroweak.

EWSB electroweak symmetry breaking.

FCal forward calorimeter.

FCNC flavor-changing neutral current.

FSR final state radiation.

GMSB Gauge-mediated Supersymmetry Breaking.

GSC global sequential corrections.

GUT grand unified theory.

HCAL hadronic calorimeter.

HEC LAr hadronic endcap calorimeter.

HLT high-level trigger.

IBL insertable *B*-layer.

ID inner detector.

IP interaction point.

ISR initial state radiation.

JER jet energy resolution.

JES jet energy scale.

JVF jet vertex fraction.

JVT jet vertex tagger.

L1Calo level 1 calorimeter trigger.

LAr liquid argon.

LHC Large Hadron Collider.

LSP lightest supersymmetric particle.

LUCID LUminosity measurement using Cherenkov Integrating Detector.

MACHO massive compact halo objects.

MC Monte Carlo.

MDT monitored drift tube.

ME matrix element.

MOND Modified Newtonian Dynamics.

MSSM Minimum Supersymmetric Standard Model.

mSUGRA minimum supergravity.

NbTi niobium-titanium.

NN neural network.

PDF parton distribution function.

PMSB Planck-scale-Mediated Supersymmetry Breaking.

pMSSM Phenomenological Minimum Supersymmetric Standard Model.

PS parton shower.

QCD quantum chromodynamic.

RF radiofrequency.

RoI region of interest.

RPC resistive plate chambers.

SCT semiconductor tracker.

SM Standard Model.

SR signal region.

SUSY supersymmetry.

TDAQ trigger and data acquisition.

TGC thin gap chambers.

TileCal tile calorimeter.

TRT transition radiation tracker.

TST track soft term.

UE underlying event.

UV ultraviolet.

VEV vacuum expectation value.

VR validation region.

WIMP weakly interacting massive particle.

ZDC Zero-Degree Calorimeter.

REFERENCES CITED

[1] ATLAS Collaboration. *Search for the Supersymmetric Partner of the Top Quark in the Jets+Emiss Final State at sqrt(s) = 13 TeV*. Tech. rep. ATLAS-CONF-2016-077. Geneva: CERN, Aug. 2016. URL: https://cds.cern.ch/record/2206250.

[2] ATLAS Collaboration. "Summary of the ATLAS experiment's sensitivity to supersymmetry after LHC Run 1 — interpreted in the phenomenological MSSM". In: *JHEP* 1510 (2015), p. 134. DOI: 10.1007/JHEP10(2015)134. arXiv: 1508.06608 [hep-ex].

[3] Chaowaroj Wanotayaroj. "The effect of ATLAS Run-1 supersymmetric searches in the pMSSM". In: *23rd International Conference on Supersymmetry and Unification of Fundamental Interactions (SUSY2015), Tahoe, CA, USA*. Aug. 2015. URL: https://cds.cern.ch/record/2047858.

[4] Chaowaroj Wanotayaroj. "Poster for LHCP2014: Search for direct pair production of the top squark in all-hadronic final states in proton-proton collisions at $\sqrt{s} = 8$ TeV with the ATLAS detector". In: *Proceedings, 2nd Conference on Large Hadron Collider Physics Conference (LHCP 2014): New York, USA, June 2-7, 2014*. June 2014. URL: https://cds.cern.ch/record/1707904.

[5] Benjamin Nachman et al. "Jets from Jets: Re-clustering as a tool for large radius jet reconstruction and grooming at the LHC". In: *JHEP* 02 (2015), p. 075. DOI: 10.1007/JHEP02(2015)075. arXiv: 1407.2922 [hep-ph].

[6] ATLAS Collaboration. "Search for direct pair production of the top squark in all-hadronic final states in proton–proton collisions at $\sqrt{s} = 8$ TeV with the ATLAS detector". In: *JHEP* 1409 (2014), p. 015. DOI: 10.1007/JHEP09(2014)015. arXiv: 1406.1122 [hep-ex].

[7] Spencer Chang et al. “Revisiting Theories with Enhanced Higgs Couplings to Weak Gauge Bosons”. In: *Phys. Rev.* D86 (2012), p. 095015. DOI: 10.1103/PhysRevD.86.095015. arXiv: 1207.0493 [hep-ph].

[8] ATLAS Collaboration. “Observation of a new particle in the search for the Standard Model Higgs boson with the ATLAS detector at the LHC”. In: *Phys. Lett. B* 716 (2012), p. 1. DOI: 10.1016/j.physletb.2012.08.020. arXiv: 1207.7214 [hep-ex].

[9] CMS Collaboration. “Observation of a new boson at a mass of 125 GeV with the CMS experiment at the LHC”. In: *Phys. Lett. B* 716 (2012), p. 30. DOI: 10.1016/j.physletb.2012.08.021. arXiv: 1207.7235 [hep-ex].

[10] Yuval Grossman. “Introduction to flavor physics”. In: *Flavianet School on Flavour Physics Karlsruhe, Germany, September 7-18, 2009*. [,73(2014)]. 2014, pp. 111–144. DOI: 10.5170/CERN-2010-002.111,10.5170/CERN-2014-003.73. arXiv: 1006.3534 [hep-ph]. URL: https://inspirehep.net/record/858514/files/arXiv:1006.3534.pdf.

[11] D. Green. *High PT Physics at Hadron Colliders*. Cambridge University Press, 2005. ISBN: 0521835097.

[12] S. Bethke. “Standard model physics at LEP”. In: *NATO Advanced Study Institute on Particle Production Spanning MeV and TeV Energies (Nijmegen 99) Nijmegen, Netherlands, August 8-20, 1999*. 2000. arXiv: hep-ex/0001023 [hep-ex]. URL: http://alice.cern.ch/format/showfull?sysnb=2168419.

[13] K. A. Olive et al. “Review of Particle Physics”. In: *Chin. Phys.* C38 (2014), p. 090001. DOI: 10.1088/1674-1137/38/9/090001.

[14] Nazar Bartosik. *tt decay channels*. June 2016. URL: http://bartosik.pp.ua/hep_sketches/tt_decay_channels.

[15] Cliff Burgess and Guy Moore. *The Standard Model: A Primer*. Cambridge University Press, 2007. ISBN: 0521860369.

[16] Stephen P. Martin. "A Supersymmetry primer: Version 7". In: (2016). [Adv. Ser. Direct. High Energy Phys.18,1(1998)]. DOI: 10.1142/9789812839657_0001, 10.1142/9789814307505_0001. arXiv: hep-ph/9709356 [hep-ph].

[17] Planck collaboration. "Planck 2015 results. I. Overview of products and scientific results". In: (2015). arXiv: 1502.01582 [astro-ph.CO].

[18] Steven Weinberg. "The Cosmological Constant Problem". In: *Rev. Mod. Phys.* 61 (1989), pp. 1–23. DOI: 10.1103/RevModPhys.61.1.

[19] J. R. Brownstein and J. W. Moffat. "The Bullet Cluster 1E0657-558 evidence shows modified gravity in the absence of dark matter". In: *Monthly Notices of the Royal Astronomical Society* 382.1 (2007), pp. 29–47. DOI: 10.1111/j.1365-2966.2007.12275.x. eprint: http://mnras.oxfordjournals.org/content/382/1/29.full.pdf+html. URL: http://mnras.oxfordjournals.org/content/382/1/29.abstract.

[20] Scott W. Randall et al. "Constraints on the Self-Interaction Cross-Section of Dark Matter from Numerical Simulations of the Merging Galaxy Cluster 1E 0657-56". In: *Astrophys. J.* 679 (2008), pp. 1173–1180. DOI: 10.1086/587859. arXiv: 0704.0261 [astro-ph].

[21] Felix Kahlhoefer et al. "Colliding clusters and dark matter self-interactions". In: *Mon. Not. Roy. Astron. Soc.* 437.3 (2014), pp. 2865–2881. DOI: 10.1093/mnras/stt2097. arXiv: 1308.3419 [astro-ph.CO].

[22] Boris Kayser. "Neutrino Physics". In: *TRISEP Summer School 2016*. June 2016.

[23] S. Weinberg. *The Quantum Theory of Fields*. Quantum theory of fields v. 2-3. Cambridge University Press, 2000. ISBN: 9780521660006. URL: https://books.google.com/books?id=Mqj6bCJd9MQC.

[24] D. I. Kazakov. "Beyond the standard model: In search of supersymmetry". In: *2000 European School of high-energy physics, Caramulo, Portugal, 20 Aug-2 Sep 2000: Proceedings*. 2000, pp. 125–199. arXiv: hep-ph/0012288 [hep-ph]. URL: http://alice.cern.ch/format/showfull?sysnb=2235897.

[25] Thomas G. Rizzo. "The Zoo of BSM Physics at the LHC". In: *The 40th SLAC Summer Institute*. Aug. 2012.

[26] Michele Papucci, Joshua T. Ruderman, and Andreas Weiler. "Natural SUSY Endures". In: *JHEP* 09 (2012), p. 035. DOI: 10.1007/JHEP09(2012)035. arXiv: 1110.6926 [hep-ph].

[27] Johan Alwall, Philip Schuster, and Natalia Toro. "Simplified Models for a First Characterization of New Physics at the LHC". In: *Phys. Rev.* D79 (2009), p. 075020. DOI: 10.1103/PhysRevD.79.075020. arXiv: 0810.3921 [hep-ph].

[28] Carola F. Berger et al. "Supersymmetry Without Prejudice". In: *JHEP* 02 (2009), p. 023. DOI: 10.1088/1126-6708/2009/02/023. arXiv: 0812.0980 [hep-ph].

[29] Lyndon Evans and Philip Bryant. "LHC Machine". In: *JINST* 3 (2008). Ed. by Lyndon Evans, S08001. DOI: 10.1088/1748-0221/3/08/S08001.

[30] Cinzia De Melis. *The CERN accelerator complex. Complexe des accélérateurs du CERN*. General Photo. Jan. 2016. URL: http://cds.cern.ch/record/2119882.

[31] ATLAS Collaboration. "The ATLAS Experiment at the CERN Large Hadron Collider". In: *JINST* 3 (2008), S08003. DOI: 10.1088/1748-0221/3/08/S08003.

[32] M Capeans et al. “ATLAS Insertable B-Layer Technical Design Report”. In: CERN-LHCC-2010-013. ATLAS-TDR-19 (Sept. 2010). URL: http://cds.cern.ch/record/1291633.

[33] D. Green. *At the Leading Edge: The ATLAS and CMS LHC Experiments*. World Scientific, 2010. ISBN: 9789814277617.

[34] ATLAS collaboration. *TRT performance in Run 1*. Tech. rep. ATL-COM-INDET-2015-041. Geneva: CERN, June 2015. URL: https://cds.cern.ch/record/2021497.

[35] James E. Brau and Tony A. Gabriel. “Comments on “on the energy resolution of uranium and other hadron calorimeters””. In: *Nuclear Instruments and Methods in Physics Research Section A: Accelerators, Spectrometers, Detectors and Associated Equipment* 275.1 (1989), pp. 190–191. ISSN: 0168-9002. DOI: http://dx.doi.org/10.1016/0168-9002(89)90351-3. URL: http://www.sciencedirect.com/science/article/pii/0168900289903513.

[36] James E. Brau, John A. Jaros, and Hong Ma. “Advances in Calorimetry”. In: *Annual Review of Nuclear and Particle Science* 60.1 (2010), pp. 615–644. DOI: 10.1146/annurev.nucl.012809.104449. eprint: http://dx.doi.org/10.1146/annurev.nucl.012809.104449. URL: http://dx.doi.org/10.1146/annurev.nucl.012809.104449.

[37] ATLAS Collaboration. *2015 start-up trigger menu and initial performance assessment of the ATLAS trigger using Run-2 data*. Tech. rep. ATL-DAQ-PUB-2016-001. Geneva: CERN, Mar. 2016. URL: https://cds.cern.ch/record/2136007.

[38] ATLAS Collaboration. *Trigger Operation Public Results*. URL: https://twiki.cern.ch/twiki/bin/view/AtlasPublic/TriggerOperationPublicResults.

[39] F. Krauss. “QCD and Monte Carlo Event Generators”. In: *TRISEP Summer School 2016*. June 2016.

[40] T. Gleisberg et al. “Event generation with SHERPA 1.1”. In: *JHEP* 02 (2009), p. 007. DOI: 10.1088/1126-6708/2009/02/007. arXiv: 0811.4622 [hep-ph].

[41] Nazar Bartosik. *Event simulation in HEP experiments*. July 2016. URL: http://bartosik.pp.ua/hep_sketches/event_simulation.

[42] Nazar Bartosik. *MC simulation of a pp collision*. July 2016. URL: http://bartosik.pp.ua/hep_sketches/pp_collision_ttH.

[43] T. Sjöstrand, S. Mrenna and P. Skands. “PYTHIA 6.4 Physics and Manual”. In: *JHEP* 05 (2006), p. 026. DOI: 10.1088/1126-6708/2006/05/026. arXiv: hep-ph/0603175.

[44] Torbjorn Sjostrand, Stephen Mrenna, and Peter Z. Skands. “A Brief Introduction to PYTHIA 8.1”. In: *Comput. Phys. Commun.* 178 (2008), pp. 852–867. DOI: 10.1016/j.cpc.2008.01.036. arXiv: 0710.3820 [hep-ph].

[45] Simone Alioli et al. “A general framework for implementing NLO calculations in shower Monte Carlo programs: the POWHEG BOX”. In: *JHEP* 06 (2010), p. 043. DOI: 10.1007/JHEP06(2010)043. arXiv: 1002.2581 [hep-ph].

[46] J. Alwall et al. “The automated computation of tree-level and next-to-leading order differential cross sections, and their matching to parton shower simulations”. In: *JHEP* 07 (2014), p. 079. DOI: 10.1007/JHEP07(2014)079. arXiv: 1405.0301 [hep-ph].

[47] David J. Lange. “The EvtGen particle decay simulation package”. In: *Nuclear Instruments and Methods in Physics Research Section A: Accelerators, Spectrometers, Detectors and Associated Equipment* 462.1–2 (2001). BEAUTY2000, Proceedings of the 7th Int. Conf. on B-Physics at Hadron Machines, pp. 152–155. ISSN: 0168-

9002. DOI: http://dx.doi.org/10.1016/S0168-9002(01)00089-4. URL: http://www.sciencedirect.com/science/article/pii/S0168900201000894.

[48] S. Agostinelli et al. "GEANT4: A Simulation toolkit". In: *Nucl. Instrum. Meth.* A506 (2003), pp. 250–303. DOI: 10.1016/S0168-9002(03)01368-8.

[49] ATLAS collaboration. *Performance of the ATLAS Inner Detector Track and Vertex Reconstruction in the High Pile-Up LHC Environment*. Tech. rep. ATLAS-CONF-2012-042. Geneva: CERN, Mar. 2012. URL: http://cds.cern.ch/record/1435196.

[50] ATLAS collaboration. *The Optimization of ATLAS Track Reconstruction in Dense Environments*. Tech. rep. ATL-PHYS-PUB-2015-006. Geneva: CERN, Mar. 2015. URL: https://cds.cern.ch/record/2002609.

[51] R. Frühwirth. "Application of Kalman filtering to track and vertex fitting". In: *Nuclear Instruments and Methods in Physics Research Section A: Accelerators, Spectrometers, Detectors and Associated Equipment* 262.2 (1987), pp. 444–450. ISSN: 0168-9002. DOI: http://dx.doi.org/10.1016/0168-9002(87)90887-4. URL: http://www.sciencedirect.com/science/article/pii/0168900287908874.

[52] ATLAS Collaboration. "Topological cell clustering in the ATLAS calorimeters and its performance in LHC Run 1". In: (2016). arXiv: 1603.02934 [hep-ex].

[53] Gavin P. Salam and Gregory Soyez. "A Practical Seedless Infrared-Safe Cone jet algorithm". In: *JHEP* 05 (2007), p. 086. DOI: 10.1088/1126-6708/2007/05/086. arXiv: 0704.0292 [hep-ph].

[54] Matteo Cacciari, Gavin P. Salam, and Gregory Soyez. "The Anti-k(t) jet clustering algorithm". In: *JHEP* 04 (2008), p. 063. DOI: 10.1088/1126-6708/2008/04/063. arXiv: 0802.1189 [hep-ph].

[55] Stephen D. Ellis and Davison E. Soper. "Successive combination jet algorithm for hadron collisions". In: *Phys. Rev.* D48 (1993), pp. 3160–3166. DOI: 10.1103/PhysRevD.48.3160. arXiv: hep-ph/9305266 [hep-ph].

[56] Yuri L. Dokshitzer et al. "Better jet clustering algorithms". In: *JHEP* 08 (1997), p. 001. DOI: 10.1088/1126-6708/1997/08/001. arXiv: hep-ph/9707323 [hep-ph].

[57] Matteo Cacciari and Gavin P. Salam. "Dispelling the N^3 myth for the k_t jet-finder". In: *Phys. Lett.* B641 (2006), pp. 57–61. DOI: 10.1016/j.physletb.2006.08.037. arXiv: hep-ph/0512210 [hep-ph].

[58] Matteo Cacciari, Gavin P. Salam, and Gregory Soyez. "FastJet User Manual". In: *Eur. Phys. J.* C72 (2012), p. 1896. DOI: 10.1140/epjc/s10052-012-1896-2. arXiv: 1111.6097 [hep-ph].

[59] ATLAS Collaboration. "Jet Calibration and Systematic Uncertainties for Jets Reconstructed in the ATLAS Detector at $\sqrt{s} = 13$ TeV". In: ATL-PHYS-PUB-2015-015 (July 2015). URL: https://cds.cern.ch/record/2037613.

[60] ATLAS Collaboration. "Performance of jet substructure techniques for large-R jets in proton–proton collisions at $\sqrt{s} = 7$ TeV using the ATLAS detector". In: *JHEP* 1309 (2013), p. 076. DOI: 10.1007/JHEP09(2013)076. arXiv: 1306.4945 [hep-ex].

[61] ATLAS Collaboration. "Selection of jets produced in 13TeV proton-proton collisions with the ATLAS detector". In: ATLAS-CONF-2015-029 (July 2015). URL: https://cds.cern.ch/record/2037702.

[62] D W Miller, A Schwartzman, and D Su. *Pile-up jet energy scale corrections using the jet-vertex fraction method*. Tech. rep. ATL-PHYS-INT-2009-090. Geneva: CERN, Sept. 2009. URL: https://cds.cern.ch/record/1206864.

[63] D0 collaboration. "Measurement of the $p\bar{p} \to t\bar{t}$ production cross section at $\sqrt{s} =$ 1.96-TeV in the fully hadronic decay channel." In: *Phys. Rev.* D76 (2007), p. 072007. DOI: 10.1103/PhysRevD.76.072007. arXiv: hep-ex/0612040 [hep-ex].

[64] ATLAS Collaboration. "Tagging and suppression of pileup jets with the ATLAS detector". In: ATLAS-CONF-2014-018 (May 2014). URL: https://cds.cern.ch/record/1700870.

[65] ATLAS Collaboration. "Performance of *b*-Jet Identification in the ATLAS Experiment". In: *JINST* 11.04 (2016), P04008. DOI: 10.1088/1748-0221/11/04/P04008. arXiv: 1512.01094 [hep-ex].

[66] ATLAS Collaboration. "Commissioning of the ATLAS *b*-tagging algorithms using $t\bar{t}$ events in early Run-2 data". In: ATL-PHYS-PUB-2015-039 (Aug. 2015). URL: https://cds.cern.ch/record/2047871.

[67] Nazar Bartosik. *b-jet tagging*. June 2016. URL: http://bartosik.pp.ua/hep_sketches/btagging.

[68] ATLAS Collaboration. "b-tagging in dense environments". In: ATL-PHYS-PUB-2014-014 (Aug. 2014). URL: https://cds.cern.ch/record/1750682.

[69] ATLAS collaboration. *Electron efficiency measurements with the ATLAS detector using the 2015 LHC proton-proton collision data*. Tech. rep. ATLAS-CONF-2016-024. Geneva: CERN, June 2016. URL: http://cds.cern.ch/record/2157687.

[70] W Lampl et al. *Calorimeter Clustering Algorithms: Description and Performance*. Tech. rep. ATL-LARG-PUB-2008-002. ATL-COM-LARG-2008-003. Geneva: CERN, Apr. 2008. URL: https://cds.cern.ch/record/1099735.

[71] ATLAS Collaboration. *Photon identification in 2015 ATLAS data*. Tech. rep. ATL-PHYS-PUB-2016-014. Geneva: CERN, Aug. 2016. URL: http://cds.cern.ch/record/2203125.

[72] ATLAS Collaboration. "Measurement of the muon reconstruction performance of the ATLAS detector using 2011 and 2012 LHC proton–proton collision data". In: *Eur. Phys. J. C* 74 (2014), p. 3130. DOI: 10.1140/epjc/s10052-014-3130-x. arXiv: 1407.3935 [hep-ex].

[73] ATLAS Collaboration. "Muon reconstruction performance of the ATLAS detector in proton–proton collision data at $\sqrt{s} = 13$ TeV". In: (2016). arXiv: 1603.05598 [hep-ex]. PERF-2015-10.

[74] J. Illingworth and J. Kittler. "A survey of the hough transform". In: *Computer Vision, Graphics, and Image Processing* 44.1 (1988), pp. 87–116. ISSN: 0734-189X. DOI: http://dx.doi.org/10.1016/S0734-189X(88)80033-1. URL: http://www.sciencedirect.com/science/article/pii/S0734189X88800331.

[75] ATLAS Collaboration. *Expected performance of missing transverse momentum reconstruction for the ATLAS detector at* $\sqrt{s} = 13$ *TeV*. Tech. rep. ATL-PHYS-PUB-2015-023. Geneva: CERN, July 2015. URL: http://cds.cern.ch/record/2037700.

[76] W. Beenakker et al. "Stop production at hadron colliders". In: *Nucl. Phys.* B 515 (1998), pp. 3–14. DOI: 10.1016/S0550-3213(98)00014-5.

[77] Wim Beenakker et al. "Supersymmetric top and bottom squark production at hadron colliders". In: *JHEP* 08 (2010), p. 098. DOI: 10.1007/JHEP08(2010)098. arXiv: 1006.4771 [hep-ph].

[78] W. Beenakker et al. "Squark and gluino hadroproduction". In: *Int. J. Mod. Phys.* A 26 (2011), pp. 2637–2664. DOI: 10.1142/S0217751X11053560.

[79] Christoph Borschensky et al. “Squark and gluino production cross sections in pp collisions at $\sqrt{s} = 13, 14, 33$ and 100 TeV”. In: *Eur. Phys. J.* C74.12 (2014), p. 3174. DOI: 10.1140/epjc/s10052-014-3174-y. arXiv: 1407.5066 [hep-ph].

[80] ATLAS Collaboration. *Summary plots from the ATLAS Standard Model physics group*. Aug. 2016. URL: https://atlas.web.cern.ch/Atlas/GROUPS/PHYSICS/CombinedSummaryPlots/SM/index.html#ATLAS_b_SMSummary_FiducialXsect.

[81] ATLAS Collaboration. “Search for squarks and gluinos with the ATLAS detector in final states with jets and missing transverse momentum using 4.7 fb^{-1} of $\sqrt{s} = 7$ TeV proton-proton collision data”. In: *Phys. Rev.* D87.1 (2013), p. 012008. DOI: 10.1103/PhysRevD.87.012008. arXiv: 1208.0949 [hep-ex].

[82] Thomas Junk. “Confidence level computation for combining searches with small statistics”. In: *Nucl. Instrum. Meth.* A434 (1999), pp. 435–443. DOI: 10.1016/S0168-9002(99)00498-2. arXiv: hep-ex/9902006 [hep-ex].

[83] A L Read. “Presentation of search results: the CL s technique”. In: *Journal of Physics G: Nuclear and Particle Physics* 28.10 (2002), p. 2693. URL: http://stacks.iop.org/0954-3899/28/i=10/a=313.

[84] Glen Cowan et al. “Asymptotic formulae for likelihood-based tests of new physics”. In: *Eur. Phys. J.* C71 (2011). [Erratum: Eur. Phys. J.C73,2501(2013)], p. 1554. DOI: 10.1140/epjc/s10052-011-1554-0,10.1140/epjc/s10052-013-2501-z. arXiv: 1007.1727 [physics.data-an].

[85] ATLAS Collaboration. “Search for a supersymmetric partner to the top quark in final states with jets and missing transverse momentum at $\sqrt{s} = 7$ TeV with the ATLAS detector”. In: *Phys. Rev. Lett.* 109 (2012), p. 211802. DOI: 10.1103/PhysRevLett.109.211802. arXiv: 1208.1447 [hep-ex].

[86] Tongyan Lin, Edward W. Kolb, and Lian-Tao Wang. “Probing dark matter couplings to top and bottom quarks at the LHC”. In: *Phys. Rev.* D88.6 (2013), p. 063510. DOI: 10.1103/PhysRevD.88.063510. arXiv: 1303.6638 [hep-ph].

[87] Daniel Abercrombie et al. “Dark Matter Benchmark Models for Early LHC Run-2 Searches: Report of the ATLAS/CMS Dark Matter Forum”. In: (2015). Ed. by Antonio Boveia et al. arXiv: 1507.00966 [hep-ex].

[88] Gavin Grant Hesketh et al. “Monte Carlo Generators for the Production of a W or Z/γ^* Boson in Association with Jets at ATLAS in Run 2”. In: ATL-PHYS-PUB-2016-003 (Jan. 2016). URL: https://cds.cern.ch/record/2120133.

[89] Christian Gutschow et al. “Multi-Boson Simulation for 13 TeV ATLAS Analyses”. In: ATL-PHYS-PUB-2016-002 (Jan. 2016). URL: https://cds.cern.ch/record/2119986.

[90] Benjamin Philip Nachman and Andrea Knue. “Simulation of top quark production for the ATLAS experiment at sqrt(s) = 13 TeV”. In: ATL-PHYS-PUB-2016-004 (Jan. 2016). URL: https://cds.cern.ch/record/2120417.

[91] Josh Mcfayden et al. “Modelling of the $t\bar{t}H$ and $t\bar{t}V$ ($V = W, Z$) processes for $\sqrt{s} = 13$ TeV ATLAS analyses”. In: ATL-PHYS-PUB-2016-005 (Jan. 2016). URL: https://cds.cern.ch/record/2120826.

[92] Maria Moreno Llacer and Leonid Serkin. “Validation of Monte Carlo event generators in the ATLAS Collaboration for LHC Run 2”. In: ATL-PHYS-PUB-2016-001 (Jan. 2016). URL: https://cds.cern.ch/record/2119984.

[93] Leif Lönnblad and Stefan Prestel. “Merging Multi-leg NLO Matrix Elements with Parton Showers”. In: *JHEP* 03 (2013), p. 166. DOI: 10.1007/JHEP03(2013)166. arXiv: 1211.7278 [hep-ph].

[94] Richard D. Ball et al. “Parton distributions with LHC data”. In: *Nucl. Phys. B* 867 (2013), pp. 244–289. DOI: 10.1016/j.nuclphysb.2012.10.003. arXiv: 1207.1303 [hep-ph].

[95] ATLAS Collaboration. “ATLAS Run 1 Pythia8 tunes”. In: ATL-PHYS-PUB-2014-021 (Nov. 2014). URL: https://cds.cern.ch/record/1966419.

[96] Hung-Liang Lai et al. “New parton distributions for collider physics”. In: *Phys. Rev.* D82 (2010), p. 074024. DOI: 10.1103/PhysRevD.82.074024. arXiv: 1007.2241 [hep-ph].

[97] Peter Zeiler Skands. “Tuning Monte Carlo Generators: The Perugia Tunes”. In: *Phys. Rev.* D82 (2010), p. 074018. DOI: 10.1103/PhysRevD.82.074018. arXiv: 1005.3457 [hep-ph].

[98] Haipeng An and Lian-Tao Wang. “Opening up the compressed region of top squark searches at 13 TeV LHC”. In: *Phys. Rev. Lett.* 115 (2015), p. 181602. DOI: 10.1103/PhysRevLett.115.181602. arXiv: 1506.00653 [hep-ph].

[99] Sebastian Macaluso et al. “Revealing Compressed Stops Using High-Momentum Recoils”. In: *JHEP* 03 (2016), p. 151. DOI: 10.1007/JHEP03(2016)151. arXiv: 1506.07885 [hep-ph].

[100] Paul Jackson, Christopher Rogan, and Marco Santoni. “Sparticles in Motion - getting to the line in compressed scenarios with the Recursive Jigsaw Reconstruction”. In: (2016). arXiv: 1607.08307 [hep-ph].

[101] ATLAS Collaboration. “Search for direct pair production of the top squark in all-hadronic final states in proton-proton collisions at $\sqrt{s} = 8$ TeV with the ATLAS detector”. In: *JHEP* 09 (2014), p. 015. DOI: 10.1007/JHEP09(2014)015. arXiv: 1406.1122 [hep-ex].

[102] ATLAS Collaboration. "ATLAS Run 1 searches for direct pair production of third-generation squarks at the Large Hadron Collider". In: *Eur. Phys. J.* C75.10 (2015). [Erratum: Eur. Phys. J.C76,no.3,153(2016)], p. 510. DOI: 10.1140/epjc/s10052-015-3726-9,10.1140/epjc/s10052-016-3935-x. arXiv: 1506.08616 [hep-ex].

[103] ATLAS Collaboration. "Search for top squark pair production in final states with one isolated lepton, jets, and missing transverse momentum in $\sqrt{s}$ =8 TeV *pp* collisions with the ATLAS detector". In: *JHEP* 11 (2014), p. 118. DOI: 10.1007/JHEP11(2014)118. arXiv: 1407.0583 [hep-ex].

[104] ATLAS Collaboration. "Search for direct top-squark pair production in final states with two leptons in pp collisions at $\sqrt{s}$ = 8TeV with the ATLAS detector". In: *JHEP* 06 (2014), p. 124. DOI: 10.1007/JHEP06(2014)124. arXiv: 1403.4853 [hep-ex].

[105] ATLAS Collaboration. *Luminosity summary plots for 2016 pp data taking*. Oct. 2016. URL: https://twiki.cern.ch/twiki/bin/view/AtlasPublic/LuminosityPublicResultsRun2#Luminosity_summary_plots_for_201.

[106] Ian Snyder. Private communication. Sept. 6, 2016.

[107] David Krohn, Jesse Thaler, and Lian-Tao Wang. "Jets with Variable R". In: *JHEP* 06 (2009), p. 059. DOI: 10.1088/1126-6708/2009/06/059. arXiv: 0903.0392 [hep-ph].

[108] ATLAS Collaboration. *Search for top squarks in final states with one isolated lepton, jets, and missing transverse momentum in $\sqrt{s}$ = 13 TeV pp collisions with the ATLAS detector*. Tech. rep. ATLAS-CONF-2016-050. Geneva: CERN, Aug. 2016. URL: https://cds.cern.ch/record/2206132.

[109] ATLAS Collaboration. *Summary plots from the ATLAS Supersymmetry physics group*. Aug. 2016. URL: https://atlas.web.cern.ch/Atlas/GROUPS/PHYSICS/CombinedSummaryPlots/SUSY/index.html.

[110] Glen Cowen. "Statistical Methods for Particle Physics". In: *TRISEP Summer School 2016*. June 2016.

[111] Daniel Whiteson. "Practical Statistics for Particle Physics". In: *HCPSS 2014*. Aug. 2014.